WEANING-INDUCED LIVER INVOLUTION: A NOVEL MECHANISM OF METASTASIS IN POSTPARTUM BREAST CANCER

By

Erica T. Goddard

A THESIS/DISSERTATION

Presented to the Cancer Biology Program
& the Oregon Health & Science University
School of Medicine
in partial fulfillment of
the requirements for the degree of

Doctor of Philosophy

January 2017

School of Medicine

Oregon Health & Science University

CERTIFICATE OF APPROVAL

This is to certify that the PhD dissertation of

Erica Thornton Goddard

has been approved

_____
Pepper J. Schedin, PhD, Mentor/Advisor

_____
Virginia F. Borges, MD, MMSc, Clinical Mentor/Advisor

_____
Melissa H. Wong, PhD, Oral Exam Committee Chair

_____
Lisa Coussens, PhD, Member

_____
Amanda W. Lund, PhD, Member

_____
Caroline Enns, PhD, Member

_____
Willscott E. Naugler, MD, Member

Table of Contents

List of Figures

List of Tables

List of abbreviations

3D	Three-dimensional
ACN	Acetonitrile
ADH	Adipic acid dihydrazide
AJCC	American Joint Committee on Cancer
ALT	Alanine aminotransferase
ANOVA	Analysis of variance
AST	Aspartate aminotransferase
ATP	Adenosine triphosphate
BMDC	Bone marrow derived cell
BMDM	Bone marrow derived monocyte
BMI	Body mass index
B_{Reg}	B regulatory cell
CAF	Cancer-associated fibroblast
CC3	Cleaved caspase 3
CCl_4	Carbon tetrachloride
CCL9	C-C motif chemokine ligand 9
CCL21	C-C motif chemokine ligand 21
CCR1	C-C motif chemokine receptor 1 (CD191)
CCR2	C-C motif chemokine receptor 2 (CD192)
CCR7	C-C motif chemokine receptor 7 (CD197)
CD11b	Integrin alpha M
CD11c	Integrin alpha X
CD16	Cluster of differentiation 16 (FcγRIII)
CD3	Cluster of differentiation 3
CD32	Cluster of differentiation 32 (FcγRII)
CD34	Cluster of differentiation 34
CD4	Cluster of differentiation 4
CD45	Cluster of differentiation 45
CD68	Cluster of differentiation 68
CD8	Cluster of differentiation 8
CDAA	Choline deficient L-amino acid-defined diet
cDNA	Complementary deoxyribonucleic acid
CI	Confidence interval
CK18	Cytokeratin 18
CNBr	Cyanogen bromide
CO_2	Carbon dioxide
Cox-1	Cyclooxygenase-1
Cox-2	Cyclooxygenase-2

CSF1	Colony stimulating factor 1
CSF1R	Colony stimulating factor 1 receptor
CTC	Circulating tumor cell
CTL	Cytotoxic T lymphocyte
CU	University of Colorado
CV	Coefficient of variation
CXCL12	C-X-C motif chemokine ligand 12 (SDF-1)
CXCR4	C-X-C chemokine receptor type 4
CYP	Cytochrome P450
DAB	3,3'-diaminobenzidine
DAVID	Database for annotation, visualization, and integrated discovery
DC	Dendritic cell
DCIS	Ductal carcinoma in situ
DFCI	Dana Farber Cancer Institute
DICOM	Digital imaging and communications in medicine
DMEM	Dulbecco's modified eagle medium
DMN	Dimethylnitrosamine
DMSO	Dimethyl sulfoxide
DNA	Deoxyribonucleic acid
DP	PGD_2 receptor
DTC	Disseminated tumor cell
Dx	Diagnosis
ECL	Enhanced chemiluminescence
ECM	Extracellular matrix
EDTA	Ethylenediaminetetraacetic acid
EET	Epoxyeicosatrienoic acid
eGFP	Enhanced green fluorescent protein
EGF	Epidermal growth factor
EHS	Engelbreth-Holm-Swarm
EP	PGE_2 receptor
ER	Estrogen receptor
F4/80	EGF-like module-containing mucin-like hormone receptor-like 1
FA	Formic acid
FACIT	Fibril-associated collagens with interrupted triple helices
FACS	Fluorescence-activated cell sorting
FAH	Fumarylacetoacetate hydrolase
FAK	Focal adhesion kinase
FASP	Filter assisted sample prep
FDA	Food and Drug Administration
FFA	Free fatty acid

FFPE	Formalin fixed paraffin embedded
FoxP3	Forkhead box P3
FP	PGF_2 receptor
GAPDH	Glyceraldehyde 3-phosphate dehydrogenase
GFP	Green fluorescent protein
GH	Glowing head
GI	Gastrointestinal
G-CSF	Granulocyte-colony stimulating factor
H_2O	Hydrogen dioxide
H&E	Hematoxylin and eosin
HA	Hyaluronic acid
Her2	Human epidermal growth factor receptor 2
HETE	Hydroxyeicosatetraenoic acid
HIPAA	Health insurance portability and accountability act
HPETE	Hydroperoxyeicosatetraenoic acid
HR	Hazard ratio
HRP	Horseradish peroxidase
HSC	Hepatic stellate cell
IACUC	Institutional animal care and use committee
iECM	Insoluble ECM
IFNγ	Interferon γ
IGF-1	Insulin-like growth factor-1
IHC	Immunohistochemistry
IL-1β	Interleukin 1β
IL-10	Interleukin 10
IL-13	Interleukin 13
IL-17	Interleukin 17
IL-2	Interleukin 2
IL-4	Interleukin 4
IL-6	Interleukin 6
IP	PGI_2 receptor
IRB	Institutional review board
KEGG	Kyoto encyclopedia of genes and genomes
KEP	$K14cre^{F/F};Cdh1^{F/F};Trp53^{F/F}$ mice
LC-MS/MS	Liquid chromatography-tandem mass spectrometry
LC-SRM	Liquid chromatography-selected reaction monitoring
LLC	Lewis lung carcinoma
LN_2	Liquid nitrogen
LOD	Limits of detection
LOQ	Limits of quantification

LOX	Lysyl oxidase
LOXL1-4	Lysyl oxidase like 1-4
LXA_4	Lipoxin A4
LXB_4	Lipoxin B4
Ly6C	Lymphocyte antigen 6 complex, locus C1
Ly6G	Lymphocyte antigen 6 complex, locus G
Mac-1	Macrophage-1 antigen
Mafia	Macrophage fas-induced apoptosis
MALDI-TOF	Matrix-assisted laser desorption/ionization time of flight
MEC	Mammary epithelial cell
MHC2	Major Histocompatibility complex 2
MG	Mammary gland
MMP-2	Matrix metalloproteinase-2
MMP-9	Matrix metalloproteinase-9
MMTV	Mouse mammary tumor virus
MRI	Magnetic resonance imaging
MS	Mass spectrometry
MT1-MMP	Membrane type 1-matrix metalloproteinase 1 (MMP-14)
NET	Neutrophil extracellular trap
NK	Natural Killer cell
NSAID	Non-steroidal anti-inflammatory drug
OCT	Optimal cutting temperature
OHSU	Oregon Health & Science University
OR	Odds ratio
PBS	Phosphate buffered saline
PCA	Principle component analysis
PDAC	Pancreatic ductal adenocarcinoma
PGD	Prostaglandin D
PGE_2	Prostaglandin E_2
PGF_2	Prostaglandin F_2
PGG	Prostaglandin G
PGH_2	Prostaglandin H_2
PGI_2	Prostacyclin
PI3K	Phosphoinositide 3-kinase
PLS-DA	Partial least squares discriminate analysis
POSTN	Periostin
PPBC	Postpartum breast cancer
PR	Progesterone receptor
PSI	Pounds per square inch
PTM	Post-translational modification

PyMT	Polyoma Virus middle T antigen
QC	Quality control
QconCAT	Quantitative concatamer
Rag1	Recombination activation gene 1
RANKL	Receptor activator of nuclear factor kappa-B ligand
RBC	Red blood cell
RNA	Ribonucleic acid
RR	Relative risk
RT	Room temperature
RT-PCR	Reverse transcriptase polymerase chain reaction
RTU	Ready to use
SCID	Severe combined immunodeficiency
SDF-1	Stromal cell-derived factor 1 (CXCL12)
SDS-PAGE	Sodium dodecyl sulfate polyacrylamide gel
sECM	Soluble ECM
SEM	Standard error of the mean
SIL	Stable isotope labeled
SRM	Selection reaction monitoring
Stat3	Signal transducer and activator of transcription 3
TACS-3	Tumor-associated collagen signature-3
TAM	Tumor-associated macrophage
TGFβ	Transforming growth factor β
T_H1	T helper type 1
T_H2	T helper type 2
TLR3	Toll like receptor 3
TMEM	Tumor microenvironment of metastasis
TN	Triple negative
TNC	Tenascin-C
TNFα	Tumor necrosis factor α
TP	TXA_2 receptor
T_{Reg}	T regulatory cell
TRS	Target retrieval solution
TSP-1	Thrombospondin 1
TUNEL	Terminal deoxynucleotidyl transferase dUTP nick end labeling
TXA_2	Thromboxane A_2
TXB_2	Thromboxane B_2
UC-AMC	University of Colorado – Anschutz Medical Campus
UHPLC	Ultra-high performance liquid chromatography
UPLC	Ultra performance liquid chromatography
VCAM-1	Vascular cell adhesion molecule 1

VEGF-A	Vascular endothelial growth factor A
VEGF-C	Vascular endothelial growth factor C
VEGFR1	Vascular endothelial growth factor receptor 1
VIP	Variable of importance in projection
YWBC	Young women’s breast cancer

Acknowledgements

I would like to thank my mentor Pepper Schedin for her unwavering commitment to my training as a PhD candidate, but also for being a friend and an ally. Pepper's dedication to my graduate trainings is unquestionable, and I know that in my future scientific career her training will guide me to ask the difficult, unconventional, and exciting questions when no one else will, and to do so thoughtfully.

I would like to thank my clinical mentor Virginia Borges. One of the major motivating factors throughout my training has been a desire to positively impact breast cancer patient outcomes; Dr. Borges has given me many of the tools required to do this important translational research. I would also like to thank Courtney Betts and Qiuchen Guo, fellow graduate students who not only persevered alongside me but raised me up to be a better scientist and, more so, a better person. I also owe a huge thank you to every individual who has been a part of the Schedin and Borges labs over the years; each and every one of them has touched my work in immeasurable ways.

Finally, I would like to thank my best friend and partner, Karen. Without Karen I may still have gotten to this point, but it would not have been with so much inspiration, pride, or poise.

Abstract

A postpartum breast cancer diagnosis, defined as a diagnosis within 5 years of a pregnancy, is an independent risk factor for metastasis and death compared to breast cancers diagnosed in nulliparous or pregnant patients. The work described here investigates potential mechanisms unique to the postpartum woman that might be responsible for increased metastasis. Metastatic success requires tumor cells to successfully navigate the metastatic cascade, including immune escape, local dissemination, intravasation/entry into vasculature, survival in the circulation, extravasation/exit from vasculature, and finally seeding, survival, and outgrowth at secondary sites. Work by the Schedin lab has identified post-weaning mammary gland involution, physiologic tissue regression characterized by ECM remodeling and immune influx, as a major contributing factor to the increased risk for metastasis observed in postpartum breast cancers. Specifically, mammary gland involution promotes early steps of the metastatic cascade including primary tumor growth, immune escape, local dissemination, and increased intravasation. However, later events in the metastatic cascade, particularly survival and outgrowth at the secondary site, represent major bottlenecks to metastatic efficiency. One identified way of overcoming these bottlenecks is establishment of tumor-educated pro-metastatic niches, defined as secondary microenvironments supportive of tumor cell seeding and outgrowth. I hypothesized that secondary sites are altered post-weaning, establishing pro-metastatic niches in the *absence* of tumor education, such that tumor cell seeding and/or outgrowth are promoted specifically in postpartum breast cancers. This dissertation describes the discovery of weaning-induced liver involution, a tissue-remodeling event that establishes a transient

pro-metastatic microenvironment that is more supportive of disseminated tumor cell seeding and/or survival. These studies predict elevated site-specific liver metastasis in postpartum breast cancers. Importantly, I observed elevated risk for liver metastasis, but not lung, bone, or brain metastasis, in rodent models of postpartum breast cancer, and in postpartum breast cancer patients, suggesting a postpartum phenomenon unique to the liver. Additionally, non-steroidal anti-inflammatory drugs (NSAIDs) that target cyclooxygenases (Cox-1/Cox-2) have shown efficacy in abrogating early events in the metastatic cascade in preclinical models. I explored NSAIDs as an avenue of reducing liver metastasis in the postpartum setting in rodents. Data from these NSAID studies suggest that low-dose ibuprofen has effects on the liver microenvironment distinct from those in the mammary gland, but does not abrogate the increased risk for postpartum liver metastasis. Finally, to better understand the high risk for metastasis associated with postpartum breast cancer diagnoses, I have participated in a retrospective study in young women with breast cancer (n=804). This work revealed that postpartum breast cancers, particularly those diagnosed at stage II, are more likely to present with lymph node metastasis and develop distant metastasis despite similar tumor size at diagnosis. In this cohort, I have also identified that postpartum breast cancer patients with estrogen receptor negative disease represent a breast cancer subset at particularly high risk for metastasis. In sum, this dissertation describes an essential role for the transient pro-metastatic microenvironment established in the post-weaning liver in facilitating postpartum breast cancer metastasis and provides new insight into the high risk for metastasis in postpartum breast cancers.

Chapter I: Background and introduction

Postpartum breast cancer is associated with a high rate of metastasis

Breast cancer is the most common cancer diagnosis and the second leading cause of cancer-related death in women worldwide[1]. The major cause of death in breast cancer is due to metastatic spread of the disease[2]. Cumulative risk for a woman being diagnosed with breast cancer increases dramatically with age (Fig.1-1A). However, it is important to note that the number of invasive breast cancers diagnosed is actually similar for women in their 40s as it is for women of relatively older age (Fig.1-1B). And even for women in their 30s the number of breast cancers being diagnosed is high (~10/1000) (Fig.1-1B). This is in part due to the fact that with increasing age women are at increased risk of death due to other causes, thus diagnosis of breast cancer in younger premenopausal women represents a considerable proportion of total breast cancer diagnoses. Importantly, a subset of young women's breast cancer is made up of a unique population of women diagnosed following a pregnancy with particularly aggressive disease, as discussed below.

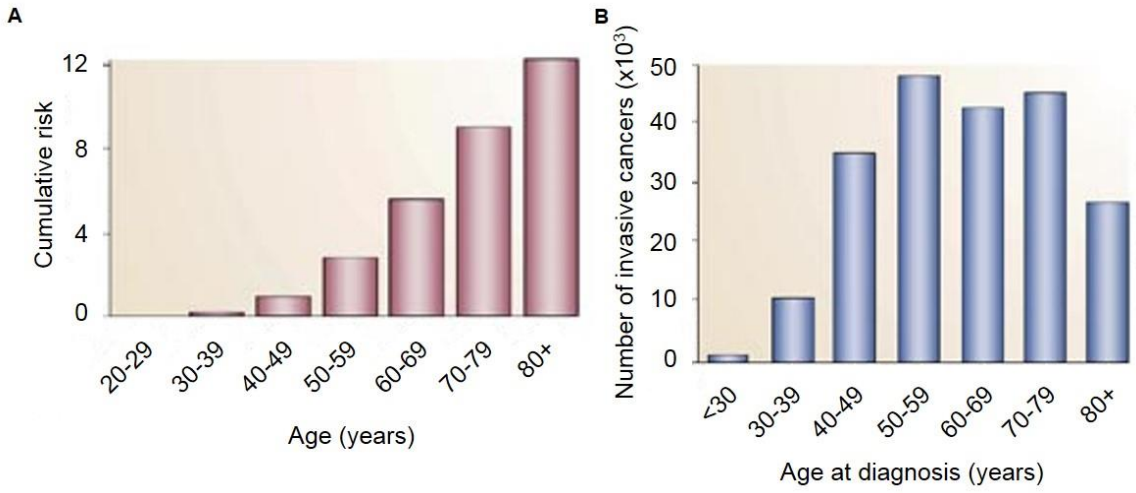

Figure 1-1: Risk for and rate of breast cancer diagnoses by age

(A) Cumulative risk for breast cancer in women, by age group. **(B)** Number of invasive breast cancers diagnosed in women, separated by age group. Figure has been adapted and reprinted with permission: Schedin P., Pregnancy-Associated Breast Cancer and Metastasis, Nature Reviews Cancer, 2006.

Postpartum breast cancer (PPBC), currently defined as a diagnosis of breast cancer within 5 years of giving birth, is associated with an increased risk for metastasis and death compared to patients who have never given birth (i.e. nulliparous) or those diagnosed while pregnant[3-12]. The high risk for metastasis is independent of poor prognostic indicators including biologic subtype, stage of disease, age, or year of diagnosis[3,6-9,11]. This data suggests that host microenvironmental factors in the postpartum period, as opposed to tumor intrinsic properties, may play a prominent role in the risk for metastasis. It is estimated that ~25,000 new young women's breast cancer diagnoses are made yearly in the United States[12-14], and an estimated 40-65% of these diagnoses are impacted by a recent pregnancy[9]. Further, older age at first birth correlates with increased risk of PPBC[15-17]. As more women are choosing to delay child bearing until relatively older ages[18-20], evidence suggests that the incidence of PPBC will increase[21-23]. Despite these findings, PPBC is still an under-recognized subset of breast cancer[23] and there is a paucity of studies addressing the high risk of metastasis in PPBC. As a result, treatment options for postpartum patients, and biomarkers to identify those PPBC patients at greatest risk for metastasis are lacking[23].

The poor prognosis of postpartum breast cancer has been attributed to the tissue remodeling process of weaning-induced mammary gland involution, as well as to hormones associated with pregnancy, delays in diagnosis, and enrichment of poor prognostic biologic subtypes in postpartum patients. During pregnancy, the breast epithelium is exposed to elevated estrogens, progesterone, and insulin-like growth factor, hormones known to support tumor progression[24-28]. An extensive analysis of 311 patients

diagnosed during pregnancy and 865 non-pregnant controls revealed no effect of a pregnancy diagnosis on disease free or overall survival[10]. These data suggest that the elevated hormones of pregnancy have minimal impact on risk of metastasis in postpartum breast cancers. Delays in diagnosis represent another explanation for the poor prognosis of PPBC, as increased breast density associated with pregnancy, lactation, and breast involution limits the efficacy of mammography and self-exam[29,30]. Although delayed diagnosis is an on-going problem in young women's breast cancer, nulliparous and postpartum breast cancer patient groups are typically diagnosed with similarly sized tumors and staged disease[3,6,9]. Thus, it is unlikely that delayed diagnosis accounts for the poor prognosis of PPBC. Another explanation for why PPBC may have poor prognosis is that they may be enriched for triple negative biologic subtype, a tumor biologic subtype associated with poor prognosis and high risk for metastasis[31]. It is well-documented that breast cancer diagnoses in young women are more likely to be triple negative[32-35]. However, the frequencies of poor prognostic biologic subtypes do not differ by parity status in a young women's breast cancer cohort[9]. In this cohort, metastasis-free and overall survival rates remain significantly increased in PPBC after adjustment for stage and biologic subtype[9]. In one study using an African American breast cancer cohort, patients with premenopausal breast cancer had similar rates of estrogen receptor (ER) negative disease, a surrogate for poor prognostic biologic subtypes, regardless of parity status[36]. In sum, these data suggest that the impact of pregnancy hormones, delayed diagnoses, and the tumor intrinsic characteristics assessed here have a marginal impact on the poor prognosis of postpartum breast cancers. These data suggest that a breast cancer diagnosis made in the postpartum period is an independent risk factor for metastasis.

Finally, these data provide further support that tumor extrinsic, as opposed to tumor intrinsic attributes, promote metastasis of postpartum breast cancers. For these reasons, this chapter will focus on what is known about pathologic tumor microenvironments that may shed light into mechanisms by which normal physiology can promote metastasis.

Mammary gland involution and the 'involution hypothesis'

One event that occurs postpartum and may explain the increased risk for metastasis with a postpartum diagnosis is post-weaning mammary gland involution. Following cessation of lactation, or directly after a pregnancy in the absence of lactation, the gland undergoes an orchestrated cell-death mediated process characterized by robust tissue remodeling. Studies in rodents have identified two distinct phases of mammary gland involution, a reversible cell death phase and an irreversible tissue remodeling phase[37]. The process of mammary gland involution begins with milk stasis in the gland, resulting in distention of the alveolar structures and initiation of cell-death programs[37,38]. During the cell death phase, greater than 80% of the mammary epithelial cells (MEC) undergo programmed cell death[39], the bulk of which is complete by day 4 post-weaning[37,40]. The mechanisms of MEC cell death are numerous and are still being elucidated. However, it is clear that lipid uptake by MECs, followed by disruption of lysosomal membranes and cathepsin protease release is a major contributing pathway to mammary epithelial cell death[41]. There appears to be an integral switch in the involution process between days 2-4 post-weaning, at which point stromal remodeling commences[37]. The remodeling phase is characterized by increased immune influx, deposition and remodeling of extracellular matrix (ECM), and lymphangiogenesis, events consistent with wound healing[37,42-49].

From these observations the involution hypothesis was proposed, which states that the physiologically regulated wound healing-like process of weaning-induced mammary gland involution represents a tumor promotional window that increases metastatic efficiency[15]. A bulk of evidence has since been produced which supports the involution hypothesis. I will discuss this evidence below, within the larger context of the metastatic cascade.

The metastatic cascade

Metastasis is the process by which tumor cells spread to distant organs via a multi-step progression that involves local dissemination away from the primary tumor, intravasation or entry into the vasculature, survival in the circulation, extravasation out of the vasculature and into the tissue, successful seeding, and finally outgrowth at secondary sites, a process coined the metastatic cascade (Fig.1-2). Despite the fact that metastasis is the major cause of death in cancer patients, from a single tumor cell perspective, the process is largely inefficient[50] and is particularly susceptible to cues from the microenvironment[51,52]. In fact, elements of the microenvironment including stromal cells, extracellular matrix (ECM), and secreted factors (cytokines, chemokines, growth factors, microvesicles, and proteases/enzymes) impact every step of the metastatic cascade (Fig.1-1). Further, recent advances in the field of metastasis suggest that host physiology, distinct from tumor physiology, may impact the metastatic cascade and metastatic microenvironments in ways that increase or decrease metastatic efficiency.

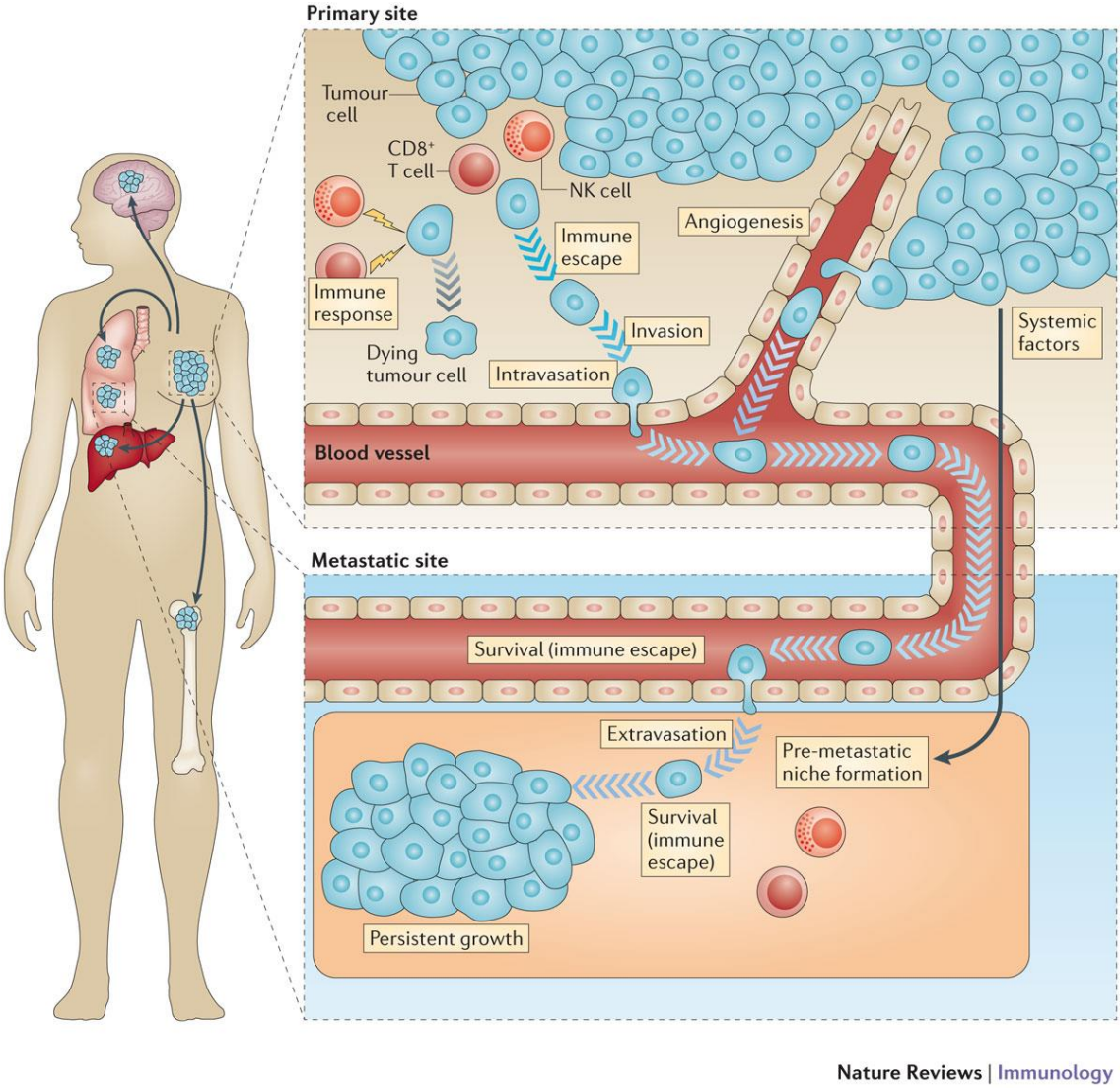

Figure 1-2: Regulation of the metastatic cascade by the microenvironment

The process of metastasis begins with local dissemination and intravasation, promoted in part by ECM remodeling, pro-tumor immune and cytokine milieus, and neovascularization. Upon intravasation, circulating tumor cells are stewarded by platelets and must evade immune cell- and shear force-mediated killing. Extravasation is an active process that may be facilitated by both endothelial and immune cells. Survival at the secondary site is considered to be a major bottleneck in the metastatic cascade as the foreign environment is often hostile and does not resemble the primary site from which the tumor cell came. Metastatic efficiency is greatly impacted by favorable microenvironments at the secondary site, known as pre-metastatic and metastatic niches. Reprinted with permission: Kitamura T et al., Immune cell promotion of metastasis, Nature Reviews Immunology, 2015.

Metastasis is thought to progress through one of two proposed models, referred to as the linear and parallel progression models[53,54]. In the linear progression model, cancers progress along a trajectory that necessitates acquisition of mutations and large tumor size prior to tumor cell escape and metastasis. The linear progression model assumes that metastasis is a late stage event and that clones within the primary tumor will be genetically similar to the secondary tumor. In comparison, the parallel progression model proposes that tumor cell dissemination is an early event in which primary and metastatic tumors progress simultaneously. Consequently, the parallel progression model assumes that the metastatic tumor will be genetically distinct from the primary tumor, suggesting an early evolutionary split between the two tumors[53,54]. The finding, in virtually all tumor types, that increasing tumor size tracks with increased risk for metastatic recurrence supports the linear progression model. Yet, numerous studies have found disseminated tumor cells (DTCs) in distant sites that lack the mutational burden observed in the primary tumor, suggesting that dissemination is indeed an early event in the progression of some tumors[55-58]. For example, in a murine model of $Her2^{+}$ breast cancer, DTCs were detected at times when only atypical ductal hyperplasia and/or ductal carcinoma in situ were detectable in mammary fat pads and prior to observable basement membrane disruption[59]. It is likely that both linear and parallel progression occurs, and that the trajectory of metastatic progression is context-dependent. The host and tumor microenvironments provide this context.

Early steps in the metastatic cascade: from primary tumor to circulation

Primary tumor growth

The metastatic process begins at the primary tumor with growth and tumor vascularization, acquisition of an invasive tumor cell phenotype, and immune evasion. Neovascularization of the primary tumor is a necessary, rate limiting event in tumor progression[60-62]. As tumors grow beyond the limits of diffusion for oxygen and nutrients, the tumor induces an angiogenic switch that facilitates tumor access to the neighboring vasculature[63,64]. Numerous studies have found that tumor-associated macrophages (TAMs) and $CD11b^{+}Gr1^{+}$ myeloid cells can promote pro-angiogenic programs in primary tumors; blockade of these programs reduces tumor angiogenesis and metastasis[65-69]. Intriguingly, blood vasculature in the mammary gland expands during pregnancy and lactation, and is higher than nulliparous vessel abundance through the first 12 days post-weaning[70] suggesting that higher blood vessel abundance may contribute to progression of tumors specifically arising postpartum. However, the blood vasculature of the involuting mammary gland regresses over time, as blood vessel abundance is highest at lactation and early involution and subsequently drops to nulliparous levels post-weaning; it is unknown if these regressing vessels support tumor growth and/or tumor cell intravasation[70]. Thus, although the role for angiogenesis is not well explored in postpartum breast cancers, other microenvironmental factors discussed below may be more important in promoting primary tumor growth in postpartum breast cancers.

Acquisition of tumor cell invasive phenotypes and local dissemination

Immune cells contribute to acquisition of invasive properties and local dissemination of tumor cells. High levels of TAMs and macrophage chemoattractants such as colony stimulating factor 1 (CSF1) are associated with poor prognosis in numerous cancers[71-73]. In rodent models, TAMs promote partnered migration with tumor cells via a paracrine-signaling loop involving tumor cell production of CSF1 and macrophage production of epidermal growth factor (EGF)[71,74]. Additionally, tumor cell fusion with macrophages is another proposed mechanism by which tumor cells gain an invasive phenotype[75,76]. Tumor cell fusion endows the fused cell with both macrophage and tumor cell gene expression patterns and is proposed to contribute to immune evasion, the tumor cell invasive phenotype, and increased metastatic efficiency[76]. Weaning-induced mammary gland involution is characterized by robust increases in $Cd11b^{+}F4/80^{+}$ macrophages observed in both rodent models[42,43] and women[77], which may promote postpartum breast cancer dissemination away from the primary tumor. In sum, immune populations, particularly macrophages, play an integral role in promoting acquisition of invasive phenotypes, thus contributing to local dissemination.

In addition to a role for macrophages in promoting dissemination away from the primary tumor, extracellular matrix composition, organization, and stiffness are also integral to tumor cell acquisition of an invasive phenotype and local dissemination. Tumor-associated collagen signature-3 (TACS-3), characterized by collagen fibers aligned perpendicular to the tumor (radial alignment), is associated with collective cell migration along the length of the collagen fiber[78]. TACS-3 is an independent poor prognostic

indicator in breast cancer, independent of tumor intrinsic properties including stage and biologic subtype[79]. Further, tumor and normal mammary epithelial cell dissemination is preferentially upregulated in collagen I enriched, but not basement membrane enriched, environments[80]. In addition to collagen, the oligosaccharide hyaluronan (HA)[81], and the matricellular protein tenascin-C (TNC)[82-86], are associated with invasive tumor cell behavior, are localized at the invasive front, and serve as predictors of distant recurrence in breast cancer. Matrix metalloproteinases (MMPs) proteolytically cleave ECM proteins, thereby facilitating local dissemination by clearing paths for tumor cells, and by releasing biologically active ECM fragments and growth factors that influence numerous cell types within the tumor microenvironment[87]. For example, membrane type-1 MMP (MT1-MMP) is involved in formation of holes or tracks through collagen that facilitate single cell and collective migration[88]. Further, MMP-2 and other proteases are elevated in pre-neoplastic disease in a mouse model of $Her2^{+}$ breast cancer and may contribute to early dissemination prior to invasive disease[59]. ECM stiffening and collagen crosslinking enzymes also correlate with poor prognosis in breast cancer[89,90]. Upregulation of the hypoxia inducible collagen crosslinking enzyme lysyl oxidase (LOX) in breast cancer contributes to tumor cell motility and invasion via collagen stiffening and adhesion to matrix in a β_1-integrin-FAK dependent manner[89,91]. Thus numerous attributes of the ECM contribute to local dissemination of tumor cells into the surrounding tissue.

ECM composition and organization described in the involuting mammary gland shares several characteristics with the ECM intimately involved in early steps of the metastatic cascade described above. Proteases, including matrix metalloproteinases, cathepsins, LOX, lysyl oxidase-like 2 (LOXL2), and plasmin serine protease begin to increase as

early as day 2-3 post-weaning and are functionally involved in cell death pathways and adipogenesis, as well as basement membrane degradation and ECM remodeling[37,43,45,49,92,93] (Guo et al., data unpublished). The involuting mammary gland has a unique ECM composition characterized by increased levels of pro-tumorigenic ECM proteins including tenascin-C, fibronectin, and radially aligned fibrillar collagen[43,47-49,94,95] (Guo et al., data unpublished). Further, the highly active protease setting of weaning-induced mammary gland involution results in degradation of matrix proteins. As mentioned above, ECM cleavage by proteases releases sequestered growth factors and cytokines and simultaneously results in production of bioactive matrix cleavage products, called matricryptins[96]. Although the ECM composition in the involuting breast in women has not yet been characterized, a role for patient primary tumor ECM signatures in supporting postpartum breast cancers are beginning to emerge. Unpublished data from the Schedin lab suggests an increased abundance of collagen post-weaning, compared to lactation breast tissue (Guo et al., data unpublished). Further, a combined high collagen I and high Cox-2 tumor signature in young women with breast cancer predicts shorter relapse-free survival[47]. Thus, in the context of a postpartum breast cancer, the ECM composition and physical organization within the tissue may support tumor cell invasive phenotypes and promote dissemination.

Immune evasion

A central dogma of tumor immunology is the concept that an immune response to the tumor changes over time, shifting from elimination of the tumor, to equilibrium, and finally to escape via pro-tumor immune suppression[97]. T_H1 immune cell polarization

supports tumor cell killing via activation of cytotoxic immune cells including $CD8^+$ T cells and natural killer (NK) cells[98]. In contrast, pro-tumor T_H2 polarized immunosuppressive responses promote tumor cell immune escape, a necessary component of every step in the metastatic cascade[98-102] (Fig.1-3). Intriguingly, a recent study suggests that development of dysfunctional T cells incapable of inhibiting tumor growth occurs during pre-malignant stages of tumorigenesis, suggesting that immune escape is an early event in tumor progression[103]. T_H2-polarized $CD4^+$ T cells produce cytokines including TGFβ, IL-10, IL-4, IL-6, and IL-13 that suppress anti-tumor cytotoxic immune cell function. T_H2 immune programs also elicit recruitment and immune suppressive activity of $FoxP3^+$ T regulatory cells (T_{Regs}), B regulatory cells (B_{Regs}), and myeloid populations[98,99,104-106]. The role of these immune modulatory populations in eliciting tumor immune escape and promoting metastasis has been recently reviewed elsewhere[98]. Importantly, targeting immune suppressive immune populations can result in control of tumor growth and metastasis for some patients, and is the basis behind cancer immunotherapy[106-112].

The high levels of cell death during the first phase of weaning-induced mammary gland involution drive a subsequent T_H2 immune suppressive response characterized by an increase in IL-4, IL-13, IL-10, and TGFβ[42,43]. Similarly, upregulation of cyclooxygenase-2 (Cox-2) and production of the eicosanoid inflammatory mediator prostaglandin E_2 (PGE_2) contribute to the immune suppressed microenvironment and drive collagen production, ECM remodeling, and lymphangiogenesis[47,113,114]. In addition, an influx in immune-suppressive, alternatively activated $CD11b^+$ macrophages, $CD11b^+Gr1^+$ myeloid

cells, and FoxP3^{+} T_{Regs} occurs during the second phase of mammary gland involution[42,43,49]. This immune milieu resembles that seen during wound healing, where immune suppressive myeloid and lymphoid populations contribute to both immune regulation and tissue repair[115,116]. In sum, the immune microenvironment of the involuting gland is consistent with tumor immune escape in the context of an evolving postpartum breast cancer. Importantly, a similar influx of IL-10^{+} macrophages and FoxP3^{+} T regulatory cells characterize the involuting breast in women, suggesting similar support of early steps in the metastatic cascade in postpartum women[42,77]. Further, the immune microenvironment of weaning-induced mammary gland involution resembles the pro-tumor immune milieus that contribute to local dissemination and intravasation, as discussed above.

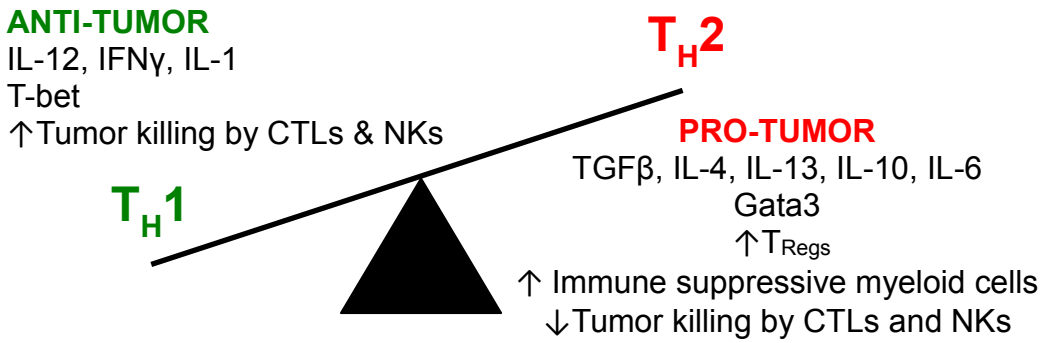

Figure 1-3: T_H2-skewed immune microenvironments drive tumor progression and metastasis

$CD4^+$ T cells are programmed as T_H1 anti-tumor T helper cells via signaling from cytokines including IFNγ. Differentiation towards a T_H1 phenotype is supported by the transcription factor T-bet. T_H1 cells produce inflammatory cytokines and promote tumor cell killing by immune populations including cytotoxic T lymphocyte (CTLs) and natural killer (NK) cells. Differentiation into T_H2 pro-tumor T helper cells occurs via cytokine signaling, primarily from IL-4, and is facilitated by Gata3 driven transcriptional programs. T_H2 immune activation promotes production of cytokines involved in driving immune suppressive- and wound repair-like programs in myeloid cells. The result is a suppression of immune populations previously capable of killing tumor cells.

Intravasation

Tumor cells can leave the primary tumor site via hematogenous or lymphogenous routes. Elevated levels of peri-tumor lymphatic vessel density, lymphovascular invasion, and lymph node metastasis are all prognostic indicators of breast cancer metastasis[117-121]. The relative contribution of either hematogenous or lymphogenous routes of spread to the success rate of the disseminated tumor cell in establishing metastasis remains to be elucidated[122]. However, the eventual entry of tumor cells into blood circulation is necessary for seeding of the most common sites of breast cancer metastasis, including bone, lung, liver, and brain, as direct lymphatic routes from sentinel lymph nodes to these sites do not exist[122]. Nonetheless, lymphangiogenesis may contribute to primary tumor progression. For breast cancer, increased lymphatic vessel density is strongly associated with poor prognosis and increased metastasis[117,123,124]. Increased lymphatic vessel density, either within the tumor or at the tumor periphery, has been proposed to contribute to metastasis, as lymphatics may provide conduits for escape and entry into the circulation for seeding of distant sites[125]. Macrophages contribute to lymphangiogenesis during non-tumor associated inflammation[126]. Myeloid populations including TAMs express vascular endothelial growth factor C (VEGF-C), a potent lymphangiogenic growth factor, and may play a role in primary tumor-associated lymphangiogenesis[127-129]. Lymphangiogenesis promotes interactions between tumor-associated antigen presenting cells and adaptive immune cells, yet this process often fails to mount an effective immune response against the tumor, likely due to immune suppression[130,131]. In fact, lymphatic endothelial cells can participate in direct and indirect dendritic and $CD8^+$ T

cell suppression and thus contribute to progression by promoting pro-tumor immune milieus[132-135]. A hallmark of weaning-induced mammary gland involution, in both rodents and women, is lymphangiogenesis that likely supports immune cell trafficking/immune regulation and clearance of debris from the involuting gland[114]. Importantly, rodent models of postpartum breast cancer display elevated lymphatic vessel density, tumor cell invasion of lymphatics, and lymph node metastasis. In the same study, postpartum breast cancer patients diagnosed within 2-3 years of a pregnancy were shown to have increased peri-tumor lymphatic vessel density and are more likely to present with lymph node metastasis compared to nulliparous patients[114]. These data suggest that lymphangiogenesis associated with weaning-induced mammary gland involution and postpartum breast cancers may promote entry of tumor cells into the vasculature via lymphatics.

Roles for microenvironmental factors in facilitating the process of intravasation into blood vasculature have been extensively studied. For example, the co-localization of tumor cell-endothelial cell-macrophage, in structures known as TMEMs (Tumor Microenvironment of Metastasis), predicts metastasis in breast cancer patients[136,137]. Intravital imaging in rodents has shown that this cell triad facilitates tumor cell intravasation via bursts of macrophage VEGF-induced vascular permeability[138]. Macrophage-tumor cell contact, including contact at the site of the TMEM, promotes tumor cell invadopodia required for trans-endothelial migration[139,140]. Other studies have shown that directional collagen I fibers enhance intravasation in an *in vitro* model system[141]. In models of postpartum breast cancer, tumor cells can be found at increased

rates in the blood at 3 days post-injection, compared to nulliparous controls, suggesting efficient intravasation in the post-weaning microenvironment[47]. Similarly, increased intra-lymphatic invasive foci were observed in mice harboring tumors in mammary glands of involuting compared to nulliparous hosts[114]. The mechanism of increased tumor cell lymphatic intravasation in the involuting mammary gland microenvironment is currently unknown, but may be Cox-2 dependent, as NSAID intervention reduces lymphovascular invasion[47,114].

Survival in the circulation

Once in the circulation, tumor cells spread throughout the body. Experimental metastasis modeling, which often involves direct injection of tumor cells into the circulation via the left ventricle, tail vein, spleen, or portal vein, has shown that tumor cells survive in the circulation and arrest in vasculature with remarkable efficiency[50,142-144]. Intriguingly, several small studies assessing circulating tumor cell (CTC) viability in cancer patients found that a large percentage of CTCs were apoptotic[145-147]. One explanation for this difference between rodent and human studies is that rodent models often employ robust, established tumor cell lines that may be enriched in pro-survival pathways. Travel through the circulation increases a tumor cell's exposure to leukocytes with tumor cell killing ability as well as shear force from high blood flow rates. Studies have identified tumor cell coating by platelets as a mode of protection from targeted killing by NK cells, either by providing a physical barrier or by direct inhibition of NK function[148-153]. T_{Regs} provide important survival signals to breast cancer cells via receptor activator of nuclear factor-κB ligand (RANKL) which boost lung metastasis[154]. Intriguingly, when tumor

cells are injected directly into the circulation after pre-incubation with RANKL they survive in the circulation and extravasate at higher rates, suggesting that T_{Regs} provide survival signals that impact cells within the circulation, or at even earlier stages of the metastatic cascade[154].

Tumor cell arrest in vasculature

There is some evidence for tumor cell 'homing' to metastatic sites through chemokine production at the secondary site (SDF-1/CXCL12 or CCL21) and chemokine receptor expression on breast cancer cells (CXCR4 and CCR7)[155,156]. However, it is more likely that cells are carried passively through circulation and site-specific metastasis is dictated more so by tumor cell fate upon entry into the secondary site[122]. It is currently unclear whether stromal cells play a role in active tumor cell arrest in vasculature or whether tumor cell arrest is due to size restriction. Studies have shown that tumor cells primarily arrest in capillaries that are the same diameter as the tumor cell, supportive of the hypothesis that size restriction dictates arrest[143,157-162]. However other studies observed tumor cell arrest in vessels significantly larger than the tumor cell diameter, implying that arrest may be an active process in some circumstances[163-165]. In fact, a number of studies have found a role for microenvironmental factors at the secondary site in aiding the process of tumor cell arrest in vasculature and subsequent extravasation, as reviewed below.

Extravasation

Early studies suggested that the endothelial cell adhesion molecule E-selectin aids in melanoma cell arrest in the liver microvasculature and directs site-specific metastatic patterns[166]. Similarly, extravascular tumor cells elicit resident liver macrophage (Kupffer cell) production of pro-inflammatory TNFα and IL-1β resulting in E-selectin upregulation by hepatic sinusoidal endothelial cells[167-169]. This immediate reaction of the hepatic microenvironment to CTCs aids tumor cell arrest[167-169]. Intravital imaging studies have found that macrophages are closely associated with extravasating mammary tumor cells in the lung microenvironment; macrophage depletion dramatically delayed the extravasation process[170]. Subsequent studies found that $CCR2^+$ monocytes are recruited to the lung and differentiate into these metastasis-supporting macrophages. The $CCR2^+$ monocytes promote tumor cell extravasation in part through VEGF-A expression[171]. Thus macrophages in secondary sites assist with tumor cell extravasation.

Neutrophils can also contribute to tumor cell extravasation, particularly in the liver, where intravital imaging has revealed that tumor cells arrest on top of neutrophils, and neutrophil depletion reduces extravasation out of hepatic sinusoids[172,173]. Neutrophils also promote increased mammary tumor cell extravasation in the lung by inhibiting NK-mediated tumor cell killing and modulation of the endothelial cell barrier via MMPs and IL-1β[174]. Recent work has also shown that γδ T cell production of IL-17 drives neutrophil expansion and may contribute to metastasis through $CD8^+$ T cell suppression in mammary tumor bearing $K14cre^{F/F};Cdh1^{F/F};Trp53^{F/F}$ (KEP) mice[175]. In contrast, other studies have shown that 'tumor entrained neutrophils' suppress lung metastatic seeding

via direct tumor cell killing in an H_2O_2-dependent manner[176]. In the same study, brain and liver metastatic seeding efficiency were not impacted, suggesting that neutrophils may play unique roles in different tissue environments[176]. Roles for tumor-$\beta_1$integrins in both tumor cell arrest and surveying of vasculature prior to extravasation have also been revealed[161,165]. Platelets contribute to tumor cell arrest through $\alpha_{II}\beta_3$ integrin-binding interactions with tumor and endothelial cells and subsequently promote extravasation by increasing vascular permeability[177,178]. Furthermore, a transient incubation of tumor cells with platelets prior to intravenous injection shifts tumor cells toward an invasive phenotype and increases lung metastasis[179]. In sum, immune cells and platelets appear to play an integral role in facilitating active tumor cell extravasation into secondary sites.

Preclinical models of postpartum breast cancer implicate the involuting mammary gland in metastasis

Based upon the above referenced evidence for microenvironmental factors in supporting the early stages of metastasis, the involuting mammary gland may contribute to postpartum breast cancer metastasis in at least one, if not all of the following ways: 1) an influx of immune suppressive myeloid and lymphoid populations, in addition to aberrant cytokine production, may promote tumor immune evasion, growth, neovascularization, acquisition of an invasive phenotype, local dissemination and intravasation 2) the matrix composition and organization may also provide essential cues for acquisition of an invasive phenotype and support motility, local dissemination, and entry into the circulation and 3) lymphangiogenesis may provide routes of entry for tumor cells into the circulation and may contribute to the immune suppression. In short, mammary gland

involution is characterized by numerous attributes consistent with a microenvironment that supports early steps of the metastatic cascade.

Preclinical models of postpartum breast cancer involve tumor cell injection into murine mammary fat pads at involution day 1 and into nulliparous controls. The Schedin lab has utilized numerous models, including human tumor cell lines injected into immune compromised mice and syngeneic mammary tumor lines injected into immune competent mice. These models have revealed that the involuting mammary gland supports increased primary tumor growth, local dissemination, intravasation, and metastasis compared to nulliparous littermates[42,47,49,113,114]. Functional relevance for a number of the pro-tumor attributes of mammary gland involution has been demonstrated. Targeting the immune suppressive macrophage population present during weaning-induced mammary gland involution via IL-10 blockade reduced involution tumor volumes and increased presence of intratumoral T lymphocytes[42]. ECM isolated from nulliparous and actively involuting rat mammary glands and co-injected with breast cancer cells into naïve immune-compromised mice showed a significant growth and metastasis advantage for those cells co-injected with involution ECM[49]. A similar study utilized isolated fibroblasts from nulliparous and actively involuting mouse mammary glands which were co-injected with mammary tumor cells into naïve immune competent mice (Guo et al., submitted). This study revealed that tumors co-injected with involution-associated fibroblasts resulted in a primary tumor growth advantage, a unique pro-tumor immune milieu, and increased blood vasculature compared to tumors co-injected with nulliparous-associated fibroblasts (Guo et al., submitted and data unpublished). Further, studies targeting Cox-2 with non-

steroidal anti-inflammatory drugs (NSAIDs) have shown a reduction in lymphangiogenesis, ECM deposition, radially aligned collagen, and a shift in the immune milieu to one resembling an anti-tumor environment during mammary involution[47,48,113,114] (Schedin lab, data unpublished). Importantly, these studies also demonstrated a reduction in primary tumor growth, local dissemination, and metastasis in preclinical models of postpartum breast cancer[47,113,114]. In sum, these studies identify weaning-induced mammary gland involution as a tumor-promotional window that supports early steps of the metastatic cascade.

The pro-metastatic attributes of weaning-induced mammary gland involution, culminating in the increased presence of CTCs in murine models may be sufficient to explain the high risk of metastasis in PPBC. However, *the fate of these tumor cells at the secondary site is entirely unknown*. Importantly, it is well-documented that metastatic efficiency is, in large part, dictated by tumor cell fate upon entry into the secondary organ[50,142]. Thus, I sought to determine whether later stages of the metastatic cascade are similarly supported by post-weaning microenvironmental changes that may further explain the high risk of metastasis in postpartum breast cancer patients. The microenvironmental contribution to later stages of the metastatic cascade, as well as my findings regarding a role for post-weaning secondary site microenvironmental changes in postpartum breast cancer metastasis are explored below.

The microenvironment at secondary sites represents a major barrier to metastatic efficiency

What determines site-specific metastatic patterns in cancer?

Different tumor types present with unique metastatic patterns, raising the question of what drives site-specificity (Fig.1-4). In 1889 Stephen Paget proposed the 'seed and soil' hypothesis, which suggested that the efficiency by which a metastatic cell (the 'seed') survives and grows into clinically impactful metastases is dictated by the presence of a suitable microenvironment (the 'soil')[180]. Subsequently, James Ewing proposed the anatomical/mechanical hypothesis that the preference for site-specific metastases can be explained entirely by circulatory patterns leading away from the tumor[181]. In fact, tumors commonly metastasize to organs anatomically downstream from the primary tumor site of origin. Colorectal and pancreatic adenocarcinomas frequently metastasize first to the liver. In contrast, breast cancer frequently metastasizes first to the bone or liver, despite mammary blood flow first reaching the heart and lungs before entering the general circulation[182,183]. Furthermore, numerous autopsy studies have found incongruity between rates of certain sites of metastasis and blood flow rates from the tumor of interest, suggesting that patterns of circulation cannot solely explain metastatic patterns[184-187]. Taken together, these data suggest that a combination of the 'seed and soil' and anatomical hypotheses explain tumor site-specific metastatic patterns.

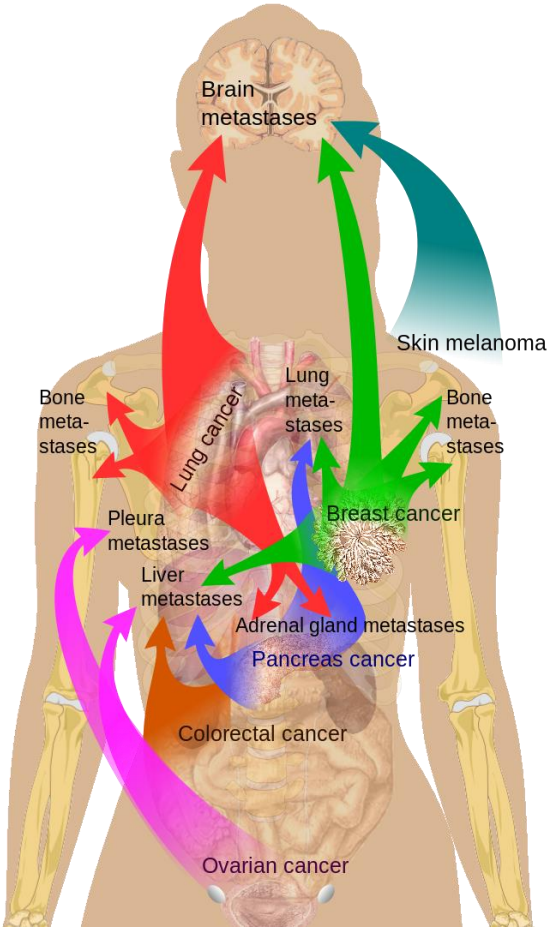

Figure 1-4: Site-specificity of metastasis in common cancers

Different primary tumors are characterized by unique site-specific metastatic patterns. Breast cancers most commonly metastasize to bone, lung, liver, and to a lesser extent brain. In contrast, colorectal cancers primarily metastasize to the liver. Image used is in the Public Domain.

Metastatic efficiency is dictated by the microenvironment at the secondary site

Despite numerous rate-limiting steps in the metastatic cascade discussed above, metastatic efficiency is largely determined by post-extravasation survival at the secondary site. Studies in rodents to determine the metastatic success rate suggest that <1% of disseminated tumor cells successfully establish metastatic lesions[50,142,144,188,189]. Seminal work has shown that DTCs, injected into either the circulation of mice or into the chorioallantoic membrane of the chick embryo extravasate at a very high success rate[50,142,144]. Melanoma metastasis modeling in the liver and lung found that major bottlenecks in the formation of overt metastases were the survival and proliferation of single cells into micro-metastases and the growth of micro-metastases into overt metastases[50,142]. In these models, 0.02% of cells grew into overt metastases in the liver, whereas ~10% grew into medium and large sized (80-300+ μm) metastases in the lung. Importantly, metastatic outgrowth varies markedly between lung and liver, at least in mice, where the liver may represent a more hostile environment for metastasis in these models[50,142]. Intravital imaging in brain metastasis models revealed major bottlenecks to metastatic efficiency that included extravasation, localization away from vasculature upon seeding, and outgrowth from single cells to micro-metastases and from micro-metastases to overt metastases[143]. These data suggest that bottlenecks to metastatic efficiency are site-specific, in that liver and lung metastases are stalled at the point of outgrowth, whereas in brain metastasis extravasation also incurs a heavy toll on metastatic efficiency[143]. Further, in these models, tumor cell localization adjacent to vasculature was associated with greater rates of survival and outgrowth, suggesting a particularly important role for the perivascular microenvironment in metastatic

efficiency[50,142,143]. Perhaps the greatest evidence in support of pro-metastatic niches can be found in the fact that tumor cells can enter and exit states of dormancy in a niche-dependent manner. Early studies identified persistence of viable single tumor cells in numerous organs for several months[190,191]. When removed from the secondary site, dormant tumor cells were able to produce primary tumors and lung metastases at rates similar to the parental cell lines, suggesting that the tissue site, and thus the niche, dictates tumor cell behavior[192]. Taken together, these studies strongly implicate the secondary site in dictating metastatic success.

Establishment of the pre-metastatic niche

Identifying the pre-metastatic niche

Prior to detection of DTCs at the secondary site, numerous studies have identified the presence of tumor-educated pre-metastatic niches. Pre-metastatic niches are metastasis-promoting tissue microenvironments in secondary organs that are established by factors secreted by the primary tumor[193-195]. These pre-metastatic niches are defined by their ability to provide seeding, survival, and outgrowth advantages to disseminated tumor cells. Although it is likely that single tumor cells exist in, and contribute to formation of some pre-metastatic niches, it is apparent that the primary tumor plays an integral role in the process. A seminal study, which first described that primary tumors alter the metastatic site prior to tumor cell arrival, found that B16 melanoma and Lewis lung carcinoma (LLC) tumors implanted into the mouse flank induce MMP-9 expression in endothelial cells and macrophages in the lung, in a vascular endothelial growth factor

receptor 1 (VEGFR1) dependent manner[196]. As a result, the number of metastatic lung lesions was greatly increased upon subsequent tail-vein injection of tumor cells, leading to the concept of lung microenvironment education by the primary tumor[196]. A subsequent study using the same tumor lines found that tumor-cell secreted factors promote fibronectin production by resident fibroblasts in future metastatic sites[197]. This fibronectin deposition contributes to recruitment of $VEGFR1^+$ bone marrow derived cells (BMDCs) expressing $\alpha_4\beta_1$ integrin. It is thought that these pre-metastatic niches provide a survival and outgrowth advantage compared to homeostatic tissues. In these studies, the recruited $VEGFR1^+$ BMDCs form clusters and contribute to pre-metastatic niche establishment via MMP-9 and SDF-1 production. Importantly, this phenomenon was observed in tumors with diverse site-specific metastatic patterns and only occurred in future metastatic sites of these tumors[197]. B16 and LLC tumor-secreted factors including TNFα, TGFβ, and VEGF-A also induce upregulation of calcium binding pro-inflammatory S100A8 and S100A9 proteins by $Mac1^+$ macrophages and endothelial cells in the lung microenvironment, ultimately increasing metastatic efficiency to the lung[198]. Interestingly, one study has shown that metastasis-incompetent variants of breast and prostate tumor lines similarly recruit $CD11b^+$ myeloid populations to the lung, but these cells have anti-metastatic capacity via thrombospondin-1 expression[199]. These data suggest that tumor education of the pre-metastatic niche is essential to metastatic efficiency, including subverting the active suppression of successful outgrowths at the metastatic site. Since these paradigm-shifting studies, a number of other mechanisms of pre-metastatic niche induction have been elucidated[194].

Secreted factors from the primary tumor establish pre-metastatic niches

One mechanism by which tumors establish a pre-metastatic niche is via secretion of exosome vesicles that can deliver bioactive proteins, RNAs, and DNAs to stromal cells at the secondary site[200]. Recently, it has been shown that exosomes secreted by melanoma and pancreatic ductal adenocarcinomas (PDACs) promote pre-metastatic niche formation in the lung and liver, respectively[201,202]. B16-F10 melanoma exosomes increased expression of MET, an important signaling molecule in bone marrow cell mobilization, in BMDCs, thus facilitating their mobilization and subsequent establishment of the lung pre-metastatic niche[202]. Further, pre-metastatic niche education with purified exosomes prior to tumor cell injection resulted in markedly increased lung metastasis compared to education with exosomes from the less aggressive B16-F1 cell line[202], suggesting that exosomes are sufficient to establish pre-metastatic niches. In contrast, PDAC exosomes are selectively taken up by Kupffer cells in the liver and elicit upregulation of TGFβ and subsequent activation of peri-sinusoidal vitamin A storing hepatic stellate cells (HSCs)[201]. HSCs deposit fibronectin in the liver pre-metastatic niche, promoting recruitment of bone marrow derived macrophages and PDAC liver metastasis[201]. Recently, it was also shown that exosomal RNAs induce Toll-like receptor 3 (TLR3) signaling in lung epithelial cells, promoting neutrophil recruitment and increasing metastatic efficiency of LLC and B16-F10 tumor cells[203]. A recent study has shown that niche education by exosomes from a lung-tropic tumor line redirected preferential site-specific metastasis of a bone-tropic cell line to the lung[204]. In these studies, the investigators found that integrins on tumor cell-derived exosomes, presumably reflecting integrin expression patterns on the cell lines from which exosomes are derived, may

direct organ and target cell-specific uptake[204]. Specifically, $S100A4^+$ lung fibroblasts and endothelial cells take up exosomes expressing integrin $\alpha_6\beta_4$ or integrin $\alpha_6\beta_1$, whereas exosomes expressing integrin $\alpha_v\beta_5$ bind Kupffer cells. Exosome uptake by these cells results in S100 protein production and subsequent establishment of pre-metastatic niches[204].

Other secreted factors also play an important role in pre-metastatic niche establishment. For example, secretion of a collagen cross-linking enzyme, lysyl oxidase (LOX), by hypoxic breast cancer cells accumulates in the lung and results in pre-metastatic niche formation[205]. LOX crosslinks collagen IV in the lung, leading to recruitment of an MMP-2-expressing $CD11b^+$ myeloid cell population from the bone marrow. MMP-2 cleavage of collagen at the metastatic site further promotes myeloid cell recruitment and metastatic outgrowth[205]. Importantly, LOX expression is associated with high risk for metastasis in ER^- breast cancer patients and head-and-neck squamous cell carcinoma patients[89]. Subsequent studies have identified similar pre-metastatic niche establishment in murine lungs downstream of hypoxic breast cancer secretion of LOXL1-4 proteins[206]. A potential role for other tumor-secreted factors including tissue factor has also been observed[207].

While a major role for immature monocytes and macrophages has been described, emerging evidence suggests that other immune populations may also contribute to pre-metastatic niche establishment. Neutrophils accumulate in lungs via tumor secreted granulocyte-colony stimulating factor (G-CSF) and increase metastasis of several distinct tumor types, likely due to neutrophil production of MMPs and S100A8/9 proteins[208]. In

contrast, evidence that T cells contribute to pre-metastatic niche establishment is largely lacking, although one publication did show that $CD4^+$ T cells promote pre-metastatic bone lysis and establish a pro-metastatic microenvironment prior to 4T1 mammary tumor cell arrival[209]. Additional roles for T cells in pre-metastatic niche establishment have yet to be elucidated. In sum, tumor education of the pre-metastatic niche can occur via numerous mechanisms and occurs in a tumor-specific and tissue-specific manner.

Pre-metastatic and metastatic niches impact early cell fate decisions and outgrowth

The perivascular niche is the first point of interaction upon entry into the secondary site

Extravasated tumor cells first come into contact with the perivascular niche comprised of endothelial cells and their basement membrane. Numerous studies have implicated the perivascular niche in dictating early cell fate decisions including decisions to proliferate, die, or become quiescent. One study found that quiescent breast cancer cells were co-localized to mature lung vasculature expressing high levels of thrombospondin-1 (TSP-1), suggesting a mechanism by which tumor cell adherence to TSP-1 suppresses metastatic outgrowth, via induction of tumor cell dormancy. These studies also revealed that tumor cell proliferation instead occurs adjacent to neovascular regions with low TSP-1 and high levels of TGFβ and the matricellular protein periostin (POSTN)[210]. These findings support previous work which found that successful colonization requires induction of a permissive metastatic niche via POSTN produced by resident lung fibroblasts[211]. Similar studies have identified a number of ECM proteins that promote escape from dormancy. Interaction of quiescent mammary tumor cells with lung

fibronectin[212] and collagen I[213] also promote awakening of dormant tumor cells through β_1 integrin binding and downstream signaling.

The *metastatic niche supports tumor outgrowth*

Tenascin-C production first by disseminated tumor cells, and subsequently by the stromal component of the lung metastatic niche, promotes WNT and NOTCH signaling essential for metastatic survival and outgrowth of breast cancer cells. Intriguingly, knockdown of TNC in bone and brain-tropic variants of MDA-MB-231 showed that TNC may also be important for bone but not brain metastasis[82]. $S100A4^+$ fibroblasts in the lung metastatic niche produced TNC which facilitated mammary tumor cell outgrowth, providing further evidence that TNC is a prominent component of pro-metastatic microenvironments[214]. This study also found that $S100A4^+$ metastatic-niche associated fibroblasts produced VEGF-A which contributed to the angiogenesis in metastatic lesions[214].

As previously eluded to, macrophages play essential roles in every step of the metastatic cascade. Thus, it may not be surprising that macrophages also promote end-stage metastatic outgrowth. $CCR2^+$ monocytes are constantly recruited to the metastatic site where they differentiate into $VEGFR1^+$ metastasis-associated macrophages that promote breast cancer metastatic outgrowth in the lung[171,215]. Studies have also shown that macrophage VCAM-1 binding to breast cancer integrin $\alpha_v\beta_4$ drives downstream AKT cell survival signaling and contributes to metastatic outgrowth[216]. In the MMTV-PyMT spontaneous breast cancer model, versican produced by recruited $CD11b^+Ly6C^{hi}$ monocytes was sufficient to promote the micro-metastasis to macro-metastasis switch in

the metastatic lungs of MMTV-PyMT mice[217]. In a colorectal cancer model of liver metastasis CCL9-CCR1 signaling recruits a unique $CD34^{+}Gr1^{-}VEGFR1^{-}$ immature monocyte population to metastatic lesions concurrent with the micro-metastasis to macro-metastasis switch[218]. Targeting this monocyte population by abrogating CCL9-CCR1 signaling resulted in delayed metastatic outgrowth[218].

Another major component of micro-metastatic outgrowth into clinically detectable lesions is the neovascularization of growing metastases, called the angiogenic switch. Using both MMTV-PyMT and LLC metastasis models, one study found recruitment of bone marrow derived endothelial progenitor cells to the metastatic lung is essential to the micro-metastasis to macro-metastasis switch[219]. In sum, these and numerous other studies have implicated microenvironmental factors in establishing the pre-metastatic niche and promoting tumor cell seeding and outgrowth in the secondary site.

Establishment of pro-metastatic microenvironments in the absence of tumor-education

Emerging evidence suggests that physiologic events, as opposed to tumor-derived processes, may also impact metastatic microenvironments in ways that increase or decrease metastatic efficiency. Obesity is clinically associated with worse prognosis in breast cancer[220,221]. Importantly, retrospective analyses have found that obese breast cancer patients may be at increased risk for lung and liver metastases and reduced risk for bone metastases compared to non-obese patients[222]. Although the mechanisms underlying obesity promotion of metastasis are largely unexplored, one study has shown that obesity promotes liver-specific inflammation and increased hepatic metastatic burden in a murine

model of colorectal cancer[223]. The effect of obesity on liver metastasis was dependent upon insulin-like growth factor (IGF)[223]. Another example of physiologic changes are those that occur with aging. The aged microenvironment is characterized by senescent fibroblasts that resemble both wound healing-associated and cancer-associated fibroblasts (CAFs)[224]. Although a specific role for aged fibroblasts in the metastatic niche has not been elucidated, a recent study has found that senescent fibroblasts contribute to melanoma metastasis by promoting early steps in the metastatic cascade[225].

Tissue microenvironments are impacted by infection and by interventions commonly utilized in treating cancer, including surgery, radiation, and chemotherapy. Neutrophil extracellular traps (NETs), DNA traps released by neutrophils in response to inflammatory stimuli, function by capturing and clearing pathogens[226]. Work has shown that NETs are formed in the post-surgical setting and during infection. In the context of hepatic metastasis resection NETs correlate with disease recurrence in the liver[227]. Infection-derived NETs facilitate CTC trapping, aid in tumor cell arrest in vasculature, and promote metastasis[228]. These data suggest that surgical stress and inflammation may contribute to pro-metastatic microenvironments. Radiation and the chemotherapeutic bleomycin induce pulmonary fibrosis, promoting deposition of collagen I and fibronectin and increased LOX expression[229]. Similarly, in a model of hepatic fibrosis induced by dimethylnitrosamine (DMN) a similar fibrotic environment is established, characterized by activated HSCs, deposition and cross-linking of collagen, and increased LOX expression[229]. Importantly, in these radiation, bleomycin, and DMN induced lung and liver fibrosis models, no impact on orthotopic mammary tumor growth was observed.

However, fibrosis did support elevated metastatic seeding and outgrowth that was reversed with LOX inhibition, suggesting that fibrosis establishes pro-metastatic microenvironments in these tissues[229].

The fate of tumor cells at metastatic sites in the postpartum setting

The bulk of data discussed above has collectively identified that a major bottleneck in the metastatic cascade is survival and outgrowth of tumor cells in the secondary site. Thus, we hypothesized that the poor prognosis of postpartum breast cancers may be, in part, due to physiologic changes at secondary sites that are conducive to metastatic seeding or outgrowth. Further, we reasoned that secondary sites most likely to be altered post-weaning would be those most intimately involved with the metabolic demand of pregnancy and lactation. In fact, the mammary gland and liver can be thought of as a functional unit facilitating milk production. During lactation, β-oxidation and gluconeogenesis increase in the liver[230-232]. Fatty acid oxidation provides necessary substrate (ATP) for glucose production. The glucose is subsequently shuttled to the mammary gland where it is used for milk components including carbohydrates and the glycerol backbone of triglycerides[230-232]. Thus, I investigated the rodent liver across the reproductive cycle. With this work, I discovered a novel biology of the liver, namely weaning-induced liver involution, characterized by increased hepatocyte apoptosis and a shift from catabolic to anabolic metabolism[233]. My investigations also revealed an increase in $CD11b^{+}Ly6C^{hi}Ly6G^{-}$ immature monocytes and mature Kupffer cells which formed clusters, and ECM deposition of pro-metastatic proteins including collagen I and

tenascin-C, data consistent with establishment of a pro-metastatic niche post-weaning. Using two experimental liver metastasis models I found that mice injected immediately post-weaning, during the window of weaning-induced liver involution, were ~1.5-3-fold more likely to develop metastases compared to nulliparous controls[233]. Patients with postpartum breast cancer develop liver-specific metastasis at higher frequencies compared to nulliparous patients[233]. Importantly, I observed no difference in lung, bone, or brain metastasis rates in postpartum compared to nulliparous patients, suggesting that similar establishment of a pro-metastatic microenvironment in the liver post-weaning may occur in women[233]. Taken together, these data suggest that physiologic events may also educate pro-metastatic niches in the *absence* of a primary tumor. Although unprecedented, our results may not be a unique phenomenon isolated to young, postpartum mothers; evidence for non-tumor education of pro-metastatic microenvironments is starting to become apparent, as previously discussed. However, one major limitation to understanding establishment of pro-metastatic microenvironments established by physiological or pathological processes is rodent metastasis models that allow for site-specific metastasis studies.

Limitations to studying site-specific metastasis and the metastatic niche

Major limitations to studying site-specific metastasis and the impact of pro-metastatic microenvironments on metastatic efficiency have hampered progress in the field. These limitations include 1) Models that do not represent the tumor complexity and heterogeneity observed in breast tumors, 2) poor spontaneous metastasis models that do not recapitulate site-specific metastatic patterns observed in patients, 3) use of human and

mammary tumor cell lines injected as a bolus into orthotopic sites or directly into the circulation, models which often still fail to recapitulate site-specific metastatic patterns observed in patients[183,234,235] and which bypass early stages of metastatic progression, 4) difficulty with accurate tracking and quantification of tumor cells as they progress along the metastatic cascade, and 5) a lack of models that accurately model tumor cell dormancy at the secondary site. The development of intravital imaging techniques and fluorescent labeling of cell types of interest has greatly impacted the study of metastasis at high resolution[236,237]. Importantly, tissue specific responses to common therapeutics used during the course of cancer treatment suggest that studying site-specific metastasis is essential, despite a lack of models useful for this purpose. To address site-specificity, studies have often utilized experimental metastasis models, which involve tumor cell injection into the circulatory system, to study metastases in sites other than the lung. These models allow for the study of late stages of the metastatic cascade in non-pulmonary sites and represent an essential step towards the development of 'gold-standard' spontaneous mouse models of metastasis that replicate the patterns of metastatic disease seen in patients. To study liver metastasis in our postpartum breast cancer models, I developed an intraportal injection experimental metastasis model to directly target mammary tumor cells to the liver; this model is described in detail in Chapter II[238]. I hypothesized that the process of post-weaning liver involution establishes a tissue microenvironment consistent with a pro-metastatic niche and thus will increase metastatic efficiency to the liver during this window of involution.

Chapter II: A portal vein injection model to study liver metastasis of breast cancer[1]

Published Manuscript

Goddard ET, Fischer J, Schedin P. A Portal Vein Injection Model to Study Liver Metastasis of Breast Cancer. *J Vis Exp*. 2016 Dec;(118), e54903, doi:10.3791/54903

Contributions

ETG and PS developed the model. ETG performed all studies, staining, and data analysis.

JF contributed to model development and assisted with studies.

[1] The majority of this chapter was re-printed with permission from the Journal of Visualized Experiments (Goddard ET, Fischer J, Schedin P. A Portal Vein Injection Model to Study Liver Metastasis of Breast Cancer. *J Vis Exp*. (118), e54903, doi:10.3791/54903 (2016).

Short abstract

A surgical procedure was developed to deliver mammary tumor cells to the murine liver via portal vein injection. This model permits investigation of late stages of liver metastasis in a fully immune competent host, including tumor cell extravasation, seeding, survival, and metastatic outgrowth in the liver.

Long abstract

Breast cancer is the leading cause of cancer-related mortality in women worldwide. Liver metastasis is involved in upwards of 30% of cases with breast cancer metastasis, and results in poor outcomes with median survival rates of only 4.8-15 months. Current rodent models of breast cancer metastasis, including primary tumor cell xenograft and spontaneous tumor models, rarely metastasize to the liver. Intracardiac and intrasplenic injection models do result in liver metastases, however these models can be confounded by concomitant secondary-site metastasis, or by compromised immunity due to removal of the spleen to avoid tumor growth at the injection site. To address the need for improved liver metastasis models, a murine portal vein injection method that delivers tumor cells firstly and directly to the liver was developed. This model delivers tumor cells to the liver without complications of concurrent metastases in other organs or removal of the spleen. The optimized portal vein protocol employs small injection volumes of 5-10 ul, ≥32 gauge needles, and hemostatic gauze at the injection site to control for blood loss. The portal vein injection approach in Balb/c female mice using three syngeneic mammary tumor lines of varying metastatic potential was tested; high-metastatic 4T1 cells, moderate-metastatic D2A1 cells, and low-metastatic D2.OR cells.

Concentrations of ≤10,000 cells/injection results in a latency of ~20-40 days for development of liver metastases with the higher metastatic 4T1 and D2A1 lines, and >55 days for the less aggressive D2.OR line. This model represents an important tool to study breast cancer metastasis to the liver, and may be applicable to other cancers that frequently metastasize to the liver including colorectal and pancreatic adenocarcinomas.

Introduction

Breast Cancer Metastasis to the Liver

The liver is a common site of breast cancer metastasis, along with bone and lung[239-241]. Liver metastasis in breast cancer patients is an independent prognostic factor for very poor outcomes[242,243], as median survival of breast cancer patients with liver metastasis ranges from 4.8 to 15 months[244-247]. In contrast, breast cancer patients with lung or bone metastasis have median survival rates of 9 to 27.4 months[246,247] and 16.3 to 56 months[246,248-250], respectively. Metastasis is a multistep process, referred to as the metastatic cascade, which begins with tumor cell dissemination in the primary tumor and ends with patient mortality due to the seeding and outgrowth of circulating tumor cells within a distant organ[52,122,251]. Rodent models of metastasis have revealed that the metastatic cascade is remarkably inefficient, with only 0.02-10% of circulating tumor cells establishing overt metastasis[50,142]. One major bottleneck of metastatic inefficiency is dictated by the unique tissue microenvironments at secondary sites, called metastatic niches[252], highlighting the importance of understanding site-specific metastasis. The metastatic niche is unique to the site of recurrence, and is, in part, characterized by deposition of distinct extracellular matrix proteins[82,201], infiltration of various immune

cell populations[197,205,253], and altered tissue homeostasis including dysregulated production of numerous cytokines, chemokines, and growth factors[52,194,252,254]. Thus, an understanding of the tissue specific metastatic niche precedes an understanding of how to target metastatic disease. However, robust models of liver metastasis are lacking. Further, improved models of liver metastasis will be essential to identifying novel targets and effective treatments for breast cancer patients with liver metastases.

Established Models to Study Breast Cancer Metastasis to the Liver

Currently available models to study breast cancer metastasis to the liver include human cancer cell xenografts in immune compromised mice. These models typically use well-studied human breast cancer cell lines such as MCF-7 and MDA-MB-231 and Nude, $Rag1^{-/-}$, or SCID immune compromised murine hosts[255-258]. Xenograft models provide the advantage of involving human derived cancer cell lines, however, given the recent appreciation for immune cells in metastasis[98,175,259] and in therapeutic resistance[260-262], the study of metastasis in a fully immune competent host is paramount. Models to study breast cancer metastasis to the liver in immune competent hosts include orthotopic injection of syngeneic tumor cells (e.g. 4T1 and D2A1 cell lines) into the mammary fat pad, with or without surgical resection of the primary tumor, and subsequent assessment of metastasis[234,235,263]. Of note, the rate of liver metastasis from orthotopic transplant models is very low or non-existent compared to other metastatic sites such as lung[264,265], or occurs after lung metastasis is established, complicating the study of liver-specific metastasis[234,264].

Tumor explants from spontaneous genetically engineered breast cancer models can be re-injected into the mammary fat pads of naïve hosts as syngeneic tumor cells. For example, it was recently reported that spontaneous tumors from $K14^{Cre}ECad^{f/f}P53^{f/f}$ mice, which model invasive lobular breast carcinoma, develop tumors when orthotopically injected into wildtype hosts. Following surgical resection of these tumors once they reach 15 mm^2, 18% of the mice progressed to liver metastasis[265,266]. A third approach to model liver metastasis utilizes spontaneous metastasis in genetically engineered mice. To date, reports of spontaneous murine models of breast cancer metastasis that readily spread to the liver are uncommon. Exceptions include the H19-IGF2, the $p53^{fp/fp}$ MMTV-Cre Wap-Cre, and the $K14^{Cre}ECad^{f/f}P53^{f/f}$ genetically engineered mouse models, where liver metastasis develops in a low percentage of mice[235,266-268]. Thus, while genetically engineered mouse models facilitate the study of all stages of the metastatic cascade, providing powerful and clinically relevant models, they are limited due to low rates of liver metastasis[235].

Several metastasis models bypass the initial steps of the metastatic cascade including dissemination of tumor cells from the primary tumor and intravasation. These models permit investigation into the later steps of the metastatic cascade, from extravasation to establishment of tumors at secondary sites. The intracardiac injection model delivers tumor cells into the left ventricle, which distributes tumor cells into the circulatory system via the aorta. Intracardiac injection requires ultrasound guided imaging of the injection site or other imaging modalities such as bioluminescence of luciferase tagged cells to confirm successful injection. Tumor cell injection via the left ventricle may result

in bone, brain, lung, and/or liver metastasis, amongst other organs[269-273]. Because of multi-organ metastases, these mice frequently need to be euthanized prior to development of overt liver metastasis, negating the ability to fully investigate metastatic growth within the liver. An alternative approach that significantly minimizes the development of multi-site metastasis is the intrasplenic injection model. Intrasplenic injection delivers tumor cells via the splenic vein that joins with the superior mesenteric vein to become the portal vein[274,275]. Animals can be monitored for outgrowth of metastatic lesions in the liver because formation of metastases at other sites is rare, and as a result, the animal's overall health is maintained[274,275]. However, it is important to note that the intrasplenic model requires splenectomy to avoid splenic tumors[274,275], a procedure that impacts immune function. For example, myocardial ischemia reperfusion injury is characterized by infiltration of $Ly6C^+$ monocyte subsets that originate from the spleen and are responsible for phagocytic and proteolytic activity during the wound healing following ischemia[276,277]. With splenectomy, there is an observed reduction in monocyte populations that assist in wound healing[277]. Further, splenectomy has been shown to reduce primary tumor growth and lung metastases in a non-small cell lung cancer model, specifically through a reduction in the number of circulating and intra-tumor $CCR2^+CD11b^+Ly6C^+$ monocytic myeloid cells[278]. Additionally, splenectomy following intrasplenic injection of colon cancer cells resulted in reduced levels of anti-tumor natural killer cells in mesenteric lymph nodes and elevated liver metastasis[279]. In sum, these findings suggest that splenectomy compromises the immune system's role with subsequent consequences for metastatic cell fate. Finally, there is the intrahepatic injection model, whereby tumor cells are injected directly into liver tissue following

laparotomy and left lobe exposure. In our hands, this model resulted in 40% of injections visibly leaking from the injection site into the surrounding peritoneal space at time of injection (data not shown). Of the remaining mice, ~90% exhibited tumor growth at the incision site in addition to liver and diaphragm involvement (data not shown). These pilot studies suggested that intrahepatic injection resulted in tumor cell leakage into the peritoneal cavity in most or all cases. It is important to point out that other groups have had success with the intrahepatic injection model, in which post-injection pressure was applied for 1 minute [280].

Portal Vein Injection Model of Liver Metastasis

To investigate breast cancer metastasis to the liver in a fully immune competent host, under conditions where mice are not compromised due to multi-organ metastases, a portal vein injection model was developed. Intraportal injection models have been used previously to study liver metastasis of colorectal[281,282] and melanoma[50] cell lines; here we describe application of the intraportal injection to model syngeneic mammary tumor cell metastasis. This model can be used to study the later stages of the metastatic cascade including breast cancer cell extravasation and seeding, tumor cell fate decisions regarding death/proliferation/dormancy, and outgrowth into overt lesions. In this model, syngeneic mammary tumor cell lines are injected via the portal vein of immune competent Balb/c female mice, a method that delivers tumor cells firstly and directly to the liver without removal of the spleen. To develop this model, the use of four mammary tumor cell lines that range in their metastatic capability from low to high were employed: D2.OR, D2A1, and 4T1, and have employed D2A1 tagged with green fluorescent protein (D2A1-GFP)

to investigate early time-points after tumor cell injection. 4T1 is a highly metastatic cell line derived from the 410.4 tumor that spontaneously arose in an $MMTV^+$ Balb/c female mouse[234,263] and metastasizes to lung, liver, brain, and bone from mammary fat pad primary tumors[264,283,284]. D2A1 tumor cells were also originally derived from a spontaneous mammary tumor arising in a Balb/c host after transplant of D2 hyperplastic alveolar nodule cells, and are confirmed to be metastatic from the primary tumor to the lung[285,286]. D2.OR tumor cells are a non-metastatic sister line to the D2A1 line and, although they escape the primary tumor and arrive at secondary sites, they rarely establish distant metastases[213,286].

Additionally, it is important to avoid use of commonly employed pain management drugs including non-steroidal anti-inflammatory drugs (NSAIDs) during or following the surgical procedure. NSAIDs have anti-tumor activity in certain breast cancers[47,287-289], and some classes of NSAIDs increase the risk of hepatotoxicity[290,291], potentially compromising the study of liver metastasis and the liver metastatic niche. Further, studies suggest that NSAIDs directly influence the tissue microenvironment, reducing pro-metastatic extracellular matrix proteins tenascin-C[113] and fibrillar collagen[47,289]. Alternatively, the use of an opioid derivative, buprenorphine, was used because of its efficacy in rodent pain management[292] and due to the lack of evidence that opioids have anti-tumor activity[293]. This portal vein injection model was optimized for smaller injection volumes of 5-10 µl to avoid unnecessary damage to the liver. The model was also optimized to include needles with smaller diameter (≥32 gauge) and use of hemostatic gauze immediately following injection to minimize blood loss during the

procedure. In contrast to these optimized injection parameters, cell numbers should be determined on an individual basis, based on the tumorigenic potential of the cell line. However, starting at ≤10,000 cells/injection for long-term studies is recommended. For shorter endpoints (e.g. 24 hours post-injection) considerably more tumor cells (e.g. $1x10^5$-$1x10^6$) may be used if warranted. In summary, the portal vein injection model detailed here represents a useful tool for the study of breast cancer metastasis to the liver and circumvents a number of the limitations of other liver metastasis models. This model facilitates study of tumor cell extravasation, seeding, early fate decisions of survival, proliferation, and dormancy, and metastatic outgrowth in immune competent murine hosts.

Protocol:

All animal procedures in this article were reviewed and approved by the Oregon Health & Science University Institutional Animal Care and Use Committee.

Table 2-1: Materials

Name of Material/ Equipment	Company	Catalog Number	Comments/Description
1 ml Syringe w/ 26-gauge Needle	BD Syringe	309597	For subcutaneous buprenorphine injection; use caution, sharp
Alcohol Prep Pads	Fisher Scientific	06-669-62	For cleaning of abdomen prior to surgical incision
All Purpose Sponges, Sterile	Kendall	8044	4" x 4", use dipped in sterile saline to keep large and small intestines protected and hydrated during surgery
Artificial Tears	Rugby	370114	Mineral oil 15%, white petrolatum 83%; use to protect eyes during surgery
Sodium Hypochlorite			Use caution, corrosive; use at 10% to disinfect workspace and surfaces, multiple suppliers
Buprenorphine HCl, 0.3 mg/ml	Mfg. by Reckitt Benckiser	NDC-12496-0757-1	Use at 0.05 - 0.1 mg/kg body weight, 1-2x daily for 72 hours, injected subcutaneously
Bupivacaine HCl, 0.5% (5 mg/ml)	Mfg. by Humira Inc	NDC-04091163-01	Use at 0.5%, 1x immediately after surgery, 10 ul injected subcutaneously at incision site
Celox™ Rapid Hemostatic Gauze	Medtrade Products Ltd.	FG08839011	Cut into 5mm² pieces, use to stop blood flow out of the portal vein with pressure following injection
Chemical Depilatory			Use to remove hair from surgical area; multiple suppliers
Chlorhexidine, 2% Solution	Vet One	1CHL008	Use caution, do not get chlorhexidine in mucous membranes or ears of the mouse
Cotton Tipped Applicators, Sterile	Fisher Scientific	23-400-114	6" Wooden Shaft 2 pc/envelope
DMEM, High-Glucose	HyClone	SH30243.01	Cell culture media base for use with D2A1, D2.OR, and 4T1 mammary tumor cell lines
Dry Glass Bead Sterilizer			Use between surgeries to sterilize stainless steel tools, use caution, extremely hot; multiple suppliers
Ethanol, 70% solution			Use caution flammable; use to clean surgical area as needed; multiple suppliers
Fetal Bovine Serum	HyClone	SH30071.03	Cell culture media additive for use with D2A1, D2.OR, and 4T1 mammary tumor cell lines, use at 10% in DMEM high glucose
Gauze, Sterile	Kendall	2146	2" x 2", use dipped in chlorhexidine 2% solution for cleaning of abdomen prior to surgical incision
L-Glutamine 200 mM (100X)	Gibco	25030-081	Cell culture media additive for use with D2A1, D2.OR, and 4T1 mammary tumor cell lines, use at 2 mM (1x) in DMEM high glucose
Heating Pad, x2-3			Use to maintain body heat during surgery and recovery; multiple suppliers
Hemocytometer	Hausser Scientific	1483	For use in cell culture to count cells
Hemostatic Forceps			Stainless steel; multiple suppliers
Insulin Syringe, 0.3 ml, 29-gauge	BD	324702	For bupivacaine injection at suture site; use caution, sharp
Isoflurane	Piramal	NDC-66794-017-25	Administered at 2.5%
Isoflurane Vaporizer	VetEquip	911103	Use caution, vaporizes anesthetic gases
Light Source			Use for visualizing the surgical field; multiple suppliers
Neutral buffered formalin, 10%	Anatech Ltd.	135	Use caution, toxic; use as a tissue fixative for metastasis endpoints and assesment of metastatic burden by histology
Operating Scissors			Stainless steel; use caution, sharp; multiple suppliers
Penicillin/Streptomycin, 100x	Corning	30-002-CI	Cell culture media additive for use with D2A1, D2.OR, and 4T1 mammary tumor cell lines, use at 1x in DMEM high glucose
Phosphate-buffered Saline			Use at 1x for resuspending tumor cells prior to injection, multiple suppliers
Removable Needle Syringe, 25 ul, Model 1702	Hamilton	7654-01	For portal vein injection; use caution, paricularly while working with tumor cell-loaded needles, sharp when needle is attached
Small Hub Removable Needles, 32-gauge	Hamilton	7803-04	For portal vein injection, 1" length, point style 4, 12°angle, 33- to 34-gauge reusable needles can also be used; use caution, paricularly while working with tumor cell loaded needles, sharp
Sterile Saline	Fisher Scientific	BP358-212	0.9% NaCl solution; alternatively, can be homemade and sterile filtered
Surgical Gloves, Sterile			Multiple suppliers
Sutures, Sterile	Ethicon	J310H	4-0 27" coated vicryl w/ 22 mm 1/2c taper ethalloy needle; use caution, sharp
Table Top Portable Anesthesia Machine	VetEquip	901801	Use with isoflurane vaporizer for mouse anesthesia
Thumb Dressing Forceps			Stainless steel; multiple suppliers
Towel Drapes, Sterile	Dynarex	4410	18" x 26", to cover heating pad and provide a sterile workspace during surgery
Trypan Blue	Life Technologies	T10282	For use in cell culture to assess viability, use 1:1 with cells in 1x PBS
Trypsin/EDTA, 0.05% (1x)	Gibco	25300-054	Use in cell culture to detach tumor cells from tissue culture plates

1. Preparation of the surgical area and instruments

1.1) Prepare the scissors, forceps, and hemostat by autoclaving at 124 °C for 30 minutes, 1-2 days prior to the planned surgeries. Ensure access to autoclaved or sterile bedding, cages, and food for post-surgical recovery.

1.2) Prepare an aseptic surgical area, preferably in a laminar flow hood.

1.2.1) Wipe down all surfaces of the surgical area with 10 % bleach, including the heating pad, light source, anesthesia tubing and nose cone, and any other part of the surgical suite that will be in close proximity to the surgical procedure while it is being performed.

1.2.2) In the aseptic surgical area, place the cleaned heating pad with sterile drape, light source, anesthesia tubing and nosecone, insulin syringes, 1 ml syringes, bupivacaine, artificial tears, sterile saline, 2x2" sterile gauze sponges, 4x4" sterile gauze, hemostatic gauze cut into 0.5-1 cm^2 pieces, scissors, forceps, hemostat, 4-0 vicryl sutures with taper needle, and 50 ml 2% Chlorhexidine in an autoclaved container.

1.2.3) Ensure that there is room in this space for prepared tumor cells stored on ice.

1.2.4) On the bench adjacent to the surgical area, prepare the recovery area with a second heating pad and clean cages with sterile bedding.

NOTE: This area can also house items such as a bead sterilizer.

2. Portal vein injection

2.1) One-hour prior to the planned injections, treat Balb/c female mice aged 8-15 weeks with 100 µl of 0.015 mg/ml buprenorphine, subcutaneously, for pain management.

NOTE: This injection protocol may be applied to any strain of female or male mouse at any age, using the appropriate cell lines for changes to the strain.

2.2) Prepare the tumor cells for injection based on protocols for the cell line or tumor explant of choice.

2.2.1) For syngeneic Balb/c tumor cell lines including D2A1, D2.OR, and 4T1 tumor cells, thaw cells into a 10 cm tissue culture plate 3 days prior to injection such that the following day cells are at ~90-100% confluency.

2.2.2) 1 day following tumor cell thaw wash cells once with 1x phosphate buffered saline (PBS) and trypsinize the confluent tumor cells using 2 ml of 0.05 % trypsin at 37 °C for 5 minutes. Add 8 ml of complete media (DMEM high glucose, 10 % fetal bovine serum, 2 mM L-glutamine, and 1x penicillin/streptomycin) and passage 1:10 into a fresh 10 cm dish with 10 ml of complete media.

2.2.3) On the day of the injections, wash cells once with 1x PBS and trypsinize as described above.

2.2.4) Resuspend trypsinized cells in 8 ml of complete media, spin for 5 minutes at 1500 x g, remove the media and resuspend in 5 ml 1x PBS.

2.2.5) Count cells on a hemocytometer using trypan blue exclusion for viability assessment. Resuspend cells for injection in 1x PBS at a pre-determined concentration and volume.

NOTE: 5-10 μl is recommended as smaller injection volumes prevent unnecessary damage to the liver.

2.2.6) Keep cells on ice for the duration of the injections. Following completion of injections, return a sample of cells to the laboratory and place in culture in complete media for 1 day to ensure viability.

2.3) Place the mouse under anesthesia with 2-2.5% isoflurane (2-chloro-2-(difluoromethoxy)-1,1,1-trifluoro-ethane) delivered in oxygen. Maintain body temperature using the heating pad. Ensure complete anesthetization by assessing for a reaction to a toe pinch, and then maintain anesthesia at 2-2.5 % isoflurane.

NOTE: It is important to monitor the animals breathing rate and adjust the isoflurane flow-rate accordingly throughout the procedure.

2.4) Place a small amount of artificial tears or vet ointment over each eye to avoid excessive drying of the eyes during the surgical procedure.

2.5) Place the mouse in a supine position, on its back with abdomen exposed.

2.6) Remove hair on the ventral left side of the rodent from the second rib space down to the 4^{th} inguinal mammary gland nipple by wiping the area with chemical depilatory. Allow the depilatory to sit for 1-2 minutes and then remove completely with gauze and H_2O. This step can be done 1-2 days in advance to save time if numerous surgeries are planned.

2.7) Take one 2x2" sterile gauze sponge (soaked in 2 % Chlorhexidine) and wipe down the mouse at the site of hair removal. Sterilize the entire surrounding area, including the tail, to minimize bacterial contamination of instruments.

2.8) Wipe the site of hair removal and surrounding area down with an alcohol prep pad.

2.9) Repeat 2 % Chlorhexidine and alcohol steps once more and finish with a final Chlorhexidine wipe down for a total of three 2 % Chlorhexidine and two alcohol prep

pad washes. Do the final Chlorhexidine wipe such that the chemical is not dripping around the surgical site to avoid getting Chlorhexidine on internal organs.

NOTE: Application of large amounts of chlorhexidine and alcohol to the skin and surrounding fur may result in a significant drop in body temperature. Do not wipe with excess volume during steps 2.7-2.9. Maintain body temperature with a heating pad.

2.10) Using sterile gloves, autoclaved scalpel with sterile blade and autoclaved forceps, or scalpel with sterile blade and forceps that have been bead sterilized between surgeries, make a single 1-inch incision into the skin between the median and sagittal planes on the left side of the mouse, starting above the plane of the fourth inguinal mammary gland teat and ending just below the ribs.

2.11) Using autoclaved or bead sterilized scissors and forceps, make a similar 1-inch incision into the peritoneum. Avoid cutting into the mammary fat pad and ensure not to cut the intestines, liver, or diaphragm.

2.12) Place a 4x4” gauze pad soaked in sterile saline on the left side of the mouse, where the incision was made, such that internal organs can be placed on the gauze and not come into contact with the surrounding skin or surgical area.

2.13) Prepare tumor cells by pipetting up and down several times as tumor cells will settle during preparation of the mouse. Prepare a 25 ul removable needle syringe and 32-

gauge needle with tumor cells. Push on the syringe until tumor cells are at the tip of the needle and the plunger is at the appropriate volume for injection; avoid injection of air bubbles.

2.14) Wipe the outside of the needle with a sterile alcohol pad to remove any external tumor cells. Use caution to avoid needle sticks.

2.15) Hold the median side of the incision, including skin and peritoneal lining, aside with the forceps and use a sterile cotton swab to carefully pull the large and small intestines out, placing them on the sterile gauze soaked in sterile saline. Pull out large and small intestines until the portal vein is visualized.

2.16) Cover the internal organs in the saline soaked gauze to maintain internal moisture and sterility.

2.17) Have an assistant, also wearing sterile gloves, hold the intestines wrapped in the saline soaked gauze gently out of the way with a sterile cotton tipped swab to fully reveal the portal vein. Additionally, it may be necessary to use the autoclaved hemostat or forceps to hold tissue aside on the median side of the incision.

2.18) Insert the needle loaded with tumor cells ~3-5 mm into the portal vein ~10 mm below the liver at an angle <5° to the vein, with bevel facing up. Slowly inject the full volume containing tumor cells. Allow blood to flow past the needle head for several

seconds to avoid back flow of tumor cells out of the vein. Minimize moving the needle in the vein during the injection. Again, use caution to avoid needle sticks.

NOTE: Visualization of the portal vein is done without magnification, however a stereo microscope may be used if preferred.

2.19) Remove the needle while simultaneously placing a sterile cotton tip applicator on the vein with pressure. With the assistant still holding the intestines aside place one piece of 0.5-1 cm^2 hemostatic gauze over the injection site on the vein. Hemostatic powder was also attempted for this step in the protocol but was not effective in stopping venous blood loss following injection.

2.20) Hold the hemostatic gauze at the injection site with pressure from a sterile cotton tip applicator for 5 minutes.

2.21) Assess closure of the vein by carefully lifting the hemostatic gauze, if the gauze sticks to the surrounding tissue, a small amount of sterile saline can be used to soak and lift the gauze.

2.22) If blood loss occurs at this time, place an additional piece of hemostatic gauze at the site with pressure for an additional 5 minutes. When blood flow has ceased completely, remove the gauze from the mouse.

NOTE: Blood loss during the surgical procedure must be carefully assessed and if the total allowed blood loss volume is met or exceeded (based on regulatory standard operating procedures for the investigator's institutional review boards) the mouse must be euthanized while under anesthesia by cardiac perfusion.

2.23) Once the injection site is deemed intact, with no blood leaving the injection site, place the internal organs gently back into the abdominal cavity.

2.24) Suture the peritoneal lining and then the skin with sterile 4-0 vicryl suture and taper needle using a simple continuous or interrupted suture pattern. Typically, closing the incision requires 10-15 sutures.

2.25) Inject 100 µl of bupivacaine (5 mg/ml) along the incision site for local pain management using an insulin syringe. Inject 0.5 ml of sterile saline subcutaneously using a 1 ml syringe with 26-gauge needle for hydration. Surgeries take 15-25 minutes to complete.

2.26) To maintain sterile conditions throughout the surgery ensure that all tools and materials coming into contact with the mouse, including gloved hands, are cleaned appropriately prior to contact. Where possible use sterile materials and gloves, or minimally utilize a 70% Ethanol solution or 10% bleach solution to clean.

2.27) If multiple surgeries are planned for a single session remake the initial surgical area with fresh sterile drape, insulin syringes, 1 ml syringes, sterile saline, 2x2" sterile gauze sponges, 4x4" sterile gauze, hemostatic gauze cut into 0.5-1 cm^2 pieces, 4-0 vicryl sutures with taper needle, and 2% Chlorhexidine. Bead-sterilize the scissors, forceps, and hemostat in between surgeries and allow to adequately cool prior to re-use.

3. Recovery, monitoring rodent health, and end-point analyses

3.1) After the surgical procedure is complete, maintain mice on a heating pad for recovery in bedding-free, clean cages for a minimum of 20 minutes. Mice typically take 2-4 minutes to wake up from anesthesia.

3.2) Do not return an animal that has undergone surgery to co-habitation with other animals until it has fully recovered from anesthesia. Do not leave an animal unattended while it is regaining consciousness and monitor until the animal has regained the ability to maintain itself in sternal recumbency.

3.3) Give mice 0.05-0.1 mg/kg buprenorphine for pain management every 6-12 hours following surgery, for up to 72 hours.

3.4) Check sutures daily to ensure they remain intact during healing. In the case that sutures come undone, place the mouse under anesthesia, remove remaining sutures, and

replace. In the case of infection or inflammation consult veterinarian staff. Infection or inflammation have not been encountered with this protocol.

3.5) For metastasis studies, perform daily health checks until outward signs of metastatic disease are observed including, but not limited to: >10% weight loss/gain, scruffiness, loss of attention to surroundings, abdominal edema/ascites, pale eyes and ears, or a hunched position.

NOTE: Daily health checks are particularly important when developing the model for use with a new cell line or cell concentration until the timeline of metastasis is well understood.

3.6) At study end-point, euthanize mice by CO2 inhalation followed by cervical dislocation.

NOTE: Alternative methods of euthanasia approved by the investigators' oversight committee may be used, including perfusion with 1x PBS while under anesthesia. Perfusion of the liver is performed by cannulating the portal vein, snipping the inferior vena cava, and pushing 1x PBS through the liver vasculature at a rate of 4 ml/min for 1-2 minutes to remove circulating blood and leukocytes.

NOTE: Depending on the endpoint for the study, the cell line, and the concentration used, overt liver metastasis may or may not be apparent at necropsy. Micrometastatic lesions

may be revealed with histological analysis of the liver. Endpoints will vary based on the study design.

3.7) Extract the liver with scissors and forceps by first removing the gallbladder, then cut through the inferior vena cava superior to the liver. Cut through the vena cava, portal vein, and hepatic artery inferior to the liver.

3.8) Remove the whole liver gently and wash 5x in 1x PBS.

3.9) Separate the liver into left, right, median, and caudate lobes.

3.10) Formalin fix liver in 10% neutral buffered formalin for 48 hours while shaking at room temperature. Process tissues through a series of alcohols in increasing concentration and xylene; paraffin embed the fixed tissue[294].

NOTE: Alternatively, the liver may be snap-frozen by placing tissue in a cryomold with optimum cutting temperature (OCT) formula and freezing on dry ice pellets submerged in 95% ethanol.

3.10.1) Using a microtome, cut into the paraffin embedded tissue block such that a match-head size of tissue is revealed.

3.10.2) Cut five 4-micron serial sections, this constitutes the first level for analysis.

3.10.3) Cut through 250 microns of tissue, throw these sections in the waste.

3.10.4) At 250 microns cut a second level of five 4-micron serial sections.

3.10.5) Repeat as necessary to section through the entire liver. Hematoxylin and eosin stain the first section of every level to assess for metastasis[295].

NOTE: For snap-frozen tissue use a cryostat to cut sections.

NOTE: Detection of micrometastatic disease will require tumor cell specific staining.

3.11) Remove mice from study if there is tumor growth at the incision site, as this indicates tumor cell leakage into the peritoneal cavity following injection.

NOTE: This problem has not been observed.

Representative results

The portal vein injection model, in which tumor cells are delivered directly to the liver via a surgical procedure, allows for tumor cell injection into the portal vein. Under antiseptic conditions, in an anesthetized mouse, a ~1-inch surgical incision is made on the left side of the mouse between the median and sagittal planes, starting just above the plane of the fourth inguinal mammary gland teat and ending just below the ribs. The large

and small intestines are gently pulled through the incision to provide visualization of the portal vein (Fig.2-1A). Accurate anatomical identification of the portal vein and successful intra-portal injection can be confirmed by practicing the injection protocol with India ink or a similar dye. Correct injection via the portal vein will result in the ink being delivered immediately and specifically to the liver, and will not result in India ink spread to the lung (Fig.2-1B). Further, using D2A1 mouse mammary tumor cells tagged with GFP, dispersal of tumor cells throughout the liver is apparent at ninety minutes post-injection, confirming portal vein injection delivery to the liver (Fig.2-1C). At higher magnification it becomes apparent that at 90 minutes post-injection, tumor cells are found within sinusoids, as well as within the liver parenchyma in close proximity to portal triads, where the portal vein blood enters the liver (Fig.2-1C). These data suggest that active tumor cell extravasation is occurring at 90 minutes post-tumor cell injection. Taken together, these data confirm that the portal vein injection model delivers the injection volume directly to the liver, with ink or tumor cells dispersed throughout the liver and no appreciable transport of injection volume to the lung.

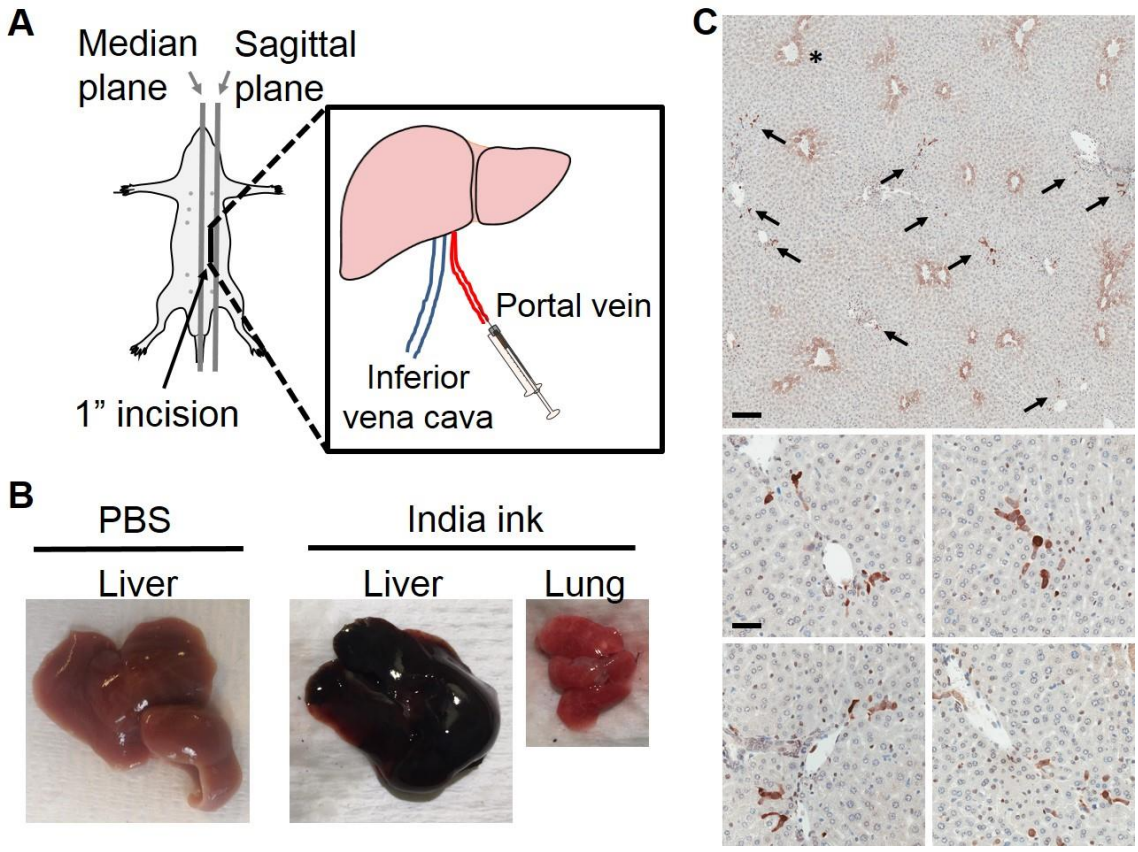

Figure 2-1: Portal vein injection delivers tumor cells directly to the liver

(A) Portal vein injection; the incision is made between the median and left sagittal planes, from above the plane of the fourth inguinal mammary gland teat and ending just below the rib cage. **(B)** Balb/c liver with PBS injection (left). Following India ink injection via the portal vein, the liver (middle) but not the lung (right) takes up ink. **(C)** Representative thin section images of D2A1 mouse mammary tumor cells tagged with GFP in a Balb/c mouse liver at 90 minutes post-injection of $1x10^6$ tumor cells via the portal vein. Livers were formalin fixed, paraffin embedded, sectioned, and stained with anti-GFP antibody for tumor cell detection. Top panel shows dark brown stained tumor cells (arrows) dispersed throughout the liver, asterisk denotes non-specific hepatocyte staining around central veins; scale bar=300 µm. Lower panels show representative images of tumor cells at 90 minutes post-injection still closely associated with vasculature; scale bar=50 µm.

To assess robustness of the portal vein injection model, three separate syngeneic mouse mammary tumor cell lines were tested in adult female Balb/c mice. These mammary tumor lines were selected based on their characterized behavior in mammary fat pad models and include the highly aggressive and metastatic 4T1 cell line, the less aggressive metastatic D2A1 line, and the low/non-metastatic D2.OR line[42,213,234,296]. 2,000 and 10,000 cells per injection were tested with no notable differences in the time to development of overt metastasis with these low cell concentrations. For these studies surrogate markers of metastasis were used such as lack of grooming, pallor, and weight loss to justify necropsy, upon which the presence or absence of liver metastases were confirmed by visual assessment of the liver and other organs to confirm intra-portal delivery. These data confirm previous reports that the 4T1 and D2A1 cell lines represent more aggressive mammary tumor lines, as shorter metastasis free survival rates are observed compared to mice injected with the less aggressive D2.OR line (Fig.2-2A). Mice injected with 4T1 or D2A1 tumor cells developed overt liver metastasis by ~30-40 days post-injection, and some developed metastasis as early as 18 days post-injection (Fig.2-2A), whereas only one mouse injected with D2.OR cells had developed overt liver metastasis by study end, which was 60-65 days post-tumor cell injection. Metastases were subsequently confirmed by sectioning through the liver in 250 μm levels and analyzing hematoxylin and eosin (H&E) stained sections (Fig.2-2B-D).

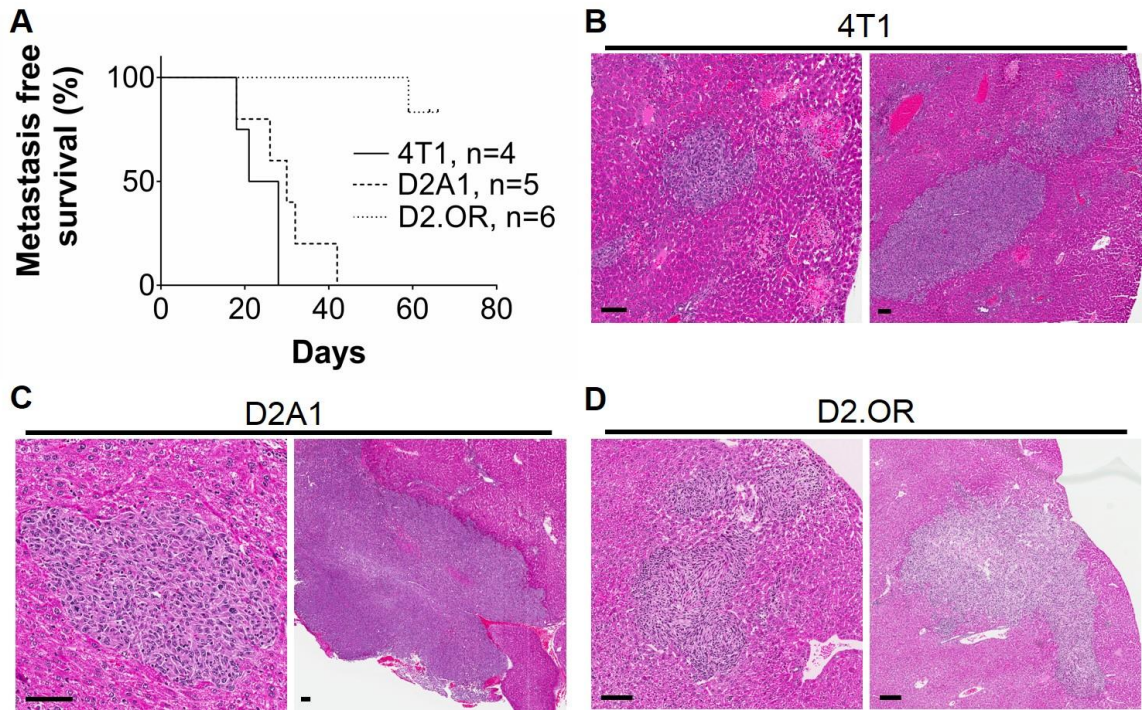

Figure 2-2: Outgrowth of mouse mammary tumor cell lines in the liver following portal vein injection

(A) Kaplan-Meier curve showing metastasis-free survival rates in mice injected with 2,000-10,000 4T1, D2A1, or D2.OR mouse mammary tumor cells. Mice were injected with tumor cells and monitored for signs of metastasis including lack of grooming, pale eyes, and weight changes. Metastasis was confirmed at time of necropsy and by H&E on histological sections of the livers. N=2 4T1 2,000 cells; 2 4T1 10,000 cells. N=2 D2A1 2,000 cells; 3 D2A1 10,000 cells. N=3 D2.OR 2,000 cells; 3 D2.OR 10,000 cells. Representative H&E images of **(B)** 4T1 lesions at 21 days post-injection of 10,000 cells **(C)** D2A1 lesions at 26 days post-injection of 10,000 tumor cells, and **(D)** D2.OR lesions at 59 days post-injection of 10,000 cells; scale bars=75 µm. Similar lesions are observed when 2,000 4T1 or D2A1 tumor cells were injected. No lesions were detected with 2,000 D2.OR cells. No evidence of metastasis in other organs or at the surgical incision site was apparent in any mouse on these studies.

In addition to detection of overt metastatic lesions in the mouse liver, the portal vein model can also be utilized to study earlier events in the metastatic cascade including detection of single cells/cell clusters following extravasation, and formation of micro-metastatic lesions. Multiplex immunofluorescence-staining was used to detect 4T1, D2A1, and D2.OR mammary tumor cells in liver when they are present as single cells or micro-metastatic lesions, as H&E is not sufficient to confirm the presence of small lesions. Figure 2-3A shows a representative Balb/c mouse liver with a putative micrometastatic foci of D2A1 tumor cells that are positive for the epithelial keratin CK18, negative for the pan-immune marker CD45, and negative for the hepatocyte marker Heppar-1. Hepatocytes also stain positive for CK18, necessitating use of Heppar-1 in this staining panel. One important note is that bile duct epithelium and liver progenitor cells stain positive for CK18, requiring careful discrimination between tumor cells and bile ducts, particularly when assessing periportal regions (Fig.2-3A). An alternative to multiplex immunofluorescence to identify single disseminated cells and micrometastatic foci is to utilize syngeneic mammary tumor lines tagged with enhanced green fluorescent protein (eGFP) and/or luciferase and perform IHC for the tag (Fig.2-1C). Due to the immunogenicity of eGFP, luciferase, and other proteins, it is essential to use mouse models that are tolerized to these proteins, such as the novel immune competent "glowing head" mouse that expresses eGFP and luciferase in the anterior pituitary gland[297]. For identification of macrometastatic lesions of untagged syngeneic lines such as the D2A1 tumor line, the CK18/Heppar-1/CD45 multiplex immunofluorescence is ideal (Fig.2-3B).

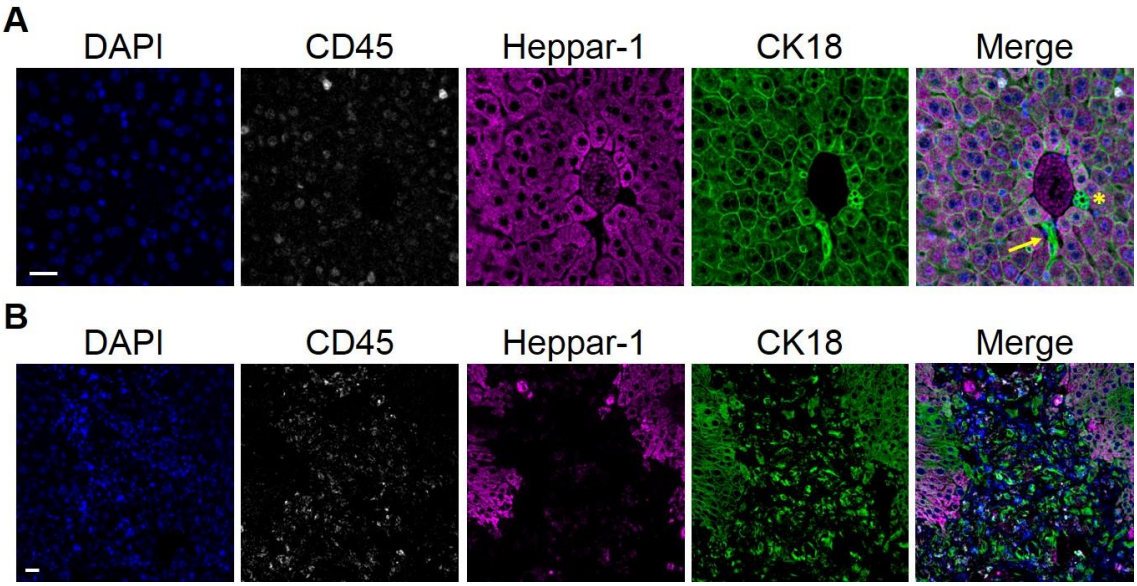

Figure 2-3: Detection of single cells and metastatic lesions in the mouse liver using multiplex immunofluorescence

(A) Representative multiplex immunofluorescence of D2A1 tumor cells in a Balb/c mouse liver at 90 minutes post-injection using the portal vein injection model. Staining was done using a multiplex kit. From left to right shows DAPI; CD45 to mark leukocytes; Heppar-1 to mark hepatocytes; and CK18 to mark tumor cells, hepatocytes, and bile duct epithelium. Merged image shows a putative cluster of $CK18^{+}$Heppar-1^{-} $CD45^{-}$ D2A1 tumor cells closely associated with a portal triad. Arrow=D2A1 tumor cells, asterisk=bile duct epithelium; scale bar=25 µm. **(B)** A representative overt D2A1 metastatic lesion using the same staining panel as in A. Tumor cells are $CK18^{+}$ whereas adjacent hepatocytes are $CK18^{+}$Heppar-1^{+}; scale bar=25 µm. Images were captured on a microscope with 20x0.8, 40x1.3, and 60x1.4 objectives and CCD camera, using the microscope software.

Discussion

The Balb/c mouse portal vein injection model permits the study of mammary cancer lesions in the liver in the absence of confounding multi-organ metastasis and in a fully immune competent host. Our protocol is an advancement of previously published surgical procedures that permit access to the portal vein for injection of tumor cells directly into the liver[50,281,282]. One advancement we have made is to significantly reduce the number of injected tumor cells from $\geq 1x10^5$ cells/injection[50,281,282] down to ≤10,000 tumor cells/injection. We have also expanded the model for the study of breast cancer metastasis to the liver. Using this protocol, two mammary cancer cell lines with known metastatic potential develop liver metastases with shorter latency than a more quiescent mammary tumor cell line. Further, at early time points, tumor cells are distributed throughout the liver parenchyma as single or small groups of single cells after tumor cell injection. The model is poised to address questions of metastatic efficiency including tumor cell extravasation, cell survival, dormancy, and proliferation - all phenotypes that contribute to the development of micro-metastatic and overt metastatic disease in the liver.

It is important to consider numerous aspects of the portal vein injection protocol prior to initiating studies. Carefully deciding on cell lines, cell concentration, total cell number, and end-points of interest based on smaller exploratory studies is highly recommended. Further, the use of immune competent hosts and syngeneic cell lines is of utmost importance for understanding host-tumor cell interactions. The newly developed "glowing head" mouse that expresses eGFP and luciferase from the anterior pituitary

gland is an important tool for eliminating host responses to exogenous eGFP and luciferase, proteins often used to tag mammary tumor lines[297]. Use of the "glowing head" mouse and syngeneic tagged tumor cells will facilitate easy identification of single disseminated cells and micrometastatic foci by IHC without the concern of inflammatory responses to eGFP or luciferase. Similarly, choosing pain management strategies carefully to ensure minimal anti- or pro-tumor impact from the drug treatment regimen is strongly recommended. Critical steps in this protocol include maintaining sterile conditions throughout surgeries to ensure that infection does not occur, as this will confound any results. It is also important that the needle is properly placed in the portal vein to ensure that tumor cells are delivered to the liver. Practicing the protocol with dyes such as India ink will help with this issue. Tumor growth at the skin incision site is the best indicator that improper needle placement occurred. Finally, it is critical that blood loss from the portal vein is adequately controlled and ceases entirely prior to suturing the animal. The use of hemostatic gauze greatly diminishes the risk of uncontrolled blood loss from the portal vein following injection. In our hands, procedural related mortality due to blood loss from the portal vein following injection was reduced from 30% to 2% of mice with the use of hemostatic gauze.

It is important to note that the portal vein injection model does not replicate the full metastatic cascade, but is limited to the study of tumor cell extravasation, tumor cell-niche interactions following extravasation and tumor growth. Models that accurately replicate the full metastatic cascade to the liver, such as occurs in patients, are urgently needed. An additional limitation of the portal vein injection model is that it is confounded

by the impact of surgery on the host, with wound healing known to impact disease progression[298,299].

The portal vein injection model represents an improvement on other injection models to study liver metastasis, including intracardiac and intrasplenic models. Specifically, the portal vein injection model allows for the study of a larger range of disease progression than the intracardiac model, which is often limited by concomitant metastases in other tissues. Further, the portal vein model is not complicated by removal of the spleen, as is done in the intrasplenic model.

The portal vein injection model may prove a useful tool for the study of liver metastasis in general. Liver metastasis is the most frequent site of metastasis in adenocarcinomas overall, with particularly high rates in pancreatic cancers (85% of metastases are to the liver), colon and rectal adenocarcinomas (>70%), as well as stomach and esophageal (>30%)[239]. Although spontaneous and orthotopic primary tumor models of pancreatic and colon adenocarcinomas more readily metastasize to the liver[300,301], the portal vein injection model may prove useful to understanding the metastatic process of these cancers as controlled delivery of tumor cells permits biochemical, molecular and histological assessments at specified times after tumor cell arrival. In summary, the portal vein injection model represents an important improvement on available liver metastasis models of breast cancer, and may also be applicable to the liver metastasis field in general.

Acknowledgements

The authors would like to acknowledge Alexandra Quackenbush for assisting with surgical procedures during filming of the video protocol, Hadley Holden for histological support, Sonali Jindal for input on tumor and liver pathology during method development, and Breanna Caruso for critical review of the manuscript. The D2A1 and D2.OR mammary tumor cells were a gift from Dr. Ann Chambers, the D2A1-GFP tumor cells were a gift from Dr. Jeffrey Green, and the 4T1 tumor cells were a gift from Dr. Heide Ford. The OHSU Advanced Light Microscopy Core at the Jungers Center was utilized for imaging. The work included in this manuscript includes funding from NIH/NCI NRSA F31CA186524 (to ETG) and NIH/NCI 5R01CA169175 (to PS).

Chapter III: The Rodent Liver Undergoes Weaning-Induced Involution and Supports Breast Cancer Metastasis[2]

Published Manuscript

Goddard ET, Hill RC, Nemkov T, D'Alessandro A, Hansen KC, Maller O, Mongoue-Tchokote, Mori M, Partridge AH, Borges VF, Schedin P. The Rodent Liver Undergoes Weaning-Induced Involution and Supports Breast Cancer Metastasis. Cancer Discovery, 2016 Dec. Epub ahead of print. doi: 10.1158/2159-8290.CD-16-0822

Contributions

VFB and PS were responsible for hypothesis development, conceptual design, all data analysis and interpretation. ETG developed the intracardiac and intraportal injection mouse models and designed and performed all animal experiments, biochemical and molecular analyses, and data interpretation. RH, TN, AD and KH developed methodology and performed all metabolomic and proteomic analyses. ETG and OM contributed to design conception and model development. SMT and MM performed the patient data statistical analyses. AP was responsible for extensive chart review and selection of human cases for this study. VFB, AP, and ETG were responsible for regulatory oversight of human data acquisition. ETG, VFB, and PS wrote the manuscript. The authors declare no competing financial interests.

[2] The majority of this chapter was re-printed with permission from Cancer Discovery (Goddard ET, Hill RC, Nemkov T, D'Alessandro A, Hansen KC, Maller O, Mongoue-Tchokote, Mori M, Partridge AH, Borges VF, Schedin P. **The Rodent Liver Undergoes Weaning-Induced Involution and Supports Breast Cancer Metastasis.** Cancer Discovery, doi: 10.1158/2159-8290.CD-16-0822 (2016))

Abstract

Postpartum breast cancer patients are at increased risk for metastasis compared to age-matched nulliparous or pregnant patients. Here, we address whether circulating tumor cells have a metastatic advantage in the postpartum host and find the post-lactation rodent liver preferentially supports metastasis. Upon weaning, we observed liver weight loss, hepatocyte apoptosis, ECM remodeling including deposition of collagen and tenascin-C, and myeloid cell influx, data consistent with weaning-induced liver involution and establishment of a pro-metastatic microenvironment. Using intracardiac and intraportal metastasis models, we observed increased liver metastasis in post-weaning Balb/c mice compared to nulliparous controls. Human relevance is suggested by a ~3-fold increase in liver metastasis in postpartum breast cancer patients (n=564) and by liver-specific tropism (n=117). In sum, our data reveal a previously unknown biology of the rodent liver, weaning-induced liver involution, which may provide insight into the increased liver metastasis and poor prognosis of women diagnosed with postpartum breast cancer.

Statement of Significance

We find that postpartum breast cancer patients are at elevated risk for liver metastasis. We identify a previously unrecognized biology, namely weaning-induced liver involution that establishes a pro-metastatic microenvironment, and which may account in part, for the poor prognosis of postpartum breast cancer patients.

Introduction

Breast cancers diagnosed within 5 years of childbirth impart a ~3 fold increased risk for metastasis compared to breast cancers diagnosed in age-matched nulliparous or pregnant women[8-10]. Increased metastasis has been found to be independent of tumor ER, PR, or Her-2 expression, or tumor stage[9], implicating a host biology specific to the postpartum period. In rodents, the postpartum event of weaning-induced mammary gland involution promotes early stages of breast cancer metastasis, including tumor cell escape from the mammary gland[42,47,49]. However, late stages of the metastatic cascade are rate limiting, including survival at secondary sites[50], and highlight the critical role of the 'soil' in determining fate of the metastatic 'seed'. For example, in experimental metastasis models, tumor cells extravasate into secondary tissues at high rates but subsequently die off or fail to efficiently establish overt metastatic lesions[50]. Pro-metastatic microenvironments can shift this bottleneck such that tumor cells are more likely to successfully establish metastatic lesions[82,197,205]. Here, we tested whether breast cancer cells have a metastatic advantage at secondary sites in the postpartum host. Rationale for this hypothesis is based upon the assumption that organs with increased metabolic output during pregnancy and lactation, such as the liver, might undergo postpartum involution to return the organ to its baseline metabolic state. This tissue involution process is anticipated to enhance metastasis, as physiologic tissue involution is mediated by wound healing-like programs known to support tumor growth[42,47]. Here, using rodent models, we report that pup weaning induces maternal liver involution characterized by hepatocyte cell death and stromal remodeling consistent with establishment of a pro-metastatic microenvironment. Experimental metastasis models demonstrate increased liver

metastasis in post-weaning mice compared to nulliparous hosts. Potential human significance is suggested by a preferential increase in liver metastasis in postpartum patients compared to nulliparous controls. In summary, our studies identify a heretofore-unrecognized biology of the rodent liver, weaning-induced liver involution, a tissue remodeling process that establishes a pro-metastatic microenvironment. These findings address the role of normal physiology on metastatic niche education in the absence of a primary tumor, and provide a novel mechanism that may explain poor outcomes of postpartum breast cancer patients.

Materials and Methods

Postpartum rodent models

The UC-AMC and OHSU Institutional Animal Care and Use Committees approved animal procedures. Age-matched female Sprague-Dawley rats (Harlan, Indianapolis, IN) and Balb/c mice (Jackson Laboratories, Bar Harbor, ME) were housed and bred as described[42,49]. For tissue collection, rodents were euthanized across groups either by CO_2 asphyxiation or while under anesthesia by exsanguination via portal vein perfusion with PBS. Whole livers and/or lungs were removed, washed 3x in 1x PBS, and weighed. Median and right liver lobes were digested for flow cytometry analyses, left lobes were fixed in 10% neutral buffered formalin (Anatech ltd., Battle Creek, MI), and caudate lobes were flash frozen on liquid nitrogen for protein and RNA extraction.

Cell culture

4T1 cells, provided by Dr. Heide Ford in 2011 (University of Colorado, Aurora, CO), were cultured as described[284]. D2A1 cells were a gift from Dr. Ann Chambers in 2011 (London Health Sciences Centre, London, Ontario) and were cultured as described[296]. Cells were washed and resuspended in cold 1x PBS (Corning) for intracardiac and portal vein injections. 4T1 and D2A1 cells were confirmed murine pathogen and mycoplasma free, last testing date of 3/28/2011 (IDEXX BioResearch, Columbia, MO). Cell lines have not been authenticated. All cells used in the described experiments were within 2-5 passages of the tested lot.

Intracardiac model of metastasis

Anesthetized mice (2% isoflurane) with thoracic cavity hair removed with chemical depilatory were imaged using a Vevo 770 High-Resolution *In Vivo* Micro-Imaging System (Visual Sonics, Toronto, ON, Canada) and a 35 MHz mechanical transducer. 5,000 4T1 isogenic mammary tumor cells/100 µl PBS were loaded in a 1 ml syringe with a 30-gauge 1" needle and the needle tip rinsed with sterile saline to remove external tumor cells. Under ultrasound image guidance, the needle was placed into the left ventricle, tumor cells injected, and needle held within the heart for 4-6 seconds to ensure tumor cells entered the circulation. Nulliparous and involution day 2 mice were alternately injected. Mice were weighed daily and euthanized in a rolling study design, in pairs, one/group, upon weight loss (10-15% of body weight). All mice were euthanized 16-24 days post-injection (Nullip, n=24; Inv2, n=25). Presence of 4T1 tumor cells in liver, lung, bone, and brain was determined using clonogenic assays[284]. Mice were excluded if thoracic tumors were evident.

Intraportal injection model of metastasis

Mice were anesthetized, abdominal hair removed, and 5,000 D2A1 isogenic mammary tumor cells/10 µl PBS injected into the portal vein as described[238]. Mice were euthanized at 5 weeks post-injection (Nullip, n=18; Inv2, n=17; R, n=8) and visible liver metastasis assessed at necropsy. Five mice had equivocal liver lesions <3 mm in diameter that were subsequently assessed by histological evaluation of H&E thin sections by a Pathologist blinded to group. Of these mice, four had overt metastasis. Data are presented as the percentage of mice in each group with liver metastasis.

Flow cytometry

For initial flow cytometric analyses, individual mouse livers were digested in 1 mg/ml collagenase I and 0.5 mg/ml hyaluronidase for 30 min shaking at 37°C, and filtered through a 100 µ filter (BD Biosciences). Red blood cells were lysed using 1x RBC lysis buffer (eBioscience, San Diego, CA). Samples were washed 3x with 1x PBS and counted in trypan blue using a Cellometer T4 Plus Cell Counter (Nexcelom Bioscience, Lawrence, MA). $1x10^6$ cells per sample were blocked with CD16/32 (eBioscience, 1:100) for 30 min and cell surface markers were stained (CD45, 30-F11; CD11b, M1/70; F4/80, CI:A3-1; Ly6C, HK1.4; Ly6G, 1A8) for 35 min at 4°C in 100 µl FACS buffer and fixed with fixation buffer (BD Biosciences) for 30 min. Samples were analyzed on a Gallios 561 flow cytometer (Beckman Coulter, Indianapolis, IN; University of Colorado Flow Cytometry Core) and data analysis was done using Kaluza v1.2 software (Beckman Coulter). Single-color controls were used with each run and fluorescence-minus-one and

isotype controls were used to confirm $CD11b^+$, $F4/80^+$, $Ly6C^+$, and $Ly6G^+$ populations. Secondary analyses (Supplementary Fig.3-5) were performed after portal vein perfusion of livers with 1x PBS, and Fixable live-dead Aqua (Invitrogen, Thermo Fisher, San Jose, CA; 1:250) was included with the CD16/32 block. This analysis was performed on an LSRFortessa (BD Biosciences; Oregon Health and Science University Flow Cytometry Shared Resource) and analysis was performed using FlowJo (FlowJo, LLC Data Analysis Software, Ashland, OR).

Metabolomics

For metabolomics, mass spectrometry was performed on n=4 Inv4, Inv10; n=5 L, Inv2, Inv6; n=6 N, Inv8, R rats/grp. For mouse liver metabolomics, mass spectrometry was performed on n=6 N, L, Inv2, Inv4, Inv6; n=5 R; n=4 Inv8 mice/grp. Pulverized rat or mouse liver tissues were suspended at 10 mg/ml in ice-cold lysis/extraction buffer (methanol:acetonitrile:water, 5:3:2), vortexed for 30 min at 4°C, and centrifuged at 10,000g for 15 min at 4°C. For LC-MS analysis, 10 µl of samples were injected into a UHPLC system (Ultimate 3000, Thermo Fisher) and run on a Kinetex XB-C18 column (2.1 x 150 mm i.d., 1.7 µm particle size, Phenomenex, Torrance, CA) using a 3 min isocratic run at 250 µl/min (mobile phase: 5% acetonitrile, 95% 18 mΩ H_2O, 0.1% formic acid). The UHPLC system was coupled online to a Q Exactive mass spectrometer (Thermo Fisher), scanning in Full MS mode (2 µscans) at 70,000 resolution in the 60-900 m/z range, 4 kV spray voltage, 15 sheath gas and 5 auxiliary gas, operated in negative and then positive ion mode (separate runs). Calibration was performed before each analysis using positive and negative ion mode calibration mixes (Pierce, Thermo Fisher,

Rockford, IL) to ensure sub ppm error of the intact mass. Metabolite assignments were performed using the software Maven[302] (Princeton, NJ), upon conversion of .raw files into .mzXML format through MassMatrix (Cleveland, OH). The software allows for peak picking, feature detection and metabolite assignment against the KEGG pathway database. Assignments were further confirmed using chemical formula determination from isotopic patterns and accurate intact mass, and by matching retention times to an in-house library that contains 650+ metabolites (Sigma-Aldrich, St. Louis, MO, USA; IROATech, Bolton, MA, USA). Relative quantitation was performed by exporting integrated peak area values into Excel (Microsoft, Redmond, CA) for statistical analysis, including hierarchical clustering analysis (GENE-E; Broad Institute, Cambridge, MA). The metabolomics data reported in this paper are tabulated in the supplementary materials and archived at The Metabolomics Consortium Data Repository and Coordinating Center (DRCC) (Project ID PR000382: Rat metabolomics study ST000509, mouse metabolomics study ST000510).

Proteomics

For rat liver proteomics, mass spectrometry was performed on n=4 Inv4, Inv10; n=5 L, Inv2, Inv6; n=6 N, Inv8, R rats/grp. Approximately 50 mgs of flash frozen, pulverized liver tissue was processed as described[94,303]. The endogenous protein concentration of each sample was determined by Bradford assay, prior to proteolytic digestion. Samples were digested using the FASP protocol[304]. Briefly, 37.5 µg of each sample was added to a 10 kD molecular weight cut-off filter. 500 fmols of $^{13}C_6$ labeled ECM associated QconCAT standards[303] were spiked into each sample. Samples were analyzed on the

QTRAP 5500 triple quadrupole mass spectrometer (AB SCIEX, Framingham, MA) coupled with an UHPLC system (Ultimate 3000, Thermo Fisher). A targeted, scheduled Selected Reaction Monitoring (SRM) approach was performed using the QTRAP 5500. 16 µl of each sample was injected and directly loaded onto a Waters UPLC column (ACQUITY UPLC® BEH C18, 1.7 µm 150x1 mm) with 5% ACN, 0.1% FA at 30 µl/min for 3 min. A gradient of 2-28% ACN was run for 21 min to differentially elute QconCAT peptides. The mass spectrometer was run in positive ion mode with the following settings: a source temperature of 200°C, spray voltage of 5300V, curtain gas of 20 psi, and a source gas of 35 psi (nitrogen gas). Transition selection and corresponding elution time, declustering potential, and collision energies were specifically optimized for each peptide of interest using Skyline's step-wise methods set up[305]. Method building and acquisition were performed using the instrument supplied Analyst Software (Version 1.5.2).

Statistical analysis of rodent studies

All rodent data are from 2 independent breeding studies, with 4-25 animals per group, with the exception of immunoblots and zymogens, which were performed on pooled lysates with 4 samples/grp run as n=4-5 technical replicates. For intracardiac injection studies, one-tailed Chi-squared test was used to compare liver metastasis across groups based on pre-existing hypotheses; two-tailed Chi-squared test was used to compare lung, bone, and brain metastasis. For portal vein injection studies two-sided Fisher's exact test was used to compare frequency of liver metastasis across groups, student's t-test was used to compare number of lesions, lesion area, and tumor burden across groups.

Statistical analyses were performed using GraphPad Prism 6 (La Jolla, CA). All data are presented with mean and standard error of the mean (SEM), where applicable.

Statistical analysis of patient cohorts

The Colorado and OHSU Institutional Review Boards approved all human studies. All studies were conducted in accordance with the Declaration of Helsinki. Human subjects were enrolled via prospective trials where informed consent was obtained. UC cases before 2004 were obtained via consent and/or HIPAA exempt approved retrospective protocol. Cohort demographic, clinical, and treatment data are summarized in Supplementary tables 4 and 5, data analyses are summarized in Supplementary table 6. Two young women's breast cancer cohorts were analyzed, a UC cohort including all patients (≤45 y.o.) and a UC/DFCI (DFCI, <40 y.o.) cohort including only patients with metastatic recurrence. For analysis of the UC cohort (n=564) patients were defined as nulliparous if they had no evidence of complete or incomplete pregnancy, and as postpartum if they were diagnosed <5 or 5-<10 years after their last completed pregnancy. We excluded cases with incomplete parity data, if pregnant, or >10 years postpartum at time of diagnosis. Multivariate logistic regression was used to assess the effect of parity status on liver metastasis while adjusting for biologic subtype, age of the patient at diagnosis, and year of diagnosis. Patients in the subset analysis that included only metastatic patients (n=117) were excluded if site of first metastatic recurrence was unknown, or if diagnosed with multi-site metastatic disease upon initial recurrence, to limit analysis to first site of metastasis. In this subset analysis, the association between liver metastasis and parity status was assessed using one-sided (increased metastasis in

the postpartum group was predicted) as well as a two-sided Fisher's exact test; with significance (p=0.04; one-sided) or a trend towards significance (p=0.058; two-sided) demonstrated, respectfully. The association between lung, bone, and brain metastasis and parity status was assessed using two-sided Fisher's exact test because we did not have a pre-existing hypothesis.

Supplementary Methods

Immunohistochemistry

Immunohistochemical (IHC) detection was performed with a Dako autostainer universal staining system using Dako reagents unless otherwise noted. Antigen retrieval for Ki67, CD68, F4/80, Ly6C, and CD45 IHC was TRS (5 min, 95°C), Ly6G was EDTA, and tenascin-C was proteinase K (4 min, RT). Antibodies to Ki67 (SP6; 1:400), CD68 (ED1; 1:100), F4/80 (CI:A3-1; 1:100), tenascin-C (Ab19011; EMD Millipore-Merck, Darmstadt, Germany; 1:100 rat or 1:35 mouse), Ly6C (ER-MP20; 1:100), Ly6G (1A8; 1:2000) and CD45 (30-F11; 1:1000) were incubated on slides at RT for 1 hr. Secondary antibody incubations for Ki67, tenascin-C (Dako EnVision+ Rabbit), CD68 (Biocare, Concord, CA; Mouse-on-Rat HRP-Polymer), F4/80, Ly6C, Ly6G and CD45 (Biocare, Rat-on-Mouse HRP-Polymer) were all for 30 min at RT. Dako chromagen buffer substrate with hematoxylin counter stain was used to visualize positive stain. Stained slides were scanned on an Aperio ScanScope AT and image analysis and quantification was performed using Aperio ImageScope software (Leica Biosystems, Nussloch, Germany). For tenascin-C, CD68, F4/80, Ly6C, and Ly6G analysis IHC signal was normalized to area. Tenascin-C knockout mouse (C57Bl/6N-TgH) tissue was a gift from

Dr. Ana Coito (UCLA, CA). Image analyses were done using Aperio algorithms (Leica Biosystems) unless otherwise specified, and image analyses were performed by an investigator blinded to study design with results confirmed by an independent investigator.

Immunofluorescence

Primary antibody incubation for Ki67 (1:400), CK18 (Ab53118; Abcam 1:100) and Heppar-1 (OCH1E5; 1:50), was performed for 1 hr at RT. Tissues were incubated with fluorochrome conjugated secondary antibodies (goat anti-rabbit Alexa Fluor 488 or 594 and goat anti-mouse Alexa Fluor 594 or 488; Invitrogen, Thermo Fisher) for 30 min in the dark at RT. Prolong Gold Anti-Fade with DAPI (Invitrogen, Thermo Fisher) was used to mount coverslips. For multiplex staining of Ly6C, Ly6G, F4/80, Heppar-1, CK18, and/or CD45, the Opal™ 4-color IHC kit (Perkin Elmer, Inc., Waltham, MA) was used according to the manufacturer's recommendations. The first antigen retrieval was TRS or EDTA, with all subsequent retrieval steps with Citra (BioGenex, Fremont, CA). Ly6C (1:100, 1 h), F4/80 (1:200, overnight at 4°C) and Ly6G (1:2000, 1 h) were stained for in this order, all received Histofine anti-rat secondary (Nichirei Biosciences, Inc., Tsukiji, Chuo-ku, Tokyo, Japan) for 30 min. Heppar-1 (1:50, 1h) and CK18 (1:100, 1 h) were stained for in this order and were incubated with secondary Goat anti-mouse (Thermo Scientific, 1:1000) and Histofine anti-rat secondary for 30 min. For dual Ki67/Heppar-1 staining, images were acquired on an Olympus IX81 inverted motorized microscope using Intelligent Imaging Slidebook v.4.067. For dual CK18/Heppar-1 and Opal™ staining, images were acquired on a Zeiss ApoTome2 with 20x0.8 and 40x1.3 PlanApo

objectives and Zeiss AxioCam 506 CCD camera, using Zen 2™ software (Carl-Zeiss, Goettingen, Germany).

Special stains

For Masson's trichrome, FFPE liver sections were treated in Bouin's solution for 1 hour at RT, stained with Gill's #3 hematoxylin for 2 min and Biebrich scarlet-acid fuchsin solution for 2 min, differentiated in phosphomolybdic-phosphotungstic acid solution for 4 min, stained in aniline blue solution for 2 min, rinsed and differentiated in 1% acetic acid for 2 min. For reticulin staining, FFPE liver sections were stained with the American MasterTech Chandler's Reticulum Kit according to manufacturer's recommendations (American MasterTech Sci. Inc., Lodi, CA). Stained slides were scanned on an Aperio ScanScope AT and images acquired on Aperio ImageScope software.

Immunoblotting

Sample preparation of protein lysates and immunoblots were performed as described [95] on flash frozen pulverized liver tissue from 4 rodents/grp (50 mg liver/animal). Membranes were probed at 4°C with α-cleaved caspase-3 (9664; Cell Signaling Technologies, Danvers, MA, 1:500) or α-tenascin-C (Ab19011; EMD Millipore, 1:200), or for 1 hr at RT with α-GAPDH (G9545; 1:5000). Secondary goat anti-rabbit IgG (Bio-Rad, 1:10,000) or goat anti-mouse IgG (R&D Systems, Minneapolis, MN; 1:1000) were used with shaking for 1 hr at RT. Signal was detected with ECL substrate (Thermo Fisher) and an All Pro 100-Plus film developer (Air Techniques, Melville, NY).

Densitometry is from 5 immunoblots using 2 separate sets of pooled lysates and calculated using ImageJ (NIH).

In-gel zymography

Sample preparation of protein lysates and rat and mouse liver gel zymography was done as described[95]. Briefly, pooled liver samples (4/grp) were incubated at 37°C for 10 min prior to loading onto a 7.5%, 0.75 mm SDS-PAGE gel with 3 mg/ml Porcine Gelatin Type A (Sigma-Aldrich). Densitometry of gel zymogens was performed by combining data from 4 independent gels; all densitometry was done using ImageJ (NIH).

TUNEL

The TACS 2 TdT-DAB In Situ Apoptosis Detection Kit (Trevigen, Helgerman, CT) was used as per manufacturer's recommendations with Mn^{2+} ion used in the labeling reaction. Stained slides were scanned on an Aperio ScanScope AT. CK18 TUNEL dual-staining was described above with CK18 (1:100) and Dako Envision+ Rabbit secondary. DAB chromagen was used to visualize CK18 and Vina Green (Biocare) used to visualize $TUNEL^+$ cells.

Quantification of Ki67 IHC, TUNEL, mitotic hepatocytes, hepatocyte nuclei, and TNC fragment length

For rat liver $Ki67^+$ hepatocytes, rat and mouse liver $TUNEL^+$ cells, and mitotic hepatocytes, positive signal (IHC stain or mitotic figures) was hand counted from 10, $1mm^2$ fields per liver at 20x magnification, with averages presented. For mouse liver

$Ki67^+$ hepatocyte quantification, positively stained hepatocytes were hand counted from 3, $1mm^2$ fields per liver at 20x magnification, with averages presented. A trained pathologist independently verified Ki67+ hepatocytes, TUNEL positivity, and mitotic hepatocytes. For hepatocyte nuclei 2, 40x fields were hand counted for total hepatocyte nuclei per field, with averages presented. For TNC IHC fragment length quantification 3, $250mm^2$ fields per liver were hand counted at 20x magnification using the Ruler Tool in Aperio ImageScope software (Leica Biosystems) with averages presented.

Quantification of immune cell clusters

Entire sections of mouse liver were assessed for cell clusters, with clusters being identified as 4 or more positively stained cells in close or immediate proximity.

RNA isolation, cDNA synthesis, and quantitative RT-PCR

Quantitative RT-PCR was done as described[306]. Primers were used from Integrated DNA Technologies (Coralville, IA): Rat reference gene β-actin, forward: 5' TTG CTG ACA GGA TGC AGA AGG AGA 3', reverse: 5' ACT CCT GCT TGC TGA TCC ACA TCT 3'; collagen 1a1, forward: 5' TGG CCA AGA CAT CCC TGA AGT 3', reverse: 5' ACA TCA GGT TTC CAC GTC TCA CCA 3'; cxcl12, forward: 5' CCA TGC TCA TCT CTG TCT CAT C 3', reverse: 5' CCT TCT TAC TCC CTC CAT CTT TG 3'; emilin, forward: 5' CAG TGT CCT CGA AGT ATC ATG TAG 3', reverse: 5' CAT GTC TGT CAC CGT CTT GTA G 3'; tenascin-C, forward: 5' AAG ACT GCA AAG AGC AAA GGT 3', reverse: 5' TGT GAA GCC CTC ATG GCA GAT 3'; transglutaminase-2, forward: 5' GAC CTG TTC CCG ACT GAT ATG 3', reverse: 5' CCG GGC CGA TGA

TAT TC 3'. Mouse reference gene β-actin, forward: 5' GCA ACG AGC GGT TCC G 3', reverse: 5' CCC AAG GAA GGC TGG A 3'; ccl2 forward: 5' CCT GGA TCG GAA CCA AAT GA 3', reverse: 5' CGG GTC AAC TTC ACA TTC AAA G 3'; cxcl12 forward: 5' TTG CAT CTG GAT AGG GAA AGG 3', reverse: 5' GAG CCA GCA GTG TAT AA 3'. All data was normalized to actin using the delta-delta Ct method.

Data analysis for metabolomics and proteomics

SRM data obtained on the QTRAP was directly loaded into a Skyline file containing all expected precursor ions. Transition quality, peak shape, and peak boundaries were manually validated prior to export of integrated $^{12}C/^{13}C$ peak areas for each peptide. Data were exported and the average peptide ratio was determined by taking the average of the $^{12}C/^{13}C$ ratio of the four transitions selected for identification and quantification of each peptide. Ratios outside the Limits of Quantification (LOQ, 1 fmol for most peptides) and below the isotope incorporation percentage (98.4-99.8%) for each reporter peptide were thrown out. Limits of Detection (LOD), LOQ, linear dynamic range, and digestion efficiency were all controlled for and empirically determined prior to running biological samples. Briefly, for each peptide, I) LOD was defined as the lower limit to achieve a signal/noise of at least 3, II) LOQ was defined as the upper and lower limits that achieve a CV of less than 20%, III) linear dynamic range was determined by plotting the integrated peak areas of a gradient of the light peptide (^{12}C form) against constant heavy peptide (^{13}C form) and achieving an R value of at least 0.95, and IV) digestion efficiency was optimized to the method at which the presence of peptides with missed tryptic cleavage sites (Screened by MALDI-TOF) accounted for less than 1% of the fully

trypsinized peptide probe. Control peptides from yeast alcohol dehydrogenase were included in each QconCAT and a dilution series with a commercial ADH digest (Michrom Bioresources, Bruker, Billerica, MA) was used to determine the concentration of QconCAT polypeptides. Data was further analyzed using GENE-E software, in which the relative color scheme was -0.5 to 0.5 for rat liver metabolomics and -1 to 1 for ECM proteomics. Partial least squared discriminant analysis (PLS-DA) was performed for both rat liver metabolomics and proteomics using MetaboAnalyst software (v3.0) [307]. Outlier determination for the PLS-DA was done with a regression dendogram using Euclidean distance measurements and ward clustering. Using this method, one regressed rat liver sample in the proteomics dataset was found to be an outlier and excluded from the covariant analysis.

Results

Dynamic regulation of the rodent liver during pregnancy, lactation, and weaning

Evidence for weaning-induced involution in tissues other than the breast has not been reported. We focused on the liver, which increases in metabolic output during pregnancy and lactation[308,309]. Specifically, the liver increases lipid β-oxidation to facilitate production of glucose that is shuttled to the mammary gland for milk production[230,310]. Yet how the liver returns to its baseline metabolic state after weaning is unknown. To begin to address this question, we performed a pregnancy and weaning study in Sprague Dawley female rats (Fig.3-1A). We found rat liver weights increased ~2-fold during pregnancy and remained elevated during lactation, as has been previously shown[311] (Fig.3-1B, Supplementary Fig.3-1A). We also observed that liver weights rapidly

returned to nulliparous levels by 8-10 days post-weaning; data consistent with weaning-induced liver involution (Fig.3-1B). In contrast, lung weights did not change with parity, lactation or weaning status (Supplementary Fig.3-1B).

To assess if the rapid liver weight loss post-weaning is due to hepatocyte cell death, we first investigated whether hepatocyte proliferation contributed to liver weight gain during pregnancy. We reasoned that if liver weight gain during pregnancy involved new cell proliferation, then resolution of weight gain may be mediated by cell removal, i.e., hepatocyte cell death. During pregnancy, we found increased hepatocyte proliferation, as measured by elevated Ki67-positivity and mitotic figures (Fig.3-1C, Supplementary Fig.3-1C-D). During lactation, a modest increase in weight gain over pregnancy was associated with hepatocyte hypertrophy (Supplementary Fig.3-1E). In addition, hepatocyte hypertrophy correlated with an anabolic metabolome profile, consistent with the increased metabolic demand of lactation (Fig.3-1D, Supplementary Table 3-1A)[230,310]. Conversely, the post-weaning liver exhibited metabolic signatures of nucleic acid and protein catabolism and oxidative stress (Fig.3-1D, Supplementary Table 3-1A). Performing supervised clustering (partial least squares discriminate analysis, PLS-DA) of the rat liver metabolomics data revealed a step-wise, cyclical metabolic pattern across the reproductive cycle (Fig.3-1E, see Supplementary Methods). These data are consistent with dramatic functional changes to accommodate lactation, and further demonstrate a return to a nulliparous-like, baseline state upon regression at 28 days post-weaning (Fig.3-1E). The drop in liver weight and metabolic shift of the liver post-weaning is accompanied by increased detection of cleaved caspase-3 (CC3) (Fig.3-1F,

Supplementary Fig.3-1F), data suggestive of apoptotic cell death and tissue regression. Further evidence for weaning-induced hepatocyte cell death after weaning was observed by increased terminal deoxynucleotidyl transferase dUTP nick end labeling (TUNEL) staining, which labels cleaved DNA (Fig.3-1G, Supplementary Fig.3-1G). Combined, our data confirm and expand on previous studies demonstrating hepatocyte proliferation and anabolic metabolism occur to accommodate the energy demands of lactation[230,309]. Our data also show, for the first time, that weaning induces rapid hepatocyte cell death and liver involution, returning the liver to a baseline size and metabolic state within two weeks of weaning. We next addressed whether stromal remodeling accompanies weaning-induced liver involution, as stromal remodeling is known to impact breast cancer metastasis[82,205,213].

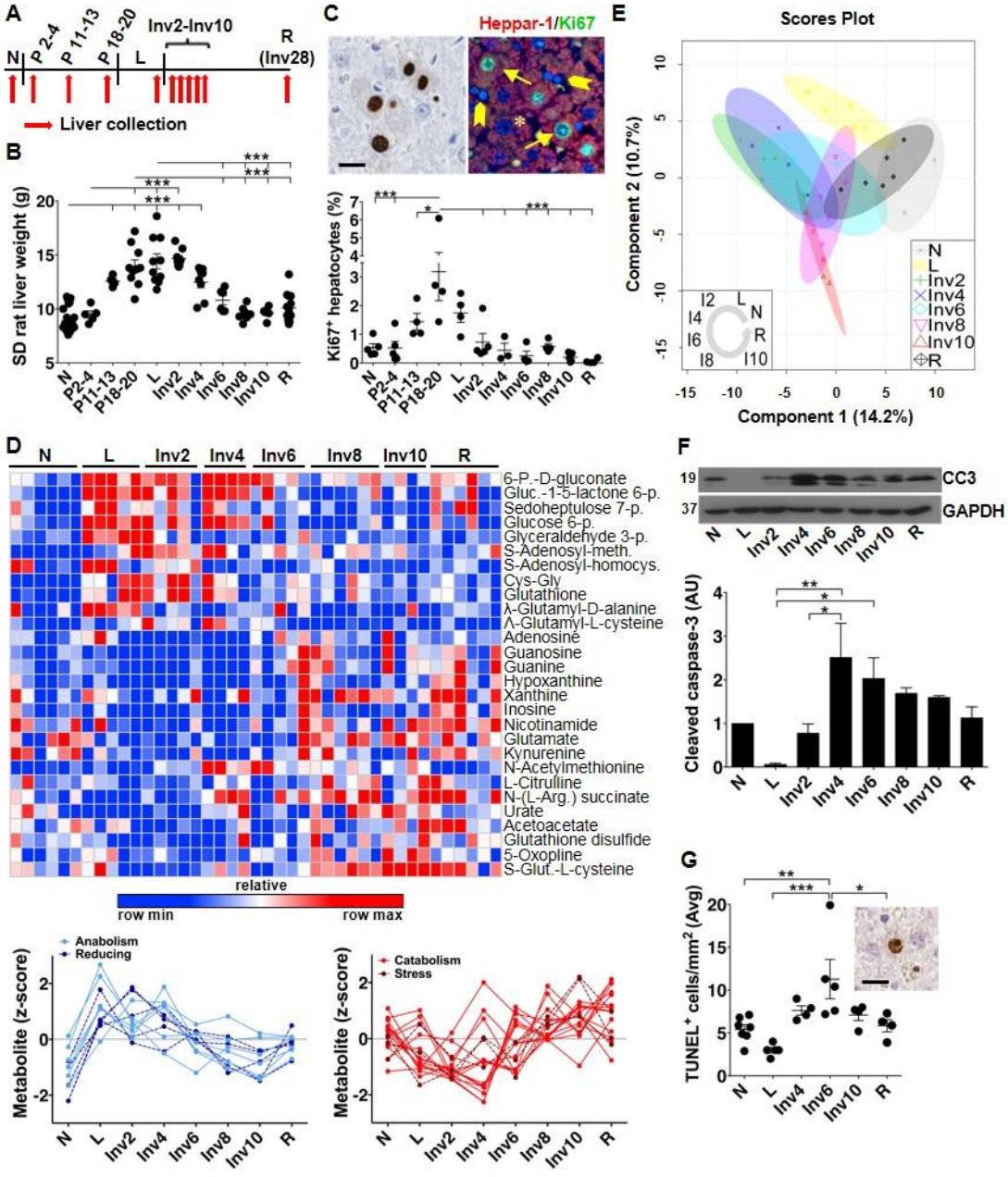
A
N
P 2-4
P 11-13
P 18-20
L
Inv2-Inv10
R
(Inv28)
Liver collection
B
SD rat liver weight (g)
C
Heppar-1/Ki67
Ki67+ hepatocytes (%)
E
Scores Plot
Component 2 (10.7%)
Component 1 (14.2%)
D
6-P.-D-gluconate
Gluc.-1-5-lactone 6-p.
Sedoheptulose 7-p.
Glucose 6-p.
Glyceraldehyde 3-p.
S-Adenosyl-meth.
S-Adenosyl-homocys.
Cys-Gly
Glutathione
λ-Glutamyl-D-alanine
Λ-Glutamyl-L-cysteine
Adenosine
Guanosine
Guanine
Hypoxanthine
Xanthine
Inosine
Nicotinamide
Glutamate
Kynurenine
N-Acetylmethionine
L-Citrulline
N-(L-Arg.) succinate
Urate
Acetoacetate
Glutathione disulfide
5-Oxopline
S-Glut.-L-cysteine
relative
row min
row max
Anabolism
Reducing
Catabolism
Stress
Metabolite (z-score)
F
CC3
GAPDH
Cleaved caspase-3 (AU)
G
TUNEL+ cells/mm2 (Avg)

Figure 3-1: Evidence for weaning induced liver involution

(A) Rat livers were harvested for biochemical and IHC analyses (red arrows) from nulliparous (N), early (P2-4), mid (P11-13), and late (P18-20) pregnancy, lactation day 10 (L), and post-weaning days 2-10 and 28 (Inv2-Inv10, R). **(B)** Liver weights from age-matched rats across the reproductive cycle; rats/grp: Nullip (N), n=25; P2-4, n=5; P11-13, n=4; P18-20 & L, n=10; Inv2, n=9; Inv4, n=8; Inv6 & Inv10, n=6; Inv8, n=7; R, n=14. **(C)** Representative Ki67 IHC (top left) and dual Ki67/Heppar-1 IHC (top right) images from P18-20 liver; $Ki67^+$ hepatocytes (arrows); $Ki67^-$ hepatocytes (asterisk); $Ki67^-$ non-parenchymal cells (arrow-heads); scale bar=20 μm. Quantification of $Ki67^+$ hepatocyte IHC by reproductive stage (bottom panel); n=4 rats/grp. **(D)** Heatmap of UHPLC-MS metabolomics by reproductive stage (top) and Z-scores of anabolic/reducing (bottom left) and catabolic/stress (bottom right) metabolites; n=4-6 rats/grp. **(E)** Partial least squares discriminate analysis (PLS-DA) of rat liver metabolomics data (see Supplementary Table 1A). **(F)** Cleaved caspase-3 immunoblot (top; n=4 rats/grp) and densitometry (bottom). **(G)** Representative apoptotic hepatocyte detected by TUNEL (inset; scale bar=20 μm), and TUNEL quantification across the reproductive cycle; N, n=7; L & Inv6, n=5; Inv4, Inv10, & R, n=4. Graphs show mean with SEM. One-way ANOVA with Tukey multiple comparisons test. *=p-value<0.05, **=p-value<0.01, ***=p-value<0.001.

Weaning-induced liver involution is accompanied by stromal remodeling

We turned to the extensively investigated post-weaning mammary gland model to guide our investigation of stromal changes that occur in the actively involuting liver[37], as extracellular matrix (ECM) remodeling is a defining characteristic of the post-weaning mammary gland[46,49,94]. Quantitative ECM proteomics on rat liver revealed widespread changes in ECM proteins post-weaning (Fig.3-2A, Supplementary Table 3-1B). Similar to our findings from the metabolomics analysis, supervised clustering (PLS-DA) of the ECM proteomic dataset demonstrated distinct liver ECM microenvironments across the reproductive cycle, including resolution to nulliparous-like levels in the fully regressed liver (R) (Fig.3-2B, Supplementary Fig.3-2). During the active window of liver involution we found elevated collagen 1-α1, collagen 4-α1, and tenascin-C (TNC) (Fig.3-2C, Supplementary Fig.3-3A-B), ECM proteins upregulated in the involuting mammary gland[46] as well as in pro-metastatic microenvironments[82,205,213,312]. Increased transcript levels for *COL1A1* and *TNC* suggested active ECM production in the involuting liver (Supplementary Fig.3-3C) and quantitative reticulin staining (Supplementary Fig.3-3D), TNC immunoblot (Fig.3-2D, Supplementary Fig.3-3E), and TNC immunostaining (Fig.3-2E, Supplementary Fig.3-3F) confirmed increased collagen and TNC protein deposition within the post-weaning liver. Of note, the timeline of TNC protein accumulation differs slightly by assay, and while these apparent discrepancies remain to be resolved, all three assays support increased liver ECM deposition shortly after weaning. Additionally, shorter TNC fragments were observed post-weaning (Fig.3-2D-F, Supplementary Fig.3-3F), and gelatin zymography demonstrated increased MMP-9 and MMP-2 levels (Supplementary Fig.3-3G), data supportive of active ECM remodeling

in the post-weaning liver, as observed in the involuting mammary gland[46,47,94]. While hepatocyte cell death and ECM deposition also occur in pathologic liver injury, the ECM deposition observed during weaning-induced liver involution occurred in the absence of overt fibrosis (Fig.3-2G, Supplementary Fig.3-3H). Taken together, these data show active, cyclical, physiologic ECM remodeling during the window of weaning-induced liver involution.

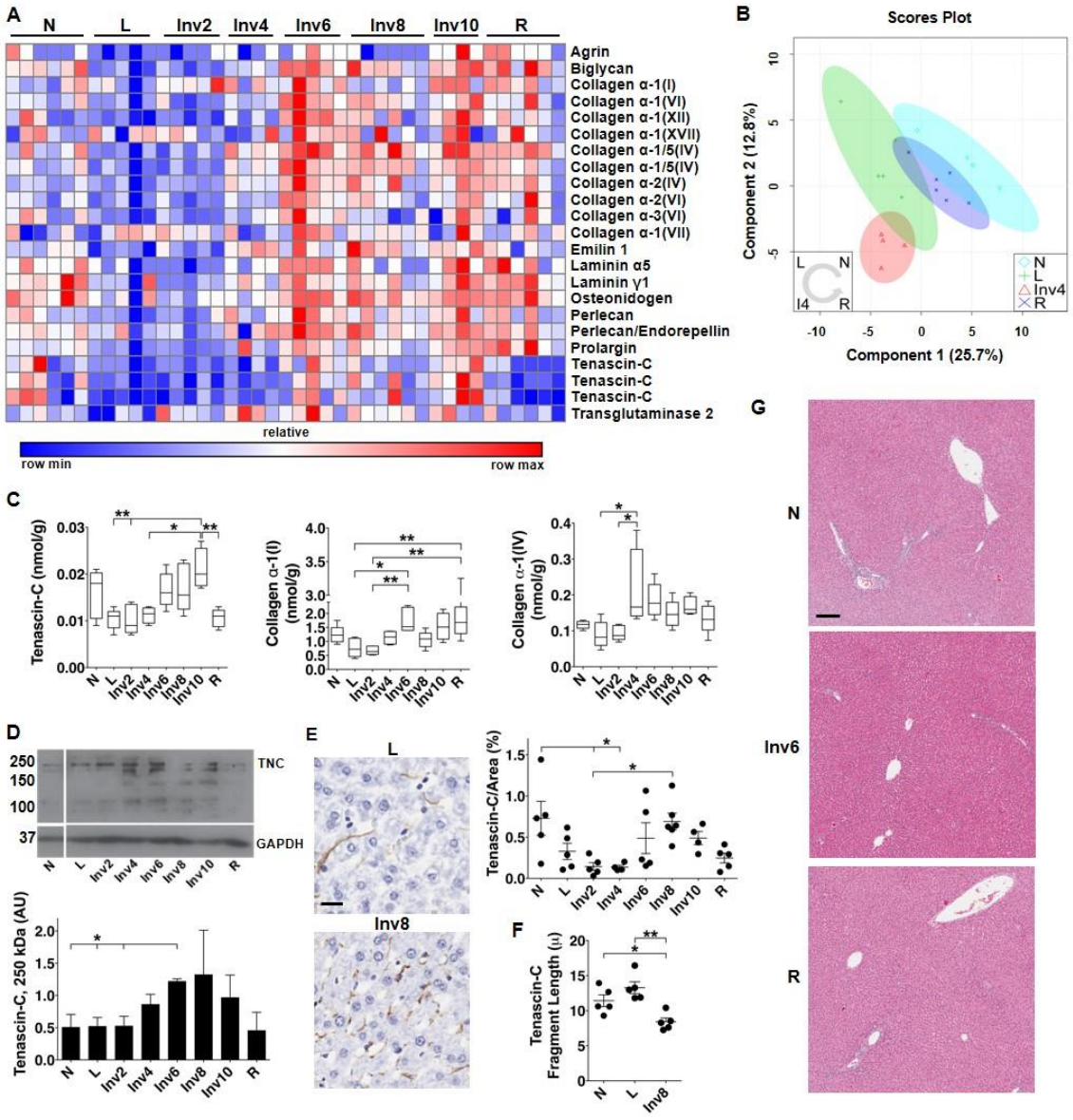
A
N
L
Inv2
Inv4
Inv6
Inv8
Inv10
R
Agrin
Biglycan
Collagen α-1(I)
Collagen α-1(VI)
Collagen α-1(XII)
Collagen α-1(XVII)
Collagen α-1/5(IV)
Collagen α-1/5(IV)
Collagen α-2(IV)
Collagen α-2(VI)
Collagen α-3(VI)
Collagen α-1(VII)
Emilin 1
Laminin α5
Laminin γ1
Osteonidogen
Perlecan
Perlecan/Endorepellin
Prolargin
Tenascin-C
Tenascin-C
Tenascin-C
Transglutaminase 2
relative
row min
row max
B
Scores Plot
Component 2 (12.8%)
Component 1 (25.7%)
N
L
Inv4
R
C
Tenascin-C (nmol/g)
Collagen α-1(I) (nmol/g)
Collagen α-1(IV) (nmol/g)
D
TNC
GAPDH
250
150
100
37
Tenascin-C, 250 kDa (AU)
E
L
Inv8
Tenascin-C/Area (%)
F
Tenascin-C Fragment Length (μ)
G
N
Inv6
R

Figure 3-2: Extracellular matrix remodeling accompanies weaning-induced liver involution

(A) Absolute quantification of rat liver ECM proteins by QconCAT based MS-MS proteomics; n=4-6 rats/grp. **(B)** Partial least squares discriminate analysis (PLS-DA) of rat liver ECM proteomics data from N, L, Inv6, and R stages (See Supplementary Fig.3-2, Supplementary Table 3-1B). **(C)** Box-and-whisker plots of TNC, collagen 1-α1, and collagen 4-α1 obtained from QconCAT proteomics in (A). **(D)** TNC expression across involution by immunoblot (top, and Supplementary Fig.3-3E), with densitometry normalized to GAPDH (bottom, and Supplementary Fig.3-3E); quantification is of 4 technical replicates, n=4-6 rats/grp. **(E)** Representative liver TNC IHC (brown stain) at L (upper left) and Inv8 (lower left) and IHC quantification across reproductive stage (upper right); scale bar=25 μm, n=4-6 rats/grp. **(F)** TNC fragment length measured in N, L, and Inv8 livers; n=5 rats/grp. **(G)** Representative H&E stained rat liver sections from N (left), Inv6 (middle), and R (right) stages; scale bar=150 μm. Graphs show mean with SEM. One-way ANOVA with Tukey multiple comparisons test. *=p-value<0.05, **=p-value<0.01.

Immune cell accumulation during weaning-induced liver involution

Immune cell infiltrate is another defining stromal change in the involuting mammary gland[42], and was suggested in the involuting rat liver by increased CD68 staining, a macrophage lysosomal marker (Fig.3-3A). To further investigate the immune milieu in the post-weaning liver we turned to the Balb/c murine model, which permits robust immune cell characterization by flow cytometry. We first confirmed murine hepatocyte proliferation and liver weight gain during pregnancy, followed by liver weight loss, metabolic catabolism/stress, and increased apoptosis upon weaning (Supplementary Fig.3-4A-D, Supplementary Table 3-2). Increased TNC, MMP-9, and MMP-2 in the post-weaning mouse liver provided further evidence that weaning-induced liver involution is conserved between rats and mice (Supplementary Fig.3-4E-H). In mice, liver immune cell phenotyping by flow cytometry revealed transient increases in $CD45^+$ leukocytes, $CD11b^{lo}F4/80^+$ macrophages, $CD11b^{hi}F4/80^-Ly6C^+Ly6G^-$ monocytes, and $CD11b^{hi}F4/80^-Ly6C^+Ly6G^+$ neutrophils with weaning (Fig.3-3B, Supplementary Fig.3-5A-B). Semi-quantitative IHC detection of $F4/80^+$, $Ly6C^+$, and $Ly6G^+$ cells confirmed a transient increase in macrophages, monocytes, and neutrophils in the post-weaning liver (Fig.3-3C-E). The observed influx of myeloid populations during weaning-induced liver involution may be, in part, due to increased production of chemokines. Thus, we looked at chemokines known to promote monocyte influx into tissues and found an increase in both CXCL12 and CCL2 expression during liver involution (Supplementary Fig.3-5C-E). Additionally, previous work has reported formation of myeloid immune foci in the pre-metastatic niche[197], an observation we also report here (Supplementary Fig.3-5F-G). Our finding of increased myeloid populations within the liver post-weaning is also consistent

with clearance of apoptotic cells and immune suppression. Specifically, professional phagocytic clearance of apoptotic cells limits exposure to self-antigen[313] and gives rise to immune-suppressive, wound-resolving macrophages[314] that support tumor cell immune evasion[315].

In sum, we provide evidence that the liver undergoes weaning-induced involution that is characterized by ECM deposition, MMP activity, and infiltration/clustering of $CD11b^{hi}F4/80^{-}Ly6C^{+}Ly6G^{-}$ monocytes reported to occur within the metastatic niche as a result of primary tumor education[82,196,197,205,253]. Our data indicate regulation of these same pro-metastatic pathways in the *absence* of tumor, under the physiologic conditions of weaning-induced liver involution. Based on these findings, we hypothesized that the post-weaning liver would preferentially support breast cancer metastasis in comparison to the nulliparous host.

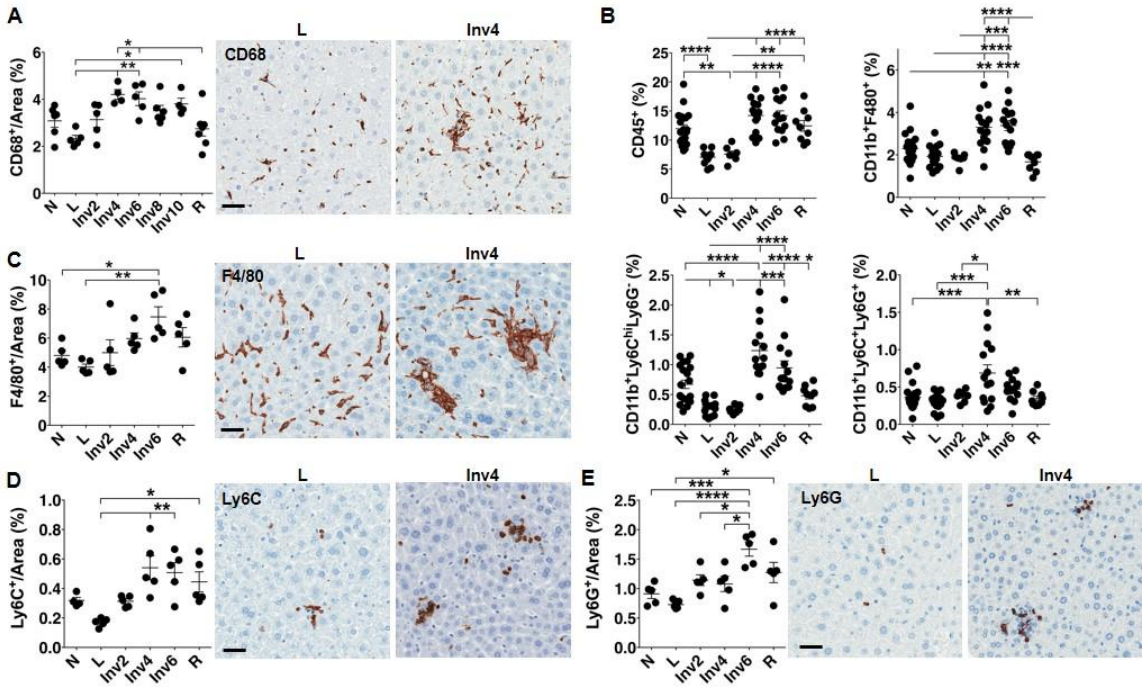

Figure 3-3: Immune populations increase in the liver during weaning-induced involution

(A) IHC quantification of CD68 positivity (left), and representative CD68 IHC images (right); scale bar=40 μm, n=4-6 rats/grp. **(B)** Flow cytometric quantification of Balb/c mouse liver immune cell populations; $CD45^+$ leukocytes (top left), $CD11b^{lo}F4/80^+Ly6C^-Ly6G^-$ mature macrophages (top right), $CD11b^{hi}F4/80^-Ly6C^+Ly6G^-$ monocytes (bottom left), and $CD11b^{hi}F4/80^-Ly6C^+Ly6G^+$ neutrophils (bottom right); Nullip (N), n=19; L, Inv4, & Inv6, n=14; R, n=9; Inv2, n=7 mice/grp. **(C)** F4/80 IHC quantification (left), and representative F4/80 IHC images (right); n=5 mice/grp. **(D)** Ly6C IHC quantification (left), and representative Ly6C IHC images (right); n=5 mice/grp. **(E)** Ly6G IHC quantification (left), and representative Ly6G IHC images (right); scale bars for c-e=40 μm, n=5 mice/grp. Graphs show mean with SEM. One-way ANOVA with Tukey multiple comparisons test. *=p-value<0.05, **=p-value<0.01, ***=p-value<0.001, ****=p-value<0.0001.

Weaning-induced liver involution establishes a pro-metastatic microenvironment

To determine if the involuting-liver supports metastasis to a greater extent than the nulliparous host, we injected 5,000 mammary 4T1 tumor cells into the left ventricle of isogenic Balb/c hosts that were nulliparous or immediate post-weaning, referred to as the involution group (Inv2) (Fig.3-4A). Intracardiac injection was necessary to ensure equal circulating tumor cell numbers in both groups, as we have previously shown increased tumor cell-dissemination from the mammary fat pad during weaning-induced mammary gland involution[47,49]. At study end, the percentage of mice with tumor cells in the liver, as assessed by a clonogenic assay for 4T1 cells[284], was higher in the involution group and cells were detected earlier in comparison to nulliparous hosts (Fig.3-4B-C). The percentage of mice with tumor cells in the lung, bone, and brain was unchanged between groups, suggesting a unique metastatic advantage within the post-weaning liver (Fig.3-4D). By immunohistochemical assessment, liver metastases were confirmed as $CD45^-$, Heppar-1^-, and $CK18^+$, and found to be highly Ki67 positive (Fig.3-4E). Micro-metastases were the dominant lesion type, likely due to the fact that systemic tumor burden and 4T1-tumor cell driven cachexia required sacrifice of mice prior to the formation of overt liver metastasis.

To assess the ability of the post-weaning liver to support macro-metastases, we developed a portal vein injection metastasis model that allows for tumor cell delivery directly to the liver. This model permits outgrowth of liver lesions without concomitant metastasis in other organs[238]. Further, to avoid cachexia, we utilized the less aggressive, isogenic, murine D2A1 mammary tumor cell line. We delivered 5,000 D2A1 cells into

the portal vein of nulliparous and immediate post-weaning Balb/c female mice (Fig.3-4F). This cell number was selected to reduce penetrance of overt liver lesions in nulliparous mice to ~20% (data not shown), permitting detection of a potential increase in metastatic frequency in the involution group. To investigate whether the pro-metastatic microenvironment of the post-weaning liver is transient or persistent, we also injected mice at 28 days post weaning, a time point where the liver is fully regressed (R) by morphologic, molecular and biochemical characterizations (Fig.3-1E, 3-2B, & Supplementary Fig.3-2, and Supplementary Table 3-3). In the immediate post-weaning group (Inv2), we observed a 3-fold increased frequency of histologically identified overt liver metastases compared to both nulliparous and fully regressed groups (Fig.3-4G). By IHC, D2A1 liver lesions were identified as Heppar-1^{-}, CK18^{+}, and CD45^{-}, and found to be highly positive for Ki67 (Fig.3-4H, Supplementary Fig.3-6).

To assess for differences in metastatic burden across groups, we quantified tumor number and size from H&E liver sections. From this analysis we found that the immediate post-weaning (Inv2) group had an increased number of tumors per liver and increased tumor burden measured as total tumor area per liver, compared to the nulliparous group (Supplementary Fig.3-7A-B). However, when we assessed only those mice with detectable metastases, differences in tumor number and area were not observed between groups (Supplementary Fig.3-7C-E). Cumulatively, these data indicate that the window of increased risk for developing liver metastasis is transient, limited to the period of active liver involution following weaning. Further, data from this metastasis model suggest that liver involution supports the early event of tumor cell seeding, but not tumor

growth. Finally, these data predict increased liver metastasis in women diagnosed with postpartum breast cancer.

Evidence for elevated risk for liver metastasis in postpartum breast cancer patients

To investigate liver metastasis in young women with breast cancer, we evaluated a unique cohort of 564 patients diagnosed at ≤45 years of age where specific clinical data not normally collated, including parity history, long-term follow-up, and sites of metastasis, were made available through detailed chart review (Supplementary Table 3-4). Compared to nulliparous women, we found a ~3.6-fold increase in liver metastasis in postpartum patients diagnosed within 5 years of giving birth, a trend that continued for up to 10 years following parturition (Fig.3-4I). This increased risk for liver metastasis persisted after adjusting for tumor biologic subtype, patient age, and year of diagnosis, which accounts for treatment advances over time (Supplementary Table 3-4, 3-6). To examine potential breast cancer preference for the postpartum liver, we next investigated site-specific metastasis in the subset of women with metastatic disease. To more accurately evaluate metastatic tropism to the postpartum liver, we restricted our analysis to cases where first site of metastasis was recorded. This approach would avoid potential confounding influences that concomitant multi-site metastasis might have on the liver metastatic niche. To increase sample size of this highly defined young women's breast cancer cohort, we extended our analysis to multiple institutions where de novo and recurrent metastatic disease data were available, and expanded the cohort to include patients diagnosed within 10 years of pregnancy (Supplementary Table 3-5). In this metastatic patient cohort, we observed increased liver metastasis in postpartum compared

to nulliparous breast cancer patients (Fig.3-4J). This increase appears to be liver specific, as we did not observe significant differences in frequencies of lung or brain metastasis between groups (Fig.3-4J, Supplementary Table 3-5, 3-6). Intriguingly, we observed a trend towards reduced frequency of bone metastasis in the postpartum group (Fig.3-4J, Supplementary Table 3-5, 3-6). Cumulatively, these data support the hypothesis that the microenvironment of the postpartum involuting liver is uniquely permissive for the formation of breast cancer metastasis (Fig.3-4K).

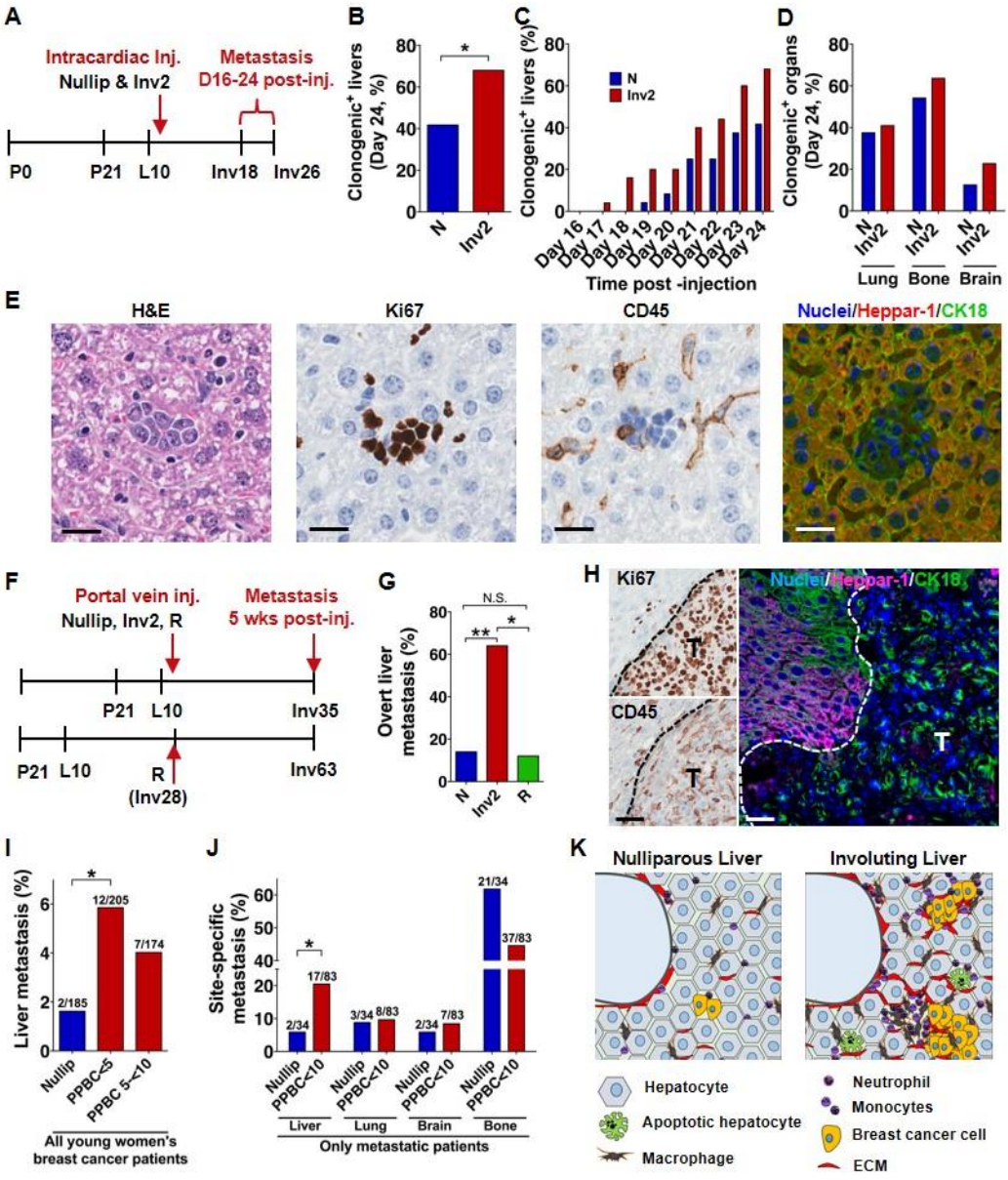
A
Intracardiac Inj.
Nullip & Inv2
Metastasis
D16-24 post-inj.
P0
P21
L10
Inv18
Inv26
B
Clonogenic+ livers (Day 24, %)
N
Inv2
C
Clonogenic+ livers (%)
N
Inv2
Day 16
Day 17
Day 18
Day 19
Day 20
Day 21
Day 22
Day 23
Day 24
Time post -injection
D
Clonogenic+ organs (Day 24, %)
Lung
Bone
Brain
E
H&E
Ki67
CD45
Nuclei/Heppar-1/CK18
F
Portal vein inj.
Nullip, Inv2, R
Metastasis
5 wks post-inj.
P21
L10
Inv35
P21
L10
R
(Inv28)
Inv63
G
Overt liver metastasis (%)
N.S.
N
Inv2
R
H
Ki67
CD45
T
Nuclei/Heppar-1/CK18
I
Liver metastasis (%)
2/185
12/205
7/174
Nullip
PPBC<5
PPBC 5-<10
All young women's breast cancer patients
J
Site-specific metastasis (%)
2/34
17/83
3/34
8/83
2/34
7/83
21/34
37/83
Nullip
PPBC<10
Liver
Lung
Brain
Bone
Only metastatic patients
K
Nulliparous Liver
Involuting Liver
Hepatocyte
Apoptotic hepatocyte
Macrophage
Neutrophil
Monocytes
Breast cancer cell
ECM

Figure 3-4: Evidence for a pro-metastatic microenvironment in the postpartum liver

(A) Intracardiac metastasis model, Nullip (N), n=24; Inv2, n=25. **(B)** Percent mice with tumor cells in liver (p=0.03; Chi-squared, RR 1.6 [95% CI:0.9-9.6]); **(C)** Tumor Cell Latency. **(D)** Percent mice with tumor cells in lung (p=0.81), bone marrow (p=0.51), and brain (p=0.36), Chi-squared. **(E)** Representative H&E image of liver micro-metastasis and staining for Ki67, CD45, and Heppar-1/CK18; scale bars=25 μm. **(F)** Portal vein metastasis model, Nullip, n=18; Inv2, n=17; R, n=8. **(G)** Percent of mice with overt metastasis at study end (**p=0.001, RR 3.9 [95% CI: 1.3-11.6]; *p=0.03, RR 2.0 [1.08-3.66]; two-tailed Fisher's exact). **(H)** Representative Ki67, CD45, and Heppar-1/CK18 staining on overt liver metastases (T) from Inv2 mice, dashed lines denote tumor border; scale bars=25 μm. **(I)** Frequency of liver metastasis in young breast cancer patients (≤45 years of age); N, n=185; PPBC<5, n=205; PPBC 5-<10, n=174 (p=0.038; multivariate logistic regression, OR=4.05 [95% CI:1.08-15.12]). **(J)** Subset analysis of site-specific metastases in women with metastatic disease (N, n=34; PPBC<10, n=83). Frequency of liver metastasis (p=0.04, one-sided Fisher's Exact; p=0.058, two-sided Fisher's Exact, OR: 4.12 [95% CI:0.90-18.94]), and lung (p=1.00), brain (p=1.00), & bone (p=0.11) metastasis by Fisher's exact (see Supplementary Table 6). **(K)** Model of the postpartum involuting liver pro-metastatic microenvironment.

Discussion

We provide the first description of a developmentally regulated, liver involution program induced by weaning; a program that returns the liver from a state of high metabolic output necessary for lactation to a baseline pre-pregnant-like state. Weaning-induced liver involution involves liver weight loss, hepatocyte apoptosis, catabolic and cell stress metabolite profiles, ECM deposition, and increases in myeloid populations associated with apoptotic cell clearance and immune suppression. Using intracardiac and intraportal tumor cell injection models of breast cancer metastasis, we found the actively involuting murine liver supports increased metastasis compared to the livers of nulliparous or postpartum hosts whose livers have completed the involution process, i.e. regressed hosts. Potential relevance to breast cancer patients is suggested by our observation that patients diagnosed postpartum experience an elevated risk for liver-specific metastasis when compared to nulliparous young women's breast cancer patients. Unresolved by our studies is a reconciliation between the narrow window of increased risk for liver metastasis observed in the murine model and the extended window of risk observed in women (5-10 years postpartum). One possible mechanism for this potential timing discrepancy is through dissemination of breast cancer cells shortly after pregnancy/lactation, as previously proposed[47], followed by a dormancy phase prior to metastatic expansion.

While physiologically regulated, the tissue-remodeling attributes of weaning-induced liver involution, including TNC, collagen I, collagen IV, and MMPs, are identified as key components of primary tumor-educated metastatic niches[82,196,197,205,213,253]. For example,

breast cancer cells depend upon TNC for successful establishment of lung metastasis in mice[82], and collagen I at secondary sites can promote tumor cell escape from dormancy through integrin-mediated cytoskeletal rearrangement and proliferation[213]. In addition, crosslinked collagen IV supports immune cell infiltration, production of MMP-2 by monocytes, and metastatic niche formation in the murine lung, brain, and liver, ultimately facilitating tumor cell recruitment and metastatic outgrowth[205]. We also observed increased $CD11b^+$ myeloid cell infiltrate in the involuting liver, and previous work has shown that $CD11b^+$ bone marrow derived monocytes (BMDM) are essential for the establishment of successful metastasis upon tumor cell arrival in the liver[253]. Similarly, seminal work has revealed that $VEGFR1^+$ BMDM, a subset of which are $CD11b^+$, are 'first-responders' in the pre-metastatic niche, where they are implicated in establishing a pro-metastatic environment hospitable to circulating tumor cells[197]. The identification of several components of the tumor-educated metastatic niche within the normal involuting liver provides mechanistic support for our functional data demonstrating increased liver metastasis in post-weaning compared to nulliparous murine hosts.

A limitation of our study is that we have yet to demonstrate causality between weaning-induced liver involution and increased metastasis. Such assessments will require abrogation of these involution-related pro-metastatic attributes by use of targeted interventions as well as genetic approaches. An additional constraint of our study is the use of metastasis models that do not recapitulate the entire metastatic cascade, but rather focus on the fate of circulating tumor cells. However, our reductionist approach is essential to isolate postpartum liver biology from that of the mammary gland, as previous

studies in our lab revealed a metastatic advantage of orthotopic tumors in postpartum hosts, including increased tumor growth, local invasion, and escape into the circulation[42,47].

The highly novel aspect of our discovery of weaning-induced liver involution and establishment of a transient pro-metastatic niche in rodents is also a potential limitation, as relevance to women is unknown. Our observations are unprecedented and to date, no published studies have examined whether weaning-induced liver involution occurs in women. Such investigation will require non-invasive, serial liver imaging studies in pregnant, lactating and post-weaning women. Studies using non-human primates, where liver biopsy is a viable option, could provide information regarding the molecular mechanisms of postpartum liver involution in primates. Of potential significance, postpartum breast involution in women occurs to a similar degree and by many of the same physiological processes as found in rodents, revealing conservation of weaning-induced breast involution[77].

Importantly, in a retrospective study of young women's breast cancer patients, we find postpartum patients are at increased risk for liver metastasis; data consistent with an unrevealed postpartum liver biology in women. Of note, we observe increased liver metastasis without observing differences in frequency of other common sites of breast cancer metastasis, including bone, lung, and brain; data suggestive of a liver specific metastatic advantage. Independent validation of increased site-specific liver metastasis in postpartum breast cancer patients is needed. Such studies will depend upon the expansion

of young women's breast cancer cohorts worldwide, as it is necessary to include time since last pregnancy histories, as well as sites of metastases; these clinical parameters are not routinely collected at present. Of note, we find the increased risk of liver metastasis persists beyond the predicted window of weaning-induced tissue involution, for up to 10 years postpartum. To test the speculation that postpartum breast involution facilitates early dissemination to the liver, prior to a diagnosis of breast cancer, new breast cancer models are needed.

In conclusion, we find an increase in site-specific metastasis to the liver in postpartum patients, and identify weaning-induced liver involution in rodents as a putative mechanism that may account for this increased risk. Importantly, breast cancer patients with liver metastasis have a median survival of ~4 months, compared to ~5 years with bone-only metastasis[244,248], raising the possibility that differences in site-specific metastasis contribute to the poor survival rates of women diagnosed postpartum. If validated, our finding that postpartum patients experience an increased risk for liver metastasis could lead to changes in treatment decisions in this vulnerable population of young mothers diagnosed with breast cancer. Finally, our study implicates unique host biology, rather than intrinsic attributes of the tumor, in mediating the poor prognosis of postpartum breast cancer and offers unexplored avenues for metastasis research and therapeutic intervention.

Supplementary Figures

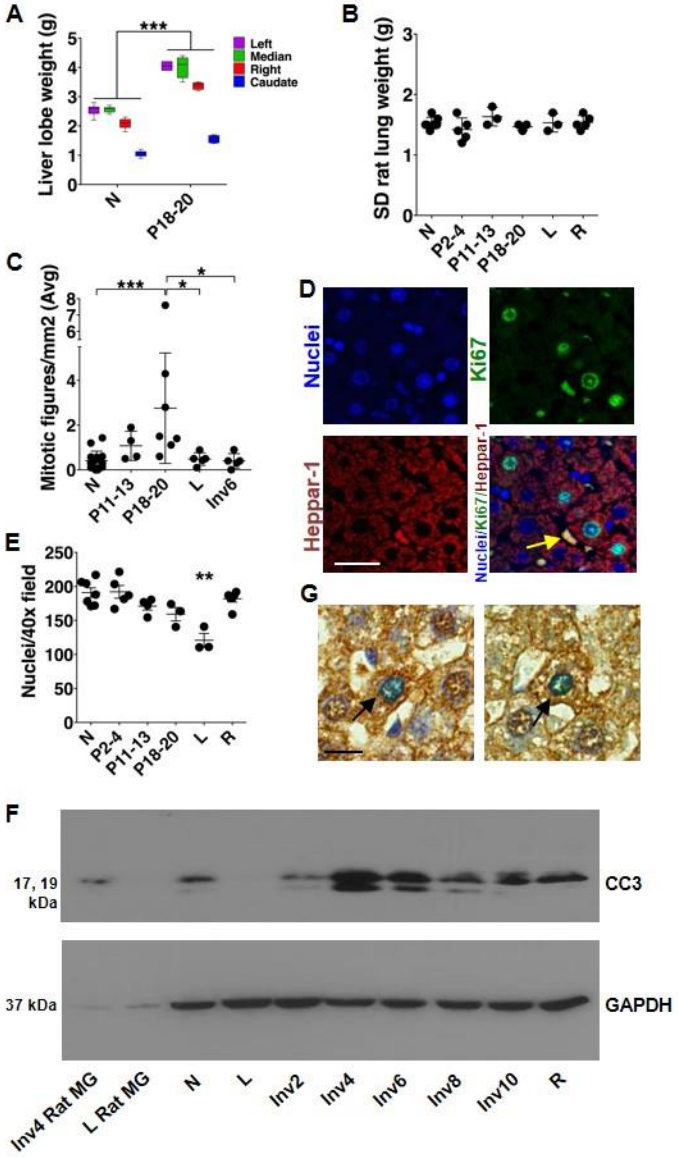

Supplementary Figure 3-1: Liver expansion and regression during pregnancy and weaning suggest weaning-induced liver involution

(A) All rat liver lobes (left, median, right and caudate) increase in weight during pregnancy; n=4-6 rats/grp, two-way ANOVA. **(B)** Lung weights do not change across the reproductive cycle; n=3-5 rats/grp. **(C)** Quantification of mitotic figures in H&E stained rat liver sections confirms increased hepatocyte proliferation during pregnancy; Nullip (N), n=15; P11-13, n=4; P18-20, n=7; L & Inv6, n=6 rats/grp. **(D)** Heppar-1 and Ki67 dual immunofluorescence single channel and merge images; arrow depicts auto-fluorescent blood; scale bar=20 μm. For clarity, brightness was enhanced uniformly across all images in Photoshop (Adobe Systems Incorporated, San Jose, CA). **(E)** Quantification of total hepatocyte nuclei per 40x field shows increased cell size at lactation day 10, 2 fields/liver were quantified; n=4-6 rats/grp. **(F)** Cleaved caspase-3 immunoblot from Fig.3-1E, with positive and negative controls (involution day 4, and lactation day 10 rat mammary gland lysate). **(G)** $CK18^{+}$ (brown) $TUNEL^{+}$ (green) dual-positive apoptotic hepatocytes from an Inv4 rat liver; scale bar=20 μm. Graphs show mean and SEM. One-way ANOVA with Tukey multiple comparisons test unless otherwise stated. *=p-value <0.05, **=p-value <0.01, ***=p-value <0.001.

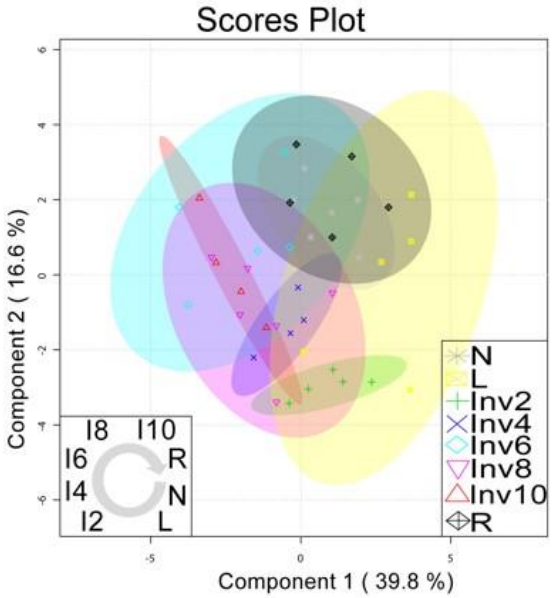

Supplementary Figure 3-2: Cycle of ECM remodeling in the rodent liver across reproductive stages

Partial least squares discriminate analysis (PLS-DA) of selection reaction monitoring (SRM) data generated from a subset of proteins of interest from rat liver ECM proteomics highlighted in Fig.3-2A. Rat liver ECM composition shifts from nulliparous to lactation to involution stages, subsequently returning to a nulliparous-like state upon regression. Inv4 & Inv10, n=4; L, Inv2, Inv6, & R, n=5; N, & Inv8, n=6 rats/grp. N=1 rat liver sample from regressed group (R) removed using outlier determination (see Supplementary Materials).

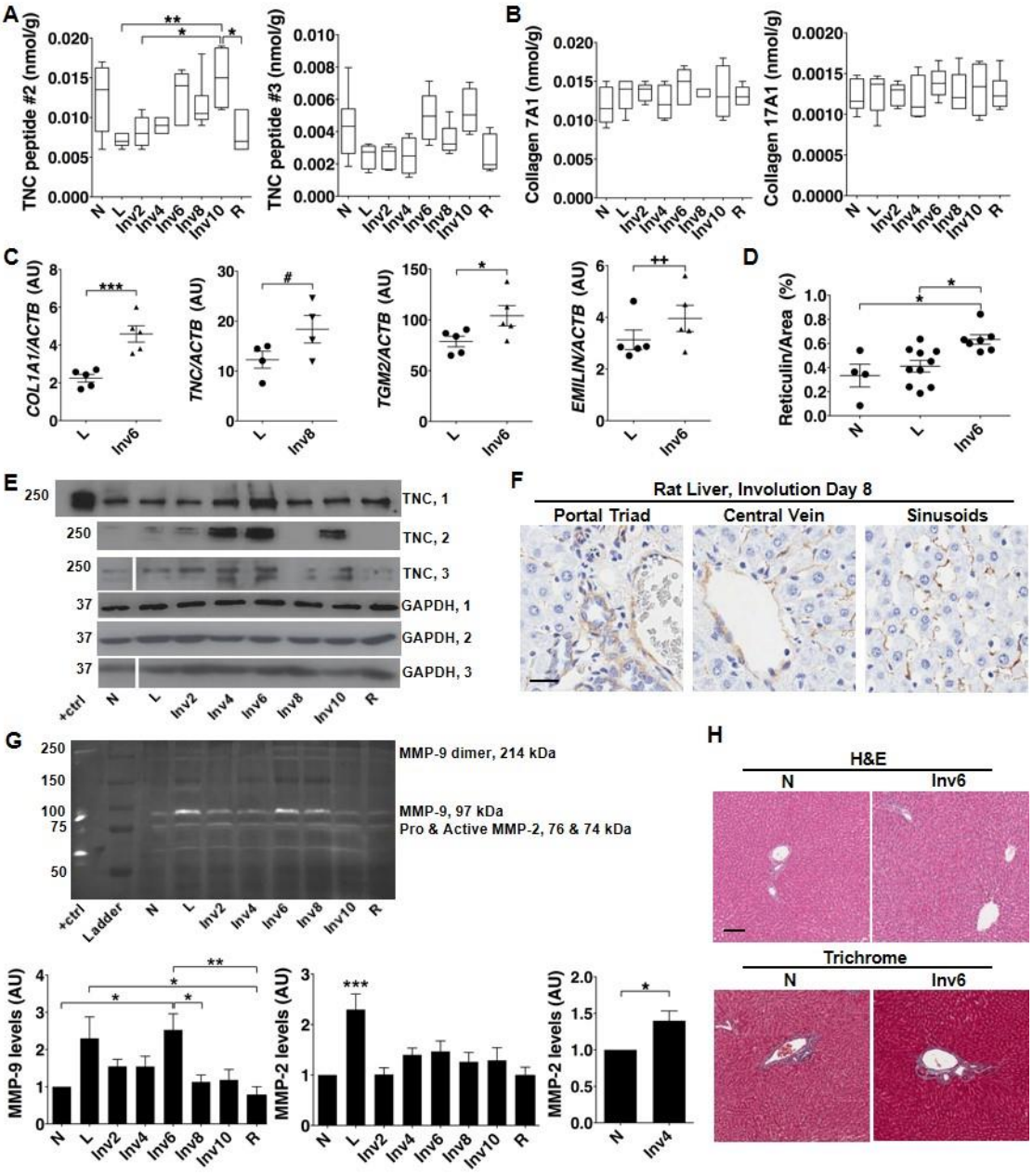
A
TNC peptide #2 (nmol/g)
TNC peptide #3 (nmol/g)
B
Collagen 7A1 (nmol/g)
Collagen 17A1 (nmol/g)
N L Inv2 Inv4 Inv6 Inv8 Inv10 R
C
COL1A1/ACTB (AU)
TNC/ACTB (AU)
TGM2/ACTB (AU)
EMILIN/ACTB (AU)
L Inv6
L Inv8
D
Reticulin/Area (%)
N L Inv6
E
TNC, 1
TNC, 2
TNC, 3
GAPDH, 1
GAPDH, 2
GAPDH, 3
+ctrl N L Inv2 Inv4 Inv6 Inv8 Inv10 R
F
Rat Liver, Involution Day 8
Portal Triad
Central Vein
Sinusoids
G
MMP-9 dimer, 214 kDa
MMP-9, 97 kDa
Pro & Active MMP-2, 76 & 74 kDa
+ctrl Ladder N L Inv2 Inv4 Inv6 Inv8 Inv10 R
MMP-9 levels (AU)
MMP-2 levels (AU)
N L Inv2 Inv4 Inv6 Inv8 Inv10 R
N Inv4
H
H&E
N Inv6
Trichrome
N Inv6

Supplementary Figure 3-3: ECM remodeling during weaning-induced liver involution occurs in the absence of overt fibrosis

(A) Absolute quantification of two tenascin-C peptides from QconCAT ECM proteomics. **(B)** Absolute quantification of collagen 7A1 (left) and collagen 17A1 (right), not altered with involution, suggesting selective *de novo* ECM deposition. **(C)** qRT-PCR for *COL1A1, TNC, TGM2,* and *Emilin*; n=4-5 rats/grp; #=p-value 0.054, ++=p-value 0.11, student's t-test. **(D)** Reticulin stain quantification; n=4-10 rats/grp. **(E)** Tenascin-C immunoblots on pooled rat liver lysates (n=4-6 rats/grp) used for densitometry in Fig. 3-2C; positive control is purified human tenascin-C. GAPDH is in the same order as corresponding TNC panels. **(F)** Representative images of TNC IHC from rat livers at Inv8 showing signal adjacent to vasculature and sinusoids; scale bar=50 μm. **(G)** Representative gelatin zymogram of rat liver lysates (top, n=4-6 rats/grp) and densitometry for MMP-9 (bottom left), and MMP-2 (bottom right plots, full zymogen: one-way ANOVA, N vs. Inv4: student's t-test; n=4 gels, positive control is 5% FBS). Converted to grey-scale using Adobe Photoshop. **(H)** Representative images of H&E (top) and Masson's trichrome (bottom) stained rat livers from N and Inv6 stages; scale bar=200 μm. Graphs show mean and SEM. One-way ANOVA with Tukey multiple comparisons test unless otherwise stated. *=p-value <0.05, **=p-value <0.01, ***=p-value <0.001.

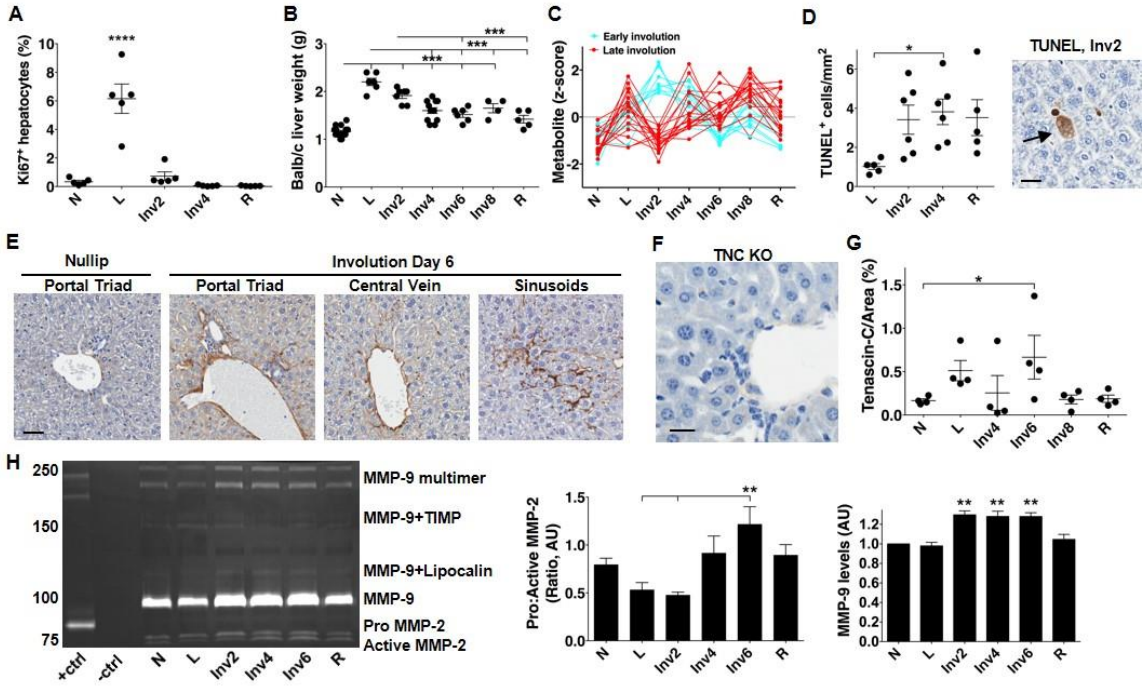

Supplementary Figure 3-4: Weaning-induced liver involution in the mouse

(A) Quantification of Ki67+ hepatocytes in 3, 1mm^2 fields per liver; n=5 mice/grp. **(B)** Liver weight gain during pregnancy and loss post-weaning in the Balb/c mouse; Inv8, n= 4; R, n=5; L & Inv6 n=6; Inv2, n=7; Inv4, n=12; Nullip (N), n=19 mice/grp. **(C)** UHPLC-MS Z-scores of catabolism and oxidative stress metabolites; n=4-6 mice/grp. **(D)** Quantification of TUNEL positive cells (left; n=5-6 mice/grp). Representative apoptotic hepatocyte by TUNEL assay at Inv2 (arrow, right); scale bar=25 μm. **(E)** Representative TNC IHC in a nulliparous (left) and Inv6 mouse liver showing TNC (brown stain) localized to vessels and sinusoids (right; scale bar=50 μm). **(F)** TNC IHC on a TNC knockout mouse liver (C57Bl/6N-TgH, sections were a gift from Dr. Ana Coito, UCLA; scale bar=20 μm). **(G)** Quantification of TNC IHC (right; n=4 mice/grp). **(H)** Representative gelatin zymogram of Balb/c mouse liver lysates (left, n=4 mice/grp; positive control is 5% FBS, negative control is serum-free media) and densitometry (right; n=4 gels). Graphs show mean and SEM. One-way ANOVA with Tukey multiple comparisons test. *=p-value <0.05, **=p-value <0.01, ***=p-value <0.001, ****=p-value <0.0001.

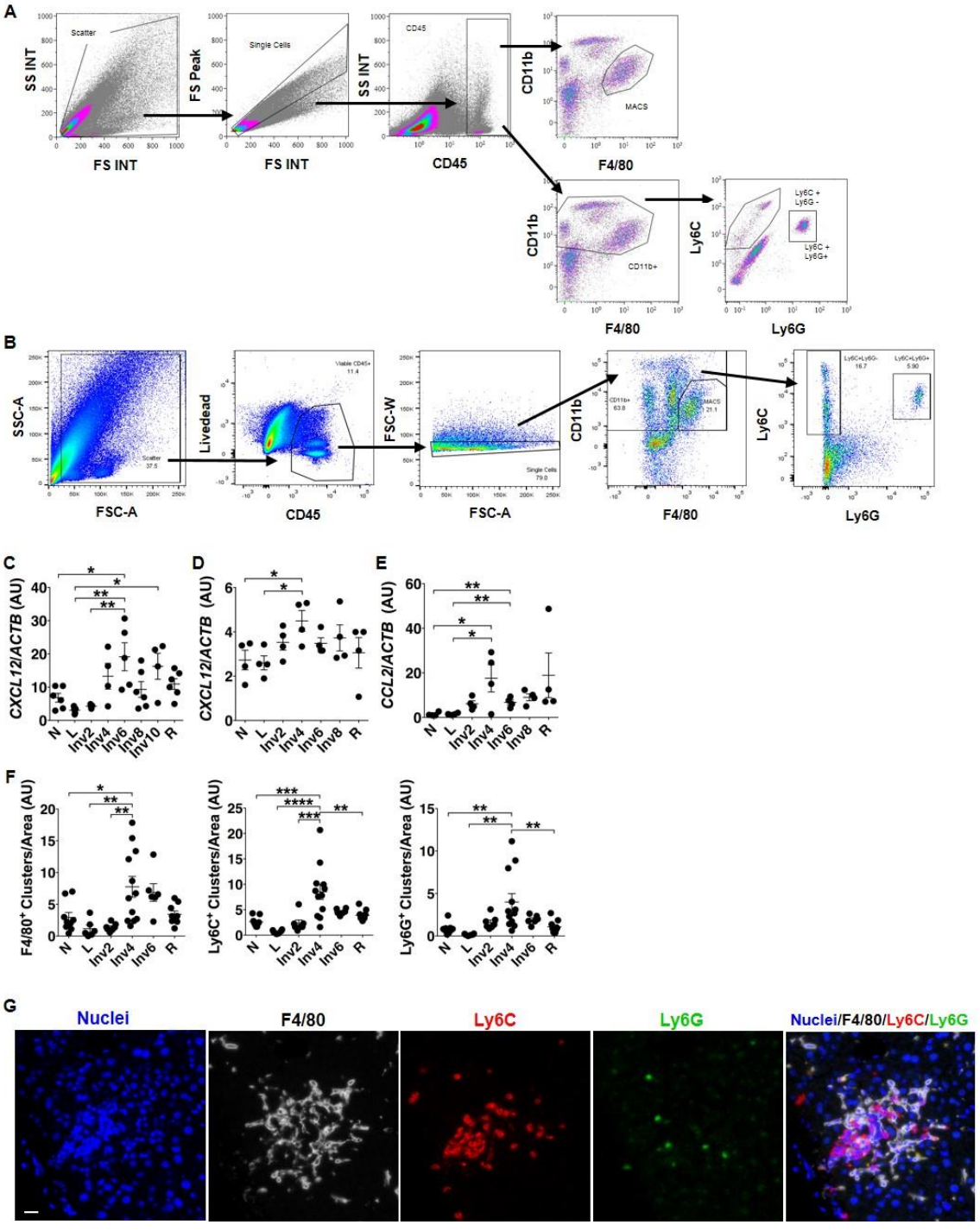
A
SS INT
FS INT
Scatter
FS Peak
Single Cells
CD45
CD11b
F4/80
MACS
Ly6C
Ly6G
CD11b+
Ly6C + Ly6G -
Ly6C + Ly6G+
B
SSC-A
FSC-A
Livedead
FSC-W
Ly6C+Ly6G-
Ly6C+Ly6G+
C
CXCL12/ACTB (AU)
N
L
Inv2
Inv4
Inv6
Inv8
Inv10
R
D
CXCL12/ACTB (AU)
E
CCL2/ACTB (AU)
F
F4/80+ Clusters/Area (AU)
Ly6C+ Clusters/Area (AU)
Ly6G+ Clusters/Area (AU)
G
Nuclei
F4/80
Ly6C
Ly6G
Nuclei/F4/80/Ly6C/Ly6G

Supplementary Figure 3-5: Myeloid cell populations increase in abundance and form foci during weaning-induced liver involution in rodents

(A) Gating scheme for flow cytometry analysis of whole mouse liver myeloid populations using Kaluza software (Beckman Coulter, Indianapolis, IN). $CD11b^{lo}F4/80^{+}$ macrophages were identified by gating on single cells positive for CD45. $CD11b^{+}F4/80^{-}Ly6C^{+}Ly6G^{-}$ monocytes and $CD11b^{+}F4/80^{-}Ly6C^{+}Ly6G^{+}$ neutrophils were further identified by gating on $CD11b^{+}$ cells. **(B)** Gating scheme for repeat flow cytometry analysis of whole mouse liver myeloid populations in which portal vein perfusion with PBS and a live/dead discriminator were used. In the repeat analysis, performed using FlowJo software (FlowJo, LLC Data Analysis Software, Ashland, OR), all populations were gated on viable $CD45^{+}$ cells. Macrophages were identified as $CD11b^{lo}$ and $F4/80^{+}$. Gating on the $CD11b^{+}$ population was performed to identify $CD11b^{+}F4/80^{-}Ly6C^{+}Ly6G^{-}$ monocytes and $CD11b^{+}F4/80^{-}Ly6C^{+}Ly6G^{+}$ neutrophils. **(C)** Quantitative RT-PCR for *CXCL12* in rat liver across the reproductive cycle, normalized to *Actin*; Inv4 & Inv10, n=4; L, Inv2, & Inv6, n=5; N, Inv8, & R, n=6. **(D)** Quantitative RT-PCR for *CXCL12* in mouse liver across the reproductive cycle, normalized to *Actin*; n=4 mice/grp. **(E)** Quantitative RT-PCR for *CCL2* in mouse liver across the reproductive cycle, normalized to *Actin*; n=4 mice/grp, two-tailed Student's t-test. **(F)** Quantification of cell clusters in IHC stained Balb/c liver sections (clusters from F4/80 staining on left, from Ly6C staining in middle, and from Ly6G staining on right), normalized to area analyzed; L & Inv6, n= 6; Inv2, n=7; N & R (4-6 wks post-weaning), n=9; Inv4, n=12 mice/grp. **(G)** Representative Opal® immunostaining for immune cell foci in an involution day 4 Balb/c liver, from left to right: Dapi, F4/80, Ly6C, Ly6G, and merged image; neutrophils show as yellow; scale bar=25 μm. Error bars are SEM. One-way ANOVA with Tukey multiple comparisons test unless stated otherwise. *=p-value <0.05, **=p-value <0.01, ***=p-value <0.001, ****=p-value <0.0001.

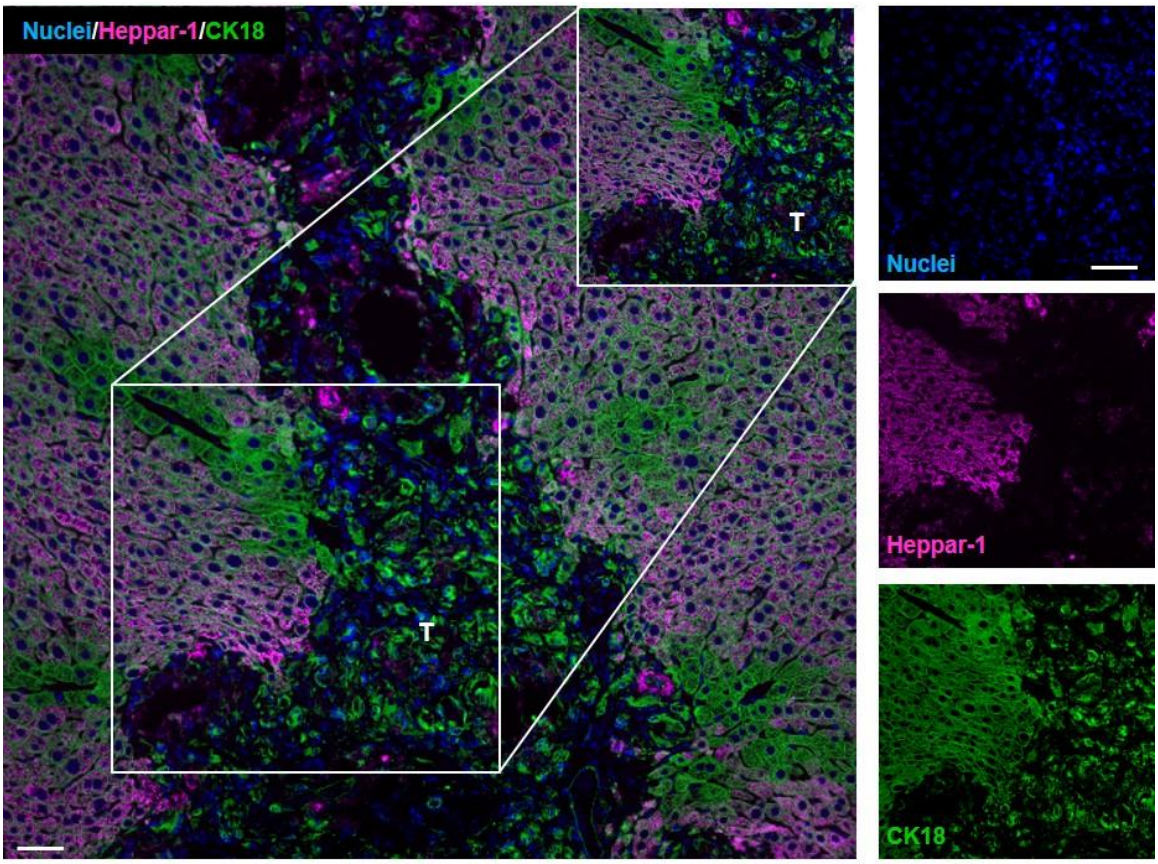

Supplementary Figure 3-6: Detection of liver metastases using multi-color immunofluorescence

Multiplex immunofluorescence for Heppar-1 and CK18 shows a $CK18^+$ D2A1 liver metastasis (T) surrounded by Heppar-1^+CK18^+ hepatocytes (left panel) with the area magnified in Fig.3-4H (inset); and single color images of the inset from Fig.3-4H, from top to bottom shows DAPI, Heppar-1, and CK18 (right panels); scale bar=50 µm.

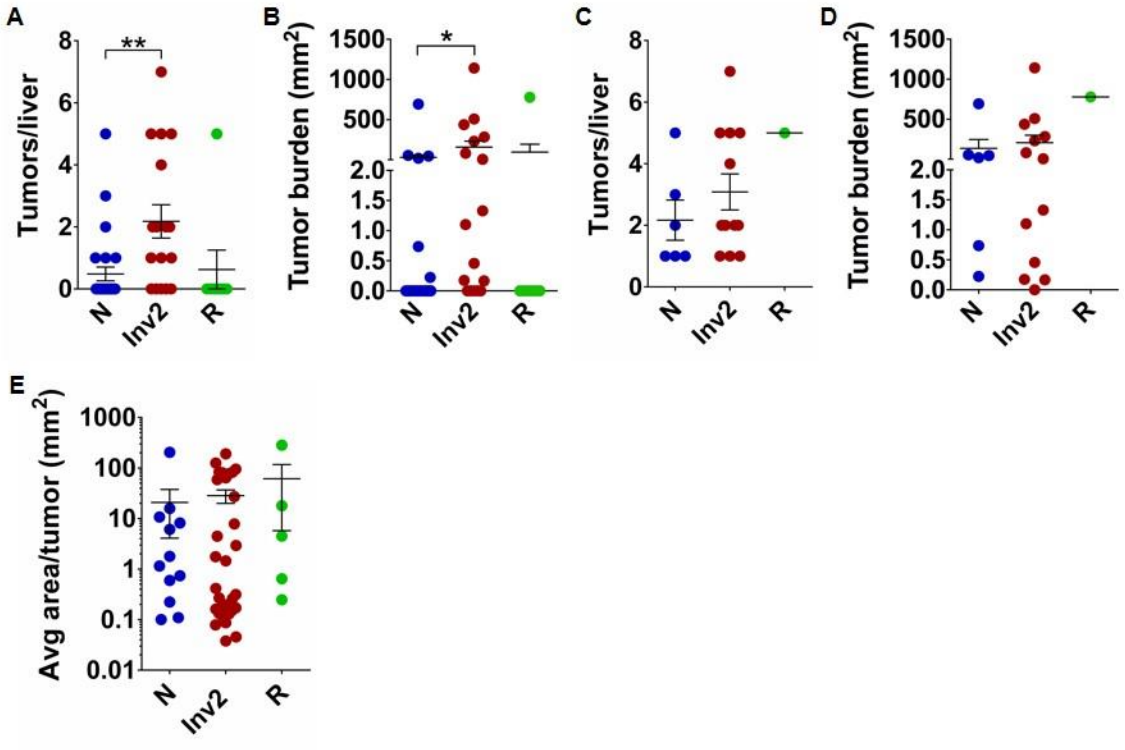

Supplementary Figure 3-7: Weaning-induced liver involution supports increased seeding but not outgrowth compared to nulliparous and regressed livers

(A-E) All metastasis end-points are calculated from intraportal injection studies described in Figure 3-4F-H. 3 H&E sections/liver were analyzed and data averaged; each section was cut 250 µm apart. **(A)** Number of lesions/liver. **(B)** Tumor burden calculated as the total lesion area (mm^2) in each liver. **(C)** Number of lesions/liver, data are presented from only those mice that developed detectable metastases. **(D)** Tumor burden calculated from only mice that developed detectable metastases. **(E)** Average lesion size (mm^2), data are presented as average size of each individual lesion identified across 3 sections stained by H&E.

Supplementary Tables

Supplementary Table 3-1A: Differentially detected Sprague-Dawley rat liver metabolite profiles across the reproductive cycle

Supplementary Table 1A | Differentially detected Sprague-Dawley rat liver metabolite profiles across the reproductive cycle

		L		Inv2		Inv4		Inv6		Inv8		Inv10		R	
	CmpdID	FC to N	P-value	FC to N	P-value	FC to N	P-value	FC to N	P-value	FC to N	P-value	FC to N	P-value	FC to N	P-value
6-Phospho-D-gluconate	C00345	1.63	0.002	1.34	0.084	1.8	0	1.3	0.044	1.22	0.086	1.11	0.55	1.23	0.035
D-Glucono-1-5-lactone 6-phosphate	C01236	2.06	0	1.74	0.02	2.16	0.001	1.3	0.09	1.1	0.4	0.84	0.95	1.36	0.069
Sedoheptulose 7-phosphate	C05382	1.65	0.023	1.48	0.119	1.59	0.068	1.46	0.221	1.19	0.826	1.04	0.733	1.6	0.129
D-Glucose 6-phosphate	C02965	1.82	0	1.46	0.057	1.86	0.003	1.13	0.346	0.87	0.904	0.69	0.452	1.02	0.376
D-Glyceraldehyde 3-phosphate	C00118	1.22	0.002	1.06	0.238	1	0.548	1.01	0.668	0.98	0.734	0.99	0.664	1	0.633
S-Adenosyl-L-methionine	C00019	1.86	0.04	2.67	0.002	2.62	0.028	2.2	0	2.35	0.004	2.03	0.004	1.96	0.001
S-Adenosyl-L-homocysteine	C00021	1.58	0.211	1.17	0.394	0.95	0.284	0.81	0.171	1	0.677	0.95	0.212	1.06	0.512
Cys-Gly	C01419	1.42	0.005	1.6	0.006	1.44	0.036	1.37	0.001	1.34	0.001	1.27	0.023	1.3	0.017
Glutathione	C00051	1.4	0.005	1.55	0.006	1.42	0.045	1.29	0.001	1.28	0.003	1.24	0.019	1.29	0.027
Gamma-L-Glutamyl-D-alanine	C03738	1.73	0.031	1.19	0.927	1.1	0.818	1.31	0.375	0.88	0.303	0.99	0.938	1.21	0.973
Gamma-L-Glutamyl-L-cysteine	C00669	1.33	0.036	1.41	0.073	1.49	0.057	1.21	0.401	1.04	0.941	0.9	0.68	1.05	0.737
Adenosine	C00212	1.17	0.567	0.62	0.034	0.42	0.004	1.22	0.399	0.96	0.714	1.09	0.441	0.98	0.581
Guanosine	C00387	0.69	0.126	0.59	0.136	0.4	0.005	1.1	0.374	0.98	0.45	1.34	0.274	1.31	0.089
Guanine	C00242	0.96	0.636	0.69	0.293	0.47	0.005	1.35	0.156	1.16	0.214	1.35	0.235	1.3	0.063
Hypoxanthine	C00262	0.69	0.388	0.56	0.199	0.38	0.034	1.05	0.668	0.94	0.919	1.06	0.676	1.51	0.06
Xanthine	C00385	1.15	0.867	1.11	0.969	0.98	0.717	1.02	0.722	1.4	0.112	1.14	0.484	1.47	0.072
Inosine	C00294	0.63	0.433	0.53	0.174	0.33	0.032	1.07	0.723	0.84	0.985	0.91	0.932	1.52	0.068
Nicotinamide	C00153	0.7	0.347	0.58	0.032	0.51	0.005	0.89	0.693	0.94	0.375	1.23	0.466	1.18	0.185
Glutamate	C00025	0.76	0.194	0.75	0.109	0.8	0.238	0.74	0.331	1.03	0.507	1.05	0.31	0.91	0.933
Kynurenine	C00328	0.53	0.054	0.47	0.046	0.35	0.008	0.7	0.557	0.73	0.414	0.5	0.505	0.91	0.914
N-Acetylmethionine	C02712	1.02	0.463	1.27	0.014	1.63	0.007	1.4	0.002	1.36	0.006	1.39	0.002	1.08	0.578
L-Citrulline	C00327	1.06	0.294	0.91	0.21	1.08	0.815	0.85	0.093	1.22	0.146	1.09	0.783	1.03	0.568
N-(L-Arginino)succinate	C03406	0.74	0.02	0.84	0.266	1.32	0.018	1.03	0.646	1.33	0.013	1.13	0.452	1.46	0.025
Urate	C00366	0.73	0.004	0.81	0.021	0.98	0.433	0.77	0.047	1.06	0.924	1.11	0.094	0.95	0.612
Acetoacetate	C00164	1.02	0.725	0.87	0.048	0.9	0.348	0.88	0.114	0.96	0.893	1.01	0.436	1.06	0.139
Glutathione disulfide	C00127	0.75	0.038	0.71	0.007	0.8	0.821	0.76	0.077	0.91	0.806	1.06	0.427	1.06	0.822
5-Oxoproline	C01879	1.17	0.367	1.01	0.723	0.96	0.378	1.08	0.328	1.17	0.37	1.38	0.036	1.1	0.436
S-Glutathionyl-L-cysteine	C05526	0.94	0.639	0.79	0.012	1.03	0.506	0.89	0.169	1.16	0.016	1.39	0.001	1.19	0.155

CmpdID = Compound ID; FC to N = fold change to nulliparous

Supplementary Table 3-1B: Absolute quantification of ECM proteins in Sprague-Dawley rat livers across reproductive cycle

Supplementary Table 1B | Absolute quantification of ECM proteins in Sprague-Dawley rat livers across reproductive cycle

Protein	GENE	MW	Median Total Protein by Liver Weight (pmol/g)								Technical
			N	L	Inv2	Inv4	Inv6	Inv8	Inv10	R	
Agrin	AGRN	208646	9.2	10.7	9.6	10	9.3	10.1	9.7	9.4	20%
Agrin(iso 2,3,4,5,&6)	AGRN*	208646	5.8	4.7	5	5.4	6.2	5.2	6.2	5.9	18%
Annexin A2	ANXA2	38678	187	162.5	153.9	180.8	208.1	213.3	225	209	4%
Annexin A4	ANXA4	35849	89.3	78	75.7	104.7	107	88.1	97.1	106.1	31%
Asporin	ASPN	42573	12.5	9.8	6.2	7.6	12.6	8.2	11	15.2	11%
Biglycan	BGN	41706	50.7	36.3	38.4	43.7	58.5	52.1	56.1	54.2	8%
Bone Marrow Proteoglycan	PRG2*	25129	33.1	24.9	22.6	28.7	39.1	51.2	58.2	40.8	17%
Collagen alpha-1(I) chain	COL1A1	137953	1225.1	720.8	639.4	1158.1	1525.8	1087.9	1514	1675.4	11%
Collagen alpha-1(I) chain(C-term Propeptides (NC1 Domain))	COL1A1*	137953	36.7	34.5	39.9	40.8	45.3	35.6	47.3	43.2	21%
Collagen alpha-2(I) chain	COL1A2	129664	763.8	459.8	373.3	648.7	934.3	673.3	928.1	1053.8	9%
Collagen alpha-1(IV) chain(Arresten/Core Protein)	COL4A1*	160613	118	82.3	86.8	166.3	176.9	145.6	159.9	131.7	11%
Collagen alpha-1/5(IV) chain(Arresten/Core Protein)	COL4A1/5*	160613	154.7	118.4	112.2	181.9	241	204.7	238.5	210.2	16%
Collagen alpha-1/5(IV) chain(Arresten/Core Protein)	COL4A1/5*	160613	76.5	53	52.4	83.7	97.1	97.3	100.4	88.3	12%
Collagen alpha-2(IV) chain	COL4A2	161386	59	47.9	53.8	67.7	88.2	75.3	84.6	81.2	21%
Collagen alpha-2(IV) chain(Canstatin/Core Protein)	COL4A2*	161386	104.9	116.5	124.2	116.3	139.8	157.5	159.9	119.4	18%
Collagen alpha-5(IV) chain	COL4A5	161044	22.7	27	20.1	21.1	23	18	20.7	19.6	35%
Collagen alpha-1(V) chain	COL5A1	183987	127.5	129.7	200.6	213.9	168.4	226	273	169.6	45%
Collagen alpha-2(V) chain	COL5A2	145018	27.1	19.9	20.6	23.4	27.4	26.2	37.5	35.8	120%
Collagen alpha-1(VI) chain	COL6A1	108806	338.3	266	246.4	315.7	440.8	396.7	391.8	340.5	11%
Collagen alpha-2(VI) chain	COL6A2	108579	415.2	304.8	291.5	363.7	515.8	425.4	488.1	425.7	19%
Collagen alpha-3(VI) chain	COL6A3	288133	323.4	169.1	162	279.5	377.4	260.9	360	266.2	15%
Collagen alpha-5(VI) chain	COL6A5	289934	2.8	2.2	1.3	2.5	3.7	2.6	4	3	27%
Collagen, type VII, alpha 1(Fibronectin type-III 1 Domain)	COL7A1*	295092	11.6	14.1	13.6	12.3	14.9	13.8	13.1	13	17%
Collagen alpha-1(XII) chain	COL12A1	340214	2.9	2.2	2.5	2.8	4.4	3.3	4.3	3.3	19%
Collagen alpha-1(XIV) chain	COL14A1	191772	89.7	73.3	75.2	89.8	120.8	107.9	107.7	108.4	41%
Collagen alpha-1(XVII) chain	COL17A1	143568	1.2	1.4	1.3	1.1	1.4	1.2	1.3	1.2	20%
Collagen alpha-1(XVIII) chain	COL18A1	182881	46.8	57.1	52.9	52.2	49.5	53.9	58.2	47.7	17%
Decorin	DCN	39805	27.7	28.9	17.9	19.6	28.5	20.3	22.9	30.2	7%
Dermatopontin	DPT	24203	38.7	40.8	35.9	26.6	41.6	38.1	30.2	41.8	19%
Emilin 1	EMILIN1	106667	23.3	20.6	21.8	26.6	23.5	26.3	26.3	24.3	19%
Extracellular Matrix Protein 1	ECM1	63249	43.5	41.3	38	38.4	42.9	45.3	49.2	46	17%
Fibrillin 1	FBN1	311952	45.2	34.7	23.5	40.1	55.1	37.8	52.3	70.2	17%
Fibromodulin	FMOD	43219	33	35	28.1	29.7	36.7	36	25.8	31.1	26%
Fibronectin 1	FN1	272511	91.8	66.2	118.8	126.5	141.6	118.4	156.6	138.6	34%
Fibronectin 1(type-III 4 domain)	FN1*	272511	622.6	533.1	712.1	705.6	645.1	641.2	657.3	708.3	13%
Fibronectin 1(type-III 7 domain)	FN1*	272511	843.5	716.4	1016.3	878.9	936	864.3	1013.3	943.7	23%
Fibronectin 1(type-III 9 domain)	FN1*	272511	224.2	213	286.1	229.6	234.9	218.1	255.9	247.5	10%
Fibronectin 1(type-III 13 domain)	FN1*	272511	4.2	3.7	4.7	4.7	4.9	4.4	4.8	4.3	20%
Fibronectin 1(Anastellin/type-III 1 domain)	FN1*	272511	107.1	83.6	127.3	100.6	128.5	112.7	141.2	131.8	12%
Fibulin 4	EFEMP2	44850	80.1	89.4	78.8	91.8	84.5	91.9	92.5	97.9	23%
Fibulin 5	FBLN5	50160	26	23.6	22.9	23.2	26.2	25.3	27.3	25.2	7%
Galectin-1	LGALS1	14857	81.9	100.6	50.7	78.1	66.4	85.4	107.3	98.7	20%
Galectin-3	LGALS3	27202	3.4	4.5	4.8	7.1	6.3	4.4	4.4	3.2	25%
Laminin alpha-1	LAMA1	338195	0.7	0.3	0.6	1	1.1	1	0.9	0.3	57%
Laminin alpha-2	LAMA2	339982	2.1	2	2.1	2.3	2.1	2.2	1.2	1.9	23%
Laminin alpha-4	LAMA4	201819	3.1	2.8	2.2	2.6	3.1	3.1	3.2	3.4	26%
Laminin alpha-5	LAMA5	404444	3	2.3	1.8	2.7	3.7	2.4	3.5	3.6	18%
Laminin Beta-1	LAMB1	197090	6.2	6.1	4.9	3.5	5.3	5.1	5.5	5.7	19%
Laminin Beta-2	LAMB2	196474	4	3.2	2.6	3.2	3.7	3.5	4	4.4	34%
Laminin Gamma-1	LAMC1	177387	19.4	14.9	12.1	17.2	19.2	18.5	22	21.2	14%
Lumican	LUM	38279	114.4	93.1	79.3	86.7	119.3	104.5	116.4	126.3	13%
Lysyl oxidase	LOX	46559	1.2	1.2	1.3	1.1	1.2	1.2	1.1	1.1	34%
Lysyl oxidase-like 1	LOXL1	66589	0	0	0	0	0	0	0	7.7	47%
Matrilin 1, Cartilage Matrix Protein	MATN1	54309	69.9	75.8	62.6	55.9	76.2	80	77.8	74.2	10%
Microfibrillar-associated protein 2	MFAP2	20578	8.1	6.9	9.4	9	12.6	10.9	13.4	11.3	25%
Mimecan/Osteoglycin	OGN	34069	19.5	19.3	11.1	17.1	21.7	18.3	20.1	23.4	9%
Nidogen-1	NID1	137039	11.6	11.3	7.9	7.3	13.7	12	13.7	13.5	32%
Nidogen 1/2 (osteonidogen)(Nid1/2)	NID1/2*	136538	23.5	20.2	18.1	20.2	27.5	24	26.3	24.5	8%
Nidogen-2	NID2	152976	6.3	4.8	4	5.6	4.3	9.1	6.5	8.1	35%
Osteomodulin	OMD	49783	78.8	70	53.1	63	68.1	75.5	88.1	92.9	25%
Periostin	POSTN	93155	2.5	2.6	2.3	2.2	3	2.4	2.6	2.8	14%
Perlecan	HSPG2	375271	158.3	128.7	133.6	162.8	192	160	185.6	170.5	22%
Perlecan(Endorepellin)	HSPG2*	375271	25.2	22.4	20	28.4	33.3	26.8	31.5	27.6	8%
Prolargin	PRELP	43179	27.2	18.1	17.2	22.4	31.3	28.8	36.3	35.1	11%
Tenascin-C(Iso1,2,3)	TNC*	221756	4.3	2.7	2.8	2.5	5	3.2	5	2	16%
Tenascin-C(Iso1,2,3,4,5)	TNC*	221756	17.6	11	9.1	11.5	16.1	15.3	19.8	10.9	15%
Tenascin-C(Iso1,2,3,4,5)	TNC*	221756	13.3	7.3	7.9	8.9	14.3	10.6	14.9	7.4	20%
Thrombospondin 1	THBS1	129647	220.3	201.6	231.9	211.5	197.5	282.1	258.2	281.6	9%
TnxB Protein	TNXB	126729	3	1.9	2.3	2.2	3.1	2.7	3.3	3.1	29%
Transglutaminase 2	TGM2	77061	346.4	244.1	366.3	425.9	406.3	386.7	377.1	320	5%
Actin (All Isoforms)	ACT	42051	15374.3	16202.2	13130.8	14569.5	15577.3	16625.9	18549.5	16071.3	7%
Actin, cytoplasmic 1/2	ACTB	41737	21922.5	19841.1	19381.7	21679.7	25087	28323.5	27575	24665.2	8%
Adiponectin	ADIPOQ	26809	375	422.1	384.7	225.9	376.4	427	595.4	450.5	32%
Alpha/gamma-enolase	ENO1/2	47128	5945.1	6235.5	6437	6117.5	7008.7	6919.4	6194.7	6203.7	9%
Desmin	DES	53457	12.8	10.8	9.3	12.9	15.8	11.1	13.2	17.3	10%
Glyceraldehyde-3-phosphate dehydrogenase	GAPDH	35828	2855.1	5823.2	5141.5	3896.3	3075.8	3083.9	2542.9	3162.5	15%
Histone H1(H1.1,H1.2,H1.3,H1.4)	H1*	20863	21143.8	15514.1	14089.8	15328.6	20539.8	18175	21902.8	22627.9	6%
Histone 2A(H2A-A-K)	H2A*	14077	18764.2	13752.8	12408.4	15430.9	20590.6	24029.7	25162.9	23430.7	8%
Myosin(Myosin-3,4,6,7)	MYH*	222880	249.1	264.9	183.6	170.1	160.6	183.3	176	192	47%
Plectin	PLEC	533540	9.9	12.4	9.8	14.7	15.3	11.9	16.3	13.5	16%
Spectrin alpha chain, non-erythrocytic 1	SPTA2	284637	118.6	119	116.1	129.1	133.8	122.9	127.4	130	9%
Tubulin beta-4B chain(4b & 5 chain)	TUBB*	49586	1278.4	1313.4	1293	1479.9	1627.6	1549.1	1559.2	1268.5	5%
Transforming growth factor-beta-induced protein ig-h3	TGFBI	74597	79.7	38.9	55.8	61.6	90.2	72.8	100.6	91.8	28%
Vimentin	VIM	53733	123.6	93.2	107.2	149.8	151.3	132	158.3	114.6	12%

Pmol = picomolar; MW = molecular weight; Std = standard deviation; SEM = standard error of the mean; CV = coefficient of variation; * = reporter peptide homologous to multiple isoforms

Supplementary Table 3-2: Differentially detected Balb/c mouse liver metabolite profiles across the reproductive cycle

Supplementary Table 2 | Differentially detected Balb/c mouse liver metabolite profiles across the reproductive cycle

	CmpdID	L		Inv2		Inv4		Inv6		Inv8		R	
		FC to N	P-value	FC to N	P-value	FC to N	P-value	FC to N	P-value	FC to N	P-value	FC to N	P-value
Putrescine	C00134	1.32	0.167	3.52	0	1.29	0.215	1.17	0.247	1.77	0.007	1.63	0.081
Lysine	C00047	1.61	0.035	2.45	0	1.46	0.04	1.02	0.693	1.36	0.077	1.03	0.466
Inosine	C00294	1.86	0.028	2.2	0.017	2.2	0.027	1.27	0.288	2.02	0.014	1.47	0.116
Hypoxanthine	C00262	1.89	0.023	2.13	0.012	1.97	0.029	1.17	0.22	2.12	0.003	1.5	0.058
Hypotaurine	C00519	1.16	0.171	1.93	0.002	1.14	0.127	0.94	0.455	0.95	0.376	0.63	0.657
Guanosine	C00387	1.14	0.051	1.75	0.014	1.62	0.04	0.9	0.4	1.22	0.067	1.01	0.368
Taurine	C00245	0.96	0.827	1.68	0.008	1.55	0.019	0.99	0.952	1.47	0.037	1.41	0.056
Xanthine	C00385	1.39	0.051	1.45	0.038	1.34	0.062	1.27	0.101	1.34	0.062	1.17	0.22
Guanine	C00242	1.21	0.049	1.43	0.044	1.5	0.033	0.94	0.42	1.08	0.211	0.87	0.853
Uracil	C00106	1.19	0.042	1.4	0.015	1.45	0.011	1.07	0.427	0.96	0.951	0.84	0.825
Homomethionine	C17213	2.82	0.178	1.92	0.602	5.9	0.009	1.63	0.684	2.53	0.196	1.3	0.987
Homocarnosine	C00884	0.89	0.921	1.27	0.518	2.35	0.012	1.59	0.193	2.23	0.018	2.47	0.011
5-Oxoproline	C01879	1.35	0.069	1.27	0.234	2.07	0.003	1.39	0.091	1.78	0.046	1.25	0.07
Urate	C00366	0.4	0.139	0.66	0.392	1.94	0.332	1.88	0.743	0.66	0.244	2.01	0.707
S-Glutathionyl-L-cysteine	C05526	1.17	0.212	0.59	0.302	1.26	0.033	1.14	0.31	1.22	0.104	0.81	0.645
Glutamate	C00025	1.23	0.263	1.02	0.86	1.3	0.092	1.6	0.078	1.53	0.053	1.34	0.117
Aspartate	C00049	0.89	0.937	0.67	0.391	1.24	0.223	1.92	0.028	1.38	0.189	1.38	0.078
Gamma-L-Glutamyl-L-cysteine	C00669	1.7	0.017	1.28	0.263	1.39	0.068	1.37	0.128	1.49	0.016	1.27	0.103
Gamma-Glutamyl-gamma-aminobutyrate	C15767	1.99	0.034	0.84	0.855	1.27	0.177	1.64	0.123	1.89	0.025	1.22	0.258
Gamma-L-Glutamylputrescine	C15699	1.65	0.056	1.5	0.092	1.91	0.072	2	0.088	3.12	0	3.19	0.001
Gamma-L-Glutamyl-D-alanine	C03738	2.13	0.019	1.43	0.117	2.04	0.059	2.05	0.027	3.55	0	2.66	0.006
N-Acetyl-L-citrulline	C15532	2.18	0.044	1.31	0.492	1.63	0.174	1.99	0.098	2.57	0.01	2.62	0.039
Glutathione disulfide	C00127	1.49	0.132	1.23	0.456	1.35	0.112	1.27	0.427	2.1	0.006	1.03	0.255
Nicotinamide	C00153	1.48	0.073	1.12	0.518	1.23	0.318	1.23	0.279	1.65	0.022	1.43	0.094
Glutathione	C00051	1.39	0.085	1.05	0.51	1.15	0.307	1.28	0.203	1.42	0.05	1.23	0.164
(5-L-Glutamyl)-L-glutamine	C05283	1.63	0.053	0.98	0.546	0.96	0.46	1.3	0.221	2.3	0.002	1.48	0.106
Cystine	C00491	1.43	0.147	0.56	0.791	1.49	0.225	1.02	0.281	2.05	0.136	1.07	0.276

CmpdID = Compound ID; FC to N = fold change to nulliparous

Supplementary Table 3-3: Summary of end-points analyzed for assessment of weaning-induced liver involution

Supplementary Table 3 | Summary of end-points analyzed for assessment of weaning-induced liver involution

Figure	Description	N (mean, SEM)	L (mean, SEM)	Inv4 (mean, SEM)	Inv6 (mean, SEM)	Inv8 (mean, SEM)	R (mean, SEM)	Stat test	Inv Window (Inv4-8) vs. N	Inv Window (Inv4-8) vs. L	Inv Window (Inv4-8) vs. R	N v. R
1B	Rat liver weight	8.92, 0.22	14.41, 0.70	12.48, 0.51	10.80, 0.43	9.57, 0.25	10.09, 0.34	1-way ANOVA	<0.0001	↓ <0.0001	↑ <0.01	ns
1C	Rat Ki67+ hepatocytes	0.54, 0.13	1.75, 0.32	0.45, 0.24	0.25, 0.16	0.58, 0.10	0.07, 0.04	1-way ANOVA	ns	ns	ns	ns
S1C	Rat mitotic figures	0.42, 0.11	0.48, 0.13	n/d	0.4, 0.14	n/d	n/d	1-way ANOVA	ns	ns	n/d	n/d
1F	Rat CC3 immunoblot	1.00, 0.0	0.06, 0.03	2.52, 0.78	2.03, 0.47	1.69, 0.13	1.13, 0.25	1-way ANOVA	ns	↑ <0.01	ns	ns
1G	Rat TUNEL	5.43, 0.54	3.00, 0.32	7.63, 0.54	11.28, 2.29	n/d	5.85, 0.71	1-way ANOVA	↑ <0.01	↑ <0.001	↑ <0.05	ns
2C left	Rat proteomics TNC	0.02, 0.00	0.01, 0.00	0.01, 0.00	0.02, 0.00	0.02, 0.00	0.01, 0.00	1-way ANOVA	ns	ns	ns	ns
2C middle	Rat proteomics Col1a1	1.25, 0.12	0.77, 0.15	1.14, 0.12	1.75, 0.19	1.07, 0.12	1.81, 0.32	1-way ANOVA	ns	↑ <0.05	ns	ns
2C right	Rat proteomics Col4a1	0.12, 0.00	0.09, 0.02	0.21, 0.06	0.19, 0.02	0.15, 0.02	0.13, 0.02	1-way ANOVA	ns	↑ <0.05	ns	ns
2D	Rat Tenascin immunoblot	0.51, 0.20	0.52, 0.14	0.86, 0.16	1.22, 0.04	1.32, 0.69	0.46, 0.28	Student's t-test	↑ <0.05	↑ <0.01	ns	ns
2E	Rat Tenascin IHC	0.73, 0.21	0.33, 0.10	0.14, 0.05	0.49, 0.19	0.69, 0.10	0.25, 0.06	1-way ANOVA	↓ <0.05	ns	ns	ns
2F	Rat TNC fragment length	11.42, 0.83	13.28, 0.84	n/d	n/d	8.42, 0.55	n/d	1-way ANOVA	↓ <0.05	↓ <0.01	n/d	n/d
S3G bottom left	Rat MMP-9	1.00, 0.0	2.30, 0.57	1.54, 0.27	0.253, 0.43	1.13, 0.19	0.77, 0.23	1-way ANOVA	↑ <0.05	ns	↑ <0.01	ns
S3G bottom middle	Rat MMP-2	1.00, 0.0	2.30, 0.31	1.40, 0.13	1.47, 0.21	1.26, 0.19	0.99, 0.16	Multiple	↑ <0.05	↓ <0.05	ns	ns
3A	Rat CD68+ IHC	3.09, 0.27	2.32, 0.15	4.21, 0.21	4.03, 0.29	3.52, 0.23	2.75, 0.31	1-way ANOVA	ns	↑ <0.001	↑ <0.05	ns
S5C	Rat CXCL12 qRT-PCR	6.81, 1.31	3.06, 0.45	13.29, 3.86	19.16, 4.21	9.33, 2.37	10.94, 1.61	1-way ANOVA	↑ <0.05	↑ <0.01	ns	ns
S4A	Mouse Ki67+ hepatocytes	0.33, 0.10	6.15, 1.03	0.06, 0.02	n/d	n/d	0.04, 0.01	1-way ANOVA	ns	<0.0001	ns	ns
S4B	Mouse liver weight	1.16, 0.02	2.20, 0.08	1.60, 0.06	1.52, 0.06	1.65, 0.10	1.42, 0.08	1-way ANOVA	↑ <0.001	<0.0001	ns	↑ <0.05
S4D	Mouse TUNEL	n/d	1.02, 0.15	3.82, 0.65	n/d	n/d	3.52, 0.92	1-way ANOVA	n/d	↑ <0.05	ns	n/d
S4G	Mouse Tenascin IHC	0.17, 0.02	0.51, 0.12	0.25, 0.20	0.67, 0.25	0.18, 0.05	0.19, 0.04	Student's t-test	↑ <0.05	↑ <0.05	ns	ns
S4H middle	Mouse MMP-2	0.79, 0.07	0.53, 0.08	0.92, 0.18	1.22, 0.18	n/d	0.89, 0.11	1-way ANOVA	ns	↑ <0.05	ns	ns
S4H right	Mouse MMP-9	1.00, 0.0	0.98, 0.04	1.28, 0.05	1.28, 0.04	n/d	1.05, 0.05	1-way ANOVA	↑ <0.001	↑ <0.001	↑ <0.01	ns
3B top left	Mouse CD45+ flow	11.95, 0.68	7.05, 0.30	14.22, 0.78	14.21, 0.82	n/d	12.44, 0.92	1-way ANOVA	ns	<0.0001	ns	ns
3B top right	Mouse CD11b+F4/80+ flow	2.30, 0.17	1.93, 0.14	3.30, 0.26	3.38, 0.23	n/d	1.67, 0.14	1-way ANOVA	↑ <0.01	↑ <0.0001	↑ <0.0001	ns
3B bottom left	Mouse Ly6C+Ly6G- flow	0.67, 0.07	0.29, 0.03	1.24, 0.13	0.95, 0.12	n/d	0.48, 0.06	1-way ANOVA	↑ <0.0001	↑ <0.0001	↑ <0.0001	ns
3B bottom right	Mouse Ly6C-Ly6G+ flow	0.36, 0.04	0.29, 0.03	0.69, 0.11	0.47, 0.04	n/d	0.34, 0.03	1-way ANOVA	↑ <0.001	↑ <0.001	↑ <0.01	ns
3C	Mouse F4/80+ IHC	4.81, 0.34	4.00, 0.21	5.97, 0.38	7.46, 0.69	n/d	6.06, 0.67	1-way ANOVA	↑ <0.05	↑ <0.01	ns	ns
3D	Mouse Ly6C+ IHC	0.32, 0.02	0.17, 0.01	0.54, 0.08	0.51, 0.07	n/d	0.45, 0.07	1-way ANOVA	ns	↑ <0.001	ns	ns
3E	Mouse Ly6G+ IHC	0.91, 0.08	0.73, 0.03	1.08, 0.13	1.67, 0.12	n/d	1.27, 0.17	1-way ANOVA	↑ <0.001	↑ <0.0001	ns	ns
S5D	Mouse CXCL12 qRT-PCR	2.73, 0.44	2.60, 0.32	4.49, 0.47	3.48, 0.25	3.73, 0.59	3.05, 0.69	Student's t-test	↑ <0.05	↑ <0.05	ns	ns
S5E	Mouse CCL2 qRT-PCR	1.45, 0.43	1.51, 0.21	17.58, 6.13	6.77, 1.12	9.03, 1.55	18.90, 10.01	Student's t-test	↑ <0.01	↑ <0.01	ns	ns
S5F left	Mouse F4/80+ immune foci	2.94, 0.78	1.17, 0.57	7.75, 1.64	6.86, 1.39	n/d	3.43, 0.52	1-way ANOVA	↑ <0.05	↑ <0.01	ns	ns
S5F middle	Mouse Ly6C+ immune foci	2.64, 0.32	0.68, 0.14	8.52, 1.50	4.6, 0.24	n/d	3.92, 0.35	1-way ANOVA	↑ <0.001	<0.0001	↑ <0.01	ns
S5F right	Mouse Ly6G+ immune foci	0.86, 0.21	0.16, 0.04	4.00, 0.99	1.93, 0.22	n/d	1.07, 0.26	1-way ANOVA	↑ <0.01	↑ <0.01	↑ <0.01	ns
None	Mouse liver weight (age-matched N vs. R)	1.20, 0.00	n/d	n/d	n/d	n/d	1.42, 0.18	Student's t-test	n/d	n/d	n/d	ns

SEM = standard error of the mean; n/d = not determined; ns = not significant

Blue backgrounds display significant differences in alignment with our hypothesis

Pink backgrounds display significant differences not in alignment with our hypothesis

Green backgrounds display non-significant differences in alignment with our hypothesis that the regressed liver is similar to liver from a nulliparous host

Arrows represent directionality of significant difference (red signifies leading group is significantly increased compared to following group; green signifies significantly reduced)

Supplementary Table 3-4: University of Colorado Young Women's Breast Cancer Cohort

Supplementary Table 4 | University of Colorado Young Women's Breast Cancer Cohort

	Nulliparous (N=185)	PPBC <5 years (N=205)	PPBC 5-<10 years (N=174)
	No. (%)	No. (%)	No. (%)
Mean age at diagnosis	36.42	35.76	38.67
Biologic subtype			
Luminal (ER+, PR+/-, Her2 neu+/-)	124 (67.03%)	131 (65.37%)	116 (66.67%)
ER-, PR+, Her2 neu+/-	4 (2.16%)	3 (1.46%)	5 (2.87%)
Her2 neu positive (ER-, PR-)	11 (5.95%)	20 (9.76%)	13 (7.47%)
Triple negative	29 (15.68%)	34 (16.59%)	22 (12.64%)
Missing Her2 neu	36 (19.46%)	33 (16.10%)	30 (17.24%)
Missing ER or PR	10 (5.41%)	15 (7.32%)	14 (8.05%)
Unknown	8 (4.32%)	12 (6.34%)	10 (5.75%)
Estrogen status			
ER+	124 (67.03%)	131 (63.90%)	116 (66.67%)
ER-	51 (27.57%)	61 (29.76%)	46 (26.44%)
Missing	10 (5.41%)	13 (6.34%)	12 (6.90%)
Histologic grade			
Grade I	21 (11.35%)	13 (6.34%)	15 (8.62%)
Grade II	58 (31.35%)	60 (29.27%)	59 (33.91%)
Grade III	89 (48.12%)	111 (54.15%)	86 (49.43%)
Missing	17 (9.19%)	21 (10.24%)	14 (8.05%)
Tumor size			
DCIS	7 (3.78%)	7 (3.41%)	11 (6.32%)
0.1—≤2.0 cm	82 (44.32%)	93 (45.37%)	62 (35.63%)
>2.0—≤5.0 cm	57 (30.81%)	62 (30.24%)	59 (33.91%)
>5.0 cm	19 (10.27%)	21 (10.24%)	23 (13.22%)
Missing	20 (10.81%)	22 (10.73%)	19 (10.92%)
Stage			
0	10 (5.41%)	10 (4.88%)	10 (5.75%)
I	59 (31.89%)	56 (27.32%)	52 (29.89%)
II	100 (54.05%)	108 (52.68%)	87 (50.00%)
III	8 (4.32%)	16 (7.80%)	17 (9.77%)
IV	3 (1.62%)	8 (3.90%)	0 (0.0%)
Missing	5 (2.70%)	7 (3.41%)	8 (4.60%)
Year of Diagnosis			
1980-1998	41 (22.16%)	36 (17.56%)	24 (13.79%)
1999-2004	39 (21.08%)	40 (19.51%)	49 (28.16%)
2005-present	97 (52.43%)	119 (58.05%)	96 (55.17%)
Unknown	8 (4.32%)	10 (4.88%)	5 (2.88%)
Chemotherapy			
Yes	105 (56.76%)	129 (62.93%)	97 (55.75%)
No	29 (15.68%)	25 (12.20%)	29 (16.67%)
Missing	51 (27.57%)	51 (24.88%)	48 (27.59%)
Radiation Therapy			
Yes	83 (44.86%)	87 (42.44%)	74 (42.53%)
No	45 (24.32%)	52 (25.37%)	39 (22.41%)
Missing	57 (30.81%)	66 (32.20%)	61 (35.06%)

N = sample size; No. = number.; ER = Estrogen Receptor; PR = Progesterone Receptor; DCIS = Ductal Carcinoma In Situ.

Supplementary Table 3-5: University of Colorado and Dana-Farber Cancer Institute Combined Metastasis Cohort

Supplementary Table 5 | University of Colorado and Dana-Farber Cancer Institute Combined Metastasis Cohort

	Nulliparous (N=34)	PPBC <10 years (N=83)
	No. (%)	No. (%)
Mean age at diagnosis	35.38	35.72
Biologic subtype		
Luminal (ER+, PR+/-, Her2 neu+/-)	24 (70.59%)	52 (62.65%)
ER-, PR+, Her2 neu+/-	0 (0%)	1 (1.20%)
Her2 neu positive (ER-, PR-)	1 (2.94%)	9 (10.84%)
Triple negative	9 (26.47%)	15 (18.07%)
Missing Her2 neu	1 (2.94%)	9 (10.84%)
Missing ER or PR	0 (0%)	7 (8.43%)
Unknown	0 (0%)	3 (3.61%)
Estrogen status		
ER+	24 (70.59%)	52 (62.65%)
ER-	10 (29.41%)	27 (32.53%)
Missing	0 (0%)	4 (4.82%)
Histologic grade		
Grade I	0 (0%)	4 (4.82%)
Grade II	10 (29.41%)	26 (31.33%)
Grade III	21 (61.76%)	41 (49.40%)
Missing	3 (8.82%)	12 (14.46%)
Tumor size		
DCIS	0 (0%)	1 (1.20%)
0.1—≤2.0 cm	4 (11.76%)	15 (18.07%)
>2.0—≤5.0 cm	7 (20.59%)	18 (21.69%)
>5.0 cm	2 (5.88%)	9 (10.84%)
Missing	21 (61.76%)	40 (48.19%)
Stage		
0	0 (0%)	0 (0%)
I	3 (8.82%)	17 (20.48%)
II	16 (47.06%)	26 (31.33%)
III	7 (20.59%)	12 (14.46%)
IV	8 (23.53%)	27 (32.53%)
Missing	0 (0%)	1 (1.20%)
Year of Diagnosis		
1980-1998	6 (17.65%)	12 (14.46%)
1999-2004	1 (2.94%)	15 (18.07%)
2005-present	27 (79.41%)	56 (67.47%)
Chemotherapy		
Yes	28 (82.35%)	62 (74.70%)
No	5 (14.71%)	14 (16.87%)
Missing	1 (2.94%)	7 (8.43%)
Radiation Therapy		
Yes	21 (61.76%)	40 (48.19%)
No	12 (35.29%)	33 (39.76%)
Missing	1 (2.94%)	10 (12.05%)
Site of Metastasis		
Liver	2 (5.88%)	17 (20.48%)
Lung	3 (8.82%)	8 (9.64%)
Bone	21 (61.76%)	37 (44.58%)
Brain	2 (5.88%)	7 (8.43%)
Other	6 (17.65%)	14 (16.87%)

N = sample size; No. = number; ER = Estrogen Receptor; PR = Progesterone Receptor;

Supplementary Table 3-6: Patient Statistical Analysis

Supplementary Table 6 | Patient Statistical Analysis

UC Cohort Statistical Analysis

Group	Organ	Metastasis		Univariate P-value (a)	Multivariate P-value*	OR [95% CI]
		YES (%)	NO (%)			
Nulliparous (n=185)	Liver	1.62	98.38	Reference	Reference	Reference
PPBC<5 (n=205)		5.85	94.15	0.042	0.038	4.05 [1.08-15.12]
PPBC 5-<10 (n=174)		4.02	95.98	0.181	0.163	2.71 [0.67-11.05]

UC and DFCI Metastasis Only Cohort Statistical Analysis

Group	Organ	Metastasis		Univariate P-value (b)	OR [95% CI]
		YES (%)	NO (%)		
Nulliparous (n=34)	Liver	5.88	94.12	0.058**	
PPBC<10 (n=83)		20.48	79.52	0.041***	4.12 [0.90-18.94]
Nulliparous (n=34)	Lung	8.82	91.18		
PPBC<10 (n=83)		9.64	90.36	1.000**	1.10 [0.27-4.43]
Nulliparous (n=34)	Brain	5.88	94.12		
PPBC<10 (n=83)		8.43	91.57	1.000**	1.47 [0.29-7.49]
Nulliparous (n=34)	Bone	61.76	38.24		
PPBC<10 (n=83)		44.58	55.42	0.106**	0.50 [0.22-1.13]

(a)Chi-square
(b)Fisher's exact
* Multivariate logistic regression, adjusted for biologic subtype, age at diagnosis, and year of diagnosis
** Two-sided Fisher's Exact test
*** One-sided Fisher's Exact test
OR = Odds Ratio; UC = University of Colorado; DFCI = Dana-Farber Cancer Institute

Acknowledgments

The authors would like to acknowledge the important scientific contributions of researchers whose work could not be cited due to space limitations. The authors would also like to thank the Schedin and Borges lab members Jacob Fischer, Sonali Jindal, Jeremy Johnston, Pat Bell, Hadley Holden, Marcelia Brown, Jayasri Narasimhan, Breanna Caruso, Itai Meirom, and Ethan Cabral for IHC and technical assistance and cohort data collection; Ana Coito (UCLA) for TNC knockout mouse tissue; Maria Cavasin and the Pre-Clinical Cardiovascular Core, UC Denver, for technical contributions to the intracardiac metastasis model; the UC Denver Flow Cytometry Shared Resource (NIH/NCI P30CA046934); the UC Denver Genomics and Microarray Core for RNA quality assessment; the OHSU Flow Cytometry Shared Resource; the OHSU Advanced Light Microscopy Core at the Jungers Center; Dexiang Gao of the Department of Pediatrics, School of Medicine at UC Denver for statistical analysis of the intracardiac metastasis data; and Lisa M. Coussens and Brian Ruffell for critical review of the manuscript. Finally, we are very grateful to the patients for their contributions to this research. The data reported in this paper are tabulated in the manuscript & supplementary materials, and archived at The Metabolomics Consortium Data Repository and Coordinating Center (DRCC) (Project ID PR000382: Rat metabolomics study ST000509, mouse metabolomics study ST000510).

Grant Support

Funding for this project includes NIH/NCI NRSA F31CA186524 (to ETG), NIH/NCATS Colorado CTSI UL1 TR001082 for proteomic support and REDCap database support,

NIH/NCI R33CA183685 (to KH), DOD BC123567 (to PS), BC123567P1 (to KH), and NIH/NCI 5R01CA169175 (to VB and PS), and the Grohne Family Foundation.

Chapter IV: Low-dose ibuprofen intervention has minimal impact on postpartum breast cancer metastasis to the liver

Plan to publish

The work described in this chapter will be published at a later date upon completion of experiments in the future directions.

Contributions

Pepper Schedin, Virginia Borges, and I were responsible for hypothesis development, conceptual design, all data analysis and interpretation. I developed the portal vein injection model and performed all experiments and metastasis studies. Alexandra Quackenbush performed immunoblots as part of her rotation project in the lab, under my supervision. I performed all NSAID intervention studies on non-tumor bearing mice, in collaboration with Qiuchen Guo. Nathan Pennock provided critical discussion of the data and future directions.

Abstract

Postpartum breast cancers, diagnosed within 5 years of giving birth, impart high risk for metastasis. The high risk for metastasis in this vulnerable population is thought to be due to the pro-tumorigenic window of weaning-induced mammary gland involution. Mammary gland involution is characterized by Cox-2 dependent wound-healing-like tissue remodeling, and Cox-2 inhibition with non-steroidal anti-inflammatory drugs (NSAIDs) dampens the wound healing response and abrogates the tumor promotional attributes of involution. These observations suggest NSAID treatment in the postpartum setting may reduce the incidence and/or poor prognosis of postpartum breast cancers. However, NSAIDs have been reported to have tissue-specific effects that may result in undesirable changes in sites of breast cancer metastasis including lung and liver. The potential for postpartum NSAID treatment to significantly impact the liver has recently become apparent, as I have discovered that the rodent post-weaning liver undergoes a programmed tissue involution event characterized by tissue remodeling and increased risk for liver metastasis. Thus, we explored the effect of the NSAID ibuprofen, on weaning-induced liver involution and risk for liver metastasis. Due to the similarities between weaning-induced mammary gland and liver involution, we hypothesized that NSAIDs would reduce liver-specific metastasis by targeting the pro-metastatic microenvironment established at this time. We found that ibuprofen had marginal impact on pro-metastatic attributes of liver involution and did not impact risk for liver metastasis. Importantly, we did not observe undesirable tissue-specific effects in the liver, suggesting that NSAID intervention should be explored further as a chemopreventive agent to control primary tumor progression in the postpartum setting.

Introduction

Women diagnosed with postpartum breast cancer, defined here as a diagnosis of breast cancer within 5 years of giving birth, are at elevated risk for metastasis and death[7-9]. The risk for metastasis with a postpartum diagnosis is, in part, attributed to weaning-induced mammary gland and liver involution[47,233]. Post-weaning mammary gland involution supports early steps of the metastatic cascade including primary tumor growth, immune evasion, local dissemination, and escape into the circulation[47]. Subsequent stages of the metastatic cascade are supported by a pro-metastatic microenvironment established in the liver post-weaning[233]. Importantly, in Chapter III, I report that women diagnosed with postpartum breast cancer are at increased risk for liver-specific metastasis, whereas risk for bone, lung, and brain metastasis is similar between postpartum and nulliparous young women's breast cancer patients[233]. Currently, no unique treatment recommendations exist for postpartum breast cancer patients beyond the standard of care, despite the aggressive nature of the disease and the prominent role that the tissue microenvironment plays in disease progression[9,316,317]. Of interest, high levels of both cyclooxygenase-2 (Cox-2) and collagen I are associated with poor prognosis in young women's breast cancer[47]. Furthermore, epithelial and stromal levels of Cox-2 in the mammary gland are regulated by estrogen and progesterone and are increased over nulliparous levels in both pregnancy and involution stages of the reproductive cycle[318]. Thus, Cox-2 represents an attractive chemopreventive target for postpartum mothers or those young women diagnosed with postpartum breast cancer[47,114,318].

The role of the Cox-1 and -2 pathways in cancer have been extensively investigated, resulting in a depth of knowledge regarding this biology. In tissues, the constitutively expressed Cox-1, as well as the inducible form of the enzyme, Cox-2, are responsible for conversion of the lipid metabolite arachidonic acid, a product of diacylglycerol and membrane phospholipids, to prostaglandin H2 (PGH_2) (Fig.4-1). Subsequently, PGH_2 gets converted to a number of eicosanoid inflammatory mediators including prostaglandin D, E_2, F_2, I_2 (PGD, PGE_2, PGF_2, PGI_2), and thromboxane A_2 (TXA_2) via tissue-specific prostaglandin isomerase and synthase enzymes[319-321]. Prostaglandins primarily exert their effects via binding and activation of a family of G protein-coupled receptors called prostanoid receptors (DP, EP_1-EP_4, FP, IP and TP). Prostanoid receptors are expressed in a cell- and tissue-specific dependent manner, and the result of their activation varies widely based upon the specific prostaglandin, prostaglandin receptor expression and tissue/cellular context (Fig.4-1)[319-321]. Cox-1 activity plays an important role in maintaining gastrointestinal (GI) tissue homeostasis and in platelet aggregation and vascular integrity, whereas Cox-2 is typically upregulated by inflammatory stimuli and during carcinogenesis and tumor progression[319-323]. It is important to note that Cox-1 can contribute to prostanoid production during inflammation and cancer, although reportedly to a much lesser extent than Cox-2[319,321]. Cox-2/PGE_2 overexpression in rodent models of cancer contributes to tumor initiation, immune suppression, and tumor cell immune escape through numerous mechanisms (Fig.4-1)[289,319,324-326]. Specifically, PGE_2 has been shown to shift cytokine milieus to favor pro-tumor T_H2 polarization by increasing IL-10, IL-4, IL-6, and decreasing TNFα, IFNγ, IL-2 production[327,328], subsequently promoting regulatory T cell function[329], and inducing immune suppressive

myeloid populations[326,330]. Further, PGE_2 abolishes cytotoxic T cell activity via reduced antigen presentation, upregulation of inhibitory receptors on T cells, and induction of tolerogenic dendritic cells[331-333]. Elevated Cox-2/PGE_2 also promotes tumor angiogenesis[334,335] as well as cancer cell survival, proliferation, motility, invasion, and metastasis[47,319,336-339]. In several model systems, genetic ablation or inhibition of Cox-2 using NSAIDs results in amelioration of tumor-promotional inflammatory pathways and reduces tumorigenesis and metastasis[47,289,319,324,336,340]. Relevance to human cancer is implicated, as Cox-2 and PGE_2, are overexpressed in a number of human cancers including colorectal, stomach, lung, pancreatic, and breast cancer[341,342].

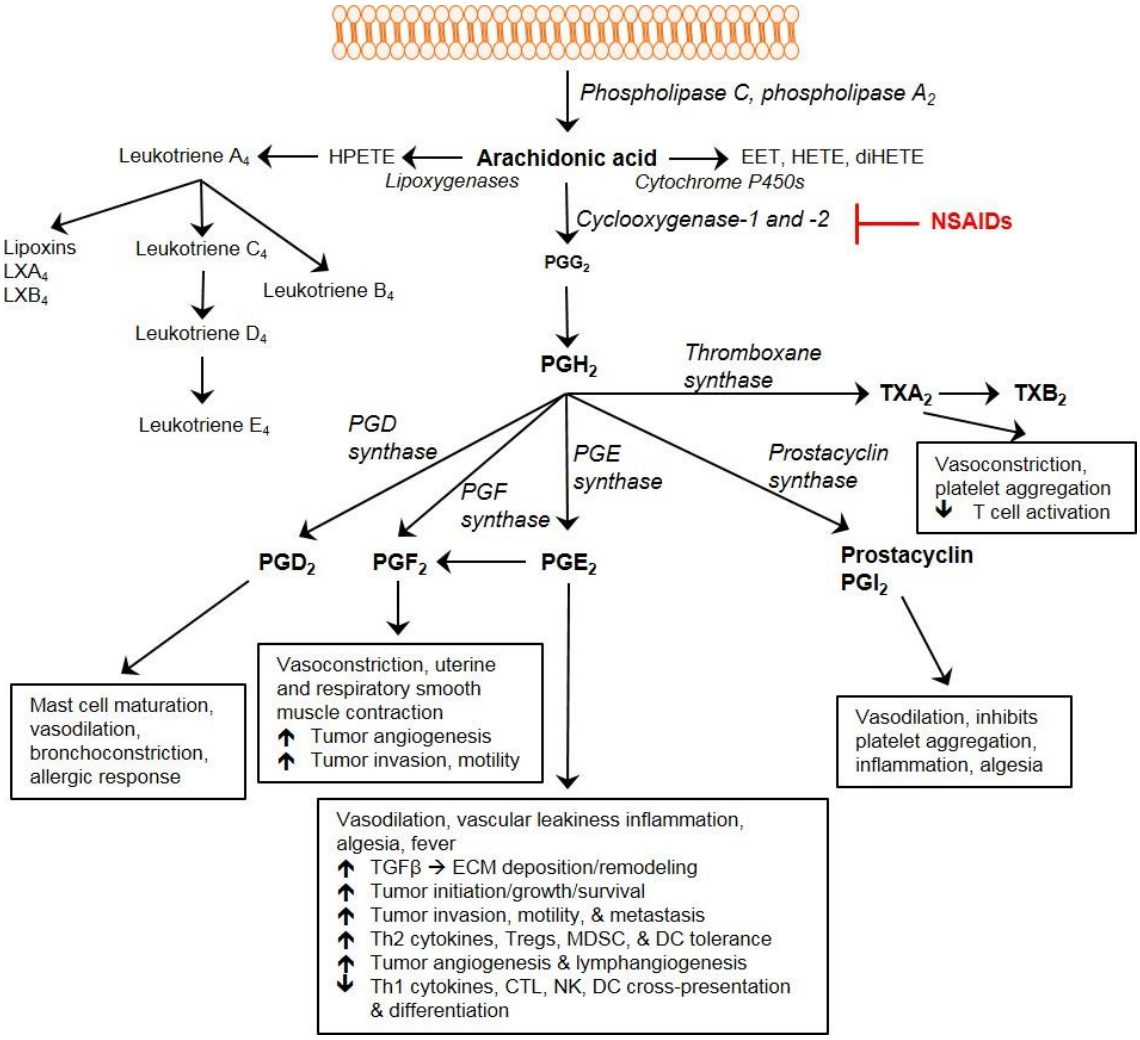

Figure 4-1: Arachidonic acid metabolism

Schematic of arachidonic acid metabolism: phospholipases mobilize esterified arachidonic acid stored in phospholipids. Free arachidonic acid can be converted to numerous eicosanoids via lipoxygenases, cyclooxygenase (Cox-1, Cox-2), or cytochrome P450 enzyme activity. Cox-1 and Cox-2 convert arachidonic acid prostaglandin G_2 (PGG_2) via the addition of 2 oxygen molecules, peroxidase activity by the Cox enzymes completes the reaction to convert PGG_2 to PGH_2. The action of NSAIDs is via inhibition of Cox-1/2 or Cox-2. PGH_2 is then converted to various other prostaglandins (PGD_2, PGF_2, PGE_2, PGI_2, and TXA_2) by tissue specific isomerases. PGE_2 can be further converted to PGF_2. Prostaglandins have far reaching and tissue/cell-specific effects, some of which have been highlighted in this diagram. Arachidonic acid can also be converted to leukotrienes, lypoxins, and various other pro- and anti-inflammatory lipid mediators via lipoxygenase or cytochrome P450 activity (Wang et al., 2010, Nature Reviews; Dennis et al., 2015, Nature Reviews Immunology).

Numerous studies have found that elevated Cox-2 levels in breast cancer associate with increased risk for recurrence and reduced overall survival rates[343-349]. Interestingly, one study suggests that the prognostic value of Cox-2 in breast cancer may be due to stromal as opposed to epithelial levels of the enzyme, highlighting a potentially important role for microenvironment-derived Cox-2 in disease progression[349]. A recent study suggests that aspirin may suppress growth in PI3K mutant breast cancer cells *in vitro* in a Cox-2 independent manner, suggesting that patients with PI3K mutations may also benefit from NSAID intervention[350], as has been shown in PI3K mutant colorectal cancer[351]. In sum, NSAID intervention may reduce breast cancer risk and prolong overall survival rates in breast cancer patients[288,352-354], suggesting that NSAID use in the postpartum breast cancer setting may similarly reduce the high risk of metastasis in this vulnerable population.

Preclinical models of weaning-induced mammary gland involution and postpartum breast cancer provide further support for the use of NSAID intervention in the background of postpartum breast cancer. The process of weaning-induced mammary gland involution returns the gland to a non-secretory, nulliparous-like histological state via epithelial cell death, extracellular matrix (ECM) deposition, active stromal remodeling, and immune influx that resembles wound healing[37,42,43,47,49,77,94]. In the post-weaning mammary gland, Cox-2 contributes to a pro-tumorigenic microenvironment, driving lymphangiogenesis, deposition of fibrillar collagen, and invasive capacity of mammary tumor cells, likely via PGE_2 production[47,48,113,114]. Importantly, PGE_2 receptor EP_1 is upregulated specifically during post-weaning mammary gland involution, and EP_{2-4} are also present at this

time[334]. In pre-clinical murine models of postpartum breast cancer, the Schedin lab has observed efficacy of NSAIDs in reducing pro-tumorigenic attributes of mammary gland involution including deposition of pro-tumor ECM proteins, collagen and tenascin-C (TNC), and influx of pro-tumor immune populations[47,113,114] (Schedin Lab, data unpublished). The functional impact of NSAID intervention during mammary gland involution is evident, as orthotopic mammary tumor growth, local invasion, lymph node involvement, and lung metastases are all reduced[47,114] (Schedin Lab, data unpublished). The mechanism of action for NSAID abrogation of these pro-tumorigenic modalities is thought to be, in part, through mammary fibroblast specific targeting (Guo et al., submitted). Fibroblasts isolated from involuting murine mammary glands are tumor promotional when re-implanted with D2A1 mammary tumor cells into naïve (nulliparous) mice. This effect is reversed when fibroblasts are isolated from NSAID treated mice undergoing involution. In this model, NSAIDs were shown to reduce TGFβ, CXCL12, and collagen production by involution fibroblasts. Taken together these data suggest that numerous pro-tumorigenic attributes of the involuting mammary gland are targetable by NSAID intervention and that even short duration of NSAID intervention during the window of mammary gland involution results in a reduction in primary tumor growth and metastasis. For these reasons, the Schedin lab is actively investigating the safety and efficacy of NSAIDs in abrogating pro-tumorigenic microenvironments supportive of postpartum breast cancer progression.

Importantly, Cox-2, and thus NSAIDs, have tissue-specific effects including differences in prostaglandin production by macrophages in distinct tissues[355] and a potential

protective role for PGE_2 in lung inflammation, fibrosis and repair[356-358]. In these lung pathology studies, prostaglandins serve to curtail collagen production[356-358]. These data suggest that NSAID intervention may promote collagen production and exacerbate the metastasis-supporting attributes of the lung. The fact that unique tissues respond differentially to NSAID treatment suggests that NSAIDs may also promote pro- or anti-metastatic microenvironments simultaneously, in distinct sites. Understanding the impact of NSAIDs on potential future metastatic sites will further inform our studies on NSAID safety and efficacy in the postpartum setting. Studies in the normal liver have revealed low or non-existent levels of Cox-2, PGE_2, and the PGE_2-specific EP receptors[359-361]. However, in states of liver pathology including cirrhosis, hepatocellular carcinoma, and liver metastasis, Cox-2 and PGE_2 are markedly elevated[361-365]. In rodent models of liver cirrhosis and fibrosis NSAID intervention has shown some efficacy in reducing pathological ECM deposition and liver damage[362-364].

I previously discovered that the rodent liver undergoes an orchestrated tissue involution program post-weaning, returning the liver to a pre-pregnant-like steady state, similar to what is observed in the mammary gland. This work is described in detail in Chapter III[233]. Although weaning-induced liver involution in rodents occurs in the absence of overt fibrosis, it is characterized by hepatocyte cell death, catabolic metabolism, deposition of ECM, immune influx, and evidence for stromal remodeling[233]. In chapter III, I report that the process of weaning-induced liver involution establishes a pro-metastatic microenvironment and increases the risk for liver metastasis compared to nulliparous controls[233]. Further, my analysis of a young women's breast cancer cohort

suggests that postpartum breast cancer patients are at increased risk for liver metastasis[233]. Based on these data and evidence that NSAIDs are efficacious in subduing the pro-tumorigenic microenvironment of the involuting mammary gland[47,113], we hypothesized that ibuprofen intervention during the window of weaning-induced liver involution will reduce the pro-metastatic attributes of liver involution and thus reduce the risk for postpartum liver metastasis. However, the impact of NSAID intervention with ibuprofen on breast cancer liver metastasis may result in 1) added benefit by ameliorating the pro-metastatic niche in the post-weaning liver, 2) no measurable impact, or 3) promotion of liver metastasis due to tissue-specific effects, resulting in recommendations not to use NSAIDs to prevent or treat postpartum breast cancers. Using rodent models of PPBC and ibuprofen intervention (Fig.4-2A-C) I observed modest reduction on some attributes of the pro-metastatic microenvironment weaning-induced liver involution but no impact on liver metastasis.

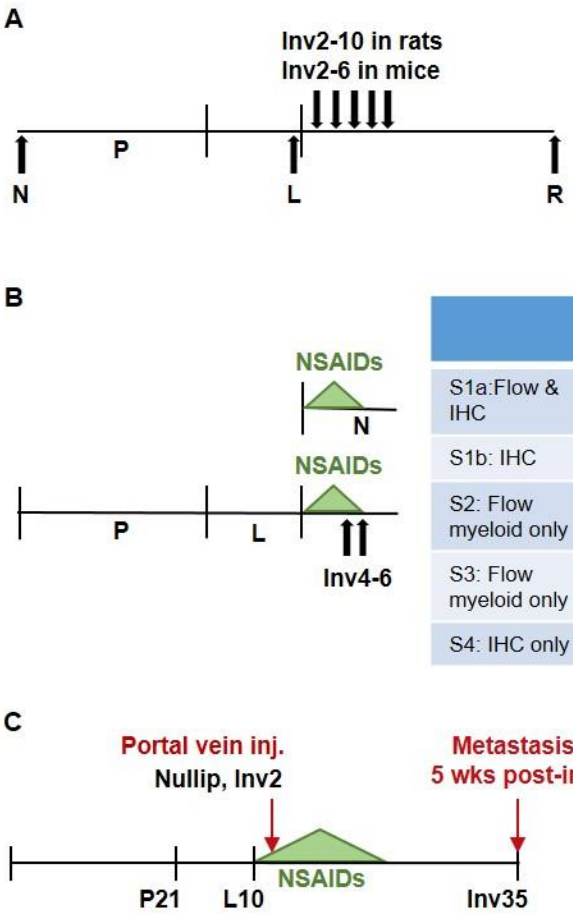

	N	N Tx	L	Inv4	Inv4 Tx	Inv6	Inv6 Tx
S1a:Flow & IHC	6	6		4	4	4	4
S1b: IHC	6		5	5		5	
S2: Flow myeloid only	6					3	6
S3: Flow myeloid only						4	8
S4: IHC only	8	3				5	6

Figure 4-2: Rodent study designs

(A) Rodent studies for acquisition of liver tissues to understand arachidonic acid metabolism at nulliparous (N), lactating (L), Involuting (Inv2-10), and fully regressed 4 weeks-post-weaning (R) stages. Pregnancy time points were not assessed in these studies. N=4 rodent lysates/grp were utilized for tissue lysates. n=4 Inv4, Inv10; n=5 L, Inv2, Inv6; n=6 N, Inv8, R rats/grp were utilized for metabolomics. **(B)** Schematic for assessing the impact of Ibuprofen on Balb/c mouse livers from nulliparous, and Inv4 and 6 stages. The table shows sample size numbers collected for flow cytometry and/or IHC across 4 studies. **(C)** Study design for intraportal injection metastasis studies; Nullip, n=21; Nullip+Ibu, n=21; Inv2, n=20; Inv2+Ibu, n=25.

Materials and methods

Postpartum rodent models

The UC-AMC and OHSU Institutional Animal Care and Use Committees approved animal procedures. Age-matched female Sprague-Dawley rats (Harlan) and Balb/c mice (Jackson Laboratories) were housed and bred as described[42,49]. Tissue collection was performed as described[233].

Ibuprofen intervention

Ibuprofen doses utilized for rodent studies (150 mg ibuprofen/kg chow or 300 mg ibuprofen/kg chow) are equivalent to 117 mg/day and 234 mg/day of ibuprofen, respectively, taken daily (for a 65 kg/143.3 lbs person) according to the U.S. Food and Drug Administration (FDA) calculator for human dose equivalents[366]. Ibuprofen chow was made using pulverized irradiated base chow 5L0D Laboratory Rodent Diet (Purina, LabDiet® PicoLab®, St. Louis, MO). Ibuprofen (I7905, Sigma Aldrich) was added to dry pulverized chow at 150 mg/kg (IbuL) or 300 mg/kg (IbuH) and mixed with a Kitchen Aid® Professional 550 HD mixer until well mixed. Sterile water was then added to the mix until chow was moist enough to form patties. Patties were dehydrated using a LEM™ 5-tray dehydrator (Model #1009) set to 105°F for 6 days. Efficacy of ibuprofen delivery in this manner, via chow feeding, has been confirmed in previous studies[47,367] (and data unpublished, Martinson et al., Schedin Lab). Balb/c female mice were fed 5L0D base chow or 5L0D ibuprofen chow at the appropriate dosage for 4 or 6 days for involution day 4 and 6 groups (respectively), 6 days for nulliparous controls, or for 14 days post-weaning for metastasis intervention studies.

Cell culture

D2A1, D2.OR, and 4T1 cells were cultured and injected as described[233,296]. $Braf^{V600E}$ melanoma cells and $Braf^{V600E}$ *ptgs1/ptgs2*$^{-/-}$ CRISPR/Cas9 engineered cells[324] were a gift from Drs. Santiago Zelenay and Caetano Reis e Sousa (The University of Manchester, Manchester, UK and The Francis Crick Institute, London, UK). B16 cell lysates were a gift from Dr. Amanda Lund (Oregon Health & Science University, Portland, OR).

D2A1 tumor cell ibuprofen dose curve

D2A1 mammary tumor cells were plated in 24 well plates at a density of $5x10^4$ and cultured for 24 h in DMEM high glucose (Hyclone, South Logan, UT) with 2 mM L-glutamine (Gibco, Grand Island, NY), 1X Penicillin/Streptomycin (Corning), and 10% FBS (Hyclone). Media was removed and replaced with complete media and 5, 25, 50, or 100 μm of Ibuprofen (Sigma) diluted in DMSO. Vehicle treated wells were incubated in an equal volume DMSO alone; untreated wells were incubated in complete media without any additives. At 5 days wells were washed and incubated in 0.1% crystal violet for 30 min, washed 3x, and allowed to dry completely. 1 ml methanol was added to each well to extract crystal violet and samples were read at 560 nm using a Promega plate reader.

Intraportal injection model of metastasis

Balb/c female mice injected with 5,000 D2A1 isogenic mammary tumor cells into the portal vein as described[238]. Mice were euthanized at 5 weeks post-injection (Nullip, n=21;

Nullip+Ibu, n=21; Inv2, n=20; Inv2+Ibu, n=25) and visible liver metastasis assessed at necropsy. Data are presented as the percentage of mice in each group with liver metastasis. Tumor area was assessed on H&Es of n=10 Inv2 and n=10 matched Inv2+Ibu mice injected on the same days using Aperio ImageScope software (Leica Biosystems).

Flow cytometry

For flow cytometric analyses, individual mouse livers were perfused and prepared for immune cell profiling by flow cytometry as described[233].

Immunohistochemistry, reticulum silver stain, and image analysis

Immunohistochemical (IHC) for F4/80, Ly6C, and Ly6G was done as described[233]. FoxP3 IHC is described in Chapter III. Reticulum silver stain was done using the Chandler's Precision® Reticulum Stain Kit as per manufacturer's recommendations (American Mastertech Scientific, Inc.). Image analysis was done as described[233] and as in Chapter III.

Immunoblotting

Sample preparation of protein lysates and immunoblots were performed as described[95] on cell pellets and tissue. 5 μg of protein for cell pellets and D2A1 mammary tumors, and 30-60 μg of protein for tissue lysates, was loaded. Membranes were probed at 4°C overnight with αCox-1 (4841, Cell Signaling, 1:1000), αCox-2 (D5H5, 12282, Cell Signaling, 1:1000), αTNC (ab19011, Millipore, 1:200) or for 1 hr at RT with αGAPDH (G9545, Sigma, 1:5000). Secondary goat anti-rabbit IgG (Bio-Rad, 1:10,000) was used

with shaking for 1 hr at RT. Signal was detected with ECL substrate (Thermo Fisher) and an All Pro 100-Plus film developer (Air Techniques, Melville, NY).

Metabolomics and data analysis

For rat liver metabolomics, mass spectrometry was performed on n=4 Inv4, Inv10; n=5 L, Inv2, Inv6; n=6 N, Inv8, R rats/grp and data analyzed as described[233]. The full metabolomics dataset is available at The Metabolomics Consortium Data Repository and Coordinating Center (DRCC) (Project ID PR000382: Rat metabolomics study ST000509).

Results

Arachidonic acid metabolism in the liver

Because high levels of Cox-2, PGE_2, and EP_1 are characteristics of weaning-induced mammary gland involution[47,113,334] we first sought to characterize arachidonic acid metabolism and Cox-2 expression/activity in the homeostatic liver. Studies suggest that Cox-2 levels are low or undetectable in healthy liver, and upregulated in viral hepatitis, cirrhosis, and fibrosis of the liver[361-364,368]. Cox-2 is primarily expressed by resident liver macrophages, known as Kupffer cells, although other cell types including hepatic stellate cells have been reported to express Cox-2[369,370]. In contrast, Cox-1 is constitutively expressed by various non-parenchymal cells[368,371], seemingly regardless of liver pathology[361,368]. Cox-1 and -2 levels and activity have not previously been assessed in rodent livers in the postpartum setting. To this end, we undertook a breeding study to obtain mouse and rat livers from nulliparous, lactating, involuting, and fully regressed rodents (Fig.4-2A) for Cox-1 and Cox-2 protein expression by western blot. We did not assess for Cox enzymes in samples from pregnancy time points despite high levels of Cox-2 observed in mammary glands from pregnant rats[318] as the window of risk for highly metastatic breast cancers is specific to those breast cancers diagnosed postpartum[10]. We found that liver Cox-1 is similarly expressed in rodents from nulliparous, lactation, involution, and regressed stages. In contrast, Cox-2 was specifically upregulated in the liver during lactation and involution (Fig.4-3A-B). Immunoblots for Cox-1 and Cox-2 on BrafV600E wild type cells that express Cox-1 and Cox-2, as well as the BrafV600E cell line with a Cox-1/2 double knockout[324], served to confirm antibody specificity (Fig.4-3C). Mass spectrometry metabolomics assessing for

arachidonic acid metabolism on whole rat livers similarly suggested modest changes in arachidonic acid metabolism postpartum. Specifically, we observed a significant, but modest ~1.2-fold decrease in PGE_2 at early-involution with recovery to nulliparous levels by mid-involution (Fig.4-3D-E). We also observed increased levels of the more stable prostanoid, $PGF_{2\alpha}$, during lactation, with high levels maintained through Inv6 (Fig.4-3D, 4-3F). Levels of the prostacyclin PGI_2 were not detected. Metabolomics also detected a small subset of eicosanoids downstream of lipoxygenase activity that were not altered across the reproductive cycle (data not shown). Cumulatively, our data suggest that Cox-2/PGE_2 levels change only modestly post-weaning, and may not mediate liver involution. Nonetheless, our observations of increased Cox-2 protein expression and a ~3-fold increase in prostaglandin $PGF_{2\alpha}$ levels during lactation and involution suggest liver Cox-2 activity or available substrate (arachidonic acid) may be functional, necessitating further investigation into the potential side effects of NSAID intervention on weaning-induced liver involution.

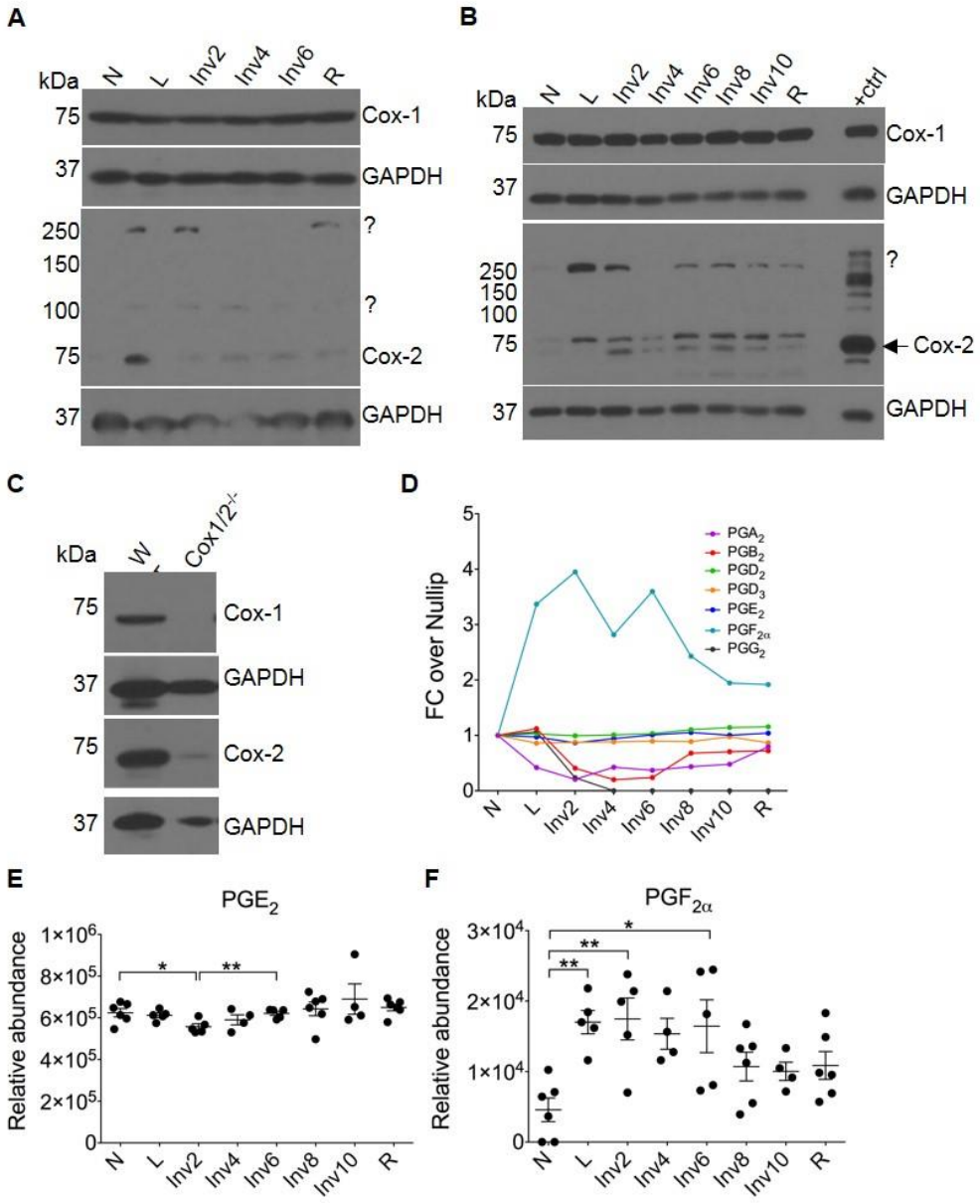

Figure 4-3: Arachidonic acid metabolism in rodent liver across the reproductive cycle

(A-B) Immunoblot of Cox-1 and Cox-2 in **(A)** Balb/c female mouse livers and **(B)** Sprague Dawley rat livers across the reproductive cycle; n=4 pooled livers/grp. +ctrl=BrafV600E cells. **(C)** Immunoblot for Cox-1 and Cox-2 in the melanoma cell lines BrafV600E WT and BrafV600E Cox1/2 knockout. Incomplete knockdown of Cox-2 is apparent in the control cell line with longer exposure times. **(D)** Prostaglandins detected by metabolomics analysis on whole rat liver. Data is presented as averaged fold change over nulliparous. **(E)** Prostaglandin E_2 and **(F)** Prostaglandin $F_{2\alpha}$ on biologic replicates from metabolomics analysis on whole rat livers. One-way ANOVA. *=p-value<0.05, **=p-value<0.01.

Evidence for increased liver weight by NSAID intervention during weaning-induced liver involution

We next sought to determine whether NSAID intervention delays or abrogates weaning-induced liver involution, both undesirable side effects. Female Balb/c mice were placed on a low-dose ibuprofen chow diet of either 150 mg (Ibu-L) or 300 mg (Ibu-H) ibuprofen/kg chow at time of pup weaning. Human dose equivalents are ~117 mg/day and ~234 mg/day, respectively[366]. Treatment was continued for 4 days (Inv4), or 6 days (N, Inv6) (Fig.4-2B). Inv6 mice on the Ibu-H diet weighed more at time of euthanasia compared to untreated controls (Fig.4-4A). Similarly, mice in the Inv6 group on either Ibu-L or Ibu-H diets had heavier livers compared to the untreated controls (Fig.4-4B). When normalized to body weight, we see that liver weight differences with ibuprofen were nullified, suggesting the weight increase was due to overall increased body weight (Fig.4-4C). Of interest, mice in the Inv4 group and in the nulliparous group showed no difference in body or liver weights (Fig.4-4A-B), however, sample size was smaller, impacting our ability to detect potential size differences. Taken together, these data suggest that a slight delay in body and liver weight loss post-weaning occurs with NSAID intervention, and should be followed up in more detail prior to making conclusions regarding the safety of NSAIDs during weaning-induced liver involution.

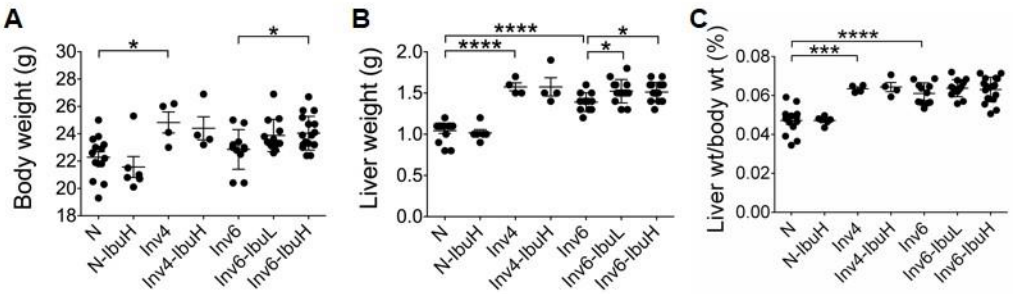

Figure 4-4: Ibuprofen diet may impact liver weight post-weaning

(A) Balb/c mouse body weight at time of euthanasia (IbuL= 150 mg Ibuprofen/kg chow; IbuH = 300 mg Ibuprofen/kg chow). **(B)** Balb/c mouse liver weight at time of euthanasia. **(C)** Balb/c mouse liver weight normalized to body weight at time to euthanasia. One-way ANOVA to compare across parity groups, Two-tailed Student's T-test to compare untreated to treated within each stage, *=p-value<0.05, ***=p-value<0.001, ****=p-value<0.0001.

Ibuprofen intervention during weaning-induced liver involution does not reduce deposition of pro-metastatic ECM proteins

Previous work has shown that tumor-promotional fibrillar collagen and TNC are deposited at increased rates during weaning-induced mammary gland involution[43,94,113], and this deposition is ameliorated by NSAID intervention[47,113]. The impact of NSAID treatment on ECM deposition during this tumor promotional window is likely essential to its' anti-tumor effect, as mammary involution ECM alone drives tumor progression in naïve mice[49]. We have previously shown deposition of collagen and TNC in the post-weaning liver[233], both of which have been shown to play important roles in pro-metastatic microenvironments[82,205,213,312]. Thus, we next investigated whether ibuprofen intervention reduced collagen and/or TNC levels in the post-weaning murine liver. We first performed reticulum silver stain to assess Collagen III levels in the mouse liver and found that ibuprofen may reduce collagen reticular fiber levels in livers from nulliparous hosts (Fig.4-5A-B). However, we observed no differences in reticular fiber stain in the involution groups (Fig.4-5A). Attempts to assess for Collagen I levels by IHC were unsuccessful. We next assessed the impact of NSAID treatment on the levels of TNC by immunoblot and found that TNC levels show a trend towards reduction in the Inv6 group with ibuprofen treatment compared to controls (Fig.4-5C-D). However, intra-animal variation was greater than inter-group variation, raising the possibility of assay limitations, such as inconsistent protein solubilization of high molecular weight ECM proteins between samples. In sum, these data do not suggest that NSAID intervention during the window of weaning-induced liver involution either reduces or increases deposition of Collagen III or the pro-metastatic ECM protein TNC. However, these data

need to be corroborated and expanded upon in additional studies utilizing larger sample sizes and more robust methods including quantitative targeted ECM proteomics as described in Chapter VI[94,372].

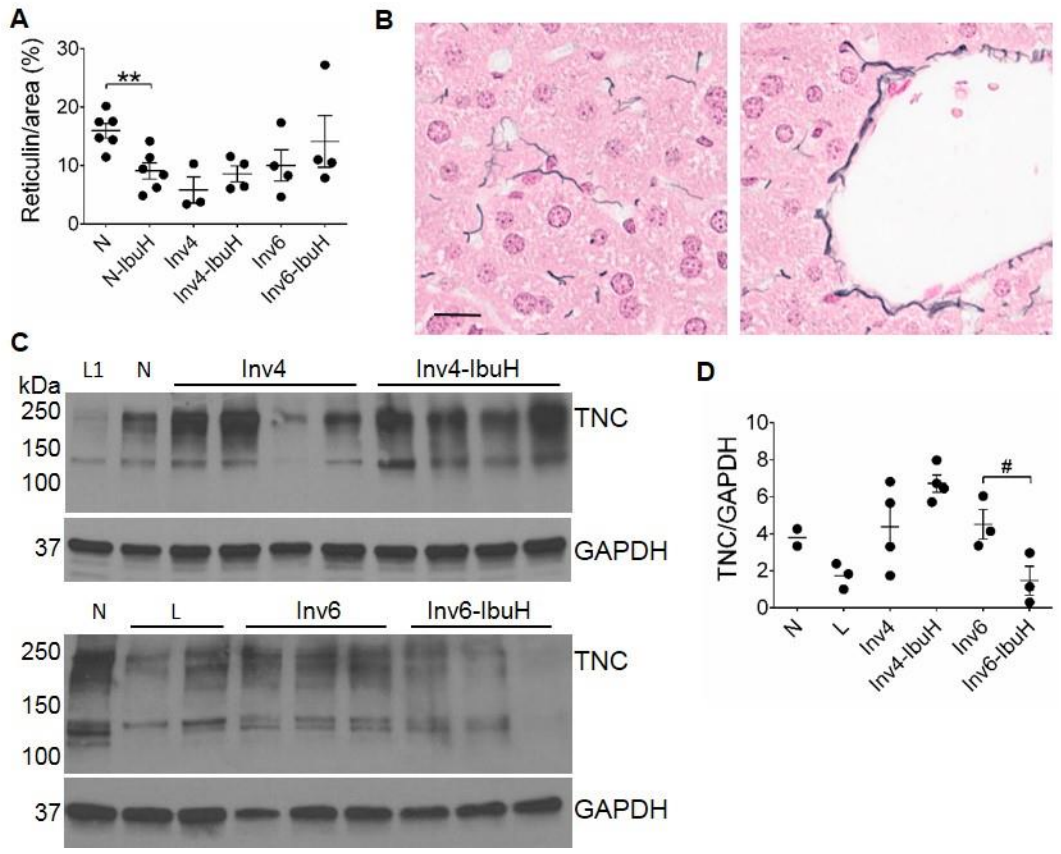

Figure 4-5: ECM changes with NSAID intervention during weaning-induced liver involution in rodents

(A) Quantification of reticulum silver stain in Balb/c mouse livers across the reproductive cycle, treated with Ibuprofen or vehicle for 4-6 days. **(B)** Representative images of reticulum stain on Balb/c mouse liver. Black stain is the reticular fiber network; scale bar=25 um. **(C)** Tenascin-C (TNC) immunoblots on mouse liver lysates from across the reproductive cycle; mice were treated with Ibuprofen or vehicle for 4-6 days. L1 is the lactation sample to which all other samples were normalized, all other samples are labeled based upon their respective group. **(D)** Densitometry of immunoblots from (B), normalized to GAPDH; data is presented as fold change over L1 in the upper blot. Two-tailed student's t-test to compare untreated to treated, within each stage. #=p-value 0.053, **=p-value<0.01.

Ibuprofen intervention modestly reduces Ly6C$^+$ monocyte influx during weaning-induced liver involution

I have previously shown that myeloid populations increase in abundance during weaning-induced liver involution by both flow cytometry and semi-quantitative IHC[233]. Thus, I assessed the impact of ibuprofen intervention on immune cell complexity in livers from both actively involuting and nulliparous mice, using 4-12 mice per group, with data compiled from three independent experiments (Fig.4-2B) (see Appendix B for immune cell marker descriptions). This analysis revealed the expected increase[233] in total leukocytes (CD45$^+$), macrophages (CD11b$^+$F4/80$^+$), and monocytes (CD11b$^+$Ly6C$^+$Ly6G$^-$), confirming prior work described in Chapter III (Fig.4-6A-C). However, the expected increase in neutrophils (CD11b$^+$Ly6C$^+$Ly6G$^+$) during weaning-induced liver involution was not observed (Fig.4-6D). With ibuprofen intervention at this dose we observed a reduction in total leukocytes, CD11b$^+$F4/80$^+$ macrophages, and Ly6C^{hi}Ly6G$^-$ monocytes (Fig.4-6A-C). Strikingly, we found that ibuprofen treatment increased neutrophils significantly in the nulliparous group (Fig.4-6D). Of note, liver flow cytometry analyses of myeloid populations were performed on a total of 4 independent NSAID studies (Fig.4-2B), however results from the 4th study showed a 50% reduction in expected macrophage numbers and warranted exclusion from analyses. We next sought to confirm flow cytometry data by semi-quantitative IHC for F4/80 to mark macrophages, Ly6C to mark monocytes and neutrophils, and Ly6G to mark neutrophils. This analysis revealed no appreciable impact of ibuprofen treatment on the abundance of these populations, despite the expected increase[233] in these populations during involution (Fig.4-6E-G). The discrepancy between flow cytometry and IHC data may be explained

by the fact that flow cytometry data is presented as percent of total cells following tissue processing and collagenase digestion, as opposed to area analysis as performed in IHC analyses. Another possibility is that single marker analyses by IHC are not sufficient to capture the same populations detected by flow cytometry. Analyses utilizing multiplex IHC platforms may be useful in further delineating and quantifying myeloid populations in these liver sections[109,373].

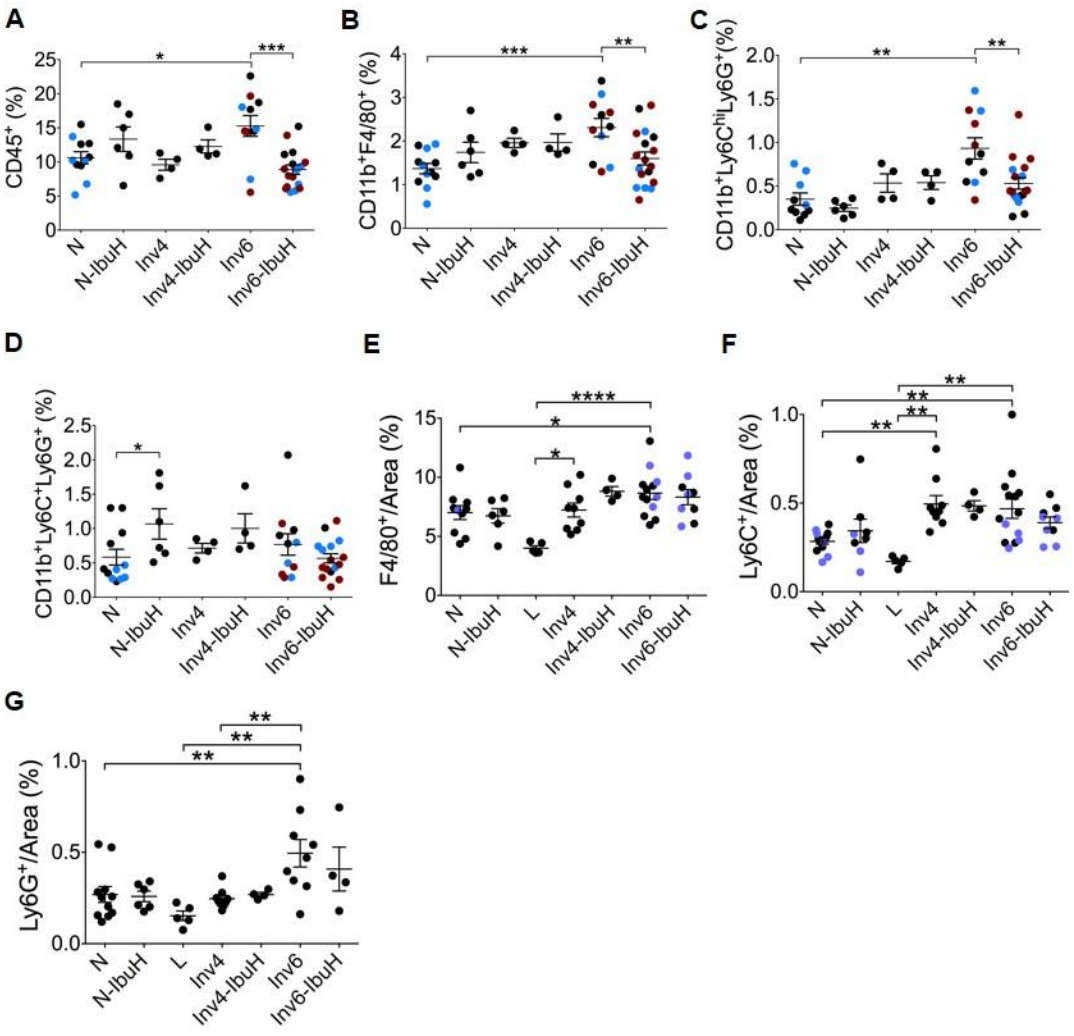

Figure 4-6: Ibuprofen intervention during weaning-induced liver involution may reduce myeloid cell influx

(A-D) Flow cytometric analysis of whole Balb/c mouse liver myeloid populations; data presented as percent of viable cells. Colors represent independent study data points. (**E-G)** IHC quantification of percent positive/area for single-color stained sections. Colors represent independent study data points. One-way ANOVA to compare N, Inv4, & Inv6; Two-tailed Student's T-test to compare untreated to treated within each stage. #=p-value<0.1, *=p-value<0.05, **=p-value<0.01, ****=p-value<0.0001.

My previous work has also shown that immune-suppressive FoxP3$^+$ T regulatory cells increase during weaning-induced liver involution (Appendix A). Thus, I assessed for CD8$^+$ cytotoxic T lymphocytes, CD4$^+$ T helper cells, and FoxP3$^+$ T regulatory cells by flow cytometry. We observed the expected increase in CD8$^+$ lymphocytes from Inv4 to Inv6, and an increase in CD4$^+$ lymphocytes at Inv6 compared to N and Inv4 groups (Appendix A) (Fig.4-7A-B). We also confirmed previously reported results that FoxP3$^+$ T regulatory cells increase at Inv6 compared to N and Inv4 groups (Fig.4-7C, see Appendix A). Quantification of lymphocytes following ibuprofen intervention revealed a modest reduction in CD8$^+$, CD4$^+$, and FoxP3$^+$ T regulatory cells (Fig.4-7A-C). Yet upon IHC confirmation of the FoxP3$^+$ T regulatory cell population showed no impact of ibuprofen on this population (Fig.4-7D). Because these data are from one study, replication of the results will be essential to understand how ibuprofen impacts lymphocyte populations in the liver during weaning-induced liver involution.

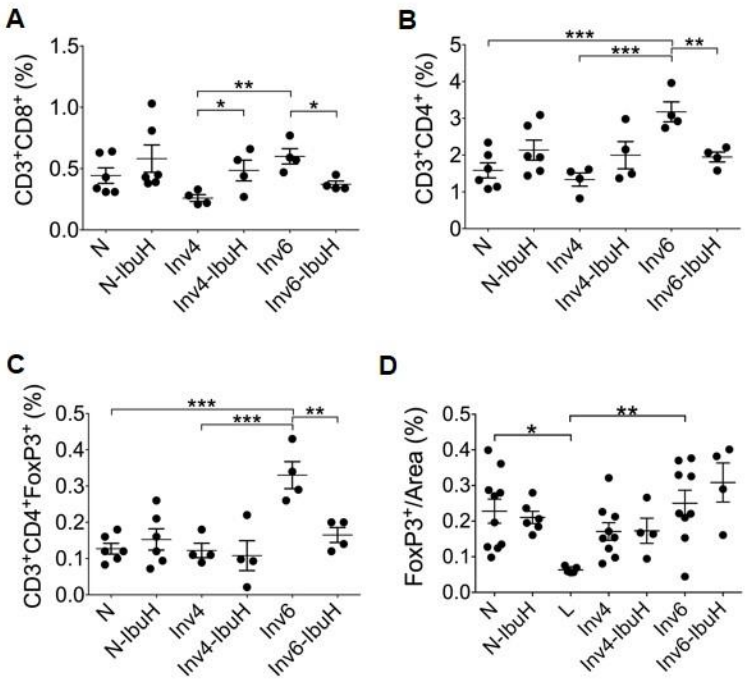

Figure 4-7: Ibuprofen intervention during weaning-induced liver involution may reduce T regulatory cells

(A-C) Flow cytometric analysis of whole Balb/c mouse liver leukocyte populations; data are presented as percent of total. **(D)** IHC quantification of FoxP3+ cells as percent positive/area. One-way ANOVA to compare N, Inv4, & Inv6; two-tailed student's t-test to compare untreated to treated within each stage. #=p-value<0.1, *=p-value<0.05, **=p-value<0.01, ***=p-value<0.001.

Low-dose ibuprofen treatment does not reduce the frequency of liver metastasis in an experimental metastasis model

We next sought to determine whether low-dose ibuprofen intervention during liver involution impacts risk for developing overt liver metastasis in an experimental intraportal liver metastasis model[238] (Fig.4-2C). Previous studies have shown that ibuprofen intervention with both murine D2A1 as well as the human breast cancer MCF10A-DCIS.com cells display reduced primary tumor growth in involution hosts when treated with NSAIDs[47] (data unpublished). For these studies the syngeneic D2A1 mammary tumor cell line was utilized. D2A1 tumor cells express Cox-1 but not Cox-2 *in vitro* (Fig.4-8A). Further, we do not see an upregulation of D2A1 Cox-2 levels in mammary tumors injected orthotopically at day 1 post-weaning and grown for 3 weeks (D2A1 T1 and T2 lanes, Fig.4-8A; tumor samples were derived from unpublished studies, Martinson et al., Schedin Lab). These data are consistent with any differential response to ibuprofen between nulliparous and involution groups being attributable to differences in Cox-2 activity within the tumor microenvironment. However, to further rule out any direct effect of ibuprofen on tumor cell viability or proliferation, we treated D2A1 mammary tumor cells with various concentrations of ibuprofen for 5 days *in vitro* (Fig.4-8B). We did not observe treatment related suppression of tumor cell number, data consistent with ibuprofen not having direct cytotoxic or anti-proliferative effects on D2A1 mammary tumor cells *in vitro*. We next injected 5,000 D2A1 tumor cells into Balb/c female mice at day 2 post-weaning via the portal vein, and overt liver metastasis was assessed at 5 weeks post-injection. As previously described[233], mice injected at involution day 2 were significantly more likely to present with overt liver metastasis

when compared to nulliparous controls (Fig.4-8C). However, low-dose ibuprofen intervention during the window of weaning-induced liver involution (maintained for 14 days post-weaning) did not impact risk for developing overt liver metastasis (Fig.4-8C). Despite no impact on risk of developing overt metastasis, we did detect a trend towards reduced tumor size in the involution treatment group as compared to untreated controls (Fig.4-8D). In sum, these data suggest that a subtle delay in metastatic tumor outgrowth may occur with ibuprofen intervention, but that overall risk of developing metastasis in the involution group was not impacted. These data extend previous studies showing that NSAID intervention specifically reduces primary tumor growth and dissemination, by suggesting that ibuprofen does not have an effect on abrogating later stages of the metastatic cascade within the liver. Importantly, these studies also suggest that ibuprofen does not contribute to an enhanced pro-metastatic tissue microenvironment within the involuting liver, suggesting use in the postpartum breast cancer setting will not aggravate liver metastasis risk.

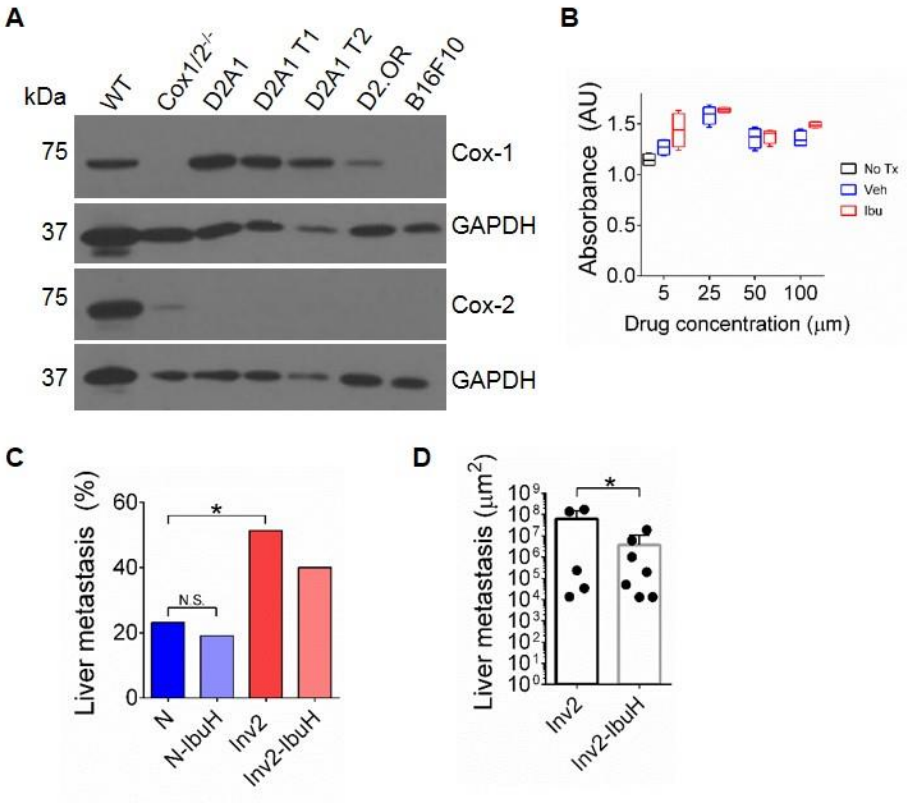

Figure 4-8: Low-dose ibuprofen intervention during weaning-induced liver involution does not reduce risk for liver metastasis

(A) Immunoblot for Cox-1 and Cox-2 in the melanoma cell lines BrafV600E WT, BrafV600E Cox1/2 knockout, the mammary tumor lines D2A1, D2A1 grown in isogenic mouse fat pads for 3 weeks (T1 and T2), D2.OR, and the murine melanoma line B16F10, all of which have varying levels of Cox-1 and Cox-2 expression levels. **(B)** Quantification of proliferation/viability of D2A1 mammary tumor cells grown in the presence or absence of varying concentrations of ibuprofen, as detected by crystal violet retention. **(C)** Frequency of overt liver metastasis detected at necropsy, 5 weeks post-injection of D2A1 mammary tumor cells; two-tailed Fisher's Exact test; Nullip, n=21; Nullip+Ibu, n=21; Inv2, n=20; Inv2+Ibu, n=25. **(D)** Tumor area analysis on H&E stained liver sections, average of 3 levels/liver; n=10 livers/grp; one-tailed student's t-test. N.S.= not significant, #=p-value<0.1, *=p-value<0.05.

Discussion and Future Directions

This work sought to understand the impact of NSAID intervention during the window of weaning-induced liver involution on the involution process, the establishment of the pro-metastatic niche, and on risk for liver metastasis. Our studies have focused on the liver because of my finding that the post-weaning liver involutes, increasing risk for liver metastasis in rodent models[233]. We hypothesized that NSAID intervention may abrogate pro-metastatic attributes of weaning-induced liver involution and thus reduce risk for developing liver metastasis in the post-weaning setting. In these studies, I have shown that low-dose ibuprofen intervention may marginally reduce some attributes of the pro-metastatic microenvironment established in the post-weaning liver, including TNC deposition as well as influx of $CD11b^{+}F4/80^{+}$ macrophages and $CD11b^{+}Ly6C^{hi}Ly6G^{-}$ monocytes. Using the intraportal injection metastasis model we observed no impact of low-dose ibuprofen treatment on frequency of metastasis in mice injected immediately post-weaning or in nulliparous controls. However, a trend toward reduced tumor size was observed with ibuprofen treatment in the postpartum group. Importantly, these data are consistent with the idea that NSAIDs, which target primary tumor growth and local invasion in rodent models of postpartum breast cancer[47,113] do not increase the risk for liver metastasis.

I observed increased Cox-2 protein levels in the rodent liver during lactation and involution. Hepatocytes degrade prostaglandins via β-oxidation[374,375], and β-oxidation is dramatically increased in the liver during lactation[230]. Thus, it is possible that the elevated lipid breakdown via β-oxidation may elicit increased Cox-2 activity during lactation to

compensate for potential eicosanoid lipid loss. I observed increased $PGF_{2\alpha}$ during lactation and involution. $PGF_{2\alpha}$ and its receptor, prostaglandin F receptor (FP), are known to increase in uterine tissues upon initiation of parturition, another dramatic tissue remodeling process[376-378]. In the liver, and other tissues, PGF may result as a downstream product of PGE and PGD via ketoreductase enzyme activity[379,380]. Interestingly, $PGF_{2\alpha}$ plays an important role in vasoconstriction and reduction of vessel permeability in the liver, data that may seem counter-intuitive when describing a pro-metastatic microenvironment[381]. However, other studies have shown that $PGF_{2\alpha}$ promotes tumor cell motility and invasion[382,383], and is upregulated during inflammation and hepatotoxicity[384-386], suggesting that high $PGF_{2\alpha}$ during early involution may contribute to the transient pro-metastatic niche established at this time. Further study of this prostaglandin may be of interest. Additionally, the expression of eicosanoid receptors in the liver during involution has not been assessed and may advance our understanding of how arachidonic acid metabolites impact the liver post-weaning.

Importantly, the increased body and liver weights observed at Inv6 in the treatment group compared to vehicle controls suggests that in-depth pathway analyses are necessary to fully understand how NSAIDs impact liver involution. Thus, conclusions regarding NSAID safety during the postpartum period should not be made until these studies are performed. The increased weight may be due to reduced hepatocyte apoptosis, a hallmark of weaning-induced liver involution and the proposed mechanism for weight loss during this window[233]. Prostaglandins have been shown to play cytoprotective roles in other tissues[320-323], thus the possibility that NSAIDs reduce involution-associated hepatocyte

apoptosis should be investigated. Furthermore, one study has identified that NSAIDs may promote weight gain in cancer patients with cachexia[387]. Future analyses should include robust gene expression profiling via RNASeq, as well as whole tissue lipidomics and eicosadomics[388]. Of potential interest, we are only just now beginning to understand involution-specific metabolic changes in the liver[233]. Preliminary data suggests a potential role for lipid deposition in liver involution (see Chapter VII) and arachidonic acid metabolism is intimately linked to regulation of cholesterol, bile acid, and β-oxidation[389,390]. These data suggest that the above mentioned omics analyses will be essential to understanding the impact of NSAIDs on major pathways altered during involution, including the anabolic-to-catabolic metabolism switch, lipid metabolism, cell death programs, and the nature of involution-associated inflammation (T_H1 vs. T_H2)[233].

As mentioned above, NSAIDs may have tissue-specific effects that are reflected in our assessment of the liver during weaning-induced involution. In states of liver pathology including cirrhosis, hepatocellular carcinoma, and liver metastasis, Cox-2 and PGE_2 are markedly elevated[361-365]. In rodent models of liver cirrhosis and fibrosis NSAID intervention has shown efficacy in reducing pathological ECM deposition and liver damage[362-364]. In contrast, a CCl_4 rat fibrosis model showed worsened fibrosis and increased hepatic stellate cell (HSC) activation when celecoxib treatment was included[391]. Other studies have shown a role for PGE_2 in inhibiting TGFβ induced collagen synthesis by HSC[392]. Thus, there are conflicting roles for NSAID intervention even within the same tissue, in a disease and model specific manner. In the data I have acquired during weaning-induced liver involution, we do see modest reductions in TNC

as well as myeloid and lymphoid populations assessed by flow cytometry with ibuprofen treatment in the Inv6 group. These data suggest that ibuprofen intervention may target similar pathways involved in ECM deposition and immune cell influx, such as TGFβ production by fibroblasts, as was shown in the mammary gland (Guo et al., submitted). However ibuprofen did not reduce liver metastasis in an intraportal injection model, suggesting that the effect of ibuprofen changes were either not sufficient or were offset by other as of yet unknown effects. Thus, the anti-tumor impact of ibuprofen intervention during the window of post-weaning involution in orthotopic fat pad models is not recapitulated in the liver.

The studies I have discussed in this thesis chapter require additional confirmatory experiments. For example, the impact of NSAID intervention on ECM deposition should be characterized in greater detail using quantitative ECM proteomics[94,303]. Studies have shown a role for Cox-2 in modulating collagen organization[47] (Guo et al., submitted), thus understanding the organization and proteolysis state of key ECM proteins in the liver may also be of interest. Of potential importance, flow cytometry data also shows that ibuprofen intervention may increase neutrophils in nulliparous rodent livers, a cell type known to have both anti-metastatic and pro-metastatic effects[173,175,176]. Thus, flow cytometry data should be followed up on in more detail. The phenotype and function of immune cells in the involuting liver, or how NSAIDs impact immune cell phenotype and function in the liver during involution, is not known. Of interest, NSAIDs have been implicated in shifting pro-tumor alternatively activated macrophages towards a more tumor-suppressive classically activated phenotype[336]. Thus, *ex vivo* phenotyping of

myeloid and lymphoid populations by flow cytometry and gene expression analyses, as well as functional assays following NSAID intervention are warranted.

Currently, no treatment options beyond standard of care regimens exist for postpartum breast cancer patients, despite the elevated risk for metastasis and death[9,23,316]. Our findings, using an experimental metastasis model, suggest that low-dose ibuprofen does not negatively impact liver metastasis, despite modest amelioration of pro-metastatic attributes of liver involution. Of potential relevance, our intraportal injection model bypasses early stages of the metastatic cascade known to be impacted by NSAID intervention, including tumor growth, immune evasion at the primary site, and invasion[47,289,324,336]. Thus, a lack of efficacy in reducing metastasis in this model may be due to NSAIDs preferentially impacting earlier stages of the metastatic cascade (described in Chapter I). Other studies have reported an NSAID effect on experimental metastasis models in which cells are injected directly into the circulation, however these studies utilized Cox-2 expressing cell lines[393,394]. A role for NSAIDs in impacting the metastatic site, and thus metastasis, using cell lines lacking Cox-2, such as the D2A1 cell line used in this work, had not previously been done to the best of our knowledge. Importantly, the ibuprofen dose we have utilized for the metastasis studies (300 mg ibuprofen/kg chow) is equivalent to 234 mgs of ibuprofen taken daily for 14 days (for a 65 kg/143.3 lbs person) according to the U.S. Food and Drug Administration (FDA) calculator for human dose equivalents[366]. Thus, it is reasonable to increase the daily dose for NSAID intervention in these rodent studies to the human dose equivalent of 400-1200 mgs daily (the cutoff for low-dose NSAIDs such as ibuprofen)[395]. However, it would be

worthwhile to ensure NSAID efficacy at the current or higher doses via PGE_2 metabolite (PGEM) ELISAs from liver tissues. Similarly, Cox inhibition has been shown to shunt arachidonic acid metabolism through the lipoxygenase pathway to favor leukotriene synthesis[396]. This will similarly be imperative to track, as increased leukotriene production by neutrophils has been shown to play an integral role in lung metastasis initiation[397]. It is also important to note that NSAIDs such as ibuprofen may result in adverse events including GI damage, and increase the risk for adverse cardiovascular events, particularly in high-risk populations[398,399]. These adverse events are thought to be due to disruption of Cox-1 maintenance of tissue homeostasis and epithelial cytoprotection in the gut, and due to an imbalance in prostaglandins (particularly TXA_2 and PGI_2) involved in platelet aggregation and vascular homeostasis[323,398,399]. These safety concerns should be evaluated in the context of the aggressive nature of postpartum breast cancer, where treatment options are lacking.

In addition to increasing the dose for future studies, it will be important to evaluate a Cox-2 specific NSAID such as celecoxib. Cox-2 specific inhibitors are relevant in our experimental modeling, as the D2A1 mammary tumor cell line expresses Cox-1, but not Cox-2, and thus complicates our interpretation of non-specific NSAID intervention on the microenvironment as opposed to direct action on the tumor cells. Alternatively, use of a mammary tumor cell line lacking Cox-2 *and* Cox-1 may be employed. Further, the trend towards a reduction in metastasis size in the Inv2 group with NSAID intervention suggests that metastatic outgrowth may be impacted more so than extravasation or seeding, however this result was very modest and needs to be validated. Use of GFP

expressing D2A1 mammary tumor cells in the Glowing Head mouse[297] allows for assessment of various stages of liver metastatic seeding and outgrowth (see Chapter VII) and may help elucidate the specific roles, if any, that NSAIDs have in limiting metastatic disease in the liver. The Glowing Head mouse is tolerized to both GFP and luciferase via constitutive expression in the anterior pituitary gland[297]. These immune competent mice facilitate use of tagged cell lines without eliciting aberrant immune responses to GFP or luciferase foreign antigen[297]. GFP tagged cell lines enable detection of single cells and micro-metastatic lesions in the tissue at early time-points post-injection, and thus efficacy of NSAIDs, as well as other targeted drugs, in targeting various stages of liver metastasis could be investigated. In sum, a role for NSAIDs in regulating postpartum breast cancer metastasis to the liver should be evaluated in greater detail, with higher doses, and with Cox-2 specific inhibitors for further evidence for safety as well as efficacy.

Although liver-specific increases in metastasis with a postpartum breast cancer diagnosis are a primary concern, site-specific analysis at other metastatic sites suggests that ~80% of metastatic postpartum breast cancer patients will also recur to lung, bone, or brain, as opposed to liver[233]. Importantly, tissue specific responses to NSAIDs exist, as previously discussed in the introduction of this chapter[355-358] and suggest that the blockade of pro-tumorigenic programs in the mammary gland may not be recapitulated in metastatic sites, as my data suggests here. Thus, the impact of NSAIDs on risk for developing lung, bone, and brain metastases should also be explored prior to recommending NSAIDs as a viable addition to standard of care treatment for postpartum breast cancer patients. To this end, studies to investigate the impact of ibuprofen treatment on the murine lung are underway.

Finally, recent studies have also shown that intervention with NSAIDs along with checkpoint blockade or anti-angiogenic therapies increases efficacy compared to single agent use in mammary, colon, and melanoma models[324,400]. These data suggest that pre-clinical postpartum breast cancer modeling of NSAID intervention may benefit from combinatorial treatment with chemotherapy and other experimental or approved therapeutics.

In sum, our data provide evidence that low-dose ibuprofen treatment during the window of weaning-induced liver involution may marginally abrogate some attributes of the pro-metastatic microenvironment established post-weaning. However, in an intraportal metastasis model, ibuprofen intervention did not reduce the high rates of liver metastasis observed in mice injected with mammary tumor cells post-weaning. These data simultaneously suggest that while low-dose ibuprofen therapy may not reduce pro-metastatic niche formation in the liver, it does not appear to increase risk for liver metastasis, an important finding in support of NSAID use to curtail primary tumor growth in postpartum patients. Our findings provide impetus for further investigations into the impact of low-dose, as well as higher doses of NSAIDs in reducing postpartum breast cancer metastasis.

Chapter V: Postpartum breast cancer represents an aggressive disease lacking biomarkers

Plan to publish

The work described in this chapter is currently being prepared for publication.

Contributions

Virginia Borges, Pepper Schedin, and I developed hypothesis and performed all data interpretation. Numerous Borges' and Schedin lab members and I performed extensive patient chart review. I specifically reviewed hundreds of patient records, performed analyses, and directed all meetings to discuss progress and next steps for the project. Solange Mongoue-Tchokote and Tomi Mori of the Knight Cancer Institute Biostatistics Shared Resource performed all time-to-metastasis analyses.

Abstract

A breast cancer diagnosis within 5 years of a pregnancy, termed postpartum breast cancer, imparts elevated risk for metastasis and death compared to nulliparous and pregnant young women's breast cancer patients. This increase in morbidity is independent of typical clinical prognostic factors, including biologic subtype, stage of disease, age, and year of diagnosis. In animal models, and in correlative human translational data, evidence suggests that the tissue remodeling programs of weaning-induced mammary gland and liver involution may, in part, contribute to the high risk for metastasis associated with a postpartum breast cancer diagnosis. In women, the underlying factors driving postpartum breast cancer metastasis have required the development of novel robust patient cohorts that include detailed parity and time-to-metastasis information. The work I describe in this chapter sought to better understand the high rate of metastasis observed in postpartum breast cancers in an expanded young women's breast cancer cohort from the University of Colorado (n=804). From this analysis we found that postpartum breast cancer patients are at increased risk for metastasis. In multivariate analysis of this data set, the difference remained statistically significant in stage II patients, but not in the overall cohort. This result differs from prior findings and on-going analysis of this data set in other projects. This difference may reflect the small numbers in individual experimental groups used in our data set and highlights the ongoing challenge of analyzing multiple parameters, even in a large dataset such as ours. Nonetheless, some interesting biology was noted in these results. The impact of stage on risk for metastasis was not due to delayed diagnoses as patients displayed similar tumor sizes regardless of parity status, as expected in a dataset not

including pregnant cases. However, we did observe an elevated frequency of postpartum breast cancer patients with tumor-involved lymph nodes at diagnosis. Further, when cases were stratified by presence or absence of estrogen receptor (ER), a clinically relevant prognostic and predictive factor in human breast cancer, several interesting observations were seen. Nulliparous women with ER positive and ER negative disease generally fared better than their postpartum breast cancer peers. Women with postpartum ER positive breast cancer had very poor long-term prognosis and women with postpartum ER negative disease had a rapid and dismal risk for metastatic recurrence. These data suggest an additive interaction of postpartum status and biologic subtype of the cancer on poor prognosis, and may also predict resistance to hormonal therapy in ER positive postpartum breast cancer. In sum, postpartum breast cancer patients display a high risk for lymph node involvement at diagnosis, and metastatic recurrence after diagnosis. This result is dependent upon stage of disease at diagnosis in this data set, which requires further evaluation. Importantly, we have shown for the first time that metastatic recurrence occurring in young women's breast cancer is significantly different depending on parity and tumor estrogen receptor status, with strong clinical implications and added avenues of research as a result.

Introduction

As described in detail in Chapter I, postpartum breast cancer (PPBC), defined as a diagnosis of breast cancer within 5 years of a pregnancy, exhibits a ~3-fold increased risk for metastasis and death when compared to nulliparous patients[7-9]. This risk is specific to patients diagnosed postpartum, as patients diagnosed during pregnancy, and treated for

their disease appropriately, have similar prognoses as nulliparous patients[10]. Older age at first birth correlates with increased risk of developing PPBC[15-17], and more women are opting to delay child bearing until later[18-20]. Thus, the current estimation that ~10,000 – 16,000 new postpartum breast cancer patients are diagnosed yearly in the United States[9,13,14] will likely increase[21-23].

Preclinical models of postpartum breast cancer have identified that the poor prognosis of postpartum breast cancer is likely due to the pro-tumorigenic microenvironment of the postpartum involuting mammary gland[15,42,43,47,49,114] (Submitted, Guo et al., and Schedin Lab, data unpublished). These results are also discussed at length in Chapter I. Briefly, mammary gland involution promotes tumor growth and higher incidence of both lymph node and distant metastasis in comparison to tumors orthotopically implanted into nulliparous mice[42,47,114]. A similar breast involution process occurs in women postpartum[77]. Further, recent work I have completed suggests that weaning-induced liver involution establishes a pro-metastatic microenvironment, which may further promote metastasis in postpartum breast cancer patients (see Chapter III)[233]. In fact, in a multi-institute cohort of young women's breast cancer patients I found that postpartum breast cancer patients are at increased risk for liver-specific metastasis, but not other common sites of breast cancer metastasis, when compared to nulliparous patients (see Chapter III)[233]. These data suggest that metastasis may be promoted by tissue remodeling events both at the primary tumor site and at the secondary liver metastatic site in postpartum breast cancer patients. Despite these findings, there is a paucity of studies addressing the high risk of metastasis in young women's breast cancer cohorts, and PPBC is still

considered an under-recognized subset of breast cancer[23]. Based on previous work, PPBC patients have a distant recurrence probability of ~30%[9], suggesting that a better understanding of what drives the high risk of metastasis associated with a postpartum diagnosis is urgently needed.

The current clinical standards for assessing breast cancer prognosis and treatment regimens include determination of biologic subtype, tumor grade, and stage of disease. Immunohistochemistry (IHC) staining for estrogen receptor (ER), progesterone receptor (PR), and human epidermal growth factor receptor 2 (Her2) are the primary markers utilized to define biologic subtype as Luminal A (ER+, PR+, Her2-), Luminal B (ER+, PR+/-, Her2+/-), Her2+ (ER-, PR-, Her2+), or triple negative (ER-, PR-, Her2-). ER+ Luminal A breast cancers exhibit a better prognosis than ER+ Luminal B and ER- breast cancers, including a reduced risk for metastasis, largely due to lower proliferation rates and the availability of anti-estrogen therapeutics such as tamoxifen[401-405]. Previous studies have identified similar frequencies of the good prognostic Luminal A and poor prognostic Luminal B, Her2+, and triple negative subtypes across parity groups in young women's breast cancer[9]. These data suggest that an increase in poor prognostic tumor intrinsic biologic subtypes in younger women is not the cause for the high rate of metastasis observed in postpartum breast cancers. Tumor stage takes into account tumor size, the number of lymph nodes positive for disease, and whether metastatic disease is present. Of note, weaning-induced mammary gland involution is characterized by lymphangiogenesis, and preclinical postpartum breast cancer models display a high rate of peri-tumoral lymphatic vessel density, invasive tumor foci within lymphatics, and

increased lymph node metastasis compared to nulliparous controls[114]. Importantly, postpartum breast cancer patients diagnosed within 2 years of a pregnancy are more likely than nulliparous patients to have lymph node metastasis, and postpartum breast cancer tumors are characterized by elevated peri-tumor lymphatic vessel density[114]. However, previous work has shown that the high rate of metastasis in postpartum breast cancers is not explained by the stage of disease at diagnosis[9], suggesting that increased lymph node metastasis may occur independent of increased tumor size. Further, preclinical studies have found that risk for metastasis is greater in mice injected with tumor cells post-weaning compared to nulliparous controls, after normalizing for tumor size (a potential surrogate for tumor stage)[47,49]. These data suggest that postpartum breast cancers display an increased propensity for lymph node metastasis despite similar tumor size.

In this chapter, I describe work that I led, which sought to explore the relationship between parity status, risk for metastasis, and other clinical parameters in a young women's breast cancer cohort from the University of Colorado. We began by performing an expanded retrospective analysis of the University of Colorado (UC) cohort previously published by Callihan et al[9]. We hypothesized that PPBC patients will continue to display increased risk for metastasis, independent of other poor prognostic indicators. Women who were diagnosed with breast cancer at age ≤45, between 1981 and 2014, were selected for based on availability of data regarding parity status and long-term follow-up (n=804). In this study, we characterized clinical and pathological features of young women's breast cancer including biologic subtype, grade, stage, tumor size, lymph node

involvement, and treatment. We also assessed time-to-metastasis in this young women's breast cancer cohort, stratified by parity status, stage of disease, and estrogen receptor status.

Materials and Methods

Human Sample Collection

All studies were approved by University of Colorado (UC) and Oregon Health and Science University (OHSU) Institutional Review Boards (IRB). Patient histories were obtained from n=804 women. Only patients aged 19-45 with known parity status at the time of diagnosis and with follow-up data including distant recurrence information available were included in analysis. Nulliparous patients were defined as patients who never completed a birth. Parous patients were defined based on time from last birth to diagnosis and stratified as a diagnosis <5, 5-<10, or 10+ years following a pregnancy, for some analyses PPBC <5 and 5-<10 were combined into a single group of PPBC<10. Patients who were pregnant at time of diagnosis were excluded from any analysis, except in Figure 4 where the percentage of patients in this young women's breast cancer cohort was determined based on parity status at time of diagnosis. Patient data were collected and managed using REDCap electronic data capture tools hosted at the UC Anschutz Medical Campus.

Clinical and demographic data analysis

Young women's breast cancer cohort clinical, demographic, and treatment data are summarized in Table 5-1. To test for intergroup differences Chi-square, Fisher's Exact,

One-way ANOVA, or Two-way ANOVA tests was utilized and is indicated in the relevant table or figure legend. All analyses were performed using Prism 6 Software (Graphpad, La Jolla, CA). A p-value of <0.05 was considered statistically significant.

Time-to-metastasis analysis

Metastatic recurrence was identified as the occurrence of metastasis after breast cancer diagnosis. Patients with no evidence of a metastatic recurrence at the end of follow-up were censored at the time of their last contact. Patients diagnosed with stage IV disease, with unknown or missing stage at diagnosis, or with unknown year of diagnosis were excluded from the analyses, resulting in n=705 patients for young women's breast cancer analysis and n=518 for stratification by ER status, as PPBC 10+ cases were excluded from this analysis and some older cases had no receptor data available. Nulliparous cases with an incomplete pregnancy were included in analyses, as preliminary analysis suggested no effect of an incomplete pregnancy (data not shown). Kaplan-Meier method was used to estimate the probability of metastasis. Kaplan-Meier curves were generated and the Log-rank test was performed to assess differences between time-to-metastasis probabilities across groups. Multivariate Cox Regression was performed to determine risk factors associated with metastasis. Hazard ratios and their 95% confidence intervals were estimated. Factors accounted for in the overall young women's breast cancer analysis were biologic subtype, stage, age, and year of diagnosis. For subsequent stage stratified analyses only biologic subtype, age, and year of diagnosis were adjusted for. For comparison of nulliparous and PPBC<10 patients by ER status we adjusted for stage,

age, and year of diagnosis. All analyses were performed using SAS, version 9.4 (SAS Institute Inc., Cary, NC). A p-value of <0.05 was considered statistically significant.

Table 5-1: University of Colorado Young Women's Breast Cancer Cohort, Stage I-III

Table 1 | University of Colorado Young Women's Breast Cancer Cohort, Stages I-III

	Nulliparous (*N*=221) No. (%)	PPBC <5 years (*N*=175) No. (%)	PPBC 5-<10 years (*N*=153) No. (%)	PPBC 10+ (*N*=156) No. (%)	Chi-square test P-value
Mean age at diagnosis	36.79	35.53	38.54	41.26	**<0.0001***
Biologic subtype					
Luminal A (ER+, PR+, Her2 neu-)	85 (36.17%)	74 (40.44%)	70 (41.42%)	61 (36.75%)	
Luminal B (ER+, PR+/-, Her2 neu+)	34 (14.47%)	22 (12.02%)	29 (17.16%)	21 (12.65%)	
Her2 neu positive (ER-, PR-)	16 (6.81%)	15 (8.20%)	13 (7.69%)	11 (6.63%)	0.46
Triple negative	33 (14.04%)	35 (19.13%)	17 (10.06%)	28 (16.87%)	
Missing Her2 neu	40 (17.02%)	20 (10.93%)	16 (9.47%)	27 (16.27%)	
Missing ER or PR	16 (6.81%)	10 (5.46%)	11 (6.51%)	10 (6.02%)	
Other	11 (4.68%)	7 (3.83%)	13 (7.69%)	8 (4.82%)	
Estrogen status					
ER+	144 (65.16%)	114 (65.14%)	104 (67.97%)	97 (62.18%)	
ER-	63 (28.51%)	53 (30.29%)	40 (26.14%)	53 (33.97%)	0.75
Missing	14 (6.34%)	8 (4.57%)	9 (5.88%)	6 (3.85%)	
Histologic grade					
Grade I	25 (11.31%)	11 (6.29%)	14 (9.15%)	22 (14.10%)	
Grade II	71 (32.13%)	51 (29.14%)	55 (35.95%)	61 (39.10%)	0.09
Grade III	106 (47.96%)	96 (54.86%)	73 (47.71%)	57 (36.54%)	
Missing	19 (8.60%)	17 (9.71%)	11 (7.19%)	16 (10.26%)	
Tumor size					
≤2.0 cm	112 (50.68%)	86 (49.14%)	63 (41.18%)	75 (48.08%)	
>2.0—≤5.0 cm	71 (32.13%)	57 (32.57%)	56 (36.60%)	54 (34.62%)	0.41
>5.0 cm	17 (7.69%)	17 (9.71%)	19 (12.42%)	20 (12.82%)	
Missing	21 (9.50%)	15 (8.57%)	15 (9.80%)	7 (4.49%)	
Stage					
I	89 (40.27%)	46 (26.29%)	46 (30.07%)	52 (33.33%)	
II	99 (44.80%)	91 (52.00%)	66 (43.14%)	64 (41.03%)	**0.01**
III	33 (14.93%)	38 (21.71%)	41 (26.80%)	40 (25.64%)	
AJCC Nodal Status					
0	125 (56.56%)	62 (35.43%)	72 (47.06%)	77 (49.36%)	
1	51 (23.08%)	58 (33.14%)	43 (28.11%)	40 (25.64%)	
2	10 (4.53%)	12 (6.86%)	15 (9.80%)	14 (8.97%)	**0.01**
3	9 (4.07%)	8 (4.57%)	7 (4.58%)	7 (4.49%)	
Unknown	26 (11.77%)	35 (20.00%)	16 (10.46%)	18 (11.54%)	
LN Positive (AJCC Status + LN#)					
Yes	85 (38.46%)	102 (58.29%)	75 (49.02%)	71 (45.51%)	
No	130 (58.82%)	70 (40.00%)	76 (49.67%)	82 (52.56%)	**0.01**
Unknown	6 (2.72%)	3 (1.71%)	2 (1.31%)	3 (1.92%)	
Year of Diagnosis					
1980-1998	46 (20.81%)	30 (17.14%)	19 (12.42%)	50 (32.05%)	
1999-2004	62 (28.05%)	32 (18.29%)	48 (31.37%)	40 (25.64%)	**<0.0001**
2005-present	113 (51.13%)	113 (64.57%)	86 (56.21%)	66 (42.31%)	
Chemotherapy					
Yes	137 (61.99%)	132 (75.43%)	100 (65.36%)	93 (59.62%)	
No	40 (18.10%)	15 (8.57%)	25 (16.34%)	22 (14.10%)	**0.02**
Missing	44 (19.91%)	28 (16.00%)	28 (18.30%)	41 (26.28%)	
Radiation Therapy					
Yes	99 (44.80%)	76 (43.43%)	74 (48.37%)	57 (36.54%)	
No	58 (26.24%)	45 (25.71%)	31 (20.26%)	41 (26.28%)	0.38
Missing	64 (28.96%)	54 (30.86%)	48 (31.37%)	58 (37.18%)	
Metastasis					
Yes	30 (13.58%)	36 (20.57%)	30 (19.61%)	27 (17.31%)	0.22**
No	187 (84.62%)	137 (78.29%)	117 (76.47%)	123 (78.85%)	
Unknown	4 (1.81%)	2 (1.14%)	6 (3.92%)	6 (3.85%)	

PPBC, Postpartum Breast Cancer; No., number of patients per group; ER, estrogen receptor; PR, progesterone receptor; DCIS, ductal carcinoma in situ; cm, centimeter

***One-way ANOVA**

****p=0.045 by One-tailed Fisher's Exact Test between Nullip and PPBC<5**

Results

Patients diagnosed up to 10 years postpartum have elevated risk for metastasis

We first sought to determine whether previously published findings that showed increased risk for metastasis in patients diagnosed within 5 years of a pregnancy[9] hold true in an extended cohort from which the published work was derived. Table 5-1 displays the clinical characteristics of this University of Colorado (UC) young women's breast cancer cohort. Patients were selected for based on quality of parity data and follow-up data necessary to test our hypothesis that PPBC patients are at elevated risk for metastasis compared to nulliparous women with breast cancer. Stage 0 and IV patients were excluded from time-to-metastasis analyses and thus are not included in Table 5-1. We assessed time-to-metastasis amongst nulliparous and postpartum young women's breast cancer patients (women diagnosed within 5 years of a pregnancy, PPBC<5; within 5-<10 years of a pregnancy, PPBC 5-<10; and 10 or more years after a pregnancy, PPBC 10+) and found that both PPBC<5 and PPBC 5-<10 patients exhibited a greater risk for metastasis compared to nulliparous patients (Cox Regression, p=0.008 and 0.006, respectively; Fig.5-1, Table 5-2). PPBC 10+ patients displayed an intermediate risk for metastasis when compared to nulliparous patients (Cox Regression, p=0.13; Fig.5-1, Table 5-2). Multivariate analysis, adjusting for biologic subtype, stage, age at diagnosis, and year of diagnosis, revealed a trend towards increased risk for metastasis in PPBC<5 patients (Cox Regression, p=0.13) as well as significantly increased risk for PPBC 5-<10 patients (Cox Regression, p=0.04), compared to nulliparous women with breast cancer (Table 5-2). PPBC 10+ patients were not at increased risk for metastasis compared to nulliparous patients (Cox Regression, p=0.19; Table 5-2). Stage of disease at diagnosis

remained a statistically significant clinical factor in multivariate analysis (Table 5-2, Cox Regression, $p<0.0001$) for metastasis-free survival in a step-wise analysis (data not shown). Thus, we assessed the relationship between parity status and metastasis-free survival in stage I, II, and III patients, independently (Fig.5-2A-C, Table 5-3). Analysis of Stage I cases revealed that postpartum breast cancer patients exhibit a trend towards increased risk for metastasis compared to nulliparous patients, after adjusting for biologic subtype, age, and year of diagnosis (Fig.5-2A and Table 5-3; Cox Regression, $p=0.06$). PPBC 5-<10 and PPBC 10+ groups showed no differnce in time-to-metastasis compared to nulliparous patients (Table 5-3). The risk for metastasis with a postpartum diagnosis remained significantly increased in stage II patients even after multivariate analysis (Fig.5-2B and Table 5-3; Cox Regression, $p=0.008$). Intriguingly the risk for metastasis was significantly increased in PPBC<5 (Cox Regression, $p=0.04$) and PPBC 5-<10 (Cox Regression, $p=0.0008$) patients, and exhibited a trend towards being increased even in PPBC 10+ patients (Cox Regression, $p=0.07$). In contrast, stage III patients exhibited a high risk of metastasis irregardless of parity status (Fig.5-2C, Table 5-3; Cox Regression, $p=0.56$), although the numbers in the subset are relatively small (range: n=33-41/group). Taken together, these data show that in this cohort, diagnosis with stage I or II postpartum breast cancer is an independent prognostic indicator for metastasis. Further, early diagnoses in nulliparous patients confer a relatively low-risk for metastasis. However, the finding that stage III young women's breast cancer has a high risk of metastasis regardless of parity status, albiet with small numbers and therefore to be interpreted cautiously, does suggest a threshold effect of stage, either due to late

diagnoses or highly aggressive cancer biology (Her2 and triple negative breast cancers) with early metastatic potential, in young women's bresat cancers.

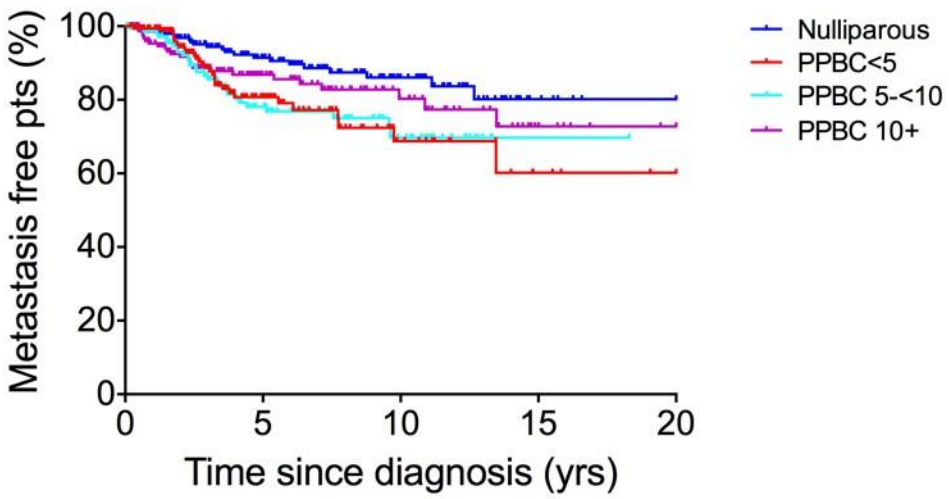

Figure 5-1: Young women diagnosed with postpartum breast cancer are at increased risk for metastasis

Time to metastasis Kaplan-Meier curve of young women's breast cancer cohort (n=705) (Log Rank Test, P=0.02, see Table 2). Analysis excluded patients with stage 0, stage IV, or stage unknown disease, and/or an unknown year of diagnosis (n=221 Nullip; n=175 PPBC<5; n=153 PPBC 5-<10; n=156 PPBC 10+).

Table 5-2: University of Colorado time-to-metastasis survival analysis

Table 2 | University of Colorado time-to-metastasis survival analysis					
UC Cohort Statistical Analysis					
	Univariate P-value (a)	**Hazard Ratio [95% CI]**	**Multivariate Overall P-value**	**Multivariate P-value***	**Hazard Ratio [95% CI]**
Overall	**0.02**				
Nulliparous (n=221)	Reference	Reference		Reference	Reference
PPBC<5 (n=175)	**0.008**	2.14 [1.22-3.76]	0.23	0.13	1.58 [0.88-2.84]
PPBC 5-<10 (n=153)	**0.006**	2.24 [1.27-3.94]		**0.04**	1.83 [1.02-3.28]
PPBC 10+ (n=156)	0.13	1.57 [0.87-2.82]		0.19	1.52 [0.82-2.82]
Stage II vs. I			**<0.0001**	0.34	1.32 [0.75-2.35]
Stage III vs. I				**<0.0001**	3.46 [1.98-6.04]
Her2+ vs. Lum A				**0.007**	2.43 [1.27-4.64]
Lum B vs. Lum A			**0.02**	0.94	1.03 [0.51-2.08]
TN vs. Lum A				**0.01**	2.13 [1.20-3.77]
Unknown vs. Lum A				0.54	1.19 [0.68-2.07]
Age at Dx			**0.04**	**0.04**	0.96 [0.92-1.00]
Year of Dx (2005+ vs. 2005-)			0.40	0.40	0.82 [0.51-1.30]

(a)Log Rank test

*** Multivariate logistic regression, adjusted for biologic subtype, stage, age at diagnosis, and year of diagnosis**

95% CI = 95% confidence interval; UC = University of Colorado; TN = triple negative; Dx = diagnosis

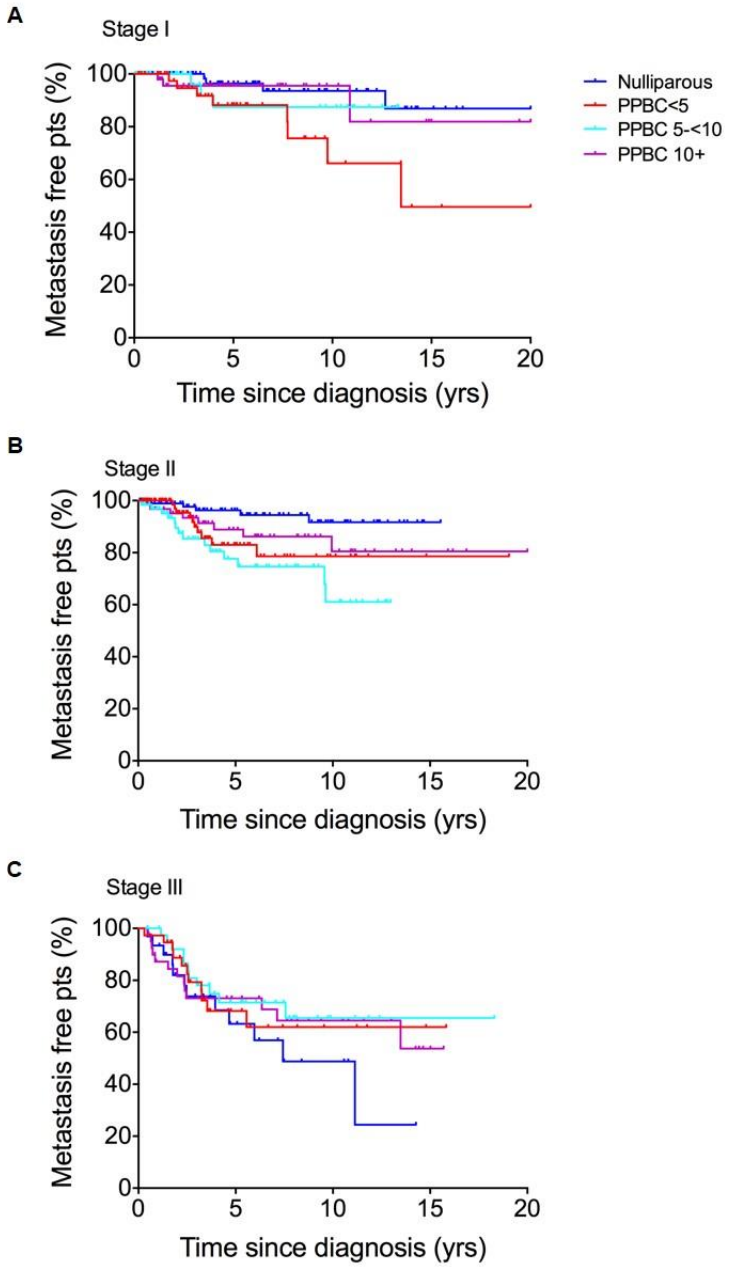

Figure 5-2: Risk for metastasis in young women's breast cancer patients, stratified by stage

(A) Time-to-metastasis Kaplan-Meier curve of Stage I young women's breast cancer patients (n=233) (Log Rank Test, P=0.06). **(B)** Time-to-metastasis Kaplan-Meier curve of stage II young women's breast cancer patients (n=320) (Log Rank Test, P=0.006). **(C)** Time-to-metastasis Kaplan-Meier curve of Stage III young women's breast cancer patients (n=152) (Log Rank Test, P=0.61). Analyses excluded patients with unknown stage of disease and/or unknown year of diagnosis. Group sample sizes are recorded in Table 3.

Table 5-3: University of Colorado time-to-metastasis survival analysis, stratified by stage

Table 3 | University of Colorado time-to-metastasis survival analysis, stratified by stage				
UC Cohort Stage I Statistical Analysis				
	Univariate P-value (a)	**Hazard Ratio [95% CI]**	**Multivariate P-value***	**Hazard Ratio [95% CI]**
Overall	0.06		0.30	
Nulliparous (n=89)	Reference	Reference	Reference	Reference
PPBC<5 (n=46)	**0.02**	4.27 [1.28-14.23]	0.06	3.35 [0.94-11.95]
PPBC 5-<10 (n=46)	0.62	1.46 [0.33-6.52]	0.42	1.91 [0.40-9.11]
PPBC 10+ (n=52)	0.36	2.03 [0.45-9.17]	0.22	2.64 [0.57-12.29]
UC Cohort Stage II Statistical Analysis				
	Univariate P-value (a)	**Hazard Ratio [95% CI]**	**Multivariate P-value***	**Hazard Ratio [95% CI]**
Overall	**0.006**		**0.008**	
Nulliparous (n=99)	Reference	Reference	Reference	Reference
PPBC<5 (n=91)	**0.03**	3.21 [1.09-9.42]	**0.04**	3.22 [1.08-9.55]
PPBC 5-<10 (n=66)	**0.002**	5.24 [1.89-14.57]	**0.0008**	5.98 [2.11-16.93]
PPBC 10+ (n=64)	0.12	2.45 [0.80-7.50]	0.07	2.91 [0.90-9.40]
UC Cohort Stage III Statistical Analysis				
	Univariate P-value (a)	**Hazard Ratio [95% CI]**	**Multivariate P-value***	**Hazard Ratio [95% CI]**
Overall	0.61		0.56	
Nulliparous (n=33)	Reference	Reference	Reference	Reference
PPBC<5 (n=38)	0.40	0.70 [0.31-1.59]	0.22	0.55 [0.22-1.41]
PPBC 5-<10 (n=41)	0.20	0.58 [0.26-1.33]	0.23	0.60 [0.26-1.38]
PPBC 10+ (n=40)	0.37	0.70 [0.32-1.54]	0.61	0.80 [0.35-1.85]

(a)Log Rank test

*** Multivariate logistic regression, adjusted for biologic subtype, age at diagnosis, and year of diagnosis**

95% CI = 95% confidence interval; UC = University of Colorado

We next sought to explore the relationship between stage of disease at diagnosis, parity status, and risk for metastasis, to understand whether postpartum breast cancers may be impacted by delayed diagnoses. We stratified patients by parity status and stage, or parity status and tumor size and did not observe any significant differences between PPBC and nulliparous groups (Fig.5-3A-C). Further, when we assessed tumor size within only stage I, II, or III patients and stratified by parity status we saw no difference between groups (Fig.5-3D-F). These data suggest that patients in this cohort were not being diagnosed with larger tumors in parous versus nulliparous groups. Therefore, a skewing of delayed diagnosis due to recent pregnancy is not a factor in risk for metastasis in postpartum breast cancers in our dataset. Importantly, we did find increased frequency of patients presenting with lymph node-positive disease at time of diagnosis in the PPBC<5 group in stage II analyses and in the full cohort (stage I-III) (Fisher's Exact, $p=0.04$ and $p=0.0002$, respectively) (Fig.5-3G-H, Table 5-1). This finding confirms previous work that found an enrichment for lymph node-positive diagnoses in patients diagnosed within 2 years of a pregnancy compared to nulliparous patients[114]. Further, as would be expected based on lymph node postivity, we found that postpartum patients were much more likely to be treated with chemotherapy (Fig.5-3I, Table 5-1). Yet, postpartum breast cancer patients are still at higher risk for recurrence, suggesting that a postpartum diagnosis may also predict relative resistence to chemotherapy, which merits further exploration. In sum, these data suggest that the high risk for metastasis in PPBC is not due to delays in diagnosis, despite stage having a significant impact on multivariate analyses. Instead, these data show that even with similar frequencies of stage and tumor sizes across groups, PPBC<5 patients were more likely to have progressed to node-positive disease

and implicate a need for early detection strategies for young postpartum women. Our data also suggest that stage remains an important influence in outcomes in the setting of postpartum breast cancer, and that lymph node positivity and treatment outcomes merit further research to identify predictive significance of parity status in addition to its prognostic influence. Finally, our data also suggest that delays in diagnosis in young women's breast cancer, regardless of parity status, results in a high risk for metastatic recurrence. Previously unreported, we found that the high risk for metastasis persists in patients diagnosed up to 10 years following a pregnancy, particularly when assessing stage II patients. In sum, our data confirm that postpartum breast cancer patients represent a high risk subset of young women's breast cancer.

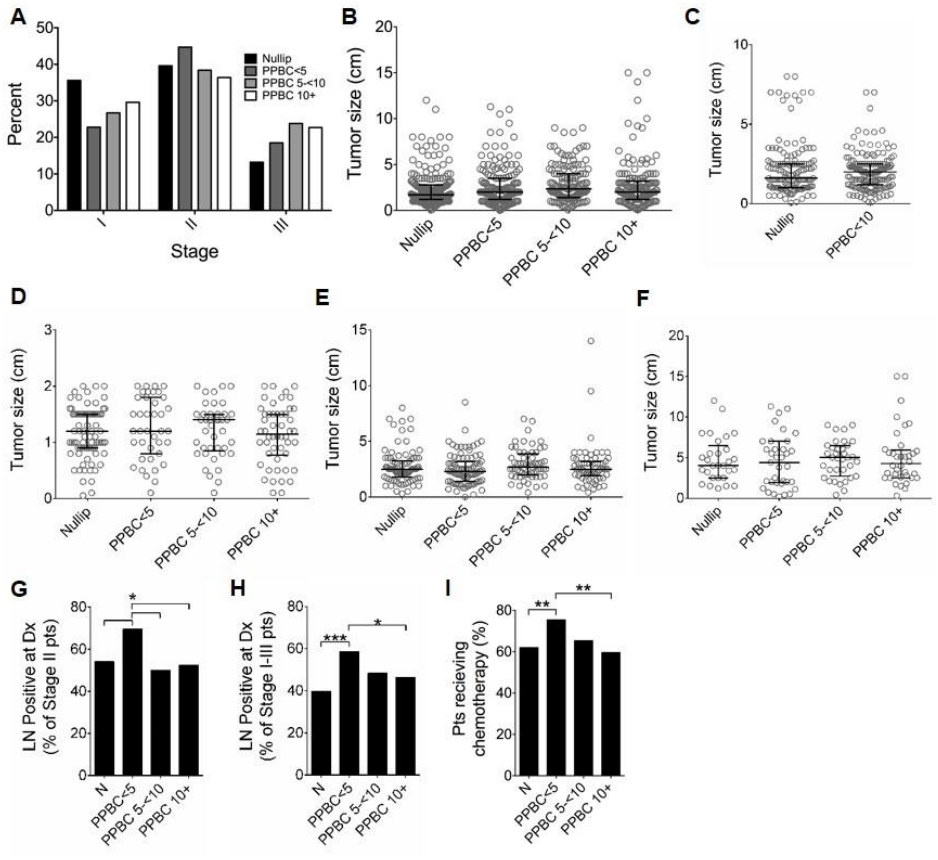

Figure 5-3: Lymph node status at time of diagnosis, but not stage or tumor size, is significantly higher in PPBC<5 patients

(A) Stage of disease; data are presented as percentage of patients diagnosed with stage I, II, or III across parity groups, stage 0 and IV patients excluded from analysis; (Two-way ANOVA, no significant differences across parity groups). **(B)** Tumor size at diagnosis in the University of Colorado young women's breast cancer cohort, stratified by parity status. Stage 0, IV, and unknown stage excluded (One-way ANOVA, no significant differences). **(C)** Tumor size in stage I and II node negative patients (Two-tailed Student's T-test, P=0.32). **(D-F)** Tumor size at diagnosis in stage I patients **(D)**, stage II **(E)**, and stage III **(F)** (One-way ANOVA, no significant differences). **(G)** Percent of stage II patients diagnosed with node-positive disease, per group (Nullip, n=98; PPBC<5, n=92; PPBC 5-<10, n=66; PPBC 10+, n=63) (Two-tailed Fisher's Exact Test, *=p-value<0.05). **(H)** Percent of stage I-III patients diagnosed with node-positive disease, per group (Nullip, n=216; PPBC<5, n=174; PPBC 5-<10, n=151; PPBC 10+, n=153) (Two-tailed Fisher's Exact Test, *=p-value<0.05, ***=p-value<0.001). **(G-H)** Node status was determined by American Joint Committee on Cancer (AJCC) guidelines and/or when patients presented with ≥1 positive lymph node at diagnosis when AJCC nodal status was not available, year of diagnosis unknown patients are included and unknown node status patients are excluded. **(I)** Percentage of patients treated with chemotherapy stratified by parity status (Nullip, n=216; PPBC<5, n=174; PPBC 5-<10, n=151; PPBC 10+, n=153) (X^2 Test, **=p-value<0.01).

Postpartum breast cancers with elevated risk for metastasis account for two-thirds of young women's breast cancer

Our finding that risk for metastasis may be elevated in postpartum patients diagnosed up to 10 years after a pregnancy suggests that a larger percentage of young women's breast cancer patients may be at elevated risk for distant recurrence, and thus should be included in the definition of high-risk PPBC. In fact, in this University of Colorado cohort, a full 45% of young breast cancer patients in this cohort have a postpartum diagnosis within 10 years of a pregnancy (Fig.5-4). Approximately 25,000 young women were diagnosed with breast cancer at <45 years of age in 2015[13,14], of which 45%, or 11,250 cases, are predicted to be PPBC<10 based upon our cohort demographics. Within our UC cohort 40-45% of PPBC<10 patients are diagnosed as stage II and translates to ~5000 young women diagnosed each year in the U.S. who are at particularly high risk for metastasis (Table 5-1).

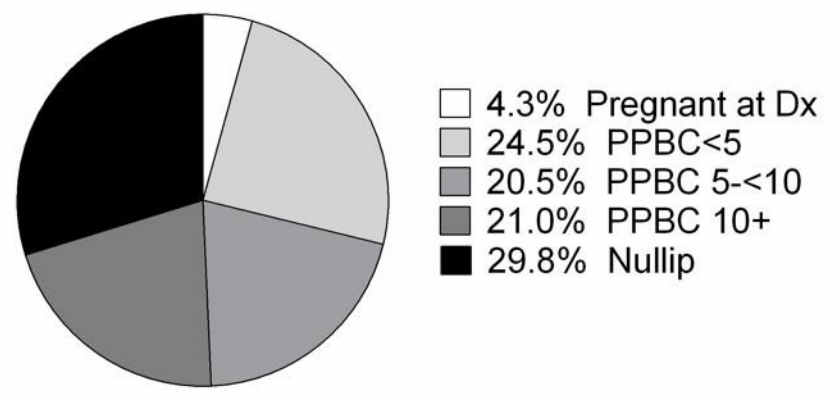

Figure 5-4: Postpartum breast cancer patients at highest risk for metastasis account for 45% of young women's breast cancer

Parts of whole analysis for the University of Colorado Young Women's Breast Cancer cohort, including the subset of patients diagnosed while pregnant. Patients diagnosed within 10 years of a pregnancy account for 45% of all patients (n=36 Pregnant at diagnosis [Dx]; n=206 PPBC<5; n=172 PPBC 5-<10; n=176 PPBC 10+; n=250 Nullip).

ER status has important clinical implications in postpartum breast cancers

To further investigate how tumor intrinsic properties such as biologic subtype impact risk of metastasis in young women's breast cancer, we compared metastasis-free survival in nulliparous and postpartum patients diagnosed within 10 years of a pregnancy (PPBC<10) and stratified cases based on ER status of the cancer. Several clinically important observations were identified. As expected, nulliparous women with ER positive and ER negative disease fared better than their postpartum breast cancer peers with similar ER disease (Fig.5-5A, Table 5-4). Suprisingly, women with postpartum ER positive breast cancer had a short term [year 0-5] risk of metastasis that was as poor as their nulliparous ER negative peers (Cox Regression, p=0.56), and an ongoing rate of developing metastatic disease at a consistent frequency through year 15, to the point that their ultimate likelihood of developing metastasis was dismal, at almost 40%. PPBC<10 patients diagnosed with ER negative disease were more likely to develop a distant recurrence compared to PPBC<10 patients diagnosed with ER positive disease (Cox Regression, p=0.01) and compared to nulliparous patients with ER positive (Cox Regression, p=0.002). The stage II analysis revealed that nulliparous patients with ER negative disease exhibit a trend towards *reduced* risk for metastasis when compared to PPBC<10 patients with ER positive disease (Fig.5-5B, Table 5-4) (Cox Regression, p=0.07). Stage II analysis also showed that PPBC<10 patients with ER negative disease displayed increased risk for metastasis compared to nulliparous patients with ER positive or ER negative breast cancer (Cox Regression, p=0.006 and p=0.01, respectively). Overall, women with postpartum ER negative disease had high short term risk for metastastatic recurrence, but if no recurrence had occurred by year 5, their risk

subsequently declined dramatically demonstating a plateau effect. Conversely, by 15 years post diagnoses, the risk for metastasis in ER positive PPBC <10 catches up to the ER negative PPBC<10 cohort and is equally poor. This observation is not currently understood by medical oncologists providing treatment for younger women with breast cancer. These data suggest that an additive interaction between postpartum status and ER status of the cancer impacts prognosis of postpartum breast cancer. Further, the data reveal the novel insight that ER positive postpartum breast cancers may be at greater risk for therapeutic resistance to hormonal therapy. These data highlight the concerning nature of later recurrences in young mothers with ER positive disease, which, despite a period of latency, still occur when the patients are of a relatively young age [35-50 years]. Thus, our findings emphasize the importance of considering long-term hormonal therapy in treating ER positive postpartum breast cancers, as well as an ongoing need to evaluate treatment resistance mechanisms in young women's breast cancer. With relatively small numbers, we found no significant difference in risk between nulliparous women with ER negative breast cancer (defined as <1% of cells positive for ER) compared to nulliparous women with ER positive disease, even after adjusting for stage, age at diagnosis, and year of diagnosis (Fig.5-5A, Table 5-4; Cox Regression, p=0.12). This finding merits further investigation, as it implies that the poor prognosis of early stage ER negative disease in younger women with breast cancer may be driven by the postpartum cases.

In sum, we have found that postpartum breast cancer patients display a high risk for lymph node involvement at diagnosis and metastatic recurrence after diagnosis. The high risk for metastasis is dependent upon stage of disease at diagnosis in this data set, which

requires further evaluation. Importantly, we have shown that risk for metastasis in young women's breast cancers is significantly different depending on parity and tumor ER status, with strong clinical implications and added avenues of research as a result.

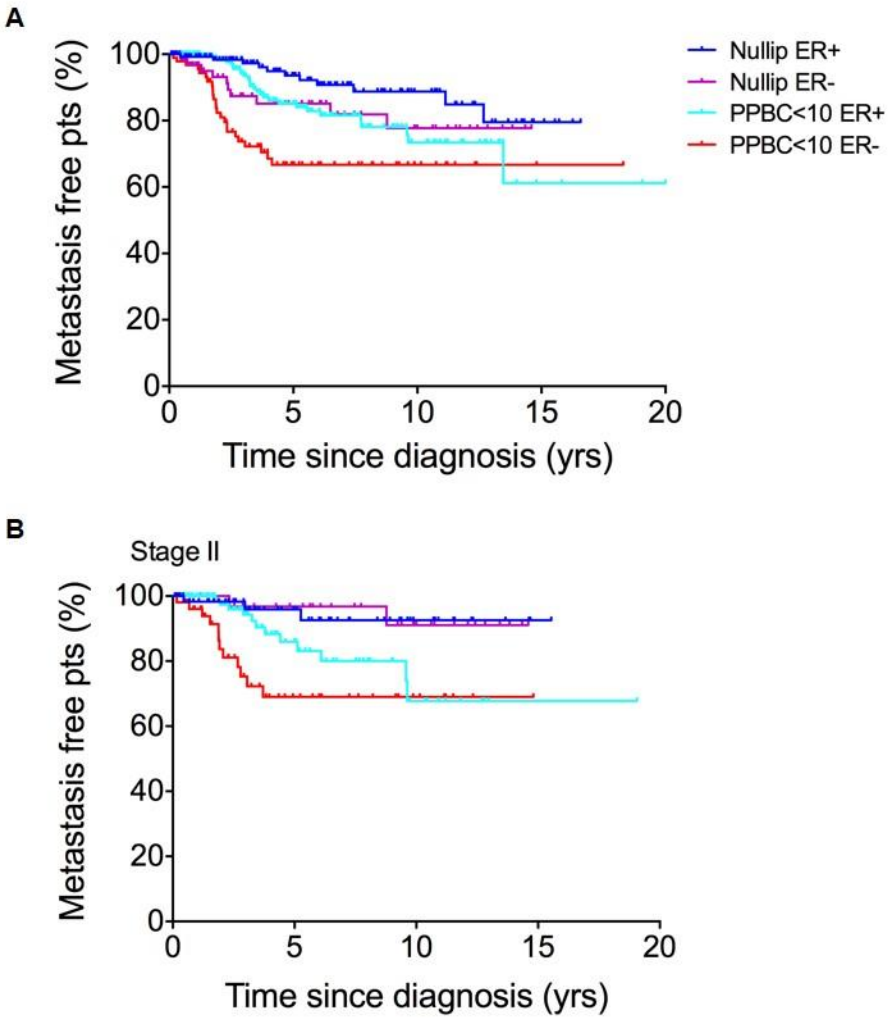

Figure 5-5: Time-to-metastasis differs across parity groups dependent upon ER status

(A) Time to metastasis Kaplan-Meier curve of a young women's breast cancer cohort, stratified by parity status (nulliparous vs. PPBC<10) and estrogen receptor status (ER+/-) (n=144 Nullip ER+; n=63 Nullip ER-; n=218 PPBC<10 ER+; n=93 PPBC<10 ER-) (Log Rank Test, P=0.0002, see Table 4). Analysis excluded patients with stage 0, stage IV, or stage unknown disease, and/or an unknown year of diagnosis. **(B)** Time to metastasis Kaplan-Meier curve for stage II young women's breast cancer patients from (A) (n=66 Nullip ER+; n=32 Nullip ER-; n=102 PPBC<10 ER+; n=52 PPBC<10 ER-) (Log Rank Test, P=0.006, see Table 4). Analysis excluded unknown year of diagnosis.

Table 5-4: University of Colorado time-to-metastasis survival analysis, stratified by ER status

Table 4 | University of Colorado time-to-metastasis survival analysis, stratified by ER status				
UC Cohort Statistical Analysis, stratified by ER status				
	Univariate P-value (a)	**Hazard Ratio [95% CI]**	**Multivariate P-value***	**Hazard Ratio [95% CI]**
Overall	**0.0002**		**0.01**	
Nullip, ER+ (n=144)	Reference	Reference	Reference	Reference
Nullip, ER- (n=63)	0.11	1.99 [0.85-4.70]	0.12	1.99 [0.83-4.74]
PPBC<10, ER+ (n=218)	0.06	1.96 [0.97-3.95]	0.20	1.59 [0.78-3.23]
PPBC<10, ER- (n=93)	**<0.0001**	4.36 [2.13-8.93]	**0.002**	3.22 [1.54-6.75]
Nullip, ER- vs. PPBC<10, ER+	0.96	1.02 [0.49-2.10]	0.56	1.25 [0.59-2.64]
PPBC<10, ER- vs. Nullip, ER-	**0.04**	2.19 [1.04-4.58]	0.21	1.62 [0.76-3.47]
PPBC<10, ER- vs. PPBC<10, ER+	**0.004**	2.23 [1.29-3.84]	**0.01**	2.03 [1.16-3.55]
UC Cohort Statistical Analysis, Stage II patients only, stratified by ER status				
	Univariate P-value (a)	**Hazard Ratio [95% CI]**	**Multivariate P-value****	**Hazard Ratio [95% CI]**
Overall	**0.002**		**0.007**	
Nullip, ER+ (n=66)	Reference	Reference	Reference	Reference
Nullip, ER- (n=32)	0.93	0.93 [0.16-5.56]	0.82	0.81 [0.13-4.88]
PPBC<10, ER+ (n=102)	0.09	3.04 [0.86-10.79]	0.06	3.32 [0.93-11.80]
PPBC<10, ER- (n=52)	**0.005**	6.25 [1.76-22.16]	**0.006**	5.84 [1.64-20.74]
Nullip, ER- vs. PPBC<10, ER+	0.12	0.31 [0.07-1.37]	0.07	0.24 [0.05-1.11]
PPBC<10, ER- vs. Nullip, ER-	**0.01**	6.73 [1.50-30.21]	**0.01**	7.22 [1.60-32.50]
PPBC<10, ER- vs. PPBC<10, ER+	0.08	2.06 [0.92-4.58]	0.17	1.76 [0.78-3.97]

(a)Log Rank test

*** Multivariate logistic regression, adjusted for stage, age at diagnosis, and year of diagnosis**

**** Multivariate logistic regression, adjusted for biologic subtype, age at diagnosis, and year of diagnosis**

95% CI = 95% confidence interval; UC = University of Colorado; ER = estrogen receptor

Discussion

The work I have described here extends upon previously published findings that postpartum patients diagnosed up to 5 years after a pregnancy are at increased risk for metastasis and death compared to nulliparous patients[9]. Univariate analysis of the expanded cohort revealed that postpartum patients diagnosed up to 10 years after a pregnancy are at elevated risk for metastasis compared to nulliparous patients, with results remaining significant in multivariate analysis of the PPBC<5 group for stage II patients. We found that both stage I and II PPBC 5-<10 patients were at increased risk for metastasis compared to nulliparous breast cancer patients regardless of biologic subtype, age at diagnosis, or year of diagnosis. However, it is important to note that small sample size in some of these cohorts may impact the results, thus highlighting the challenge of this type of statified outcomes research in young women's breast cancer. Our assessment of time-to-metastasis in young women's breast cancer stratified by stage further identified that, regardless of parity status, stage III young women with breast cancer exhibit a high risk for metastasis regardless of parity status, suggesting that delays in diagnosis are a major issue in young women's breast cancer, as has been previously described[406]. Our data suggest that postpartum breast cancers are at increased risk for lymph node and distant metastasis despite being diagnosed at similar stage, with similar tumor size, and having been treated with chemotherapy at a greater frequency.

The data discussed in this chapter does not suggest that delayed diagnoses explain the high risk for metastasis observed in the postpartum breast cancers, as the frequency of stage at diagnosis and tumor sizes are similar across parity groups. However, we did find

that postpartum breast cancer patients diagnosed within 5 years of a pregnancy are more likely to present with disease that has spread to lymph nodes, as was previously shown for PPBC<2 patients[114]. Positive lymph node status at time of diagnosis is a poor prognostic indicator in breast cancer[402]. Of potential interest, previous work has shown that the involuting mammary gland and breast are characterized by increased lymphatic vasculature, and in a tumor setting, postpartum breast cancers have elevated lymphatic vessel density[114]. These findings could potentially explain the increased lymph node metastasis observed in postpartum patients. The high rate of lymph node positivity at diagnosis in PPBC<5 patients suggests a more aggressive disease that may disseminate to lymph nodes and distant sites earlier than disease in the nulliparous setting, despite other prognositic clinical parameters being similar between the two groups.

Our data supports previous findings that PPBC patients have significantly worse overall survival rates[7-9]. Work I have recently completed shows that postpartum breast cancers display site-specific metastatic preference for the liver, and a trend towards reduced preference for the bone, when compared to nulliparous breast cancer patients (see Chapter III)[233]. Importantly, breast cancer pateints diagnosed with liver metastasis have median survival rates of ~4.5 months[244], whereas patients with bone metastasis tend to live ~5 years after metastatic recurrence is diagnosed[248]. Taken together, these findings suggest that PPBC patients diagnosed within 10 years of a pregnancy are at increased risk for metastasis, with a skewing to the liver as a metastatic site, likely adding to the observed reduced of overall survival rates[7-9]. Larger cohorts of young women's breast

cancer patients, with intact parity, site of metastasis, and follow-up data are required to further explore this hypothesis.

When we assess time-to-metastasis in nulliparous versus PPBC<10 patients stratified by ER status we find that nulliparous patients fare better than their postpartum counterparts with both ER positive and ER negative disease, although the difference is most pronounced in the ER negative subset. In fact, the prognosis of women with nulliparous ER negative disease in our cohort appears unusually good, with risk for metastasis similar to that of ER positive nulliparous pateints. This finding merits further evaluation. Most notable, PPBC<10 patients with ER positive and ER negative disease have a recurrence risk that approaches 40%, with the ER positive group developing metastases over a long time period, while ER negative patients recur rapidly in the first 5 years after diagnosis. These data highlight an under-recognized risk for metastatic disease in young mothers with ER positive breast cancer and suggest a predictive value of parity status for both ER positive and ER negative disease. Future analyses to understand the efficacy of anti-estrogen therapy in treatment of postpartum breast cancer is warranted. Furthermore, our finding in this cohort that postpartum breast cancers have a high risk for metastasis despite increased frequency of chemotherapeutic intervention suggests that additional therapeutics for this vulnerable population are needed. Because of the strong link between tissue remodeling events that occur post-weaning in the mammary gland and liver it may be of interest to pursue therapeutics specifically targeting the microenvironment[15,43,47,94,113,114,233,407].

One strength of these studies is our robust cohort with >800 patient records that have complete parity and metastasis/follow-up data recorded. Our analysis of time-to-metastasis in this cohort more than doubled the sample size previously utilized to assess risk for metastasis in multivariate analyses (n=705 in this study, compared to n=324 in the previously published study[9]). However, we are just beginning to understand the mechanisms underlying the high risk for metastasis with a postpartum breast cancer diagnosis. Further, biomarkers for detecting young women's breast cancer patients at high risk for metastasis are lacking[23]. It is important to note that genetic profiling of breast cancers has identified distinct molecularly defined subtypes, including several luminal subtypes, as well as Her2+, basal-like, and claudin-low subtypes, all based upon differential gene expression patterns[408-412]. To date this level of genetic profiling has not been performed for this cohort. Determining the frequency of molecular subtypes in young women's breast cancer may be extremely informative in understanding high risk subsets of patients. It would also be of great worth to perform gene expression profiling on samples from our young women's breast cancer cohort, and with the advent of RNASeq techniques for formalin-fixed paraffin embedded tissue blocks, this has become a possibility[413,414]. Further, quantitative ECM proteomics (described in Chapter VI) may be of interest in understanding differences in ECM composition in young women's breast cancer, and may aid in identification of novel ECM biomarkers. Relevant to this aim, one group has shown the ability of ECM-targeted proteomics to identify differences in breast cancer ECM signatures in highly- vs. lowly-metastatic xenografts in mice[415]. Finally, studies have identified immune biomarkers, including a combined high $CD68^+$ macrophage, high $CD4^+$ T cell, and low $CD8^+$ T cell ratio in predicting breast cancer

recurrence-free survival[104]. Recent advancements in multiplex IHC platforms facilitate the multi-marker panels that may be necessary to identify immune biomarkers in young women's breast cancer[109]. Thus, further investigations into the gene expression, ECM, and immune complexities of young women's and postpartum breast cancers are warranted.

In conclusion, our findings suggest that the current definition of PPBC is conservative and may not accurately capture the entirety of patients at highest risk for metastasis. PPBC 5-<10 patients have similar if not greater risk for metastasis than PPBC<5 patients in our young women's breast cancer cohort. We also note that stage II postpartum breast cancer patients, and postpartum patients that have ER negative disease represent particularly high-risk populations.

Chapter VI: Quantitative Extracellular Matrix Proteomics to Study Mammary and Liver Tissue Microenvironments[3]

Published Manuscript

Goddard ET, Hill RC, Barrett A, Betts C, Guo Q, Maller O, Borges VF, Hansen KC, Schedin P. Quantitative extracellular matrix proteomics to study mammary and liver tissue microenvironments. Int J Biochem Cell Biol, 2016 Dec; 81(Pt A):223-232. doi:10.1016/j.biocel.2016.10.014

Contributions

Pepper Schedin, Kirk Hansen, and I were responsible for hypothesis development, conceptual design, and all data interpretation. Ryan Hill, Alexander Barrett, and Kirk Hansen developed proteomics methodology and preformed proteomics on rodent samples, and prepared data for analyses. I performed all data analysis with assistance from Ryan Hill and Alexander Barrett. I wrote the manuscript with Pepper Schedin.

[3] The majority of this chapter was re-printed with permission from the International Journal of Biochemistry and Cell Biology (Goddard ET, Hill RC, Barrett A, Betts C, Guo Q, Maller O, Borges VF, Hansen KC, Schedin P. **Quantitative extracellular matrix proteomics to study mammary and liver tissue microenvironments.** *Int J Biochem Cell Biol*, doi:10.1016/j.biocel.2016.10.014 (2016))

Introduction

Mechanistic studies of rodent mammary gland development reveal requisite roles for ECM in mammary epithelial cell proliferation, differentiation, and cell-death decisions[46,416-420]. In fact, pioneering investigations identified the functional unit of the epithelium as the cell plus its adjacent ECM[421,422]. These findings shifted studies aimed at understanding epithelial cell function from a cell-intrinsic to a cell-stroma focus[423]. Investigation of the relationship between tissue ECM and epithelium has also been applied to the study of breast cancer, with important gains[424].

The functions of matrix proteins in breast cancer have been assessed primarily using single, purified ECM proteins or by admixing ECM proteins of interest with commercially available Engelbreth-Holm Swarm (EHS) matrix that is enriched in laminin-111[425-428]. Such studies identified specific ECM protein-integrin interactions, matrix stiffness, and matrix architecture as critical mediators of tumor cell function[91,429-431]. Single ECM molecules, including collagen I, fibronectin, and tenascin-C, display clear roles in promoting tumor cell proliferation, motility, and invasion[80,91,296,432,433]. ECM roles in breast cancer risk are also suggested, as high mammographic breast density, indicative of elevated collagen content in the breast, increases epithelial cell transformation by 4- to 6-fold[434,435]. The relationship between fibrillar collagen I and cancer incidence and progression have been corroborated in rodent models, where high collagen I content in the murine mammary gland results in a ~3-fold increase in tumor formation as well as increased lung metastasis[78]. There is also evidence that distinct ECM proteins at secondary sites of metastasis impact metastatic

success[82,197,201,205,210,211,213,312,436]. In particular, prominent work in the metastasis field has shown roles for lung and liver fibronectin in supporting disseminated tumor cell seeding and growth in murine models of colon, mammary, and pancreatic adenocarcinomas[197,201]. Cumulatively, these studies implicate ECM in all stages of cancer progression, from initiation to metastatic outgrowth at secondary sites.

The reductionist approach of investigating single ECM protein-cell interactions *in vitro*, or manipulating single proteins *in vivo*, while revealing, does not replicate the complex ECM milieu of an *in vivo* tissue microenvironment. One example of the importance of tissue-specific ECM is found in rodent models of postpartum breast cancer. In these models, whole tissue mammary ECM, as opposed to a single protein, has been shown to determine metastatic outcomes[49]. Relevance to women is implicated, as postpartum breast cancer patients have a ~3-fold increased risk for metastasis and death[7-9], a poor prognosis attributed, in part, to ECM remodeling during postpartum breast involution[15]. Specifically, weaning-induced mammary gland involution is characterized by deposition and partial proteolysis of radially aligned fibrillar collagen, fibronectin, and tenascin-C[47,49]. Further, evidence that involution-specific mammary ECM promotes metastasis has been demonstrated in xenograft models. Tumor cells co-injected with mammary ECM isolated from involuting glands grew larger tumors within the mammary fat pad and metastasized at much higher rate compared to tumor cells co-injected with mammary ECM isolated from nulliparous rats[49]. These data highlight the need to better understand how physiologic cues as well as disease states impact ECM composition and abundance,

and provide compelling rationale for developing improved quantitative methodologies for ECM proteomics.

Robust characterization of tissue-specific ECM complexity and abundance has been largely hindered by technical challenges in the field of proteomics. For unbiased biochemical identification of proteins, mass spectrometry provides a highly sensitive approach. However, improvements to proteomic approaches for the study of tissue-specific ECM have been hindered by the proteolytic- and solubilization-resistant properties of ECM proteins, which are often high molecular weight, extensively glycosylated, and covalently cross-linked. While significant advances in ECM protein identification have occurred recently[415,437-439], proteomics approaches still largely fail to adequately quantify many ECM proteins despite their high abundance in tissues[303]. We have recently established methods for improved tissue solubilization and absolute protein quantification to interrogate tissue-specific ECM. This approach permits quantitative assessment of a subset of ECM proteins that represent >99% of spectra matching to core ECM and ECM-affiliated proteins identified in mammary gland and liver by global proteomics[303,440,441]. To gain insight into primary breast cancer and site-specific metastasis, we utilize our quantitative proteomics approach to compare rat mammary gland and liver, as the liver is a common and lethal site of breast cancer metastasis. We also investigate ECM composition and abundance changes in the mammary gland across a reproductive cycle. Our objective was to gain insight into potential roles of ECM in the pro-tumorigenic window of weaning-induced mammary gland involution. This targeted ECM proteomics approach is anticipated to facilitate improved *in vivo* characterization,

and *in vitro* reconstruction of epithelial cell microenvironments for use in cancer, stem cell, and regenerative biology.

Methods

Rodent studies

The OHSU Institutional Animal Care and Use Committees approved all animal procedures. Sprague-Dawley female rats (Harlan), 70 +/-3 days of age, were bred and tissues collected as described[46,95]. Snap frozen, pulverized lymph node-free mammary gland [n=5/group for nulliparous, late pregnancy (day 18-21), lactation, involution days 2, 4, 6, 8, and 10, and four weeks post-weaning (regressed)] and gallbladder-free liver [n=6 for nulliparous] were used for ECM-based QconCAT proteomic analyses. Pooled samples generated from the above mentioned biologic replicates were utilized for global proteomics.

Imaging

Tissue H&E and trichrome stains were scanned on an Aperio ScanScope AT, image analysis was performed using Aperio ImageScope software (Leica Biosystems).

Sample preparation for proteomic analysis

Approximately 5 and 50 mgs of fresh frozen mammary gland and liver, respectively, was pulverized in liquid nitrogen and processed as described[303]. Briefly, tissue samples were homogenized in CHAPS buffer with 2 mm glass beads using mechanical agitation (Bullet Blender®, Next Advance) on power 8 for 3 minutes. Following homogenization, tissue samples were sequentially extracted using high-speed centrifugation after vortexing in

high salt CHAPS buffer, 6 M urea, and CNBr buffers resulting in 3 fractions for each sample: (1) cellular fraction, (2) soluble ECM, and (3) insoluble ECM (Figure 6-1). All fractions were ran by liquid chromatography-tandem mass spectrometry (LC-MS/MS) and liquid chromatography-selected reaction monitoring (LC-SRM). LC-SRM analysis was done on n=5 mammary gland/group and n=6 liver samples, with n=7 technical replicates. LC-MS/MS analysis was done on pooled biological replicates for an n=1/group.

Detergent/chaotrope removal & protein digestion

Sample cleanup and protein digestion was carried out as described[442]. QconCAT standards were spiked into each sample prior to filter assisted sample prep (FASP) to yield values of 100 fmol $^{13}C_6$ QconCAT/5 µg of protein for LC-SRM injections. Equal volumes of biological replicates were combined for LC-MS/MS analysis.

Liquid chromatography tandem mass spectrometry & data analysis

Samples were analyzed by LC-SRM and LC-MS/MS as described[442]. Equal volumes from each post-digestion sample were combined and injected every third run and used to monitor technical reproducibility. Skyline was used for method development and to extract the ratio of endogenous light peptides to heavy internal standards from LC-SRM data for protein quantification as described[305]. LC-MS/MS data was processed as previously described[303]. Limits of detection, quantification, and dynamic range were determined for each peptide as previously described[303] and provided in Supplementary Table 1 (please see published manuscript for Supplementary Tables 1-4[94]). Principal

component analysis (PCA) and partial least squares discriminate analysis (PLS-DA) were calculated using the MetaboAnalyst online platform[307].

Statistics

Statistical analysis was performed using GraphPad Prism 6. Comparison of two groups was done by two-sided Student's T-test. Comparison of >two groups was done using One-way ANOVA.

Results

Development of quantitative ECM proteomic methodology

To better understand the complexity of epithelial cell-ECM microenvironments *in vivo*, we developed novel extraction and digestion methods for proteomic characterization of ECM[48,438,443]. While these methodological advancements have furthered our understanding of ECM composition, they lacked the ability to accurately quantify ECM protein abundance in the microenvironment. To overcome this barrier, we designed six recombinantly generated Quantitative conCATamers (QconCAT)[303,444] made of 201 stable isotope labeled (SIL) peptides representing 98 ECM, ECM-associated, and common cellular proteins (Supplementary Table 1). Peptides specific to intracellular proteins from different subcellular locations were included to serve as a quality control measure for method development of tissue extraction methods and as a relative measure of cellularity. These reporter peptides are then 'spiked into' experimental protein lysates at equimolar concentrations to serve as internal quantitation controls. Figure 6-1A shows a schematic representation of the tissue extraction/fractionation, and digestion workflows

used prior to LC-SRM data acquisition. Our fractionation protocol yields three distinct fractions, cellular, soluble ECM (sECM), and insoluble ECM (iECM). The iECM fraction is then treated with cyanogen bromide (CNBr) to increase solubility. Reporter ECM peptides are added to all fractions, and samples are proteolytically digested and run by LC-SRM. The consolidated results from the three fractions yield total quantity for a given protein within a tissue. This targeted mass spectrometry method allows us to measure all 201 SIL QconCAT peptides and endogenous analogs in a single 30 minute analytical run. Molecular heterogeneity can differentially affect signal intensity during LC-SRM data acquisition, which is why the inclusion of internal standardized controls for each unique protein of interest is essential for determining accurate absolute concentrations. We find the QconCAT generated heavy peptides allow for precise quantification, as the reporter peptides behave identically to the endogenous peptides in terms of mass spectrometry fragmentation and ionization, chromatographic separation, and enzymatic digestion efficiency (Fig.6-1B).

To confirm increased detection of rat mammary and liver ECM proteins with this method, the protein identifications within the 3 fractions (cellular, sECM, and iECM) were grouped into functional classifications of cytoskeletal, other cellular, matricellular, and several ECM categories, using gene ontology terminology from the Database for Annotation, Visualization, and Integrated Discovery (DAVID)[445]. The vast majority of mammary cellular proteins fractionate with CHAPS detergent into the cellular fraction, whereas sECM and iECM fractions were highly enriched for ECM proteins (Fig.6-1C). In the rat liver, we again found that the majority of cellular proteins resolved with

CHAPS. The liver sECM fraction was enriched for matricellular proteins and the iECM fraction further enriched for fibrillar collagens (Fig.6-1C). Strikingly, 52% of mammary and 83% of liver collagen I was detected in the iECM fraction after CNBr treatment (Fig.6-1D), a fraction not routinely incorporated into traditional proteomic methods. Additionally, other residual ECM proteins failed to completely solubilize with urea (sECM fraction), highlighting the importance of CNBr solubilization and analysis of the iECM fraction (Fig.6-1C). The utility of using our targeted reporter peptide approach compared to a global proteomics approach is further realized by analyzing the ratio of collagen alpha-1(I) to collagen alpha-2(I) by LC-SRM. The expected stoichiometry between these two chains is 2:1 (COL1A1/COL1A2), based on the assembly of fibrillar collagen triple helices containing two alpha-1 chains and one alpha-2 chain. We find that the targeted approach with QconCATs more accurately reflects the theoretical ratio of 2:1 than a traditional global proteomics approach (Fig.6-1E).

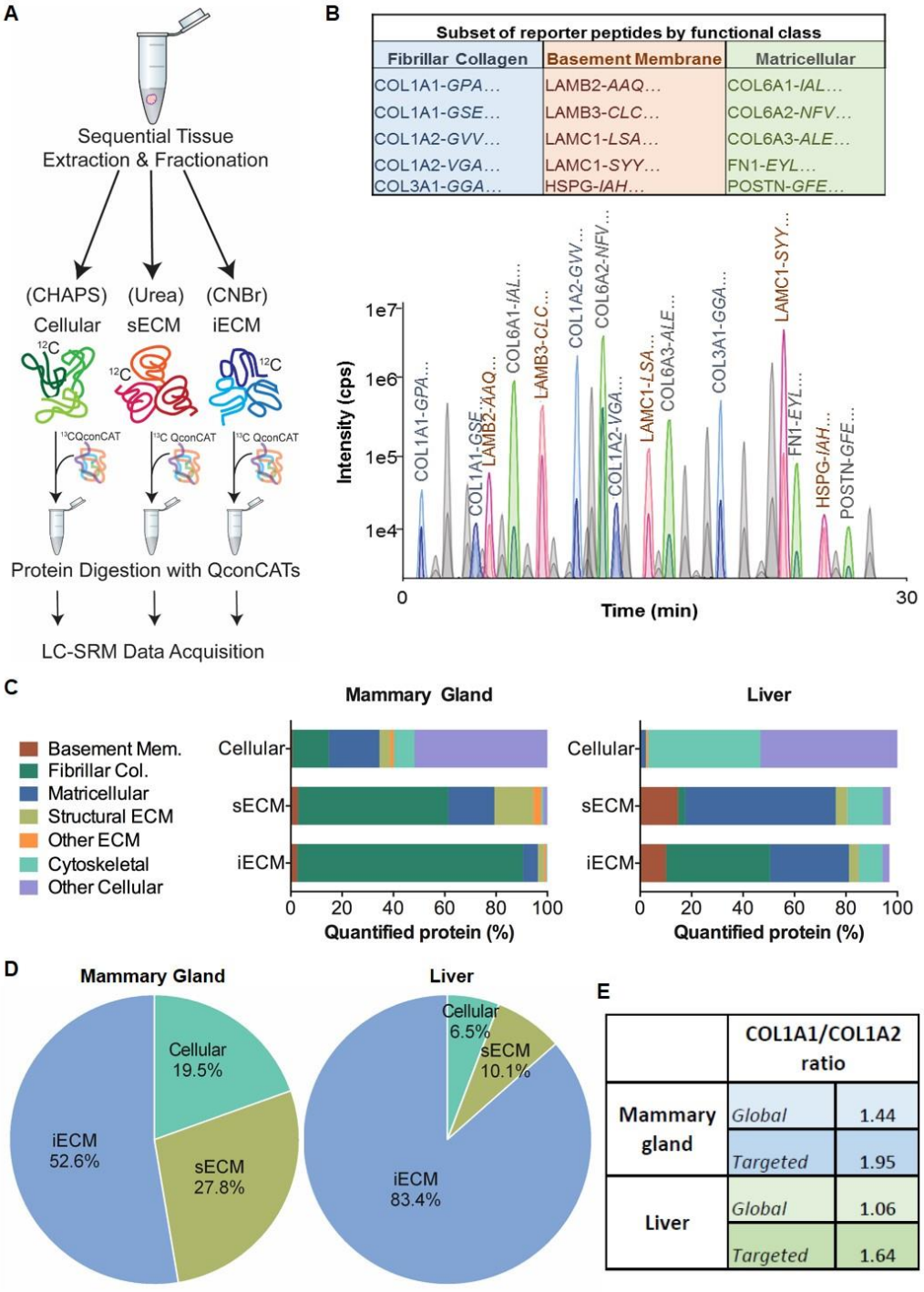
A
Sequential Tissue Extraction & Fractionation
(CHAPS) Cellular
(Urea) sECM
(CNBr) iECM
Protein Digestion with QconCATs
LC-SRM Data Acquisition
B
Subset of reporter peptides by functional class
Fibrillar Collagen
Basement Membrane
Matricellular
COL1A1-GPA…
COL1A1-GSE…
COL1A2-GVV…
COL1A2-VGA…
COL3A1-GGA…
LAMB2-AAQ…
LAMB3-CLC…
LAMC1-LSA…
LAMC1-SYY…
HSPG-IAH…
COL6A1-IAL…
COL6A2-NFV…
COL6A3-ALE…
FN1-EYL…
POSTN-GFE…
Intensity (cps)
Time (min)
C
Mammary Gland
Liver
Basement Mem.
Fibrillar Col.
Matricellular
Structural ECM
Other ECM
Cytoskeletal
Other Cellular
Cellular
sECM
iECM
Quantified protein (%)
D
Mammary Gland
Liver
Cellular 19.5%
sECM 27.8%
iECM 52.6%
Cellular 6.5%
sECM 10.1%
iECM 83.4%
E
COL1A1/COL1A2 ratio
Mammary gland
Global 1.44
Targeted 1.95
Liver
Global 1.06
Targeted 1.64

Figure 6-1: Quantitative QconCAT ECM proteomics pipeline

(A) Experimental pipeline for quantitative ECM proteomics. Tissues are sequentially extracted to obtain cellular, soluble ECM (sECM), and insoluble ECM (iECM) fractions. QconCATs are spiked into fractions and samples are then proteolytically digested (full list of Quantitative conCATamers in Supplementary Table 1). **(B)** Table of a subset of the 98 ECM/ECM-associated proteins represented in the Quantitative conCATamers (QconCAT) used to determine absolute concentration of proteins by mass spectrometry proteomics; the first three amino acids of the peptide represented are identified in italics (top). Representative chromatographic elution profile of equal molar concentration of conCATamer peptides detected by LC-SRM mass spectrometry demonstrates peptide-specific spectral profiles (bottom). For labeled peaks, darker shading indicates $^{12}C_6$ peptide (endogenous) and lighter shading indicates $^{13}C_6$ peptide (QconCAT), which is spiked in at known, equimolar concentrations. Integrated peak areas are used for ratio metric determination of endogenous peptide levels, a surrogate for protein concentration (bottom). **(C)** Percent of proteins identified within the cellular, sECM, and iECM fractions of rat mammary gland (left) and liver (right) according to the DAVID gene ontology functional group classification. **(D)** Percent of collagen I identified in cellular, sECM, and iECM fractions of rat mammary gland (left) and liver (right). **(E)** Ratio of collagen alpha-1(I) to collagen alpha-2(I) for peptide spectral matches vs. QconCAT based quantification in rat mammary gland and liver.

QconCAT based proteomics reveals unique and shared mammary gland and liver ECM profiles

A major rate-limiting step of metastatic success has been attributed to discordance between the ECM requirements of the seeding tumor cell and the ECM microenvironment at the secondary site[50,82,201,211,213]. In the context of breast cancer, we utilized our quantitative ECM proteomics to begin to address this hypothesis by elucidating tissue-specific differences as well as similarities between the primary and liver metastatic site in the nulliparous female adult rat. We focused on the liver, as one of three common sites of breast cancer metastasis[240,241,446], which confers the worst prognosis[244-246]. The resulting proteomic data were grouped into 10 functional classifications of proteins including: basement membrane, ECM regulator, fibril-associated collagens with interrupted triple helices (FACIT) collagen, fibrillar collagen, matricellular, other ECM, secreted ECM, and structural ECM, using DAVID, as described in Figure 6-1[445]. This analysis demonstrated an abundance of fibrillar collagens and matricellular proteins in mammary tissue, and high levels of cytoskeletal and cellular proteins in liver (Fig.6-2A, Supplementary Tables 2 & 3), data consistent with the high stromal and low epithelial content in the mammary gland as compared to the liver (Fig.6-2B). Further, these tissues differed markedly in overall ECM abundance, with ~100 nmol of ECM per gram of tissue in the mammary gland compared to ~8.5 nmol/gram in the liver (Fig.6-2C).

To further interrogate ECM complexity and abundance of ECM proteins between the mammary gland and the liver, we removed cellular proteins from the assessment. This

ECM-biased analysis revealed that nulliparous mammary gland ECM is >80% fibrillar collagen, ~9% matricellular proteins, 1.3% basement membrane proteins, and ~5% combined FACIT collagens and structural, regulatory, secreted and other ECMs (Fig.6-2D). In contrast, in the liver, matricellular proteins make up 44% of ECM proteins, followed by 26.4% fibrillar collagen, ~10% basement membrane, and 15.3% combined FACIT collagens and structural, regulatory, secreted and other ECMs (Fig.6-2D). Although the absolute concentration of fibrillar collagen is vastly different between mammary gland and liver, fibrillar collagen I remains the most abundant single ECM protein in both tissues (Fig.6-2E), providing further support for an essential role of collagen I in tissue structure and homeostasis[447]. Our observed molar concentrations of fibrillar collagens in mammary gland and liver (Fig.6-2F, upper left panel) correlate with relative fibrillar collagen abundance detected by trichrome stain (Fig.6-2F, upper right panel and representative images), reinforcing potential biologic relevance of the QconCAT method.

To investigate ECM complexity beyond fibrillar collagen I, we stratified QconCAT data based on the next twenty most abundant ECM proteins (Fig.6-2G, highlighted in Supplementary Tables 2 & 3). Despite the concentration of ECM in the mammary gland dropping significantly with removal of collagen I, ECM concentration of the remaining 20 proteins was still ~4-fold higher in the mammary gland compared to liver (Fig.6-2E, G). Overall, we identified the same ECM proteins in both the mammary gland and liver, however, their relative ratios were tissue specific (Fig.6-2G). For example, lumican, collagen VI, and collagen XIV were prevalent in the mammary gland and collagen VI

and fibronectin were prevalent in liver (Fig.6-2G). Further, we find that while fibronectin is present at ~equimolar concentrations in the mammary gland and liver (Supplementary Fig.6-1), it makes up only 0.64% of total ECM concentration in the mammary gland compared to 4.74% in the liver (Fig.6-2G, Supplementary Tables 2 & 3). The absolute quantitation method also permits the identification of a subset of ECM proteins, including thrombospondin 1 and fibulin 4, that are present at significantly higher concentrations in liver, in spite of the mammary gland having ~12-fold higher concentration of total ECM (Supplementary Fig.6-1). In sum, these analyses demonstrate the ability of the QconCAT method to provide absolute molar concentrations of specific ECM proteins within the mammary gland and liver and identify tissue-specific ECM complexity.

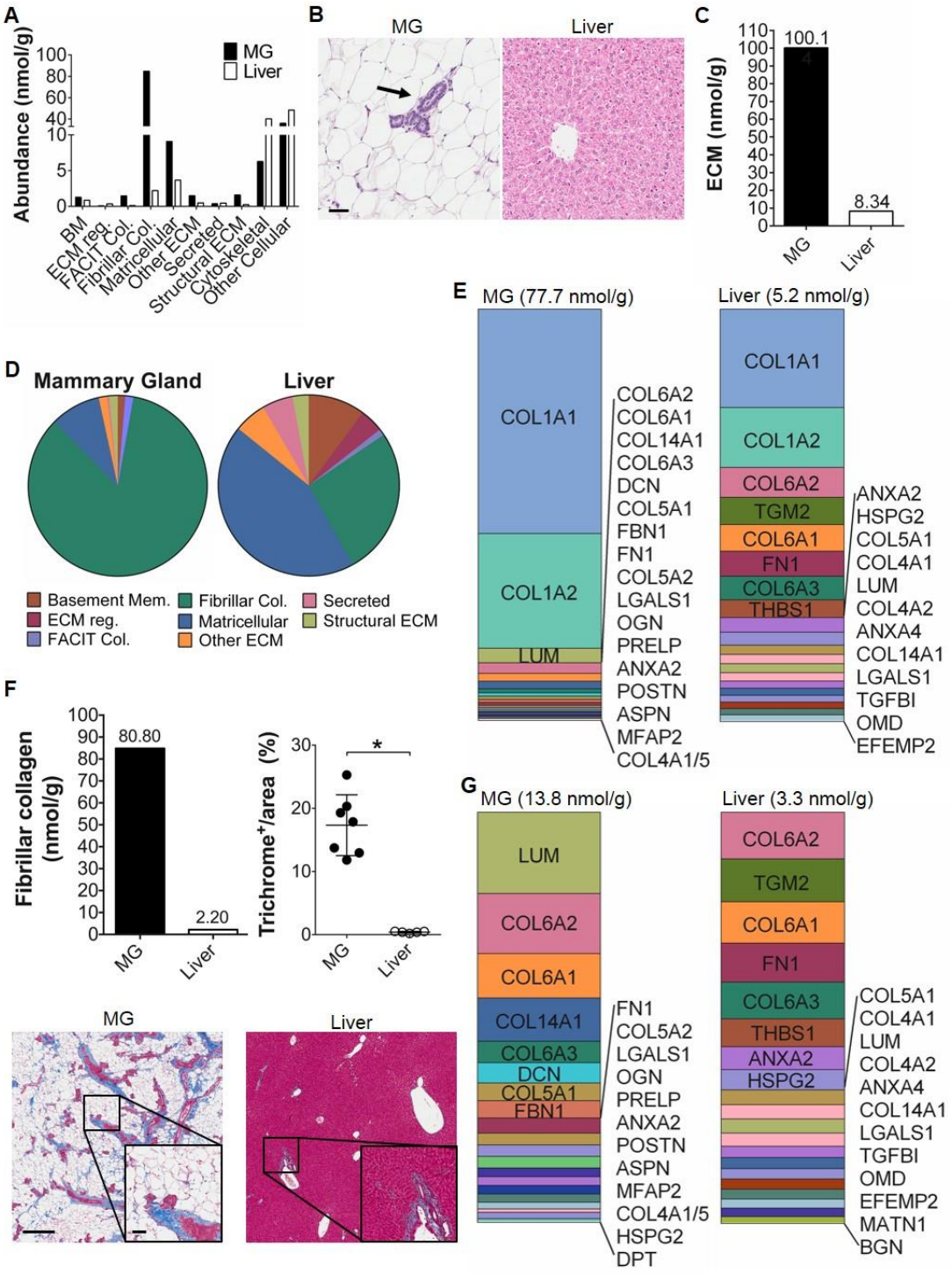
A
Abundance (nmol/g)
MG
Liver
BM
ECM reg.
FACIT Col.
Fibrillar Col.
Matricellular
Other ECM
Secreted
Structural ECM
Cytoskeletal
Other Cellular
B
MG
Liver
C
ECM (nmol/g)
100.1
8.34
MG
Liver
D
Mammary Gland
Liver
Basement Mem.
ECM reg.
FACIT Col.
Fibrillar Col.
Matricellular
Other ECM
Secreted
Structural ECM
E
MG (77.7 nmol/g)
COL1A1
COL1A2
LUM
COL6A2
COL6A1
COL14A1
COL6A3
DCN
COL5A1
FBN1
FN1
COL5A2
LGALS1
OGN
PRELP
ANXA2
POSTN
ASPN
MFAP2
COL4A1/5
Liver (5.2 nmol/g)
COL1A1
COL1A2
COL6A2
TGM2
COL6A1
FN1
COL6A3
THBS1
ANXA2
HSPG2
COL5A1
COL4A1
LUM
COL4A2
ANXA4
COL14A1
LGALS1
TGFBI
OMD
EFEMP2
F
Fibrillar collagen (nmol/g)
80.80
2.20
MG
Liver
Trichrome+/area (%)
*
MG
Liver
MG
Liver
G
MG (13.8 nmol/g)
LUM
COL6A2
COL6A1
COL14A1
COL6A3
DCN
COL5A1
FBN1
FN1
COL5A2
LGALS1
OGN
PRELP
ANXA2
POSTN
ASPN
MFAP2
COL4A1/5
HSPG2
DPT
Liver (3.3 nmol/g)
COL6A2
TGM2
COL6A1
FN1
COL6A3
THBS1
ANXA2
HSPG2
COL5A1
COL4A1
LUM
COL4A2
ANXA4
COL14A1
LGALS1
TGFBI
OMD
EFEMP2
MATN1
BGN

Figure 6-2: QconCAT based ECM proteomics reveals unique mammary gland and liver ECM profiles

(A) QconCAT based ECM proteomics of nulliparous rat mammary gland and liver tissues displayed as total abundance of proteins (nmol/gram of tissue) grouped by DAVID gene ontology functional classifications; n=5 rats/group for mammary gland and n=6 rats for liver analyses. **(B)** Representative H&E stained rat mammary gland (MG; left) and liver (right) showing tissue specific differences in stromal-epithelial cell composition; scale bar=60 μm (arrow=MG epithelium; liver H&E shows epithelium throughout the tissue). **(C)** Nanomolar concentration of total ECM per gram of tissue from QconCAT proteomics in the mammary gland and liver. **(D)** Abundance of ECM and ECM-associated proteins based on DAVID gene ontology functional groups with cytoskeletal and cellular protein groups excluded. **(E)** Twenty most abundant ECM proteins in the rat MG (left) and liver (right) as detected by QconCAT proteomics. Tabular results in Supplementary Tables 2 & 3. **(F)** Nanomolar concentration of fibrillar collagen in MG and liver from QconCAT proteomic analysis (top left) and collagen trichrome staining quantification in MG and liver (top right). Representative trichrome stained images (blue stain) of rat MG (bottom left) and liver (bottom right); scale bar=250 μm, inset scale bar=60 μm. *=p-value<0.0001, Student's T-test. **(G)** Twenty most abundant ECM proteins, excluding collagen I, in the rat MG (left) and liver (right) as detected by QconCAT proteomics, tabular results shown in Supplementary Tables 2 & 3.

Mammary gland ECM proteomics across the reproductive cycle

The microenvironment of the mammary gland can be neutral, tumor-promotional, or tumor-suppressive, dependent upon reproductive state[42,296], a phenomenon thought to be driven in large part by reproductive state-dependent changes to mammary ECM[47,49,296]. Specifically, in rodent models of breast cancer, mammary tumor cells grow most robustly in the weaning-induced involuting microenvironment, moderately in the nulliparous mammary microenvironment, and least when transplanted into parous mice, whose mammary glands have completed weaning-induced involution[42,296]. Despite this dynamic fluctuation in tumor-supportive function, mammary ECM has never been assessed across the reproductive cycle using quantitative proteomics. To this end, we analyzed rat mammary ECM in whole gland lysates from nulliparous, pregnancy, lactating, involuting (i.e., 2, 4, 6, 8 and 10 days post-weaning), and fully involuted (regressed) stages. Principle component analyses (PCA) on LC-SRM data generated from these ECM proteomics data revealed a cycle of mammary gland ECM remodeling across pregnancy, lactation and involution, upon which the gland ultimately returns to an ECM microenvironment similar to, but distinct from, the nulliparous state (Fig.6-3 & Supplementary Fig.6-2). We observed a >2-fold drop in ECM abundance when comparing nulliparous to pregnancy, lactation, and involution day 2 stages (Fig.6-4A), data consistent with the increased epithelial cellularity as well as loss of collagen staining at these reproductive stages[46]. Total ECM abundance increased to pre-pregnant levels by involution day 6, consistent with epithelial cell loss and stromal repopulation upon weaning[37]. We also observed increased abundance of ECM in the fully regressed mammary gland compared to the nulliparous host, data suggestive of unique mammary

microenvironments in nulliparous and parous hosts (Fig.6-4A), and consistent with previous reports[296].

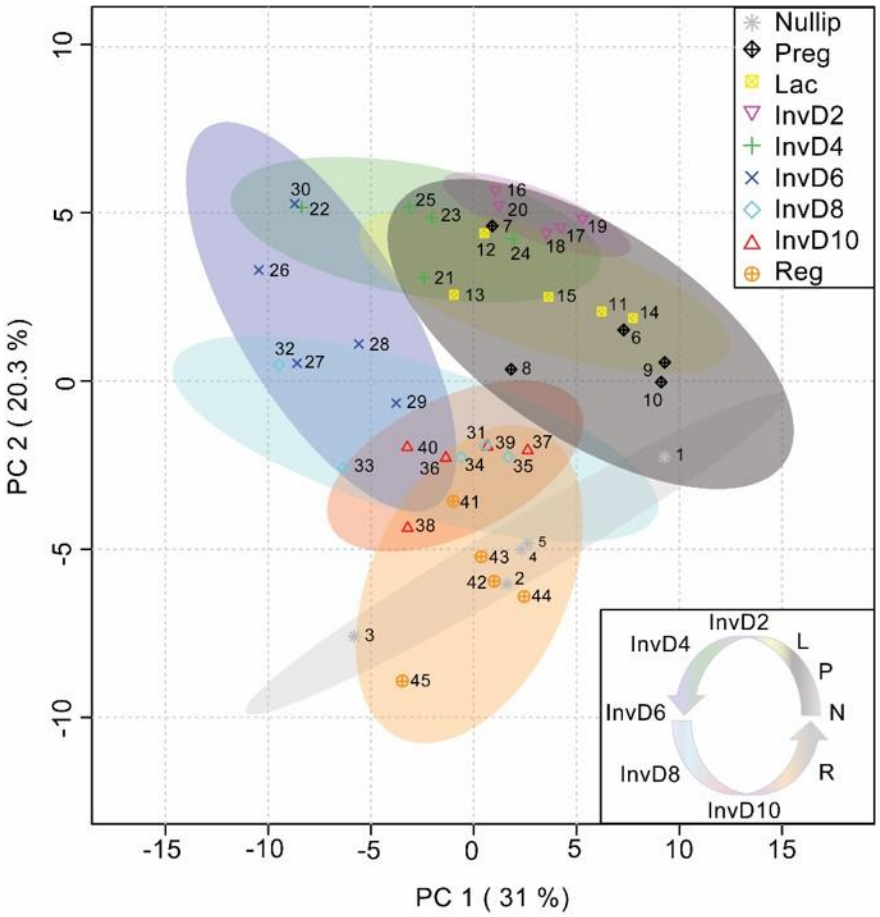

Figure 6-3: Quantitative ECM proteomics reveals dynamic and cyclical mammary gland ECM remodeling across the reproductive cycle

Principle component analysis of quantitative ECM proteomics performed on rat mammary glands across the reproductive cycle (Nullip=nulliparous; Preg=pregnancy days 18-21; Lac=lactation day 10; InvD2-InvD10=involution days 2, 4, 6, 8, and 10; Reg=regressed, 4 weeks post-weaning); n=5 rats/grp. Data shows that ECM composition in the mammary gland changes in phase with the reproductive cycle in a stepwise, cyclical fashion.

We next compared the top twenty most abundant ECM proteins in the mammary glands from nulliparous, involution days 2 and 6, and regressed stages, since these stages have differential tumor-promotional attributes[42,296]. We confirmed that collagen I is the predominant ECM protein in the gland[48,438], and extended these analyses to demonstrate that collagen abundance is dramatically reduced during pregnancy, and does not return to high levels until 6 days post-weaning (Fig.6-4A-B). To investigate ECM complexity further, we removed collagen I from the analysis and found a high abundance of lumican, collagen VI, and collagen XIV in the nulliparous and regressed rat mammary gland (Fig.6-4C-D & Supplementary Table 2). In contrast to these relatively quiescent mammary glands, actively involuting glands exhibited a prominent abundance of collagen VI, thrombospondin 1, and galectin-3 (Fig.6-4C-D). Two additional ECM proteins not found in the top 20 list, tenascin-C and collagen XII, also increased in abundance during mammary gland involution (Fig.6-4D). Intriguingly, the ECM composition of the involuting mammary gland somewhat resembles that of the liver, which share increased collagen VI and fibronectin, and reduced lumican and collagen I abundances (Fig.6-2G & 6-4C). Principle component analysis confirmed tissue specificity of liver and mammary ECM, but also revealed that liver ECM resembles the mammary gland at pregnancy, lactation, and involution days 2 and 4, compared to other reproductive stages (Supplementary Fig.6-3). Taken together, these data highlight how quantitative ECM proteomics can provide prime candidates for the investigation of the roles of ECM in breast cancer progression.

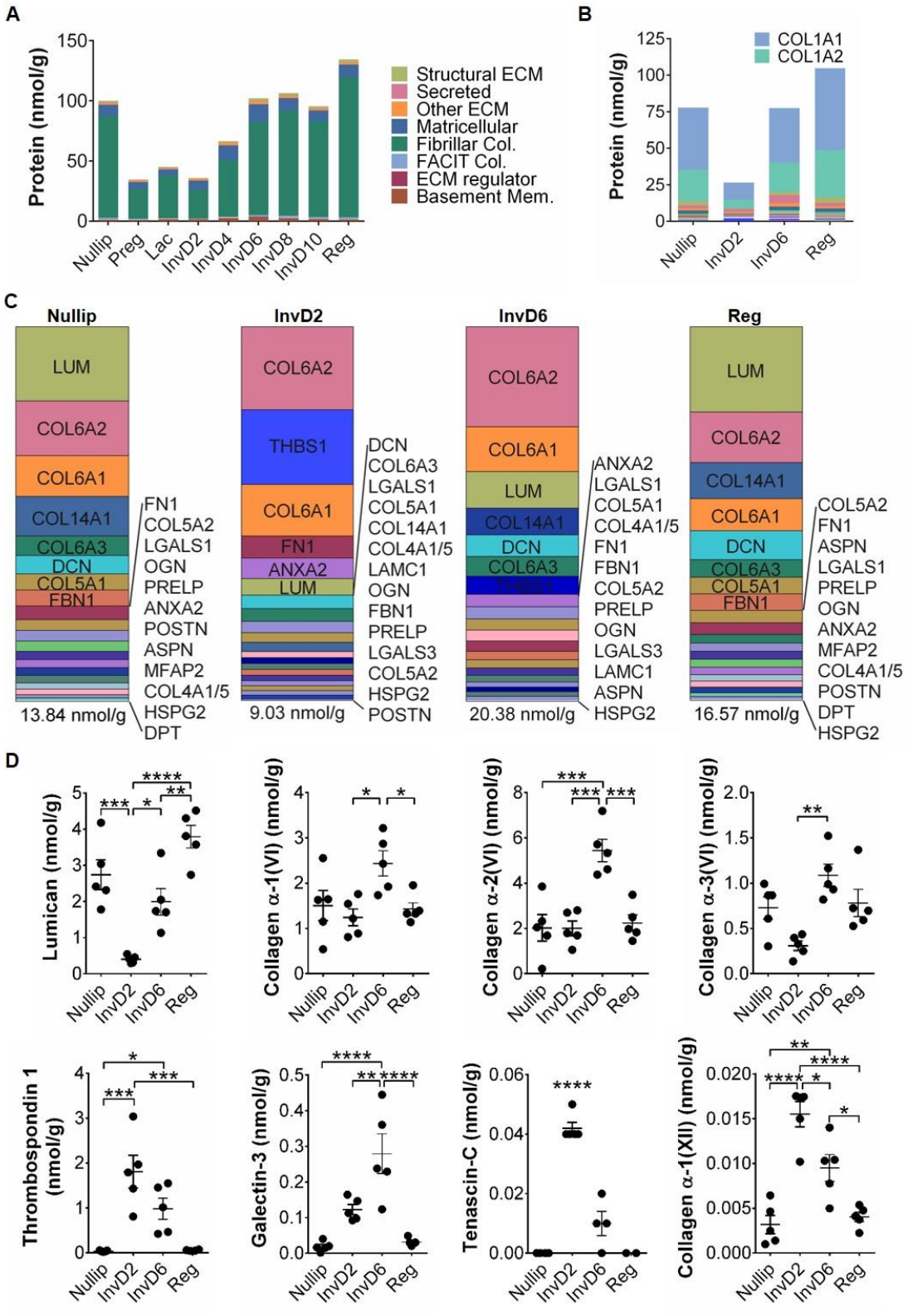
A
Protein (nmol/g)
150
100
50
0
Nullip
Preg
Lac
InvD2
InvD4
InvD6
InvD8
InvD10
Reg
Structural ECM
Secreted
Other ECM
Matricellular
Fibrillar Col.
FACIT Col.
ECM regulator
Basement Mem.
B
Protein (nmol/g)
125
100
75
50
25
0
COL1A1
COL1A2
Nullip
InvD2
InvD6
Reg
C
Nullip
LUM
COL6A2
COL6A1
COL14A1
COL6A3
DCN
COL5A1
FBN1
FN1
COL5A2
LGALS1
OGN
PRELP
ANXA2
POSTN
ASPN
MFAP2
COL4A1/5
HSPG2
DPT
13.84 nmol/g
InvD2
COL6A2
THBS1
COL6A1
FN1
ANXA2
LUM
DCN
COL6A3
LGALS1
COL5A1
COL14A1
COL4A1/5
LAMC1
OGN
FBN1
PRELP
LGALS3
COL5A2
HSPG2
POSTN
9.03 nmol/g
InvD6
COL6A2
COL6A1
LUM
COL14A1
DCN
COL6A3
THBS1
ANXA2
LGALS1
COL5A1
COL4A1/5
FN1
FBN1
COL5A2
PRELP
OGN
LGALS3
LAMC1
ASPN
HSPG2
20.38 nmol/g
Reg
LUM
COL6A2
COL14A1
COL6A1
DCN
COL6A3
COL5A1
FBN1
COL5A2
FN1
ASPN
LGALS1
PRELP
OGN
ANXA2
MFAP2
COL4A1/5
POSTN
DPT
HSPG2
16.57 nmol/g
D
Lumican (nmol/g)
Collagen α-1(VI) (nmol/g)
Collagen α-2(VI) (nmol/g)
Collagen α-3(VI) (nmol/g)
Thrombospondin 1 (nmol/g)
Galectin-3 (nmol/g)
Tenascin-C (nmol/g)
Collagen α-1(XII) (nmol/g)
Nullip
InvD2
InvD6
Reg

Figure 6-4: Quantitative ECM proteomics unravels the unique composition and abundance of ECM proteins across the reproductive cycle

(A) QconCAT based ECM proteomics of rat MG tissues across the reproductive cycle, with identified cellular protein groups removed; n=5 rats/grp. **(B)** Twenty most abundant ECM proteins in Nullip, InvD2, InvD6, and Reg stage rat MG; tabular results highlighted in Supplementary Table 2. **(C)** Twenty most abundant ECM proteins in Nullip, InvD2, InvD6, and Reg stage rat MG, with collagen I removed from the analysis. Tabular results in Supplementary Table 2. **(D)** Select tumor suppressive (lumican) and tumor-promotional (collagen VI, thrombospondin 1, galectin-3, tenascin-C) ECM protein levels, as well as collagen XII from individual rats, as determined by QconCAT based ECM proteomics of Nullip, InvD2, InvD6, and Reg stages, n=5 rats/grp; *=p-value<0.05, **=p-value<0.01, ***=p-value<0.001, ****=p-value<0.0001, One-way ANOVA.

Discussion

This work describes advances made in sample preparation techniques and quantitative proteomics methods for the study of tissue ECM composition and abundance. Using this experimental pipeline, we characterized tissue-specific ECM composition of the rodent mammary gland and liver, a lethal site of breast cancer metastasis, to a level not previously accomplished. These analyses identified putative tissue-specific ECM components, including lumican and collagen XIV, which were prevalent in the mammary gland, and fibronectin which was prevalent in the liver. We also found shared ECM components between these two tissues, including abundant proteins such as collagen types I and VI, as well as less abundant collagen types IV and V. We also show that the abundance of mammary gland ECM is altered across the reproductive cycle, building upon previous studies that have identified major shifts in mammary ECM with pregnancy, lactation, involution, and regression[43,46,47,95]. In particular, we see elevated abundance of known pro-tumorigenic ECM proteins collagen VI, thrombospondin 1, galectin-3, and tenascin-C during weaning-induced mammary gland involution. Further, to the best of our knowledge, we identify collagen XII for the first time as elevated during post-weaning mammary involution. Importantly, potential roles for each of these highlighted ECM proteins in breast cancer metastasis have been elucidated, with the exception of collagen XII[448-451]. While collagen XII has been shown to be upregulated in malignant breast cancer cell lines, and has been identified as a prognostic marker in other cancers, its role in breast cancer progression has yet to be established[452,453]. In sum, our data demonstrate tissue-specific ECM complexity and ECM protein stoichiometry

between the mammary gland and liver, and across a reproductive cycle within the mammary gland, data consistent with ECM contributing to differential tissue function.

Somewhat surprisingly, we also found that the ECM profile of the early involuting mammary gland (InvD2-InvD4) resembled that of the liver. This finding may provide insight into site-specific metastasis of postpartum breast cancers, as disseminated tumor cells may experience a survival advantage if primary and secondary sites have similar ECM compositions post-weaning. A prediction of these data are increased risk for liver metastasis in postpartum breast cancer patients; a relationship that remains unexplored. Of potential relevance, risk for liver metastasis is elevated in younger breast cancer patients[454], a significant proportion of whom are likely to be postpartum breast cancer patients[9].

Our quantitative QconCAT ECM proteomics approach facilitates in-depth characterization of tissue-specific ECM abundance and composition at a level not previously attained. The advances we report result, in part, from improved solubilization using a CNBr extraction step that permits detection of historically insoluble ECM proteins such as collagen I. Further, the use of in-house generated QconCATs for quantification of tissue ECM proteins has several advantages over traditional relative quantitative approaches, including 1) SIL peptide mimics that control for matrix effects during proteomic acquisition, allowing for direct comparison between heterogeneous tissues, 2) inclusion of full-length QconCATs during digestion, which control for sample loss and digestion variability, and 3) absolute quantitative values allowing for inter-

protein and -experiment comparisons between samples. However, as with any first-generation experimental pipeline, there are limitations to the methodology that need to be addressed in future work. First, targeted proteomics is inherently more specific and therefore will only quantitate peptides/proteins included in the QconCAT library. However, when comparing our current QconCAT library coverage to samples simultaneously run using global proteomics, only an additional 7 and 8 ECM proteins (primarily Annexins, accounting for 0.43% and 0.11% of total spectral matches) were identified that were not covered by the QconCAT library. Further, QconCAT proteomics quantified 34 and 41 proteins or protein isoforms in the mammary gland and liver, respectively, not identified by global proteomics (Supplementary Table 4). These comparisons highlight the benefits of increased sensitivity when applying a targeted proteomics approach, as this level of detection often requires deep fractionation and multiple runs to achieve similar depth using global proteomics.

An additional caveat to QconCAT proteomics is that quantification of endogenous peptides with post-translational modifications (PTMs) is not currently possible. We circumvent this problem by designing QconCAT peptides specific to proteins that either have no known PTMs or do not contain a common PTM motif so that the quantified endogenous peptide has a higher probability of representing the molar equivalent of the protein it represents. Furthermore, we attempt to include multiple peptides per protein of interest to account for splice variants, known PTMs, and matricryptic sites, however a subset of proteins are currently covered by only a single peptide. Future generations of this QconCAT library will increase confidence in protein quantification by expanding

coverage of ECM, ECM-modifying, and ECM-associated proteins, as well as adding additional peptides for all ECM protein targets. Importantly, the increased depth of ECM coverage that will be gained by design of additional QconCATs will ultimately facilitate more refined characterization of ECM abundance and composition in tissues.

Multiple studies have characterized both the mammary gland and liver in a variety of normal and tumorigenic contexts[415,437,440,441,455-458]. However, because these semi-quantitative approaches provide relative, and not absolute abundance of proteins, it is difficult to compare data across studies. For example, comparison of collagen coverage in the liver across our platform and five published datasets revealed marked variability between both identification and quantification of collagen (Supplementary Table 5). While the majority of datasets identified the abundant collagens I & VI, they varied dramatically in estimated abundance and in the identification of less abundant collagens. Significant differences in estimated abundance of collagen I between studies are likely derived from variability in enrichment strategies, and the non-uniform analysis of insoluble collagens in the iECM pellet, a protein fraction not routinely captured in standard proteomics pipelines[303]. The quantitative advantage of QconCATs is apparent with comparison of collagen alpha-1(I) to collagen alpha-2(I) ratios, as our targeted approach recapitulated the expected 2:1 ratio (Fig.6-1E & Supplementary Table 6-5). Additionally, collagen alpha-1/2/3(VI) organizes into a 1:1:1 heterotrimer[459], and again, our study is the only one to reveal such a distribution (Supplementary Table 5). The level of variability across proteomics datasets highlights the need for standardization, and

suggest that solubilization with CNBr along with absolute quantification may provide additional biological relevance to proteomics pipelines focused on ECM proteins.

To the best of our knowledge, our ECM-based QconCAT proteomics pipeline has provided the most quantitative assessment of ECM proteins and tissue composition in mammary gland and liver to date. In the future, the application of this method can be utilized to more fully interrogate breast cancer progression. For example, a comparison of young women's breast tumors and paired metastases, similar to work done by Naba et al in colorectal cancer[437], is predicted to reveal widespread ECM differences and further inform our understanding of breast cancer metastasis. Further, studies to understand liver, as well as lung, bone, and brain ECM throughout the reproductive cycle may shed insight into site-specific metastasis in premenopausal breast cancer patients. The impact of the ECM biased proteomic pipeline could be further realized in the context of regenerative medicine, where understanding the composition of ECM components and the relative stoichiometry within specific organs would be critical steps in accurately recapitulating endogenous matrices. Ultimately, compilation of similar datasets for additional organs would lay the foundation for an ECM Atlas that would be capable of comparing absolute quantitative measurements between all organs, facilitating a broader understanding of the role of ECM in physiology and pathology.

Conclusions

ECM can be quantitatively analyzed from tissues under diverse physiologic and pathologic conditions using the improved solubilization and quantitative proteomics

methodologies presented here. We report tissue-specific ECM signatures in rat liver compared to mammary gland, as well as diverse ECM complexity and abundance in the rat mammary gland throughout a reproductive cycle. These studies provide novel avenues to elucidate how ECM impacts breast cancer progression, particularly postpartum breast cancer. Our quantitative ECM proteomics approach has broad applicability and can be utilized in studies pertaining to various tissue and disease sites, treatment responses, stem cell biology, and tissue regeneration.

Supplementary Figures

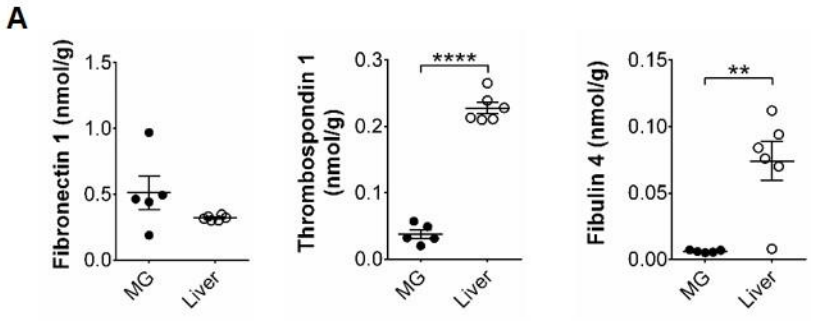

Supplementary Figure 6-1: ECM proteomics identifies matrix proteins present at different levels in mammary gland and liver

(A) Fibronectin (left), thrombospondin 1 (middle), and fibulin 4 (right) levels in mammary gland (MG) and liver from quantitative ECM proteomics. **p-value<0.01, ****p-value<0.0001, Student's T-test.

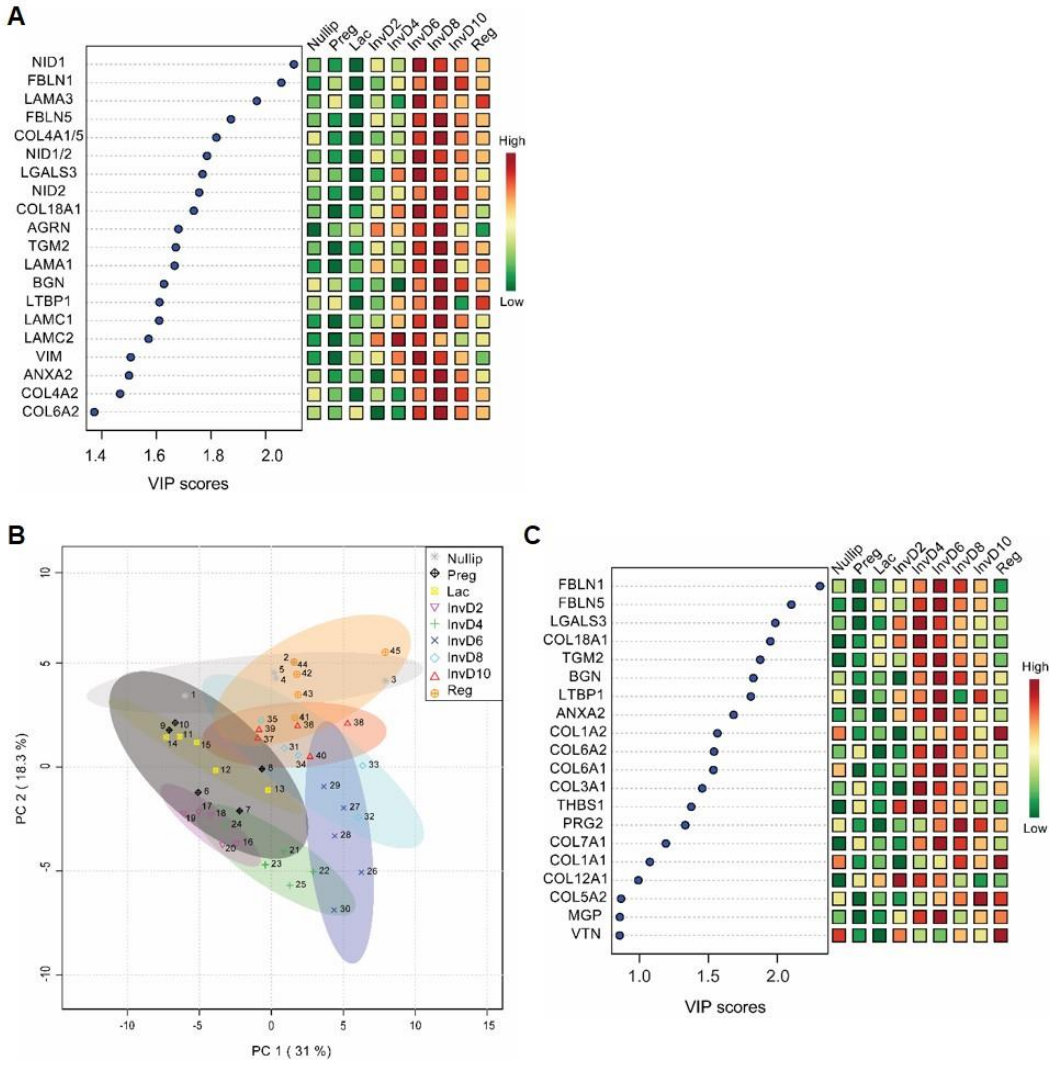

Supplementary Figure 6-2: Principle component analysis of rat mammary gland ECM proteomics across the reproductive cycle

(A) Variable of importance in projection (VIP) plot from partial least squares discriminative analysis (PLS-DA) (PCA shown in Figure 6-3) from rat mammary gland targeted ECM proteomics (Nullip=nulliparous; Preg=pregnancy days 18-21; Lac=lactation day 10; InvD2-InvD10=involution days 2, 4, 6, 8, and 10; Reg=regressed, 4 weeks post-weaning); n=5 mammary glands/grp. VIP scores are a weighted sum of squares of the PLS loadings. The weights are based on the amount of explained Y-variance in each dimension. **(B)** PCA analysis of ECM proteins (cellular proteins excluded) identified by LC-SRM of rat mammary gland across the reproductive cycle. **(C)** VIP plot from PLS-DA analysis (PCA shown in B) from rat mammary gland targeted ECM proteomics across the reproductive cycle.

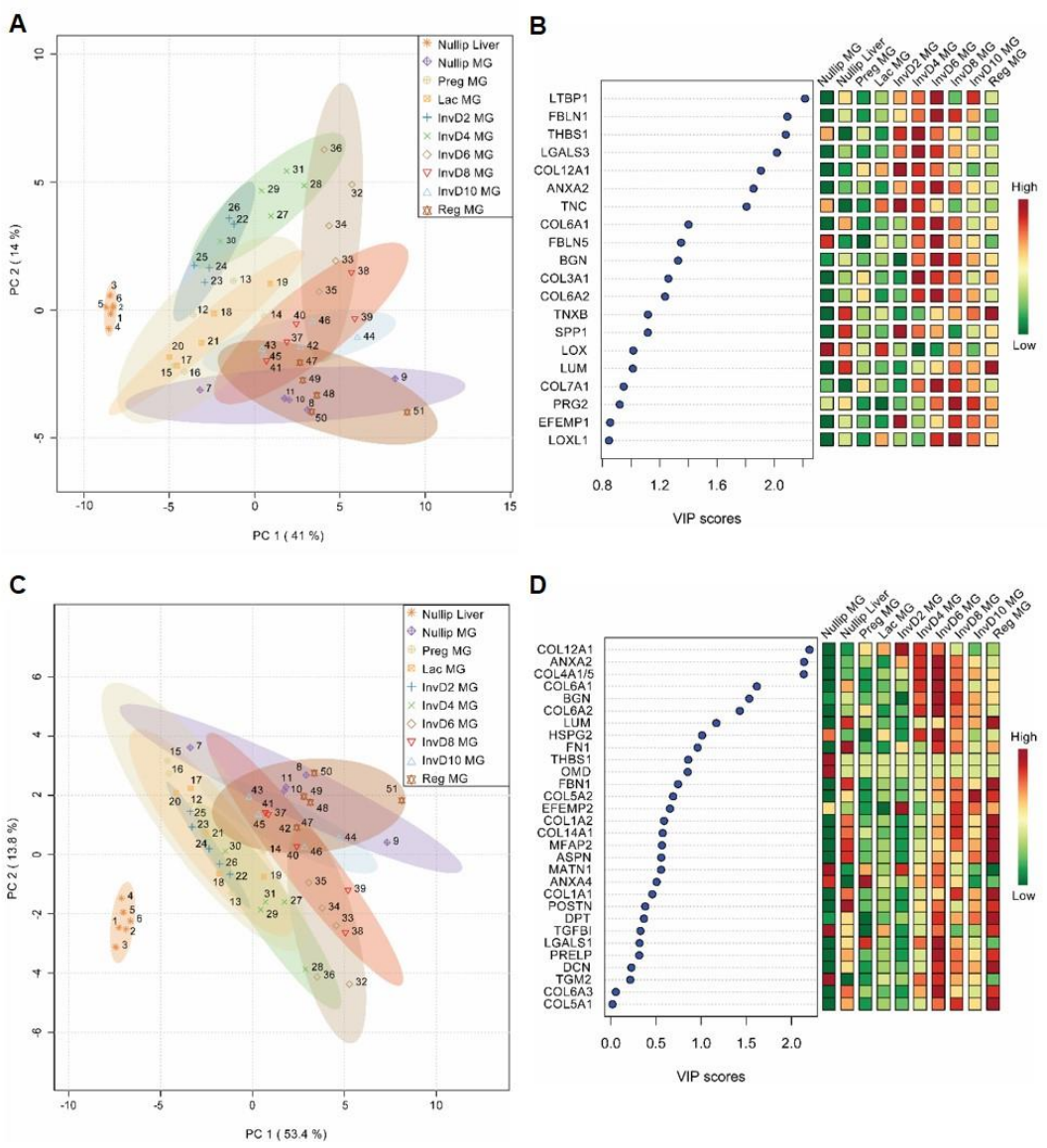
A
Nullip Liver
Nullip MG
Preg MG
Lac MG
InvD2 MG
InvD4 MG
InvD6 MG
InvD8 MG
InvD10 MG
Reg MG
PC 2 (14 %)
PC 1 (41 %)
B
LTBP1
FBLN1
THBS1
LGALS3
COL12A1
ANXA2
TNC
COL6A1
FBLN5
BGN
COL3A1
COL6A2
TNXB
SPP1
LOX
LUM
COL7A1
PRG2
EFEMP1
LOXL1
High
Low
VIP scores
C
PC 2 (13.8 %)
PC 1 (53.4 %)
D
COL12A1
ANXA2
COL4A1/5
COL6A1
BGN
COL6A2
LUM
HSPG2
FN1
THBS1
OMD
FBN1
COL5A2
EFEMP2
COL1A2
COL14A1
MFAP2
ASPN
MATN1
ANXA4
COL1A1
POSTN
DPT
TGFBI
LGALS1
PRELP
DCN
TGM2
COL6A3
COL5A1
VIP scores

Supplementary Figure 6-3: Principle component analysis of rat nulliparous liver ECM proteomics compared to mammary gland ECM proteomics across the reproductive cycle

(A) PCA analysis of all ECM proteins (cellular proteins excluded) identified by LC-SRM of rat mammary gland across the reproductive cycle, with nulliparous rat liver included in the analysis; n=5 mammary glands/grp, n=6 livers/grp. Data show that liver ECM is most comparable to ECM signatures present in mammary glands from pregnancy, lactation, and involution days 2-4 stages. **(B)** VIP plot from PLS-DA analysis of ECM proteomics on rat mammary gland and liver (PCA shown in A). VIP scores are a weighted sum of squares of the PLS loadings. The weights are based on the amount of explained Y-variance in each dimension. **(C)** PCA analysis of the combined top 20 most abundant ECM proteins in nulliparous liver (highlighted in Supplementary Table 3) and mammary gland (highlighted in Supplementary Table) across the reproductive cycle (top 20 combined resulted in 30 total proteins). **(D)** VIP plot from PLS-DA analysis of the top 30 most abundant ECM proteins identified by LC-SRM of rat mammary gland and liver.

Supplementary Table

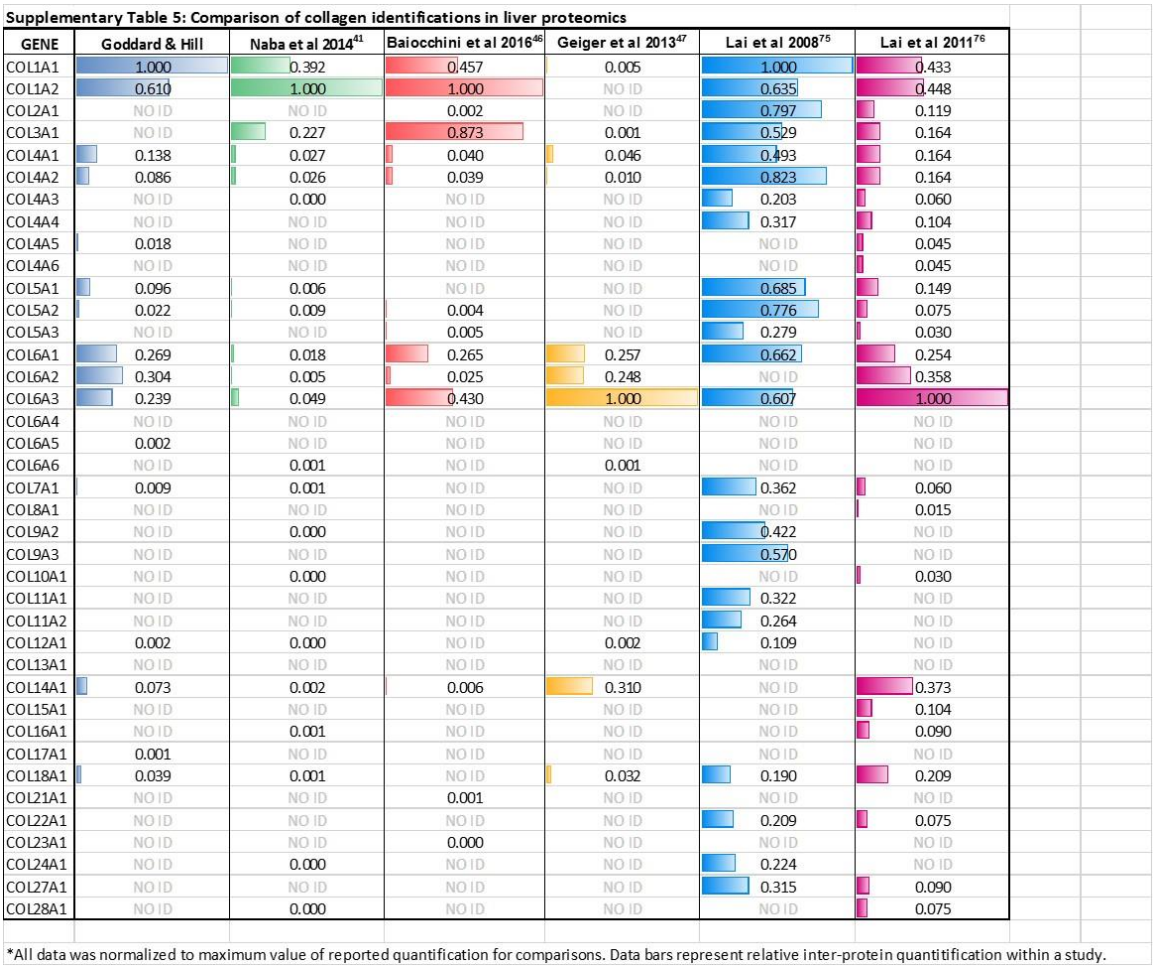

Supplementary Table 5: Comparison of collagen identifications in liver proteomics

GENE	Goddard & Hill	Naba et al 2014[41]	Baiocchini et al 2016[46]	Geiger et al 2013[47]	Lai et al 2008[75]	Lai et al 2011[76]
COL1A1	1.000	0.392	0.457	0.005	1.000	0.433
COL1A2	0.610	1.000	1.000	NO ID	0.635	0.448
COL2A1	NO ID	NO ID	0.002	NO ID	0.797	0.119
COL3A1	NO ID	0.227	0.873	0.001	0.529	0.164
COL4A1	0.138	0.027	0.040	0.046	0.493	0.164
COL4A2	0.086	0.026	0.039	0.010	0.823	0.164
COL4A3	NO ID	0.000	NO ID	NO ID	0.203	0.060
COL4A4	NO ID	NO ID	NO ID	NO ID	0.317	0.104
COL4A5	0.018	NO ID	NO ID	NO ID	NO ID	0.045
COL4A6	NO ID	NO ID	NO ID	NO ID	NO ID	0.045
COL5A1	0.096	0.006	NO ID	NO ID	0.685	0.149
COL5A2	0.022	0.009	0.004	NO ID	0.776	0.075
COL5A3	NO ID	NO ID	0.005	NO ID	0.279	0.030
COL6A1	0.269	0.018	0.265	0.257	0.662	0.254
COL6A2	0.304	0.005	0.025	0.248	NO ID	0.358
COL6A3	0.239	0.049	0.430	1.000	0.607	1.000
COL6A4	NO ID	NO ID	NO ID	NO ID	NO ID	NO ID
COL6A5	0.002	NO ID	NO ID	NO ID	NO ID	NO ID
COL6A6	NO ID	0.001	NO ID	0.001	NO ID	NO ID
COL7A1	0.009	0.001	NO ID	NO ID	0.362	0.060
COL8A1	NO ID	NO ID	NO ID	NO ID	NO ID	0.015
COL9A2	NO ID	0.000	NO ID	NO ID	0.422	NO ID
COL9A3	NO ID	NO ID	NO ID	NO ID	0.570	NO ID
COL10A1	NO ID	0.000	NO ID	NO ID	NO ID	0.030
COL11A1	NO ID	NO ID	NO ID	NO ID	0.322	NO ID
COL11A2	NO ID	NO ID	NO ID	NO ID	0.264	NO ID
COL12A1	0.002	0.000	NO ID	0.002	0.109	NO ID
COL13A1	NO ID	NO ID	NO ID	NO ID	NO ID	NO ID
COL14A1	0.073	0.002	0.006	0.310	NO ID	0.373
COL15A1	NO ID	NO ID	NO ID	NO ID	NO ID	0.104
COL16A1	NO ID	0.001	NO ID	NO ID	NO ID	0.090
COL17A1	0.001	NO ID	NO ID	NO ID	NO ID	NO ID
COL18A1	0.039	0.001	NO ID	0.032	0.190	0.209
COL21A1	NO ID	NO ID	0.001	NO ID	NO ID	NO ID
COL22A1	NO ID	NO ID	NO ID	NO ID	0.209	0.075
COL23A1	NO ID	NO ID	0.000	NO ID	NO ID	NO ID
COL24A1	NO ID	0.000	NO ID	NO ID	0.224	NO ID
COL27A1	NO ID	NO ID	NO ID	NO ID	0.315	0.090
COL28A1	NO ID	0.000	NO ID	NO ID	NO ID	0.075

*All data was normalized to maximum value of reported quantification for comparisons. Data bars represent relative inter-protein quantitification within a study.

Supplementary Table 6-5: Comparison of collagen identifications in liver proteomics

Comparison of our study (Goddard & Hill) to other recently published proteomics evaluations of liver ECM. Data highlighted in this table are specific to various collagen ECM proteins identified.

Acknowledgements

The authors would like to acknowledge Jacob Fischer for assisting with experimental metastasis studies, Hadley Holden for performing special stains, and Weston Anderson for providing editorial review of the manuscript. Monika Dzieciatkowska assisted with QconCAT generation and validation. Finally, the work included in this manuscript includes funding from NIH/NCI NRSA F31CA186524 (to ETG), NIH/NCATS Colorado CTSI UL1 TR001082 for proteomic support, NIH/NCI R33CA183685 (to KH), DOD BC123567 (to PS), BC123567P1 (to KH), and NIH/NCI 5R01CA169175 (to VB and PS). The authors declare no competing financial interests.

Chapter VII: Discussion

Summary of Key Findings

My studies have focused on the over-arching goal of understanding the ~3-fold increased risk for metastasis associated with a postpartum breast cancer diagnosis[9]. In this dissertation, I have described a novel biology of the post-weaning liver, specifically weaning-induced liver involution (Chapter III)[233]. The liver is intimately linked to the mammary gland for the purpose of milk production[230,231], and I hypothesized that this metabolic bridge between the two tissues may persist post-weaning. Weaning-induced liver involution is characterized by hepatocyte cell death and metabolic reprogramming suggestive of a liver response to reduced metabolic demands associated with cessation of lactation[233]. I found that the tissue remodeling process of weaning-induced liver involution, similar to that which occurs in the mammary gland, is not associated with the readily apparent, overt tissue-remodeling characteristic of the post-weaning, involuting mammary gland[46]. The process of involution in the liver is not evident by H&E and required molecular and biochemical assays to uncover. This is important, as it not only explains why weaning-induced liver involution went undiscovered for so long, but also suggests that the orchestrated process of involution differs across tissues, where the process is subtler in a vital organ (i.e. the liver). My findings in the post-weaning liver were highly suggestive of a tissue microenvironment consistent with pro-metastatic niches, as described in Chapter I. Specifically, I observed deposition of numerous ECM proteins including pro-metastatic TNC, collagen I, and collagen IV. Further, I also found influx of monocytes, neutrophils, and FoxP3$^+$ T regulatory cells, as well as an increase in mature macrophages in the liver post-weaning (Chapter III and Appendix A). I utilized two independent experimental metastasis models to test the role of the post-weaning liver

in promoting metastasis distinct from the pro-metastatic influences of the involuting mammary gland or a primary tumor. Further, the pro-metastatic niche established in the involuting liver is transient, as risk for metastasis returned to nulliparous levels when tumor cells were injected 4 weeks post-weaning[233]. To the best of our knowledge, these findings constitute the first direct evidence of a physiologic tissue-remodeling event educating a pro-metastatic microenvironment in the *absence* of a primary tumor. Further, in patient cohort studies where both parity status and site of metastasis data were available, I found that postpartum breast cancer patients diagnosed within 10 years of a pregnancy were at elevated risk for site-specific liver metastasis compared to nulliparous patients. Importantly, the increased risk for metastasis was specific to the liver, as risk for other common sites of breast cancer metastasis (lung, bone, and brain) were not altered in postpartum compared to nulliparous young women with breast cancer[233]. These data suggest that in women, the postpartum liver may be similarly established as a pro-metastatic microenvironment. Thus, we have initiated a first in human liver MRI study to measure volumetric changes to the tissue with pregnancy and upon weaning (Chapter VII, Future Perspective and New Questions). In sum, the involuting liver establishes a pro-metastatic microenvironment post-weaning, which may, in part, explain the high rate of metastasis observed in postpartum breast cancer patients.

With a new understanding for how post-weaning events alter the liver secondary site, priming it for postpartum breast cancer metastasis, I next sought to determine whether non-steroidal anti-inflammatory drugs (NSAIDs) target this pro-metastatic microenvironment. The Schedin lab has previously shown efficacy of NSAIDs in

reducing the pro-tumor microenvironment of the involuting mammary gland, and abrogating primary tumor growth, local dissemination, and both lymph node and lung metastasis[47,113,114] (and Martinson et al., unpublished). Treating with low-dose ibuprofen (human dose equivalent of ~234 mg/daily) during the window of weaning-induced liver involution, I have found that NSAIDs may not have the same anti-tumor effect as observed in the mammary gland (see Chapter IV). Specifically, I observed a small, minimal reduction in TNC deposition and influx of myeloid populations at involution day 6 in treated compared to untreated mice. Further, in an intraportal liver metastasis model, the low-dose of ibuprofen utilized had no impact on risk for developing overt liver metastasis. These data suggested that ibuprofen may have unique effects in the mammary gland as compared to the liver and/or that a higher dose may be necessary to impact the liver microenvironment and risk for metastasis. Importantly, these data do suggest that intervention with NSAIDs to reduce the pro-metastatic attributes of weaning-induced mammary gland involution may not increase risk for liver metastasis, an important safety parameter to consider prior to recommending to patients or in the context of postpartum breast cancer prevention.

While studying the post-weaning liver microenvironment and its impact on risk for liver metastasis in the postpartum setting, I also sought to further understand the high risk for metastasis in a young women's breast cancer cohort from the University of Colorado (see Chapter V). Univariate analysis of time-to-metastasis in this cohort revealed a high risk for metastasis that persists in postpartum diagnoses for up to 10 years after a pregnancy, when compared to nulliparous patients. However, upon multivariate analysis I observed

that only patients diagnosed within 5-10 years after a pregnancy were still at increased risk for metastasis, whereas PPBC<5 patients showed a trend towards increased risk. Intriguingly, stage of disease was highly significant in the multivariate analysis. When we assessed time-to-metastasis in stage I, II, and III patients independently, we found that stage I patients have a reduced risk for metastasis, with the exception of the PPBC<5 group which showed a trend towards increased risk for metastasis. In the stage II patient analysis, postpartum breast cancers diagnosed up to 10 years after a pregnancy were at significantly higher risk for metastasis compared to nulliparous patients. Stage III patients have a uniformly high risk for metastasis, independent of parity status, although group sizes were small for this analysis. We next explored whether enrichment for poor prognostic biologic subtype may explain this high risk for metastasis and found that PPBC patients have a high risk for metastasis after adjustment for biologic subtype, age, and year of diagnosis. In sum, when assessing stage II young women's breast cancers, a postpartum diagnosis is an independent poor prognostic indicator for metastasis. When I compared stage and tumor size across parity groups I observed no difference, even in the postpartum breast cancer group, suggesting that the high risk for metastasis is not due to delays in diagnosis. Importantly, we also observed that postpartum breast cancer patients are much more likely to present with lymph nodes positive for disease at diagnosis. Further, I found a significant increase in the frequency of postpartum breast cancer patients undergoing chemotherapy when compared to all other parity groups. Thus, despite no apparent delay in diagnosis and a higher rate of cytotoxic chemotherapy intervention compared to nulliparous patients, postpartum breast cancer patients are more likely to present with lymph node involvement and are at greater risk for metastasis.

Previously published work showed that postpartum breast cancers are characterized by increased peri-tumor lymphatic density and lymph node metastasis in PPBC<2 patients[114]. Thus, these data further support the hypothesis that the tissue remodeling events in the postpartum breast, including lymphangiogenesis, may sculpt the primary tumor and promote tumor progression. Importantly, we also found that patients diagnosed at stage III are at high risk for metastasis regardless of parity status, suggesting delayed diagnoses are a major problem in young women's breast cancer. Despite much work, biomarkers to identify young women's or postpartum breast cancer patients at highest risk for developing metastasis are lacking[23]. My recent analysis of ECM proteomics on the rodent mammary gland across reproductive stages has revealed an increase in numerous tumor-promotional or tumor-associated ECM proteins during weaning-induced mammary gland involution (Chapter VI)[94]. Although ECM composition has not yet been assessed in the human breast post-weaning, the dynamic tissue remodeling process of weaning-induced breast involution[77] likely contributes to increased postpartum breast cancer risk for metastasis. The ECM proteins elevated during weaning-induced mammary gland involution, including tumor promotional TNC and collagen 6 (see Chapter VI)[94], may aid in identification of stromal biomarkers for predicting patient prognosis.

In summary, the work I have done has contributed to our understanding of the high rate of metastasis in postpartum breast cancers. Specifically I have identified a new mechanism by which breast cancers successfully establish metastases, through a physiologic tissue-remodeling event that establishes a liver pro-metastatic microenvironment more supportive of metastatic success. I have also confirmed that

NSAID intervention during the post-weaning involution period does not appear to increase risk for liver metastasis, an important step towards promoting recommendations for this therapeutic option into the clinical setting for postpartum breast cancer patients. Further, study of a young women's breast cancer cohort has further clarified how a postpartum diagnosis relates to and interacts with other poor prognostic indicators including tumor size, lymph node positivity, and biologic subtype. All of these results support the concept that tissue microenvironments dictate risk for metastasis, and that these diverse tissue microenvironments may be targetable and/or harnessed to identify those patients at highest risk for progression.

Future Perspectives and New Questions

Understanding the mechanism underlying initiation of weaning-induced liver involution in rodents

Through my dissertation work I have discovered a novel biology of the rodent liver, namely weaning-induced liver involution described in detail in Chapter III[233]. Despite this discovery and continuous work to characterize weaning-induced liver involution and understand the underlying mechanisms of postpartum breast cancer metastasis there are still numerous unanswered questions. One major area to be explored in future studies is the underlying mechanism of how weaning-induced liver involution is initiated. We have the unique benefit of insight from published studies investigating signals that lead to mammary gland involution after weaning to aid our investigations in the liver.

Previous work has strongly implicated metabolic signals, in particular milk stasis and signal transducer and activator of transcription 3 (Stat3) signaling, in the induction of mammary gland involution[41,460-462]. Murine studies in which nursing dams had 1 teat sealed with surgical adhesive revealed that milk stasis induced involution despite the presence of systemic hormones of lactation induced by suckling on adjacent teats[462]. Conditional Stat3 knockout post-weaning resulted in delayed mammary gland involution, including reduced mammary epithelial cell death, a lack of macrophage influx, and delayed adipocyte repopulation[460,461]. Recent work has shown that Stat3 signaling drives mammary epithelial cell (MEC) uptake of lipids upon milk stasis[41]. Lysosomal accumulation of lipid in MECs induces cell death via lysosomal membrane instability and subsequent release of cathepsins[41]. Work utilizing the Mafia (macrophage fas-induced

apoptosis) mouse, in which colony stimulating factor 1 receptor (CSF1R) positive cells express a suicide transgene and GFP, has shown that macrophage depletion (and depletion of other CSF1R-expressing populations) at time of weaning results in severely delayed mammary involution via loss of cathepsin-mediated lysosomal cell death[463]. Importantly, this blockade of mammary gland involution occurs in the presence of milk stasis and pStat3, suggesting that macrophages provide an essential signal in the initiation of weaning-induced mammary involution[463]. Based on these data we hypothesized that weaning-induced liver involution is initiated by macrophage influx and/or metabolite signals, similar to mammary gland involution. I undertook preliminary studies to investigate this hypothesis:

Stat3 signaling in the post-weaning liver:

We first sought to understand whether Stat3 signaling might play a role in initiating weaning-induced liver involution. To this end we performed immunoblots for phosphorylated Stat3 (pStat3) and total Stat3 in rat liver lysates (Fig.7-1). We found that Stat3 is not phosphorylated until later time-points during weaning-induced liver involution, suggesting that the initiating signal for liver involution is not Stat3 mediated.

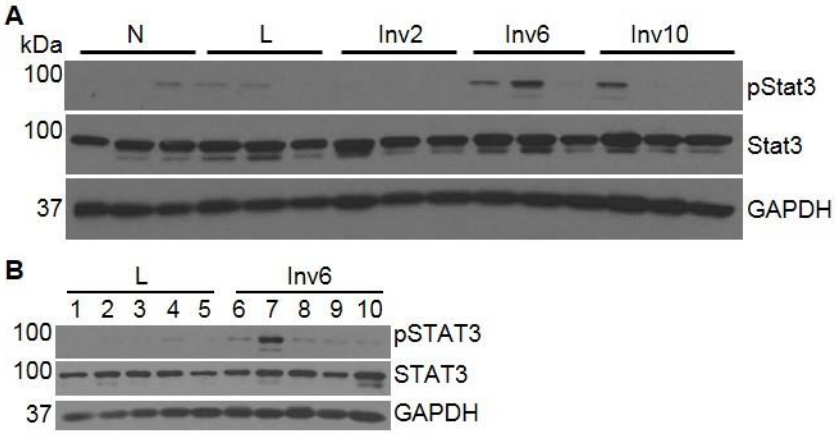

Figure 7-1: Stat3 phosphorylation does not occur at early involution in the liver

(A-B) Immunoblot for pStat3, total Stat3, and GAPDH in whole rat liver lysates; n=3 livers/grp (A) or 5 livers/grp (B).

Investigating the impact of macrophage depletion on post-weaning liver involution:

We next opted to explore the impact of macrophage depletion on weaning-induced liver involution utilizing the Mafia mouse model (see Appendix C for methods)[464]. Mice were treated with the B/B Homodimerizer drug, which induces cell death in CSF1R expressing cells, starting 3 days before weaning to ensure macrophage depletion prior to the initiation of involution. Systemic macrophage depletion was verified by a significant reduction in $CD45^+F4/80^+GFP^+$ myeloid cells in the blood (Fig.7-2A-B). We simultaneously observed that macrophage depletion results in rapid body weight loss in mice (Fig.7-2C). Weight loss was also observed in the livers of Mafia mice, translating to a premature reduction in liver weight at Inv1, prior to the onset of liver weight loss induced by involution[233] (Fig.7-2D). The liver weight loss observed was proportional to body weight loss (Fig.7-2E). To understand whether systemic macrophage depletion in this model results in a depletion of myeloid populations in the liver, flow cytometry was performed on whole livers from Mafia mice treated with vehicle or drug (Fig.7-3A-C). The flow cytometry gating schemes revealed a clear presence of $CD11b^+F4/80^+$ macrophages despite drug treatment to deplete macrophages (Fig.7-3A-B). Similarly, we observed an influx in $CD11b^+Ly6C^+Ly6G^{+/-}$ myeloid cells that do not clearly separate into the $CD11b^+Ly6C^+Ly6G^-$ monocyte and $CD11b^+Ly6C^+Ly6G^+$ neutrophil populations observed in vehicle controls (Fig.7-3A-B). We also assessed for $CD11c^+MHC2^+$ dendritic cells (Fig.7-3C). Quantification of flow cytometry data revealed an increase in both mature macrophages and $CD11b^+Ly6C^+$ myeloid cells (Fig.7-4A-B). Because differentiation between monocytes and neutrophils was not possible in drug treated mouse flow schemes, we combined the quantification of monocytes and neutrophils for

vehicle treated mice in this analysis (Fig.7-4B). We further investigated whether macrophage depletion resulted in reduction of Kupffer cells specifically expressing high levels of GFP, indicative of transgene expression[464]. These analyses showed that a large proportion (~2/3^{rds}) of macrophages in the liver express low levels of GFP, with only ~1/3rd of Kupffer cells expressing high levels of GFP, and thus the transgene (Fig.7-4C). Intriguingly, we saw the largest increases in macrophages in the GFP^{hi} expressing macrophage subset (Fig.7-4C). We did see depletion of CD11c^{+}MHC2^{+} dendritic cells, which are also targeted in the Mafia mice, confirming that the drug treatment was having an effect on other CSF1R expressing myeloid populations in the liver (Fig.7-4D). Our lack of macrophage depletion was not expected based on previous studies in the Mafia mouse liver where macrophages were reportedly depleted[464] and could be explained by numerous factors. For one, the drug concentration utilized in these studies was reduced to 1 mg/kg of vehicle or drug, a 10-fold reduction in drug concentration from previous studies[463,464]. This drug treatment strategy was enacted to reduce complicating side effects including weight loss and subsequent euthanasia[464]. Another explanation is that macrophage depletion in the liver, where Kupffer cells account for ~15% of cells by weight[465], results in catastrophic insult to the liver. This stress to the liver may result in the immediate and robust influx of immature myeloid populations as the liver responds to macrophage depletion by replenishing lost cells. Further, when this treatment strategy is introduced during a time of additional stress in the liver (i.e. liver involution) it may result in further aggravation and explain why these results were not previously reported. Finally, a lack of transgene expression in Kupffer cells may also explain the sub-optimal depletion seen in this model (Fig.7-4C). In summary this data revealed major caveats in

the Mafia mouse model, including a lack of macrophage depletion and/or an immediate compensation of the liver to macrophage depletion via influx of monocytes that subsequently differentiate into macrophages.

Despite major caveats, we did perform preliminary analyses to quantify hepatocyte apoptosis in livers from these studies using terminal deoxynucleotidyl transferase dUTP nick end labeling (TUNEL) to label cleaved DNA. These data revealed the expected increase in apoptotic hepatocytes by early-to-mid liver involution in the vehicle treated control group[233] (Fig.7-4E). We also observed an increase in hepatocyte apoptosis from day 2 to day 3 post-weaning in the drug treatment group, suggesting that weaning-induced liver involution is either still occurring and/or general tissue disruption caused by macrophage depletion in the macrophage rich liver microenvironment induces hepatocyte cell death independent from involution (Fig.7-4E). Taken together, these data suggest that disruption of myeloid populations does not result in abrogation of hepatocyte apoptosis during weaning-induced liver involution. Further, it is important that the drawbacks described above be taken into consideration if future studies focused on weaning-induced liver involution are to be done with the Mafia mouse model.

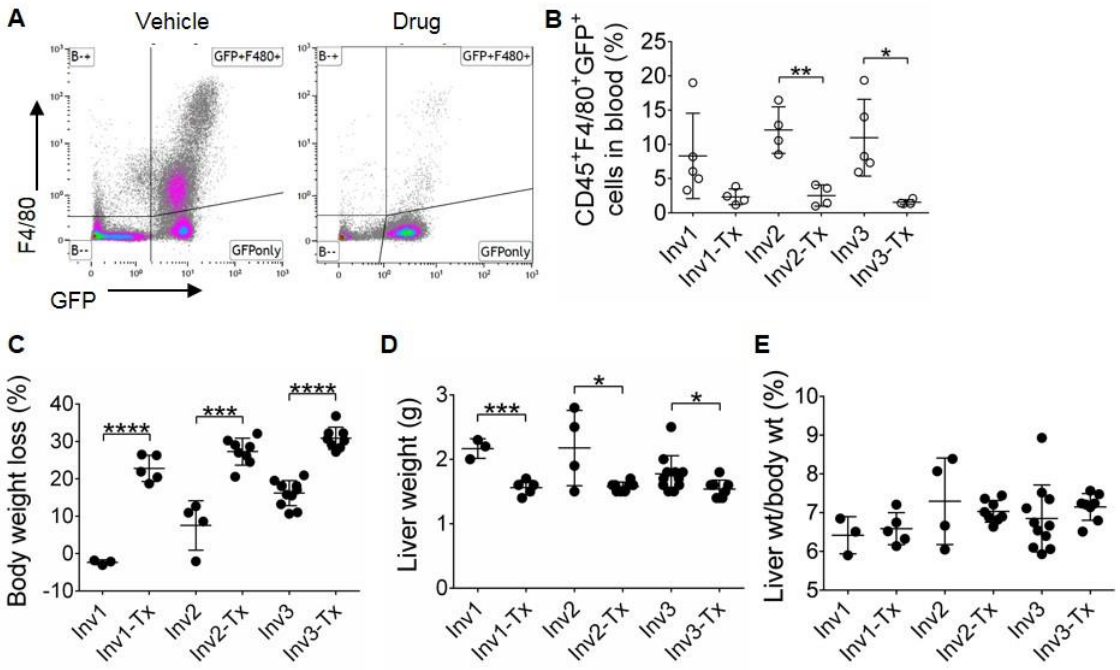

Figure 7-2: Macrophage depletion results in body weight and liver weight loss but does not impact hepatocyte cell death during weaning-induced liver involution

(A) Representative flow cytometry plots of Mafia mouse blood samples showing depletion of $F4/80^{+}GFP^{+}$ populations with drug treatment. Samples are from Inv3 mice. **(B)** Depletion of $CD45^{+}F4/80^{+}GFP^{+}$ myeloid cells in whole blood from Mafia mice. **(C)** Percent body weight loss over pre-treatment body weight in controls and drug treated Mafia mice. **(D)** Mafia mouse liver weight. **(E)** Mafia mouse liver weight normalized to body weight. Two-tailed Students T-test, *=p-value<0.05, **=p-value<0.01, ***=p-value<0.001, ****=p-value<0.0001.

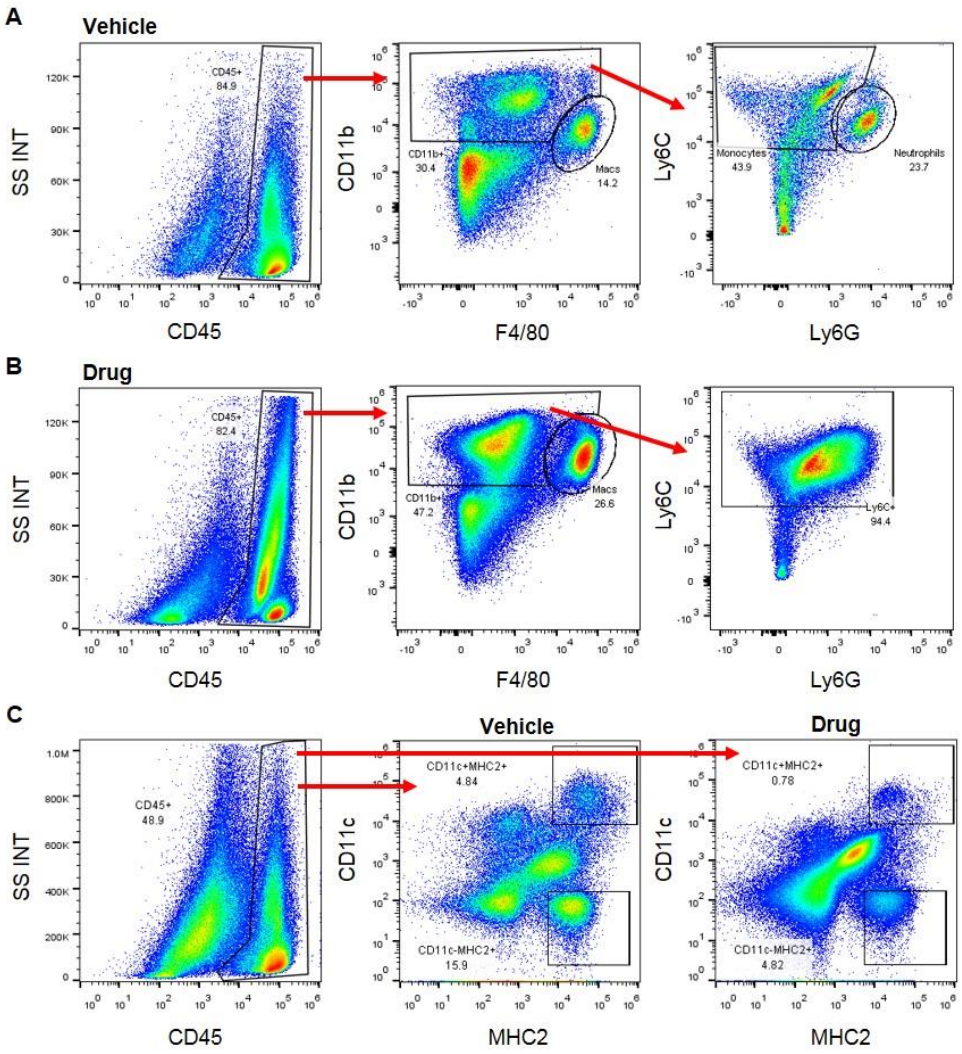

Figure 7-3: Flow cytometry liver myeloid cell gating scheme for MaFIA mouse studies

(A-B) Whole murine livers were prepared for flow cytometry. Samples were gated off of viable cells based upon forward by side scatters and singlets were removed (data not shown). Representative plots for $CD45^+$ gating (left plots), $CD11b^+F4/80^-$ gating, and $CD11b^+F4/80^+$ gating schemes (middle plots) in vehicle (B, top plots) and drug (C, bottom plots) treated mice. Right plots show $Ly6C^+$ and $Ly6G^+$ gating schemes to identify monocytes ($Ly6C^+Ly6G^-$) and neutrophils ($Ly6C^+Ly6G^+$) in vehicle treated mice (top plot). Data show a clear influx of $CD11b^+Ly6C^+$ cells in the drug treated mice (bottom plot) that does not resemble $CD11b^+$ populations in controls. **(C)** Representative plots for $CD45^+$ gating (left plot) and $CD11c^+MHC2^+$ gating to identify dendritic cells in livers of vehicle (middle plot) and drug (right plot) treated mice. Dendritic cells are identified by the upper right hand population.

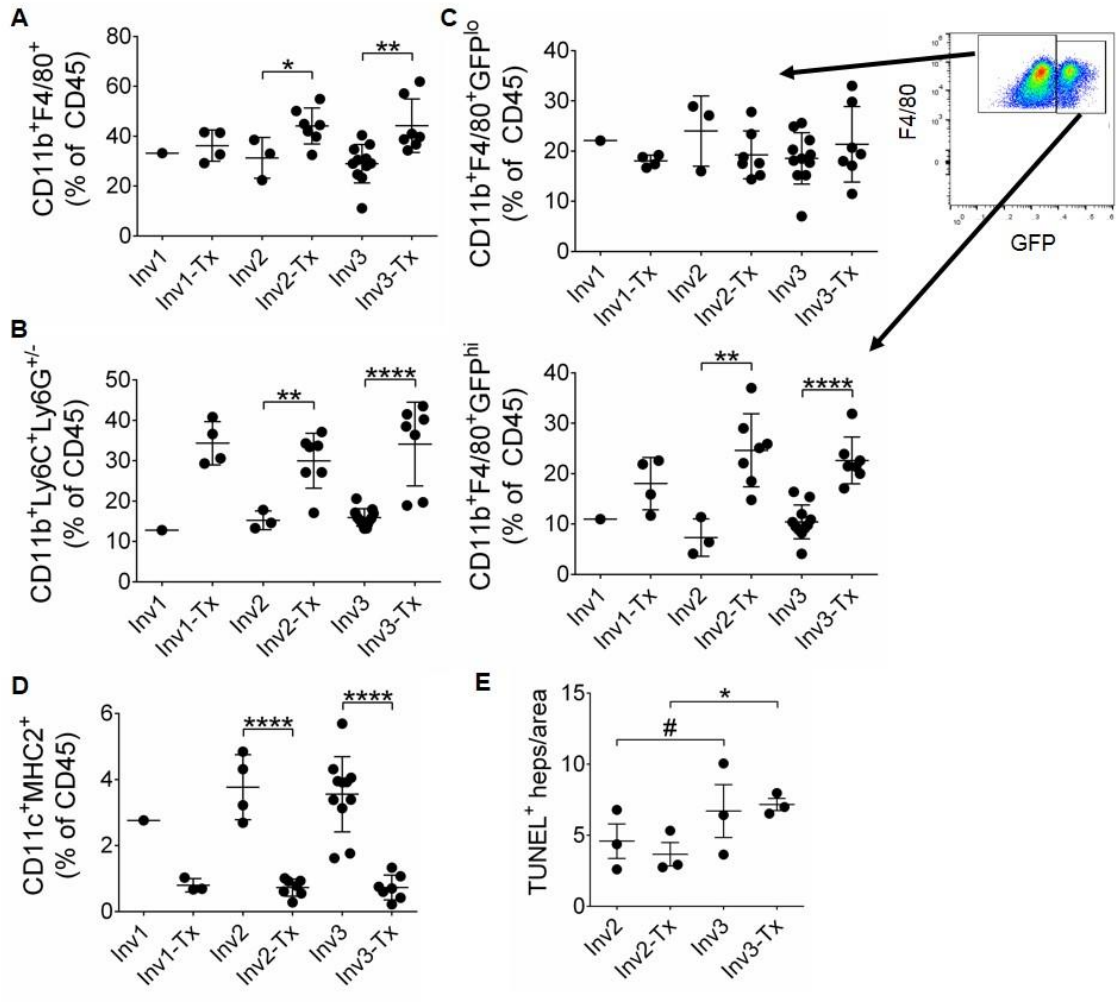

Figure 7-4: Macrophage depletion drug regimen in MaFIA mice increases macrophage and monocyte populations and depleted dendritic cells in the liver

(A) Flow cytometry for $CD11b^{+}F4/80^{+}$ macrophages from whole mouse liver of vehicle or drug treated MaFIA mice during weaning-induced involution. **(B)** Flow cytometry for $CD11b^{+}F4/80^{-}Ly6C^{+}Ly6G^{+/-}$ macrophages from whole mouse liver of vehicle or drug treated MaFIA mice during weaning-induced involution. **(C)** Flow cytometry for macrophages expressing low levels of GFP (top) and high levels of GFP (bottom), and representative flow plot (right). **(D)** Flow cytometry for $CD11c^{+}MHC2^{+}$ dendritic cells from whole mouse liver of vehicle or drug treated MaFIA mice during weaning-induced involution. **(E)** Quantification of TUNEL positive hepatocytes per liver area; whole liver sections were analyzed. Unpaired Student's T-test, *=p-value<0.05, **=p-value<0.01, ***=p-value<0.001, ****=p-value<0.0001; One-tailed Students T-test, #=p-value<0.05. Sample size limitations did not permit statistics on Inv1 groups.

Investigating metabolic flux-mediated induction of post-weaning liver involution:

We have also initiated studies to investigate whether a metabolite signal may induce weaning-induced liver involution in rodents. During lactation it is well known that the liver plays a pivotal role in fulfilling the metabolic demands of milk production[230-232]. Specifically, the liver increases lipid β-oxidation to make ATP necessary for gluconeogenesis. Glucose made in the liver is subsequently shuttled to the mammary gland, via the circulation, where it is utilized for production of lactose and glycerol backbones for triglycerides – both essential components of milk (Fig.7-5)[230-232]. In states of glucose deficiency, the mammary gland will utilize fatty acids from other sources including the liver, however, under steady-state conditions the major sources of triacylglycerol are dietary lipid and *de novo* fatty acid synthesis in the gland[231,310]. Upon weaning, the excess metabolites from milk (protein, carbohydrate, lipid) are taken up by mammary epithelial cells[41], and presumably by adipose tissue, muscle, and liver as well. Uptake of lipid by non-adipose tissues can result in lipotoxicity and apoptosis, as has been demonstrated in pancreatic β-cells[466] and hepatocytes during non-alcoholic fatty liver disease[467]. Based on these data we hypothesized that with cessation of lactation and milk stasis in the gland, there is a backlog of metabolites in the circulation and/or liver, which provide the initiating signal for liver involution to begin. We first measured glucose levels via saphenous vein blood draw in mice across the reproductive cycle using a glucometer. These data revealed that blood glucose levels are largely unaltered at early time points post-weaning and likely do not initiate weaning-induced liver involution (Fig.7-6A-B). We also assessed free fatty acid (FFA) levels in plasma collected from rats across the reproductive cycle. We found an increase in FFA at late pregnancy (P)

compared to lactation, which is not surprising considering any freely available lipid during lactation is likely to be taken up by the fat pad to facilitate milk production (Fig.7-6C). These data suggest that lipid levels may be in flux during lactation and thus may similarly shift with weaning. Thus, we stained for the lipid droplet marker adipophilin in rat livers across the reproductive cycle. Quantification of this staining revealed a significant and transient increase in lipid at Inv2 in the rat liver (Fig.7-6D). Staining for adipophilin in the mouse liver revealed a similar increase in the lipid droplet marker, although this increase in global adipophilin occurred much later, at Inv8 (Fig.7-6E). However, analysis of the peri-portal region in these murine livers revealed a specific increase in adipophilin at Inv2, consistent with what we observed in rat livers (Fig.7-6E-F). Taken together these data suggest the possibility that lipid build-up in the rodent liver may be important for initiation of post-weaning liver involution.

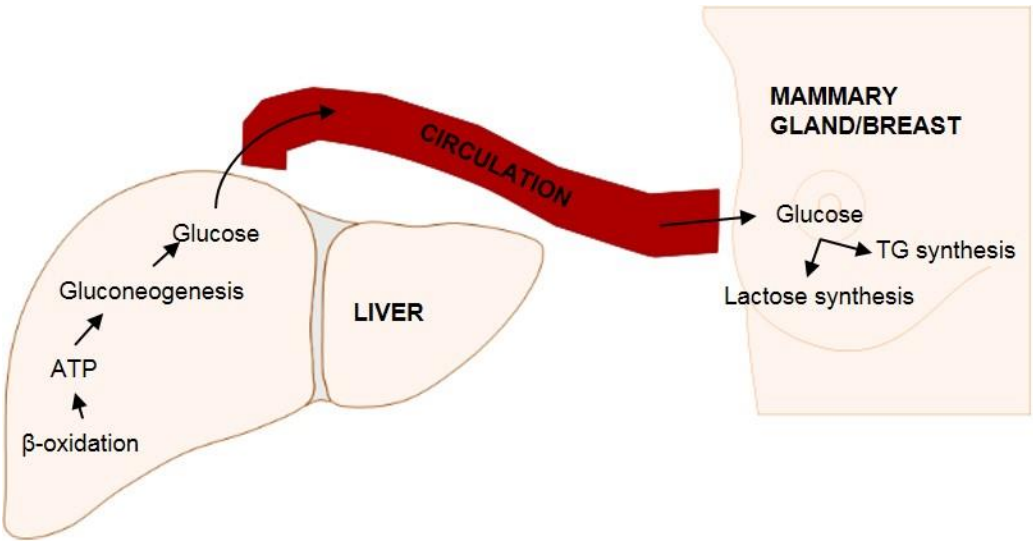

Figure 7-5: Complementary roles for liver and mammary gland in milk production during lactation

Studies have identified a role for the liver in milk production during lactation. Specifically, the lipid breakdown metabolic pathway, β-oxidation, is upregulated in the liver during lactation. It is thought that the ATP produced from b-oxidation is utilized for gluconeogenesis, resulting in elevated glucose production. Glucose is easily shuttled through the circulation to the mammary gland or breast where it is utilized for production of milk sugar and the triglyceride glycerol backbone (Rawson et al., J Proteomics, 2012; Patel et al., Funct Integr Genomics, 2011; Loor et al., Physiol Genomics, 2005). Figure made using Biomedical Toolkit.

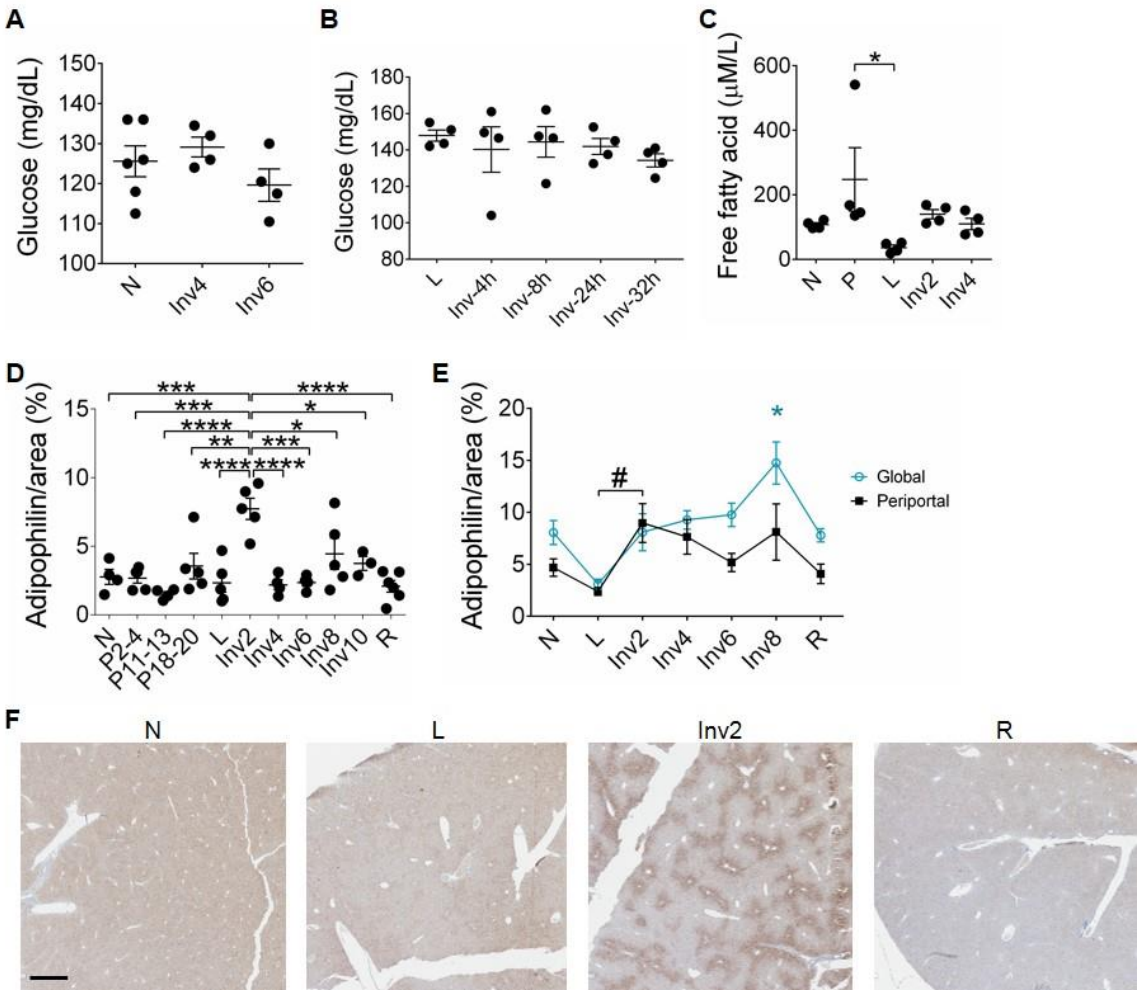

Figure 7-6: Lipids may constitute the initiating signal for weaning-induced liver involution

(A) Blood glucose readings via glucometer from saphenous vein blood draw on mice at end-point, across the reproductive cycle. **(B)** Blood glucose readings via glucometer from serial saphenous vein blood draw on mice at early time-points post-weaning. **(C)** Free fatty acid detection in rat liver plasma collected across the reproductive cycle. **(D)** Quantification of adipophilin staining in the rat liver across the reproductive cycle. **(E)** Quantification of adipophilin staining in the whole mouse liver (global, One-way ANOVA = Inv8 is significant versus N, L, Inv2, R) and in the periportal regions (periportal, Student's T-test, p=0.03) across the reproductive cycle. **(F)** Representative images of mouse liver adipophilin staining; scale bar=1 mm. One-way ANOVA, *=p-value<0.05, **=p-value<0.01, ***=p-value<0.001, ****=p-value<0.0001; One-tailed Students T-test, #=p-value<0.05. Sample size limitations did not permit statistics on Inv1 groups.

Despite these data, the question of what initiates liver involution remains largely unanswered. Studies to further elucidate the mechanism of weaning-induced liver involution are on-going and include RNA sequencing and lipidomics on murine livers and matching mammary glands across the reproductive cycle. Results from these studies should provide essential data on pathways altered at the onset of liver involution (including cell death and metabolic pathways) and identify lipids- or metabolites-of-interest that may be most important for post-weaning involution in the liver. Simultaneously, we are developing a hepatocyte culture system to study how potential mediators of weaning-induced liver involution, including purified fatty acids, impact 'naïve' hepatocytes isolated from nulliparous mice. End-points for these studies will include gene expression profiling and assays to determine changes in metabolism and cell death pathways. Based on the adipophilin staining in rodent liver, and with future lipidomic studies, we will want to understand in greater detail the fate of lipid/metabolites of interest in the liver during lactation, early involution, and late involution/regression stages. Although omic approaches facilitate identification of metabolites of interest, we are only provided a snapshot of semi-quantitative levels of these products. To understand metabolite-of-interest flux throughout the reproductive cycle it may be of interest to employ *in vivo* studies utilizing C^{13} stable isotope labeling coupled with metabolomics[468]. Importantly, the observed increase in lipid in the liver post-weaning may be due to a reduction in the gluconeogenesis and β-oxidation flux, an increase in lipid uptake or synthesis, or via more nuanced metabolic shifts. Stable isotope labeling and LC-MS will help to clarify what pathways are altered and may provide essential measurement of metabolite-of-interest flux as a follow-up to semi-quantitative metabolomics

studies[468,469]. To understand whether lipid is shuttled from the fat pad to the liver upon weaning we could inject commercially available stable isotope labeled lipid intraductally and assess for their presence in the liver at early time-points post-weaning[470]. In concert, these studies may further elucidate the complex relationship between the liver and mammary gland during lactation and upon weaning. Further, the proposed experiments may help to identify metabolic pathways essential to induction of weaning-induced liver involution.

Direct manipulation of lipid composition may have measureable effects on weaning-induced liver involution and mammary tumor metastasis. At this time, the lipid composition of the postpartum involuting liver is unknown. We hypothesize that lipid composition may play important roles in the transient pro-metastatic liver microenvironment established post-weaning. Studies to target lipid composition could include assessing weaning-induced liver involution and mammary tumor liver metastasis in the Fat-1 transgenic mouse. These mice contain a transgene expressing a fatty acid desaturase from *Caenorhabditis elegans* that facilitates conversion of inflammatory omega-6 to anti-inflammatory omega-3 fatty acids[471]. An increase in omega-3 fatty acids results in reduced risk for non-alcoholic fatty liver disease, primary tumor development in the liver, and has shown efficacy in reducing metastasis from mammary tumors[472-475]. Thus, it is possible that a shift in liver lipids from an omega-6 to an omega-3 dominant composition may not only alter the pro-metastatic attributes of weaning-induced liver involution and/or reduce the high risk for liver metastasis post-weaning[233].

Contributions: I performed Stat3 immunoblots, developed flow cytometry staining protocols, performed all Mafia mouse flow cytometry data analysis, tissue staining/analysis, as well as glucose, FFA, and rat adipophilin analysis. Jaime Fornetti and Michelle Borakove performed Mafia mouse husbandry, tissue collection, and flow cytometry. Alexandra Quackenbush performed mouse adipophilin staining and analysis.

Future studies addressing the pro-metastatic microenvironment established during weaning-induced liver involution

The post-weaning, involuting rodent liver shares numerous attributes with the metastatic niche including ECM deposition/remodeling and myeloid cell influx (see Chapter III)[233]. We have shown further that the post-weaning liver supports increased metastatic seeding but not outgrowth in two experimental metastasis models[233]. However, there is much about this pro-metastatic microenvironment that we do not currently understand. Several key areas for future research include understanding 1) the functional contribution of the ECM to the pro-metastatic niche 2) the contribution of immune-suppressive leukocyte populations to the microenvironment and 3) how the pro-metastatic microenvironment supports distinct steps in the metastatic cascade. I will discuss each of these areas briefly.

<u>Functional contribution of liver ECM to the pro-metastatic niche:</u>

Extensive studies in rodent models of mammary gland development have identified the ECM as a key regulator of progenitor and mature epithelial cell function - contributing to proliferation, differentiation, and cell death decisions. These pioneering investigations redefined the functional unit of the epithelial cell as the cell plus its adjacent ECM[421,422],

and shifted studies aimed at understanding determination of epithelial cell fate from a cell-intrinsic to an epithelial cell-stromal focus[423]. To query epithelial cell-ECM interactions in a more physiologically relevant context, many of these paradigm shifting studies utilized 3D cell culture with Matrigel™, a commercially available ECM isolated from Engelbreth-Holm-Swarm (EHS) mouse sarcomas, as cellular substratum[476]. EHS matrix is highly enriched in laminin-111, a heterotrimeric basement membrane glycoprotein that provides important attachment signals to epithelial cells via specific integrins[477]. Thus, the functions of matrix proteins have been primarily assessed using single, purified ECM proteins or by admixing ECM proteins of interest with EHS matrix for use in various 3D assays[425-428]. However, to advance our understanding of tissue-specific epithelial and tumor cell niches and their potential impact on physiology and pathology, improved models that recapitulate the complexity of *in vivo* ECM microenvironments are needed. Subsequent advancements to study epithelial cell-niche interactions include micropatterned models[478], microenvironment microarrays (MEArrays)[479,480], hydrogels with regulated stiffness[481], decellularized tissue ECM scaffolds[482,483], and enrichment of endogenous ECM for 3D culture[46,484]. Using mammary matrix isolated from nulliparous hosts, normal mammary epithelial cells recapitulate duct- and alveolar-like structures similar to those in nulliparous hosts[46]. Mammary cells form florid, alveolar-like structures reminiscent of pregnant glands when plated onto mammary matrix isolated from pregnant hosts, and undergo cell death on mammary matrix isolated from involuting glands. These same cells form smaller duct-like structures when plated onto mammary matrix from parous hosts[46]. This reduced regenerative capacity is consistent with functional changes to ECM contributing to parity-induced

protection from breast cancer[296]. During weaning-induced liver involution we found deposition of pro-metastatic ECM proteins, including collagen I, collagen IV, and TNC[233]. Thus, we opted to further develop protocols for isolation of endogenous mammary gland ECM[484] for studies of liver ECM.

Initial enrichment of ECM from rat and mouse liver revealed substantial increases in the ECM proteins laminin and TNC, and potential decreases in the cellular protein glyceraldehyde 3-phosphate dehydrogenase (GAPDH) by immunoblot (Fig.7-7A, see Appendix C for methods). Specifically, we observed 4- and 11-fold enrichments in laminin and >50-fold enrichments in TNC in mouse and rat liver ECM isolations, respectively (Fig.7-7A). Primary mouse hepatocytes cultured within liver matrix maintained hepatocyte phenotype and viability (Fig.7-7B-C). We also cultured D2A1 and D2.OR mouse mammary tumor cell lines in liver matrices to model the liver-metastatic niche and show that endogenous liver matrix supports mammary tumor cell growth (Fig.7-7D). Taken together, these findings provide rationale for utilizing enriched liver ECM to investigate the role of ECM in both hepatocyte-niche and tumor cell-niche interactions during involution. Of note, the current ECM enrichment protocol may be further optimized to reduce contamination of cellular proteins that currently remain after ECM enrichment (Fig.7-7A). Protocol steps that may impact cellular protein contamination include centrifugation speeds and time, duration of dialysis, and homogenization time and generator size[484]. Further, it is well known that primary hepatocytes maintain their phenotype and remain viable in culture for only a few days[485,486]. In particular, density of cell plating, and culture conditions including the 3D

culture model chosen[484], and incorporation of other cell types should all be considered. Assessment of hepatocyte function using standard assays to detect albumin and urea synthesis, as well as expression analyses for albumin, fumarylacetoacetate hydrolase (FAH), and cytochrome P450 (CYP) enzymes may be useful in protocol optimization[486,487]. 3D culture models, upon further optimization, may be useful in assessing the impact of involution-specific liver ECM on both hepatocytes and mammary tumor cells. We hypothesize that involution-specific liver ECM provides essential cues to hepatocytes that may include cell death signals and/or signals that elicit metabolic changes, both of which are observed during weaning-induced liver involution[233]. We also hypothesize that involution-specific liver ECM is an essential component of the pro-metastatic microenvironment established post-weaning. Studies to address this hypothesis include 3D culture of mammary tumor cells on liver ECM enriched from nulliparous, lactating, involuting, and regressed rodents. These studies will facilitate an understanding of whether involution-specific liver ECM supports differential tumor cell growth, invasive phenotype, and gene/protein expression in comparison to other more quiescent stages. Further, these *in vitro* studies will allow for targeted manipulation of ECM proteins of interest, including TNC and Collagen, utilizing blocking antibodies to the protein and/or the integrins that bind them. These studies would complement *in vivo* work utilizing knockout mice or targeting studies for ECM proteins/ECM-cell interactions designed to test the role for ECM in facilitating liver metastasis during involution. However, in vivo work in transgenic mice to understand both weaning-induced mammary gland and liver involution have been greatly hampered by the fact that normal gland development and lactation are typically aberrantly affected, rendering study of the

involution process highly compromised. Further, much work would be required prior to drawing conclusions from knockout mouse studies to ensure that abrogation of the protein of interest does not result in aberrant tissue development, lactation, or the involution process itself.

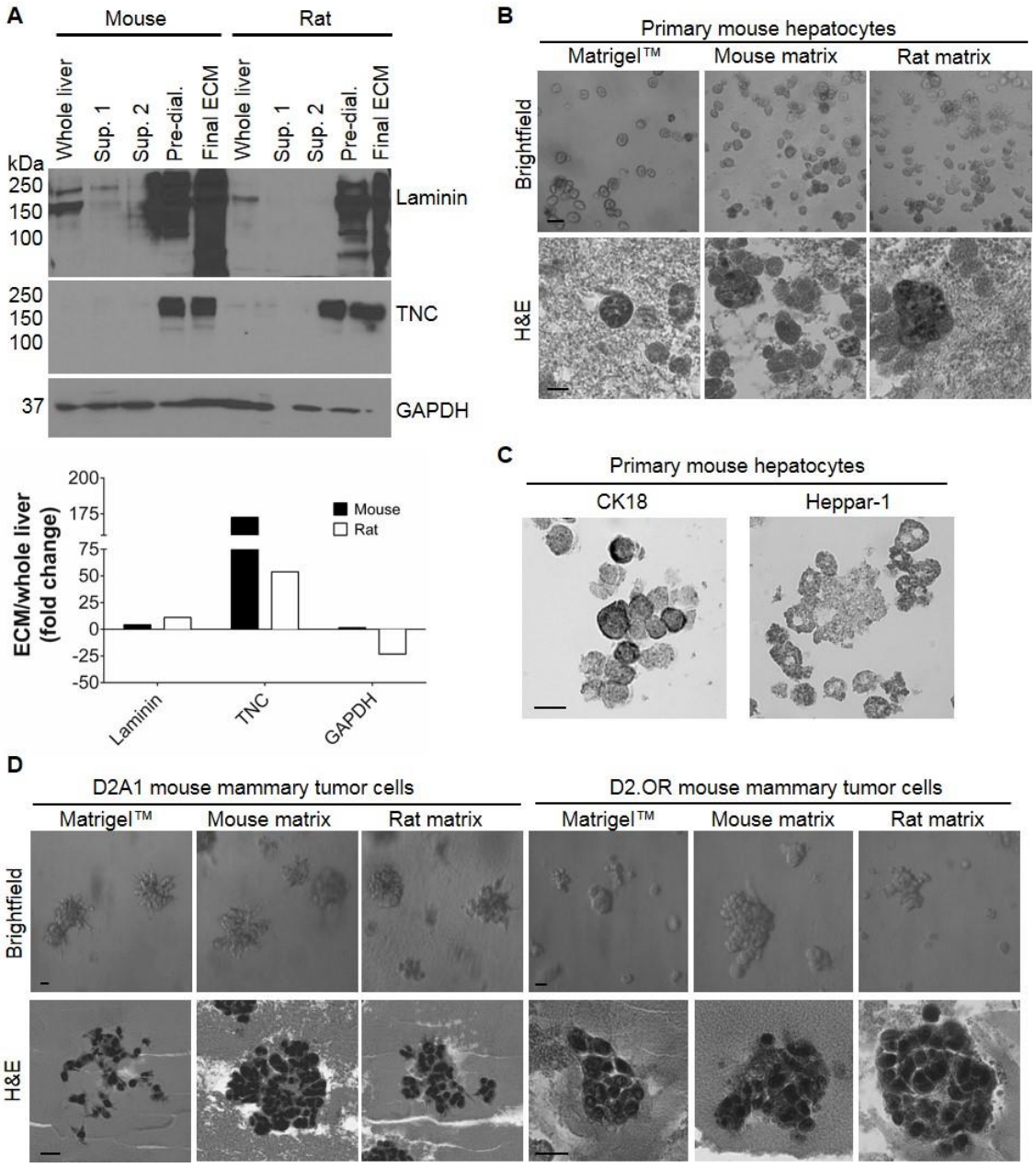
A
Mouse
Rat
Whole liver
Sup. 1
Sup. 2
Pre-dial.
Final ECM
kDa
250
150
100
Laminin
TNC
37
GAPDH
ECM/whole liver (fold change)
Mouse
Rat
Laminin
TNC
GAPDH
B
Primary mouse hepatocytes
Matrigel™
Mouse matrix
Rat matrix
Brightfield
H&E
C
Primary mouse hepatocytes
CK18
Heppar-1
D
D2A1 mouse mammary tumor cells
D2.OR mouse mammary tumor cells
Matrigel™
Mouse matrix
Rat matrix
Brightfield
H&E

Figure 7-7: Development of a 3D culture system using enriched endogenous mouse and rat liver matrix

(A) Immunoblots for laminin, TNC, and GAPDH on samples at various stages of ECM enrichment in mouse and rat liver (top), and densitometry represented as fold change of final ECM signal over starting tissue signal (bottom). **(B)** Representative images of primary mouse hepatocyte 3D cultures in Matrigel™ or enriched rodent liver matrix after 5 days in culture (top). Representative H&E images of primary mouse hepatocytes in liver matrix 3D cultures (bottom); scale bars=25 μm. **(C)** Representative images of primary mouse hepatocytes from rodent liver matrix 3D cultures, fixed with methacarn, and stained for hepatocyte markers CK18 (left) and Heppar-1 (right); scale bar=20 μm. **(D)** Representative images of D2A1 (left) and D2.OR (right) mouse mammary tumor cell 3D cultures in Matrigel™ or enriched rodent liver matrix after 7 days in culture (top). Representative H&E images (bottom) of D2A1 (left) and D2.OR (right) mouse mammary tumor cell 3D cultures; scale bars=20 μm.

Contribution of immune-suppressive leukocyte populations to the microenvironment:

We have previously shown that monocytes, neutrophils, and mature macrophages increase in the liver during weaning-induced liver involution (see Chapter III)[233]. We also observed an increase in FoxP3$^+$ T regulatory cells (Appendix A Fig.2C) but no change in the presence of CD4$^+$ or CD8$^+$ T lymphocytes (Appendix A Fig.2A-B). As described in Chapter I, the involuting mammary gland is established as an immune suppressed microenvironment. The tissue microenvironment has been shown to have high levels of IL-4 and IL-13, cytokines that induce alternatively activated macrophages[43]. Further, weaning-induced mammary gland involution is characterized by an influx of IL-10$^+$ immune-suppressive myeloid cells that suppress T cell activation *ex vivo* and contribute to primary tumor growth[42]. Furthermore, bone marrow derived monocytes and other myeloid cells play an integral role in establishing pre-metastatic niches and promote every stage of the metastatic cascade including metastatic seeding and outgrowth, summarized in detail in Chapter I[52,171,196,197,201,205]. Thus, I have sought to understand whether immune suppression also occurs during weaning-induced liver involution.

Several key studies should be completed including 1) gene expression profiling of sorted CD11b$^+$ myeloid populations 2) T cell suppression assays utilizing isolated CD11b$^+$ myeloid populations, and 3) detailed T cell phenotyping by flow cytometry. These studies will begin to elucidate the level of immune suppression occurring in the liver during weaning-induced liver involution. To this end I have performed fluorescence-activated cell sorting (FACS) of viable murine CD11b$^+$F4/80$^+$ macrophages and CD11b$^+$Ly6C$^+$Ly6G$^-$ monocytes across the reproductive cycle for gene expression

profiling (Nullip, n=10; Lactation, n=8; Inv4, n=12; Inv6, n=12 macrophage and monocyte sorted samples). Initial attempts to perform T cell suppression assays were mired by numerous procedural issues including low myeloid cell yield via FACS and a sub-optimal level of T cell activation under positive control conditions. These studies were inconclusive and must be repeated with optimized protocols. Finally, members of the Schedin and Coussens lab have developed a multi-color panel for T cell phenotyping that allows for identification of numerous T cell populations and determination of T cell phenotype using flow cytometry. Assessing for liver-specific T cell phenotypes across the reproductive cycle may provide detail about the immune status of the pro-metastatic microenvironment post-weaning.

Determining steps in the metastatic cascade that are supported by the pro-metastatic microenvironment established in the post-weaning liver:

Previous studies (see Chapter III) describe two experimental metastasis models that both show an increased frequency of mice presenting with liver metastasis when injected post-weaning compared to nulliparous controls (see Chapter III)[233]. Results from the intracardiac injection model, which only allowed for assessment of micro-metastatic disease in the liver, suggested a seeding advantage in the involuting liver. In the intraportal injection model, where overt metastatic disease could also be assessed, we again found data suggestive of increased seeding with no tumor size advantage over nulliparous controls. Historical studies in the liver and lung suggest that the majority of tumor cells injected directly into the circulation in experimental metastasis models will survive and extravasate[50,142,144]. This same work has shown that major bottlenecks in

metastatic efficiency include growth from single cells into micro-metastases and from micro-metastases into overt metastases[50,142,144]. Taken together these data suggest that the metastatic advantage endowed by the involuting liver occurs at early time-points post-injection – either at the point of 1) extravasation 2) when early fate decisions are made (i.e. proliferate, die, or become quiescent) or 3) when the fate of micro-metastases are decided. To elucidate how weaning-induced liver involution impacts these stages of the metastatic cascade, I developed a modified intraportal injection model whereby GFP labeled mammary tumor cells are injected at high numbers into Glowing Head mice that are tolerized to GFP and luciferase[238,297] (Fig.7-8A). Injection of cell concentrations ranging from 1x10^5 to 1x10^6, D2A1-GFP mammary tumor cells revealed homogenous tumor cell dispersion throughout the liver at 90 minutes post-injection (Fig.7-8B). For the purpose of easy identification of single cells at early time points post-injection, I opted to inject 5x10^5 cells for these studies. Thus far, using a rolling study design, I have performed 3 Glowing head (Gh) studies to obtain livers at 0 and 90 minutes, and 1, 3, and 5 days post-injection using 5x10^5 D2A1-GFP mammary tumor cells in nulliparous and involution day 2 Balb/c female mice (Fig.7-8C).

Analyses of the livers from these Gh studies are ongoing, however initial assessment has begun. Thus far, these studies have revealed that D2A1-GFP mammary tumor cells elicit an inflammatory response characterized by rampant $CD45^+$ cell infiltration and resultant necrosis in Gh mouse livers as early as 1 day post-injection (Fig.7-9A-D). Importantly, D2A1 and D2A1-GFP mammary tumor cells elicit similar inflammatory responses in both Balb/c WT and Balb/c Glowing Head mice as determined by presence of observable

necrosis at necropsy, suggesting this is not simply due to aberrant immune responses to GFP (data not shown). These data suggest that lower cell concentrations may be necessary to limit inflammatory responses post-injection. Further, these data also suggest that the D2A1 mammary tumor line may elicit inflammatory responses upon injection into the liver at these concentrations, despite being a syngeneic line. Thus, we are also exploring the use of other syngeneic Balb/c mammary tumor lines including D2.OR, EMT6, T945, and T946 that may be less immunogenic[234,488].

Analysis of livers at 90 minutes post-injection, a time when tumor cells are expected to be actively extravasating or still in the vasculature[50,142,144], revealed no difference in GFP^+ tumor cell number between nulliparous and Inv2 groups (Fig.7-9E). We see similar results when comparing day 1 post-injection GFP^+ tumor cell numbers across the two groups (Fig.7-9F). Importantly, these data suggest that tumor cells are delivered equally between nulliparous and Inv2 mice, implicating survival and outgrowth steps of the metastatic cascade in dictating the observed difference in risk for liver metastasis between these groups. Day 3 post-injection livers have not been analyzed for single tumor cells or micro-metastases at this time. Assessment of the day 5 post-injection livers revealed marked differences between nulliparous and Inv2 groups. Upon necropsy, 2 of the 3 livers in the Inv2 group were compromised by severe necrosis compared to nulliparous livers where severe necrosis was not evident (Fig.7-9D). For day 5 tumor analyses I excluded necrotic areas. Assessment of tumor number normalized to total tissue area (tissue area minus necrotic area) in the day 5 livers revealed no differences between groups (Fig.7-9G). I also did not observe a difference in total tumor size per

liver, normalized to tissue area analyzed (Fig.7-9H). However, assessment of individual lesions revealed a significant increase in average tumor size normalized to tissue area (Fig.7-9I). Taken together these data suggest that injection of 5x10^5 GFP^+ cells results in similar seeding capacity in nulliparous and involution livers, but a difference in outgrowth among individual lesions. While we did not see differences in tumor number or total tumor area per liver in the day 5 analyses, this study is compromised by inflammation, and necrosis, as discussed above. However, trends or significant differences between the two groups may be revealed with adequately powered sample sizes, as the involution group showed a large standard deviation between rodents. Of potential interest, I also observed a focal pattern in many livers, where metastases tended to rise in clusters near other metastases, and tended to arise near the liver exterior as opposed to more central locations within the tissue (Fig.7-10). Although these livers have not been stained for metastatic niche-associated markers such as TNC or collagen, these preliminary observations suggest that metastases arise preferentially in a collective manner and in an anatomically-dependent manner.

A

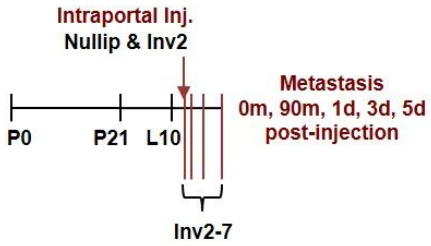

B

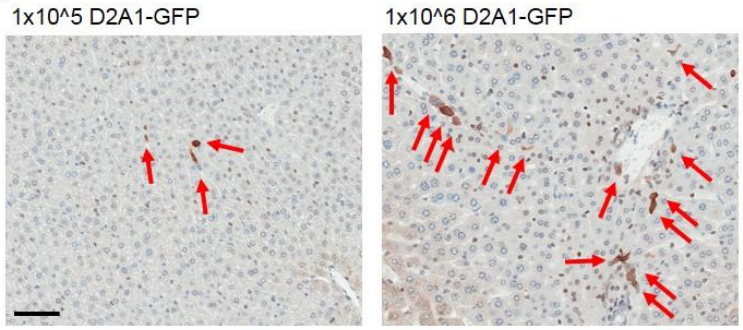

C

Time post-inj	0 min	90 min	1 day	3 day	5 day
Gh1 N		3	3	3	
Gh1 Inv2		3	3	1	
Gh2 N			5	5	
Gh2 Inv2			3	3	
Gh3	3		3	3	3
Gh3 Inv2	2		3	3	3

Figure 7-8: Glowing head intraportal injection model to study early time points post-injection

(A) Study design for glowing head studies. Nulliparous or involution day 2 Balb/c female mice are injected with D2A1-GFP mammary tumor cells intraportally and livers are dissected at 0 minutes, 90 minutes, 1 day, 3 days, or 5 days post-injection. **(B)** Representative GFP stained liver sections from 90 minute post-injection mice, injected with 1x10^5 (left) or 1x10^6 D2A1-GFP mammary tumor cells. Red arrows indicate GFP stained tumor cells; scale bar=100 μm. **(C)** Glowing head studies described in Figure 7-9 and 7-10 involved 5x10^5 D2A1-GFP mammary tumor cells into nulliparous or Inv2 mice and livers taken at various time points post-injection, sample sizes are shown.

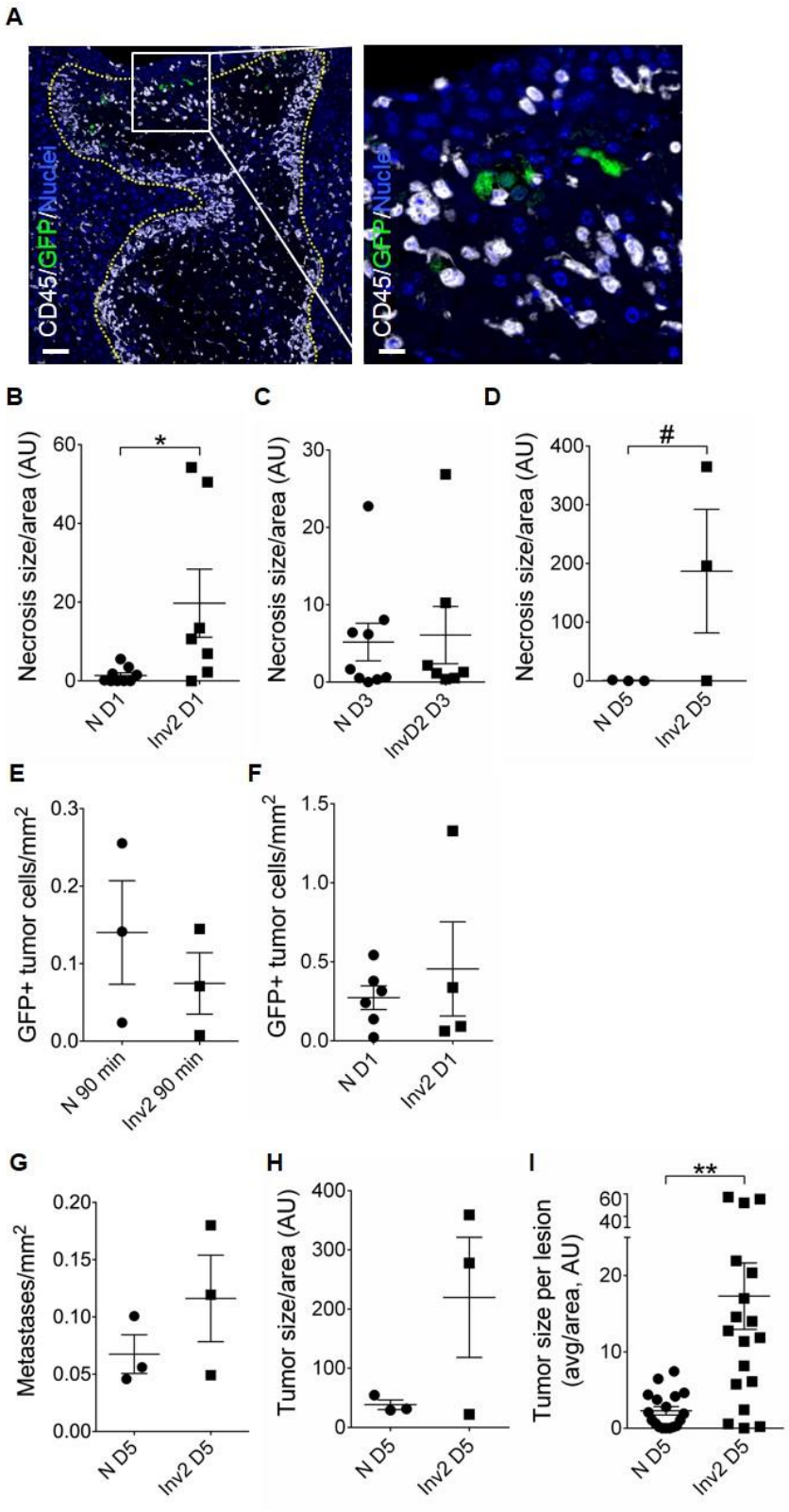
A
CD45/GFP/Nuclei
CD45/GFP/Nuclei
B
Necrosis size/area (AU)
60
40
20
0
*
N D1
Inv2 D1
C
Necrosis size/area (AU)
30
20
10
0
N D3
InvD2 D3
D
Necrosis size/area (AU)
400
300
200
100
0
#
N D5
Inv2 D5
E
GFP+ tumor cells/mm2
0.3
0.2
0.1
0.0
N 90 min
Inv2 90 min
F
GFP+ tumor cells/mm2
1.5
1.0
0.5
0.0
N D1
Inv2 D1
G
Metastases/mm2
0.20
0.15
0.10
0.05
0.00
N D5
Inv2 D5
H
Tumor size/area (AU)
400
300
200
100
0
N D5
Inv2 D5
I
Tumor size per lesion (avg/area, AU)
60
40
20
10
0
**
N D5
Inv2 D5

Figure 7-9: Outgrowth but not early seeding may be promoted by weaning-induced liver involution

(A) Representative image of a necrotic region from a glowing head study day 3 post-injection liver. Tissue was stained for CD45 (white) to mark leukocytes and GFP (green) to mark tumor cells. Necrotic region is outlined in yellow, inset shows higher magnification with a small cluster of GFP^+ tumor cells present; scale bars=75 and 10 μm. **(B-D)** Average necrosis area, normalized to whole tissue area per liver in **(B)** day 1, **(C)** day 3, and **(D)** day 5 post-injection. Analyses are the average of 3 levels per liver. **(E-F)** GFP^+ tumor cells normalized to tissue area from **(E)** 90 minutes, and **(F)** day 1 post-injection. 90 minute analyses are the average of 2 levels per left lobe, day 1 post-injection analyses are the average of 2-3 levels per left lobe. **(G)** Number of metastases per liver at day 5 post-injection, normalized to tissue area excluding necrotic areas. Data are presented as the average of 3 levels per liver. **(H)** Total tumor area per liver at day 5 post-injection, normalized to tissue area excluding necrotic area. Data are presented as the average of 3 levels per liver. **(I)** Average lesion size normalized to tissue area excluding necrotic area. Two-tailed Students T-test, #=p-value<0.1, *=p-value<0.05, **=p-value<0.01.

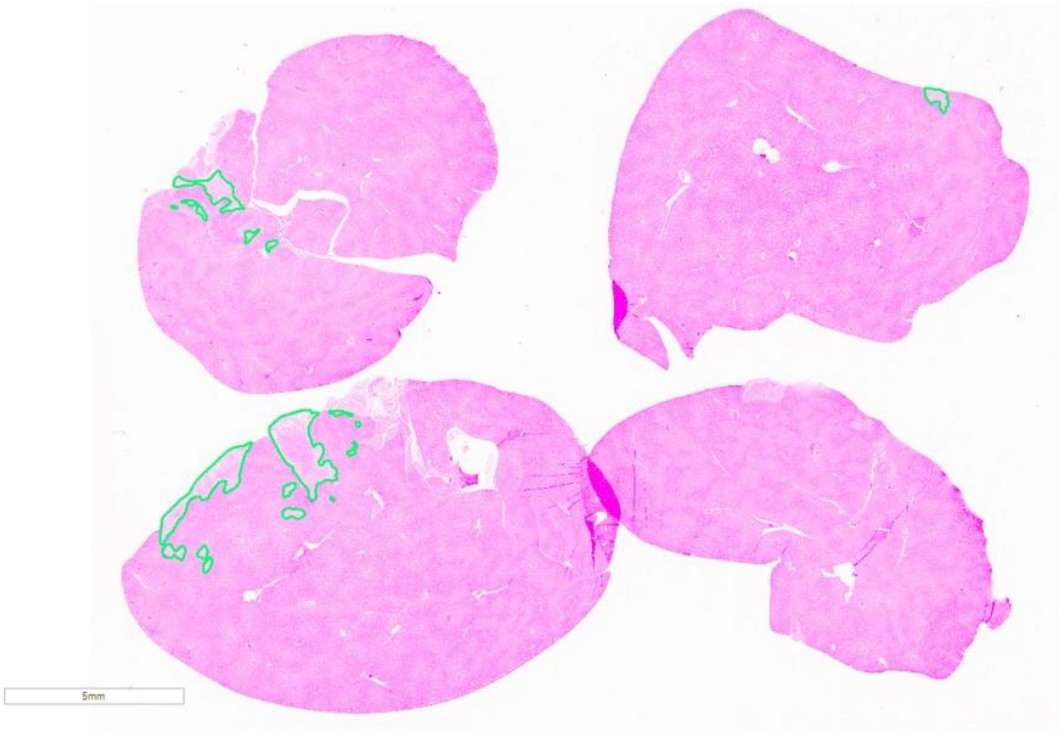

Figure 7-10: D2A1-GFP intraportal injection metastases tend to grow out at the liver edge and form in clusters

Representative H&E stained Balb/c mouse liver taken 5 days post-injection of 5x10^5 D2A1-GFP mammary tumor cells. Tumors are outlined in green, and tend to form at the edge of the tissue and appear in clusters; scale bar=5 mm.

A number of additional analyses are necessary to move forward with answering the question of which stages of the metastatic cascade are uniquely impacted by weaning-induced liver involution. To begin, it is not clear that injection of 5x10^5 D2A1-GFP mammary tumor cells is an adequate model to answer these questions. Studies are on-going to test lower cell concentrations and various cell lines, as mentioned above. Further, immunofluorescent staining of GFP in these livers is highly suggestive of loss of GFP in a large percentage of D2A1-GFP cells post-injection, as visible lesions by H&E may only have a few GFP^+ tumor cells (data not shown). In culture, these cells retain their GFP positivity through 5 serial passages in culture (data not shown). Yet, confirmation that GFP is retained in the D2A1-GFP line following injection will be essential to quantifying tumor cells and metastatic burden in these studies. One way to confirm this potential issue of GFP loss is to assess tumor cells from already completed Gh studies utilizing a Heppar/CK18/CD45 stain as described in Chapter II-III[233,238] and compare tumor cell counts to GFP^+ counts from above. Upon optimization of the model system utilized for these studies, it will be essential to confirm these findings with larger studies. Further, based on observations that tumor cells tend to localize to the external surface of the liver, near the liver capsule, and tend to arise in clusters suggests that tumor cell localization in the niche is important to metastatic success. Thus, assessment of tumor cell localization and association of proliferating/dying/quiescent cells within various liver microenvironmental structures is of utmost interest. This work will require multiplex staining platforms that include markers for tumor cells, proliferation/apoptosis markers, vascular structures, ECM, and immune cell populations of interest. These studies may reveal unique microenvironmental features that impact early cell fate

decisions and which single cells and/or micrometastases will grow out into overt lesions. Finally, it may be of interest to include future studies which assess frequency of mice presenting with overt metastases in pregnant or lactating rodents, similar to studies performed with the intraportal injection model in Chapter III. The expectation would be that the frequency of metastasis to the liver would be similar to or below nulliparous levels in both pregnancy and lactation groups based upon characterization of the liver micro-environment during these stages of the reproductive cycle[233]. Lactation in particular establishes a liver micro-environment which resembles a metastasis-inhibitory environment with reduced ECM and immune populations[233]. Further, the intraportal model could be used to study the effect of other pathologies including liver fibrosis, non-alcoholic fatty liver disease and obesity, or viral hepatitis on the metastasis supporting attributes of the liver.

Contributions: I performed all liver ECM enrichments, primary hepatocyte isolations, and 3D cultures. I performed FACS in collaboration with Miranda Gilchrist in the Flow Cytometry Shared Resource at OHSU. I developed the portal vein injection model and performed all studies, tissue staining, and data interpretation in the glowing head studies.

The Healthy Mom's LIVEr Study: seeking evidence for weaning-induced liver involution in women

As described in chapter III, we have discovered that the post-weaning rodent liver undergoes liver involution. This process is characterized by stromal remodeling consistent with establishment of a metastatic niche. Further, we have found that

postpartum breast cancer patients are at increased risk for developing site-specific metastasis to the liver, but not other sites, compared to nulliparous young breast cancer patients[233]. We hypothesized that the increased risk for metastasis in postpartum breast cancers is due to a similar postpartum liver involution process in women as we observe in rodents. It is currently unknown whether the human maternal liver undergoes weaning-induced liver involution. In fact, it is unreported whether the human liver increases in size during pregnancy, which we predict is a requisite to weaning-induced liver involution. To begin to address these questions, we sought to determine whether the maternal liver increases in volume with pregnancy and returns to pre-pregnant volume post-weaning.

Based on our rodent studies, we predicted that a woman's liver increases in size by approximately 1.5- to 2-fold during pregnancy and regresses to baseline size after weaning, or after pregnancy, in the absence of lactation. In rodents, we showed that the rodent liver doubles in weight during pregnancy, which is maintained through 14 days of lactation. Subsequently, the liver undergoes cell-death mediated tissue involution, returning to pre-pregnant weight within 8-10 days post-weaning (see Chapter III)[233]. Thus, we have initiated an inter-disciplinary multi-PI phase 0 Magnetic Resonance Imaging (MRI) study to measure volume of healthy maternal livers in lean and obese women in collaboration with Drs. Kimberly Vesco, MD (Kaiser Permanente), Jonathan Purnell, MD (OHSU School of Medicine, Knight Cardiovascular Institute, Cardiology, Endocrinology and Diabetes), and Alexander Guimaraes, MD, PhD (OHSU School of Medicine, Department of Diagnostic Radiology). To investigate whether human maternal liver increases in volume through pregnancy and returns to 'pre-pregnant' liver volume

we will perform MRI volumetric analyses on healthy women during their first trimester, third trimester, and at 3-12 months post-weaning (Fig.7-11A-B). Unpublished data from the Schedin lab suggests that post-weaning breast involution in women is largely completed as early as 8 weeks post-weaning (Jindal et al., data unpublished). In the rodent, both mammary gland and liver involution are largely completed within one week of weaning. Thus, we think it is a reasonable assumption that if the liver involutes, the size of the liver will be reduced to baseline levels in women by 3-12 months post-weaning.

From initial imaging of 26 participants who have completed their first and third trimester scans, we find that the maternal liver increases in volume significantly during pregnancy (Fig.7-11C-D). These data suggest that in most women, the liver responds similarly to the metabolic demands of pregnancy across species. Post-weaning imaging is forthcoming. Intriguingly, we observed 5 participants (19.2%) who exhibited a decrease in liver volume from 1st to 3rd trimester (Fig.7-11C-D). Nursing a child at time of study enrollment could confound data, as our hypothesis suggests that the maternal liver would not have returned to pre-pregnant volume by first trimester MRI scan. Further, in an unpublished study, the Schedin lab has identified that 10% of women were nursing a previous child when becoming pregnant for a subsequent child (Jindal et al., data unpublished). However, we have currently ruled out the possibility that these mothers were nursing a previous child at the time of their enrollment on our study (data not shown). Nonetheless, the major confounding potential of nursing at time of a subsequent pregnancy upon liver volumetrics should be considered and this variable should be

assessed in this study. Data has been collected on numerous other factors that may impact liver volume during pregnancy, including a participant's parity status, BMI, and maternal weight gain through pregnancy. These data have yet to be analyzed but we hypothesize that this group of women who exhibits reduced liver volume from 1st to 3rd trimester may be those patients in the obese study group. Obesity and associated metabolic-syndrome could be one proposed reason for a lack in liver volume increase with pregnancy, as metabolic dysregulation could certainly impact the metabolic link between the liver and the mammary gland during lactation. However, these analyses have yet to be performed.

Upon its completion, this study will constitute the first trial to investigate whether postpartum liver involution occurs in women. Although an increase in liver size during pregnancy, with subsequent loss of liver volume in the postpartum period does not directly prove that liver involution occurs through a pro-metastatic, cell death-mediated process, it is an essential first step. Further, this study will provide the necessary preliminary data to move forward with future studies to determine the underlying mechanism of postpartum liver involution in women. For such mechanistic investigations, we will need to obtain liver biopsy specimens after weaning; such a study cannot be proposed in healthy, pregnant women. One exciting avenue to advance this work is through collaboration with the Oregon National Primate Research Center at OHSU. Validation in non-human primates that liver involution occurs through a cell death-mediated tissue-remodeling process will be essential to our understanding of postpartum liver biology in women and risk for metastasis in postpartum breast cancer patients.

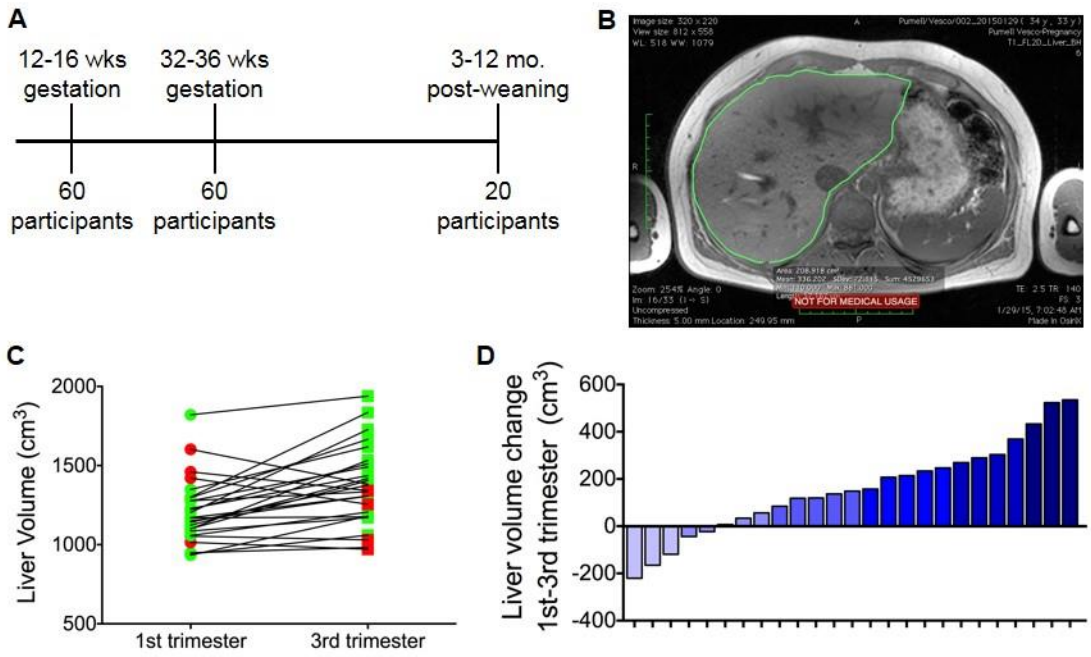

Figure 7-11: Liver volume increases in pregnant women

(A) Schematic for phase 0 liver imaging trial in healthy women. Women are enrolled during their first trimester. Liver MRI and bod pod study visits occur during late first trimester (12-16 wks gestation), early third trimester (32-36 wks gestation), and 3-12 months post-weaning. **(B)** Representative MRI scan of the abdominal cavity with liver present (green outline). Serial scans spanning the entire liver are utilized to gather liver area measurements to calculate liver volume. **(C)** Liver volumetric measurements from healthy participants at 1st trimester and 3rd trimester; green indicates an increase in volume from 1st to 3rd trimester, red indicates a decrease in volume (n=26 participants). **(D)** Change in liver volume from 1st to 3rd trimester (n=26 participants).

Contributions:

Pepper Schedin and I wrote the grant and the IRB for the third imaging time-point, based upon the original IRB by Drs. Jonathan Purnell and Kimberly Vesco. I performed all liver MRI volumetric analysis after training by Dr. Alexander Guimaraes. PIs running the study are Drs. Kimberly Vesco, Jonathan Purnell, and Pepper Schedin.

Significance

Postpartum breast cancers impart a high risk for metastasis and death, and the underlying mechanisms explaining this high risk are not fully elucidated. The work described in this thesis has advanced our understanding of how physiologic tissue remodeling events establish pro-metastatic microenvironments and increase risk for metastasis. Specifically, weaning-induced liver involution, a normal physiologically programmed event necessary to return the liver to homeostasis, establishes a pro-metastatic niche and increases postpartum breast cancer risk for metastasis in rodents. I have also observed an increased risk for liver metastasis in postpartum breast cancer patients, suggesting liver involution may occur in women too. However, future studies are necessary to understand whether weaning-induced liver involution occurs in women. My work has also found that NSAID intervention does not negatively impact risk for liver metastasis in postpartum breast cancer models, despite no positive impact either. These data suggest that NSAID intervention in postpartum breast cancer patients may reduce risk for metastasis due to its previously published effect on primary tumor growth and dissemination, without eliciting tumor promotional events in the liver. I have also found that the high risk for metastasis may persist for up to 10 years following a postpartum diagnosis, although the interaction

between a postpartum diagnosis and other poor prognostic indicators such as stage is complicated and requires further study. This work has utilized novel models including an intraportal injection model I developed (see Chapter II) and novel procedures to study the tissue microenvironment including quantitative ECM proteomics (see Chapter III and VI). Although this work raises many questions for future work, we now understand that post-weaning events that impact postpartum breast cancer prognosis extend beyond the mammary gland. In sum, this work has potential to greatly impact basic, translational, and clinical research of postpartum breast cancers and the metastasis field in general.

Appendix A: Additional Chapter III data not included in the original published manuscript

Contributions

I performed all liver weight and lymphocyte immune complexity analyses. Itai Meirom performed analysis of $Ki67^{+}Ly6C^{+}$ and $Ki67^{+}F4/80^{+}$ immune cells as part of a summer undergraduate research internship under my direction. Michelle Tran performed Lyve1 staining and performed analysis of Lyve1 and blood vessel quantification as part of a summer undergraduate research internship under my direction.

Results

Liver weight increases are not proportional to body weight increases with pregnancy and lactation

In Chapter III I described how the rodent liver weight increases with pregnancy, is maintained through lactation, and returns to near pre-pregnant weight within ~1 week post-weaning[233]. Liver weight is strongly linked to body weight in a relationship known as the 'hepatostat'; as body weight changes, the liver size also changes to match metabolic needs via mechanisms including bile acid sensing by the liver[489,490]. To understand whether the liver weight changes I have observed throughout the reproductive cycle (see Chapter III)[233] are proportional to body weight I assessed liver weight normalized to body weight in rats and mice (Appendix A Fig.1A-B). I found that livers from pregnant and lactating rodents increased beyond what would be expected if the liver weight increased proportional to body weight increases. These data suggest that the 'hepatostat' and/or additional mechanisms underlying liver size regulation may be altered

with pregnancy and lactation in a way that facilitates larger liver-to-body weight ratios. More studies will be essential to understanding this interesting preliminary result.

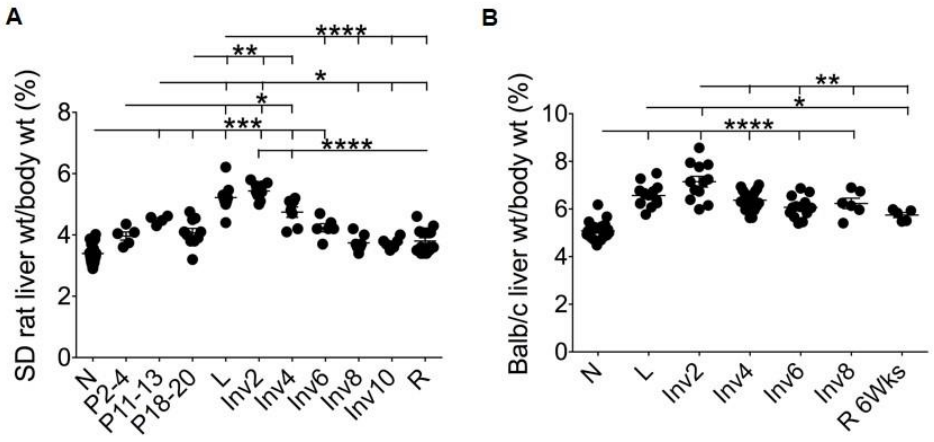

Appendix A Figure 1: Rodent liver weights normalized to body weights across the reproductive cycle

(A-C) Sprague-dawley rat (A) and Balb/c mouse (B) liver weights, normalized to body weight.

Lymphocyte immune complexity analysis on murine liver across the reproductive cycle

Weaning-induced mammary gland involution is characterized by an increase in $CD4^+$ T helper cells and $FoxP3^+$ T regulatory cells, but not $CD8^+$ cytotoxic T cells[42]. Further, these T cells are proposed to contribute to an immune suppressed pro-tumor microenvironment during the window of involution[42]. To begin to investigate whether similar lymphocyte immune complexity is altered with weaning-induced liver involution (described in Chapter III)[233] I performed flow cytometric analysis to assess for $CD8^+$, $CD4^+$, and $FoxP3^+$ lymphoid populations (Appendix A Fig.2). Analysis of flow cytometry revealed a drop in cytotoxic $CD8^+$ T cells during lactation, followed by a return to nulliparous levels during involution (Appendix A Fig.3A). $CD4^+$ T helper cells did not change in frequency across the reproductive cycle in the liver (Appendix A Fig.3B). $CD8^+$ and $CD4^+$ analyses are the accumulation of 3 independent studies, however assessment of CD8 and CD4 by IHC may be of interest in confirming flow cytometry data. IHC facilitates the study of whether cell localization changes within the tissue, as we have previously described for myeloid populations which form foci during involution in the liver[233]. Importantly, I did observe an increase in $CD4^+FoxP3^+$ T regulatory cells by involution day 6 compared to livers from lactating mice (Appendix A Fig.3C). The increased presence of FoxP3+ T regulatory cells from lactation to involution day 6 was confirmed by IHC (Appendix A Fig.3D). However, the $FoxP3^+$ flow analyses are from one study and should be replicated. Taken together these data suggest that helper and cytotoxic T cells do not change dramatically with weaning-induced liver involution, however the observed increase in $FoxP3^+$ T regulatory cells is consistent with establishment of an immune suppressed microenvironment during liver involution.

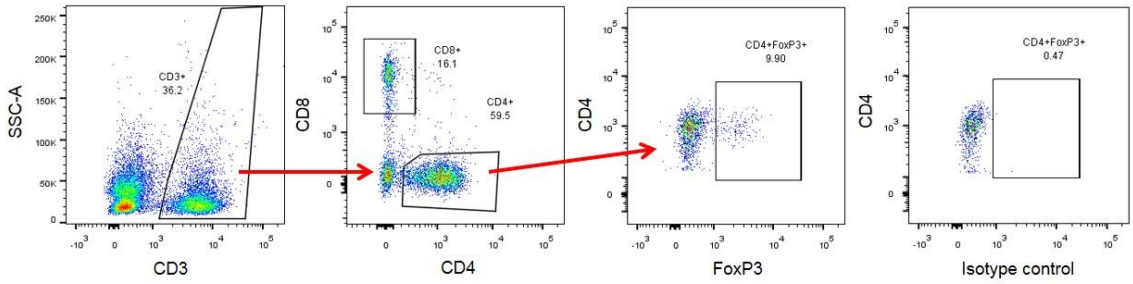

Appendix A Figure 2: Flow cytometry gating scheme for lymphoid populations in the murine liver

Cells were first gated off of scatter, singlets, and viable $CD45^+$ cells similar to plots shown in Supplementary Fig.3-5. From the $CD45^+$ gate, $CD3^+$ cells were next separated into $CD8^+$ and $CD4^+$ populations. $CD4^+FoxP3^+$ population was further identified, and confirmed by an isotype control to the FoxP3 antibody used (far right panel).

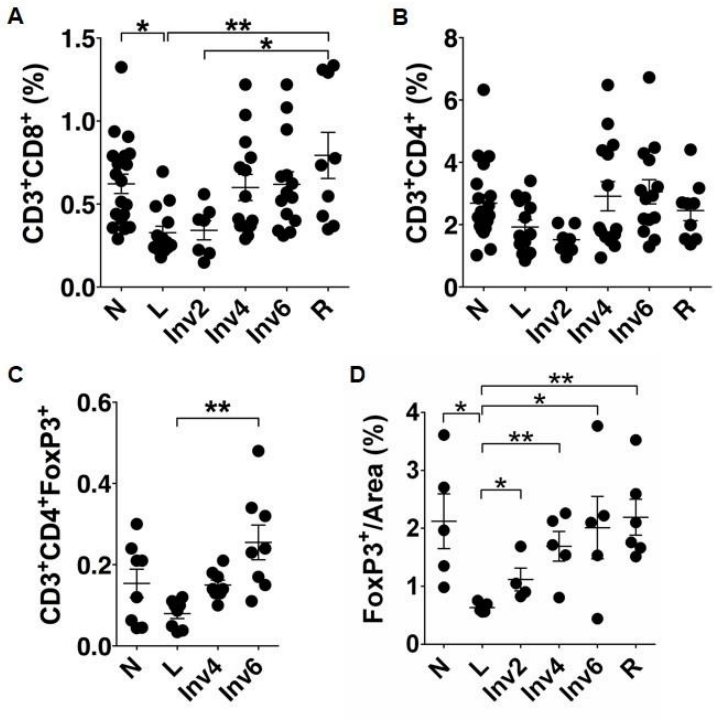

Appendix A Figure 3: T lymphocyte analysis in the murine liver across the reproductive cycle

(A-C) Flow cytometric analysis of **(A)** $CD8^+$ T cells, **(B)** $CD4^+$ T cells, and **(C)** $CD4^+FoxP3^+$ T cells. FoxP3 staining was only performed on a subset of samples; all analyzed samples are included in the graphs. One-way ANOVA, *=p-value<0.05, **=p-value<0.01. **(D)** IHC quantification of FoxP3 positive cells normalized to tissue area analyzed. Two-tailed Students T-test, *=p-value<0.05, **=p-value<0.01.

Myeloid populations are proliferating during weaning-induced liver involution

One observation I have made during weaning-induced liver involution is the accumulation of an increase in abundance of myeloid cells during involution as well as an increase in myeloid cell clusters made up of F4/80^{+}, Ly6C^{+}, and Ly6C^{+}Ly6G^{+} myeloid populations (see Chapter III). These myeloid cells and the clusters they form represent yet another example of how the post-weaning liver has numerous attributes consistent with a pro-metastatic microenvironment during involution. Previous work characterizing tumor-educated metastatic niches has identified formation of myeloid clusters that were simultaneously identified as sites of tumor cell seeding and survival[197,205]. The increase in monocytes and macrophages may be due to an influx of migratory inflammatory monocytes (CCR2^{hi}, Ly6C^{hi}) that subsequently differentiate into mature macrophages in the liver[491]. Supporting evidence for this possibility is provided in Chapter III in which infiltrating monocytes were Ly6C^{hi} and their increase was observed simultaneously with increases in CXCL12 and CCL2 chemokines. Recent work has also suggested accumulation of mature macrophages in the liver under times of sterile injury via direct influx of peritoneal macrophages[492]. I have initiated studies to understand the origin of the myeloid cell accumulation and cluster formation in the liver during weaning-induced liver involution. Thus far, we have identified that Ly6C^{+} monocytes and Ly6C^{+}F4/80^{+} myeloid cells are proliferating at greater frequency during weaning-induced involution compared to nulliparous controls (Appendix A Fig.4A-B). I also observe a trend towards increased proliferating F4/80^{+} macrophages (p=0.1, Two-tailed Student's T-test) (Appendix A Fig.4B). Furthermore, although not quantified, the bulk of proliferating Ly6C^{+} myeloid cells do appear to be associated with myeloid clusters (Appendix A

Fig.4A). These data suggest that the increase in monocytes and mature macrophages may be, in part, due to proliferation of $Ly6C^{+}$ populations. Future studies will be essential to understanding whether monocytes influx into the liver via CCL2-CCR2 mediated signaling or via other recruitment methodologies. Further, it will be of interest to determine whether peritoneal macrophages contribute to the increase in macrophages observed during weaning-induced liver involution, using markers such as Gata-6 and $CD102^{492}$.

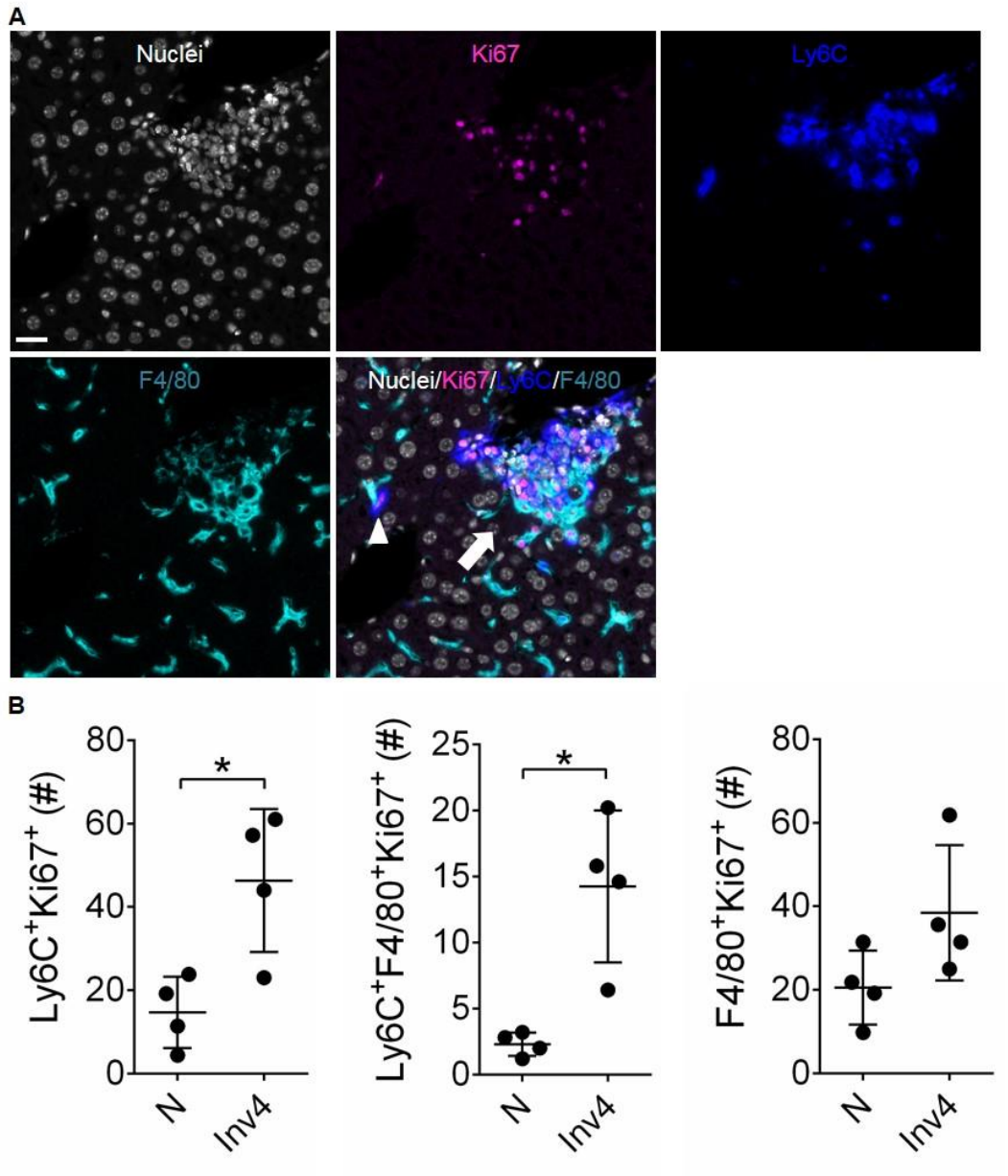

Appendix A Figure 4: Ly6C+ myeloid cells proliferate during weaning-induced liver involution

(A) Representative image of Opal™ multiplex immunofluorescence for Ki67, Ly6C, and F4/80 in which proliferating $Ly6C^+$ cells can clearly be identified (arrowhead) and the bulk of proliferating $Ly6C^+$ cells are within a myeloid cell cluster (arrow). Scale bar=20 µm. **(B)** Quantification of $Ly6C^+Ki67^+$ (left), $Ly6C^+F4/80^+Ki67^+$ (middle), and $F4/80^+Ki67^+$ (right) cells. Data are presented as average number of positive cells/field, a total of 4 fields per liver were analyzed.

Lymphatic and blood vasculature expand and regress with liver volume changes across the reproductive cycle

During weaning-induced involution in the mammary gland a major hallmark of tissue remodeling is lymphangiogenesis which occurs in the post-weaning window[114]. In contrast, blood vasculature abundance is greatest in the gland during pregnancy and lactation and regresses during involution[70]. Thus, I investigated whether lymphatic or blood vasculature was altered during weaning-induced involution in the liver. To assess lymphatics we first determined that Lyve1, a commonly used marker of mouse lymphatics, did indeed mark liver lymphatics. Previous reports in the field have found that Lyve1 also marks hepatic sinusoidal endothelial cells[493]. However, we determined using both Lyve1 and Prox-1, a transcription factor that also marks lymphatic endothelial cells[494], that Lyve1 single staining can conclusively identify lymphatics in the liver (Appendix A Fig.5A). Thus, we opted to perform single color IHC staining of livers for Lyve1, in which we again did not see Lyve1 staining of hepatic sinusoidal endothelial cells (Appendix A Fig.5B). Quantification of $Lyve1^+$ lymphatics identified a decrease in total lymphatics from nulliparous to involution day 4 stages (Appendix A Fig.5C). However in general, the number of $Lyve1^+$ lymphatics per liver area was not altered across the reproductive cycle. These data suggest that lymphangiogenesis, as is observed in the mammary gland post-weaning[114], does not occur in the liver during involution. Simultaneously, we also assessed blood vasculature on the Lyve1 stained livers. This was performed by determining small, medium, and large vessels based on size of the vessel (Appendix A Fig.6A). From this quantification we identified that fewer small vessels were present at lactation and involution day 2 time points compared to nulliparous

controls, however in general no differences were observed across stages (Appendix A Fig.6B-D). Although a much more robust methodology will need to be performed to confirm these data, such as CD31 staining and quantification, these data do suggest a similar lack of blood vasculature remodeling in the liver across the reproductive cycle.

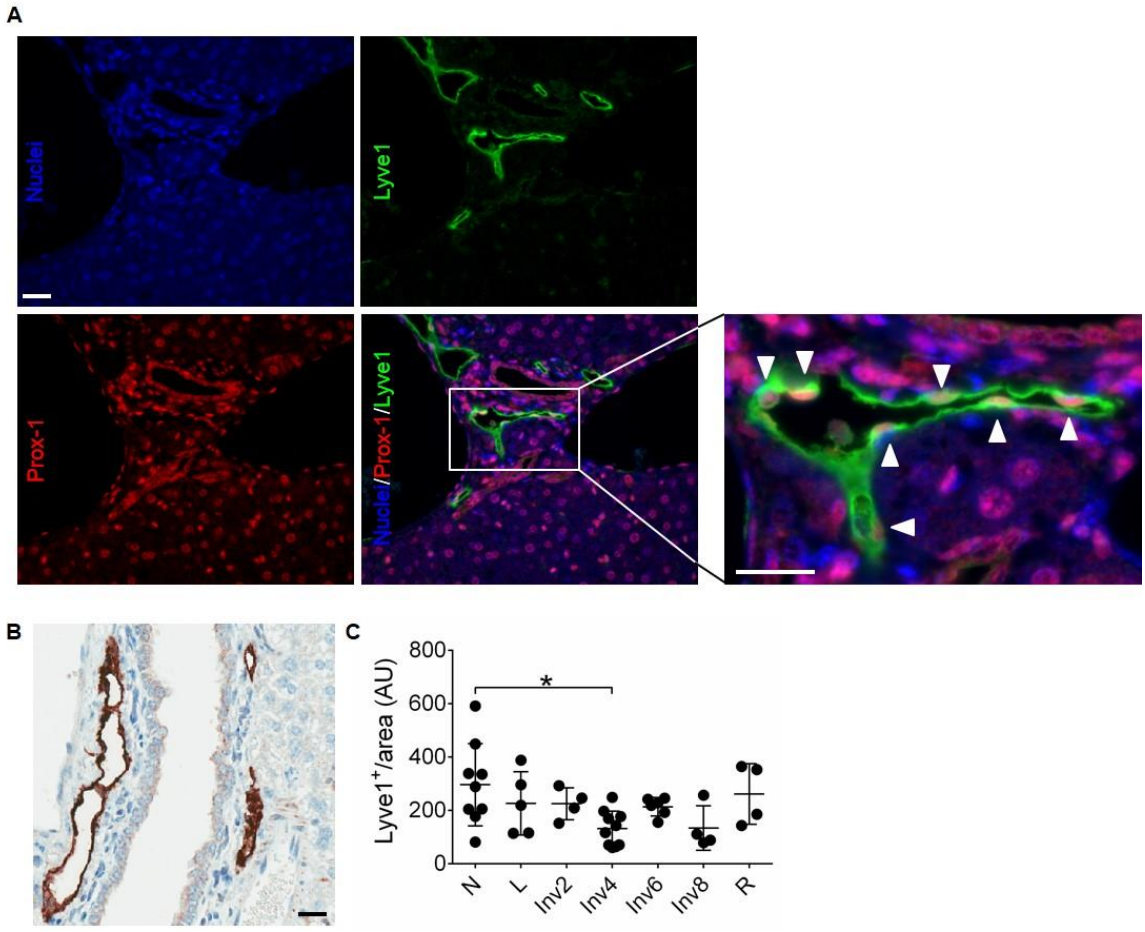

Appendix A Figure 5: Lyve1^{+} lymphatics are not dynamically altered across the reproductive cycle in the liver.

(A) Representative image of Opal™ multiplex immunofluorescence for Lyve1 and Prox-1 in which Lyve1^{+} lymphatics also stain positive for Prox-1 in lymphatic endothelial cell nuclei (arrow heads). Sinusoids do not stain positive. Inset shows higher magnification of Lyve1^{+}Prox-1^{+} lymphatic endothelial cells. Scale bars=20 µm. **(B)** Representative image of Lyve1^{+} lymphatics stained by single color IHC. Scale bar=20 µm. **(C)** Quantification of Lyve1^{+} lymphatic vessels from single color IHC stained livers, normalized to area.

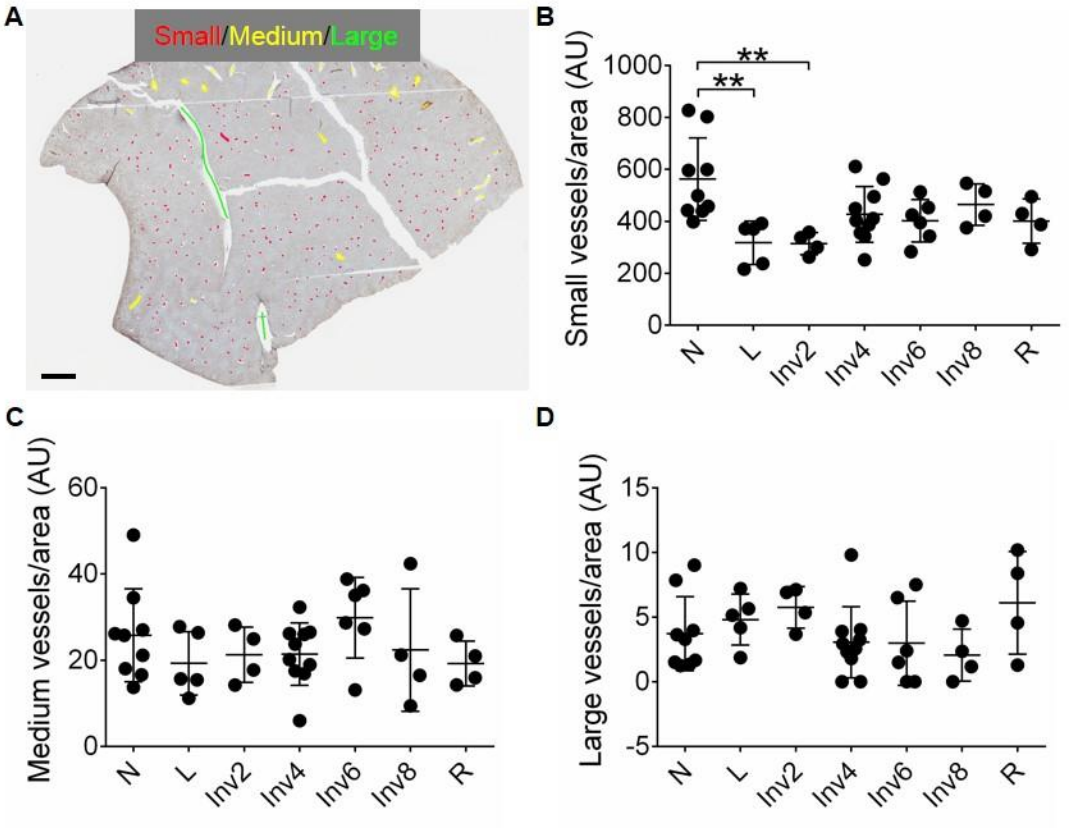

Appendix A Figure 6: Blood vasculature are not dynamically altered across the reproductive cycle.

(A) Representative image of a Lyve1 stained liver section in which blood vasculature has been quantified. Small vessels are denoted in red, medium vessels are denoted in yellow, and large vessels are denoted in green. Scale bars=1000 μm. **(B-D)** Quantification of small (B), medium (C), and large (D) blood vessels from single color Lyve1 stained livers, normalized to area.

Methods

Flow Cytometry

Flow cytometry was performed as described in Chapter III. For the lymphoid panel, cell surface markers were stained (CD45, 30-F11; CD3, 17A2; CD4, RM4-5; CD8, H35-17.2) for 35 min at 4°C in 100 µl FACS buffer and fixed with fixation buffer (BD Biosciences) for 30 min. For intracellular staining, samples were permeabilized (BD Biosciences) for 60 min at 4°C, resuspended in permeabilization buffer (BD Biosciences), spun at 1500 rpm, blocked with 2% normal rat serum for 15 min at RT, and stained (FoxP3, FJK-16s) for 30 min at RT. Samples were washed with permeabilization buffer 2x and resuspended in FACS buffer for flow cytometric analyses. Analysis was performed on an LSRFortessa (BD Biosciences; OHSU Flow Cytometry Shared Resource) and analysis was performed using FlowJo (FlowJo, LLC Data Analysis Software).

FoxP3 Immunohistochemistry

IHC was done as described in Chapter III. Antigen retrieval with TRS (5 min, 95°C) was performed. Antibody for FoxP3 (FJK-16s; 1:100) was incubated on slides overnight at 4°C. Rat-on-Mouse HRP-Polymer secondary antibody incubation was for 30 min at RT. Single cells were quantified and normalized to area. An investigator blinded to study groups performed image analyses.

Immunohistochemistry

Primary antibody incubation for Lyve1 (Ab33682, Abcam; 1:400) was performed for 1 hr at RT. Tissues were incubated with secondary antibody (Envision+ Rabbit, RTU, Dako)

for 30 min at RT. Multicolor immunofluorescence staining for F4/80, Ly6C, and Ki67 was done using the Opal™ 4-color IHC kit (PerkinElmer, Inc.) as per manufacturer's recommendations. Initial heat-mediated antigen retrieval was with TRS in a pressuer cooker. Protein block was performed for 10 min using 5% normal goat serum with 2.5% BSA. Ki67 (Rm-9106-S, 1:100, 1 h. at RT), F4/80 (MCA497, Bio-Rad, 1:100, o/n, 4°C), and Ly6C (Ab15627, Abcam, 1:100, 1 h. at RT) primary antibodies were placed on tissue, followed by secondary antibodies (α-rabbit 31461 at 1:500, Thermo Fisher and α-rat H1501, RTU, Histofine) for 30 min.

IHC analysis

Stained sections were scanned and analyzed as described[233]. Lyve1^{+} vessels were quantified per liver and normalized to area. Ki67+ myeloid populations were quantified on 5 10x fields per liver and data are presented as the average per liver/per group. All analyses were done by investigators blinded to group.

Appendix B: Immune Cell Marker Descriptions

Appendix B Table 1: Molecular markers of myeloid and lymphoid immune populations utilized for flow cytometry

Molecular markers of myeloid immune populations	
CD45	Also called leukocyte common antigen (LCA), protein tyrosine phosphatase, receptor type C (PTPRC). Signaling molecule that activates Src family kinases and is expressed by hematopoietic cells.
CD68	Member of the lysosomal/endosomal-associated membrane glycoprotein (LAMP) family. It is also a scavenger receptor, binds low density lipoprotein, and is involved in antigen processing and phagocytosis. Present on macrophages including Kupffer cells, monocytes, neutrophils, basophils, mast cells, DC's, and myeloid progenitors.
CD11b	Also known as macrophage receptor-1 (Mac-1). Integrin alpha M chain involved in cell adherence and phagocytosis. Expressed by macrophages, monocytes, and neutrophils, and dendritic cells.
F4/80	Also known as EGF-like module-containing mucin-like hormone receptor-like 1 (EMR1) in humans. Member of the adhesion G-protein coupled receptor family. Expressed on numerous macrophage populations including Kupffer cells.
Ly6C	A glcosylphosphatidylinositol- (GPI) linked protein expressed on monocytes and neutrophils. It can also be expressed on endothelial cells, memory T cells, and macrophages.
Ly6G	GPI-linked protein expessed by neutrophils and on monocytes during bone marrow development.
CD11c	Also known as integrin αX and CR4. A type I transmembrane glycoprotein that associates with integrin β2 and is present on monocytes/macrophages, dendritic cells, granulocytes, natural killer cells, and subsets of T and B cells.
MHC2	Major histocompatibility complex II involved in antigen presentation by antigen-presenting cells including dendritic cells and B cells.
Molecular markers of lymphoid immune populations	
CD3	Part of the T cell receptor which facilitates activation of T cells. Expressed by all T cells and natural killer T cells.
CD4	Immunoglobulin that is a co-receptor for the T cell receptor by recruiting Lck for downstream signaling. Expressed on T helper cells and T regulatory cells as well as B cells, macrophages, and granulocytes
CD8	Immunoglobulin that is a co-receptor for the T cell receptor. Expressed by cytotoxic T cells as well as dendritic cells.
Foxp3	Member of the forkhead/winged-helix family of transcriptional regulators involved in the development and inhibitory function of T regulatory cells. Expressed by T regulatory cells.

Appendix C: Methods from Future Perspectives and New Questions

Immunoblotting

Flash frozen pulverized rat liver tissue (50 mg/animal) were prepared and immunoblotted as described[46]; all gels were loaded as equal protein concentration. Antibodies against pStat3 (Cell Signaling Technology #4113, M9C6; 1:1000), Stat3 (Cell Signaling Technology #9132; 1:1000), Laminin (Novus Biologicals, NB300-144, 1:500), Tenascin-C (Millipore, ab19011, 1:200), incubated overnight at 4°C or GAPDH (Bio-Rad #G9454, 1:5000; Cell Signaling Technologies, #2118, 14C10; 1:1000) for 1 hr at RT. Secondary goat anti-rabbit IgG (Bio-Rad, 1:10,000) or goat anti-mouse IgG (R&D Systems; 1:1000) were used with shaking for 1 hr at RT. ImageJ[495] was used for densitometry, ECM enrichment data is presented as fold change enrichment over starting tissue.

Mafia mouse model

Mafia mice were managed as described[463] with the exception that B/B Homodimerizer (previously called AP20187) was injected at 1 mg/kg body weight daily, beginning 3 days prior to weaning.

Intraportal injection model

Intraportal injections were performed as described[233,238] (see Chapters II-III). 5x10^5 D2A1-GFP mammary tumor cells were injected in female Balb/c Glowing Head mice in 20 ul of 1x PBS. Mice were aged 8-14 weeks and were nulliparous or injected at Inv2.

Balb/c Glowing Head mice were originally provided by Dr. Lalage M. Wakefield (National Cancer Institute).

Quantification of metastatic tumor cells and metastases

For single cell and micro-metastasis quantification in 90 minute, and day 1 post-injection groups, tissue sections stained for CD45 and GFP (see IHC methods) were imaged using a Zeiss ApoTome.2 microscope and Zen Blue imaging software. GFP^+ cells were quantified in whole liver sections and cell number was normalized to area as measured on H&E serial sections. Data are presented as the average of 2-3 levels/liver. For micro-metastasis and overt metastasis quantification in day 5 post-injection groups, H&E tissue sections were analyzed and area of metastasis was normalized to area of tissue. Data are presented as the average of 3 levels/liver.

Flow cytometry and FACS

Flow cytometry on whole unperfused mouse liver was done as described[233] (see Chapter III) on a Gallios 561 flow cytometer (Beckman Coulter; University of Colorado Flow Cytometry Core) and data analyzed using FlowJo (FlowJo, LLC Data Analysis Software). Preparation of samples for FACS was identical to flow cytometry protocols with the exception that livers were perfused with 1x PBS prior to excision. FACS was performed on a BD Influx (BD Biosciences; Oregon Health and Science University Flow Cytometry Shared Resource). FACS samples were stored in LN_2.

TUNEL

TUNEL was performed as previously described[233] on n=3 livers/grp.

Blood glucose measurement

Blood was collected via the saphenous vein onto Contour®next blood glucose test strips (Bayer HealthCare LLC, Whippany, NJ) and read on a Contour®next blood glucose meter. The average of the two measurements per blood draw was reported.

Free fatty acid detection

Free fatty acids were measured using the Free Fatty Acid Fluorometric Assay Kit, on rat plasma samples collected in sodium citrate, as per manufacturer's recommendations (Caymen Chemical, #700310). Samples were run in duplicate.

Immunohistochemistry

Primary antibody incubation for Adipophilin (LS-B2168/34250 Lifespan Biosciences, 1:400 in rat; NB110-40878; Novus biological, 1:1000 in mouse), CK18 (Ab53118, Abcam; 1:100), Heppar-1 (OCH1E5; 1:50), and GFP (BA 0702, Vector Laboratories; 1:1000, overnight at 4°C) was performed for 1 hr at RT unless otherwise noted. Tissues were incubated with secondary antibodies (Envision+ Rabbit, RTU, Dako; Mouse-on-rat HRP Polymer Kit, RTU, Biocare; α-rabbit 31461 at 1:500 or α-mouse 31436 at 1:1000, Thermo Fisher; Streptavidin-HRP at 1:500 for 10 min, Dako P0397) for 30 min at RT. Dual immunofluorescent staining for GFP and CD45 was done using the Opal™ 4-color IHC kit (PerkinElmer, Inc.) as per manufacturer's recommendations. Initial heat-mediated antigen retrieval was with TRS in a pressure cooker. Protein block was

performed for 60 min using 5% normal goat serum with 2.5% BSA; avidin/biotin blocking was performed for 20 min each (Dako, X0590). CD45 (30-F11, 1:50, overnight, 4°C) and then GFP (BA 0702, Vector Laboratories, 1:1000, 1 h. at RT) primary antibodies were placed on tissue, followed by secondary antibodies (Mouse-on-rat HRP Polymer Kit, RTU, Biocare; Avidin-HRP, 1:500, Dako, P0397) for 30 min.

IHC analysis

Stained sections were scanned and analyzed as described[233]. Periportal analyses for adipophilin staining in mouse liver was done on 3 portal vein areas/liver and the adipophilin stain within 50 μm of the vessel lumen was analyzed. All analyses were done by investigators blinded to group.

Primary mouse hepatocyte isolation

Mouse primary hepatocytes were isolated from anesthetized Balb/c female mice as described[496].

ECM enrichment

Liver ECM was enriched as described[484] with the exception that day 1 ultracentrifugation steps were performed at 34,000 x*g* for 34 min at 4°C. One rat liver or four, pooled mouse livers were used per enrichment, four independent enrichments were performed and representative data shown.

3D cell culture models

3D cultures were performed as described[296]. For liver matrix + hepatocyte 3D cultures, primary mouse hepatocytes were admixed with 5 mg/ml Matrigel™ + 200 ug/ml experimental matrix and plated at 40,000 cells/well, with 4 wells/condition and cultured for 5 days. Cell counts were performed on four 10x bright field images per condition using ImageJ. For liver matrix + mammary tumor cell 3D cultures, D2A1 or D2.OR tumor cells were admixed with 1.6 mg/ml Matrigel™ + 200 ug/ml experimental matrix, plated at 2,500 cells/well and cultured for 7 days. For 3D cultures using mammary matrix isolated from tamoxifen or vehicle treated rats, MCF12A or D2.OR cells were cultured as described[46,296]. Area analysis of D2.OR cultures was done with 2 experimental replicates, and 4-7 10x images/experiment using ImageJ. Cultures were imaged on an inverted Zeiss Axiovert with Canon Powershot A640 camera. For staining, 3D cultures were fixed with methacarn (60% methanol, 30% methanol, 10% glacial acetic acid).

Healthy Mom's LIVEr study design

The OHSU and Kaiser Permanente Northwest IRBs approved the Healthy Mom's LIVEr Study. Lean and obese participants will be enrolled on the study during their first trimester and will be imaged by MRI during the first trimester (12-16 weeks gestation) and third trimester (32-36 weeks gestation; n=26 participants who have completed both scans and data analyzed). Post-parturition, participants will be tracked via once monthly emails and/or phone calls for the duration of nursing, until the participant identifies time of weaning. At this time the 3-12 month post-weaning MRI scan will be scheduled. At each study visit a physical activity questionnaire and dietary intake questionnaire were collected; a detailed lactation history questionnaire will be performed at the postpartum

study visit. Data are stored securely using RedCAP and analyzed by qualified study personnel. Power analyses were performed based on maternal rat liver weight changes across the reproductive cycle. With an estimated 2-fold increase in liver volume from 1st to 3rd trimester or a 2-fold decrease in liver volume from 3rd trimester to 3 months post-weaning a sample size of 20 participants was sufficient to obtain >95% power and an alpha-value of 0.05. The current study design is aiming for 60 participants for the 1st and 3rd trimester study visits; we aim to retain 20 of these participants for the 3-12 months post-weaning study visit.

Participant selection for Healthy Mom's LIVEr Study

Participants were recruited from Kaiser Permanente Northwest, a federally qualified health maintenance organization. Participants aged 18-40 years of age were enrolled if they had a BMI $\geq$18.5 kg/m^2 and $\leq$40 kg/m^2 at first prenatal visit. Participants were excluded from the study if they had any one of the following complications: fasting glucose levels $\geq$100 mg/dL, anemia, multi-fetal pregnancies, pre-gestational diabetes, history of bariatric surgery or other medical conditions that require specialized nutritional programs, planned to move out of the area prior to delivery, contraindications to MRI study (such as claustrophobia, metal in their body), current maternal history of drug, tobacco, or alcohol abuse, known maternal rheumatologic or chronic inflammatory state, and/or chronic hypertension.

Liver Magnetic Resonance Imaging

Participants received first trimester, third trimester, and 3-12 months post-weaning liver scans by MRI using a Siemens Magnetom Tim Trio 3 Tesla (Siemens Medical Solutions, Malvern Pennsylvania and Erlangen, Germany). Participants were placed in a supine position inside the bore of the magnet and 23-40 axial slice images were taken with 5 mm thickness and a 1 mm spanning gap between all slices from mid-lung to L5/S1 during breath holds.

Volumetric analysis of liver MRI scans

Liver MRI scan Digital Imaging and Communications in Medicine (DICOM) files were analyzed using OsiriX 7.5.1 (Pixmeo Sarl). Area measurements (cm^2) were made on each 5 mm scan containing liver, and measurements from the entirety of a single time-point were utilized to calculate volume as the sum of all areas*0.5 cm (cm^3). Volumes for each participant were compared across time points using a Two-tailed Paired Student's T-test.

Appendix D: Curriculum Vitae

7900 SW Brentwood St. #16
Portland, OR 97225
Cell/Home Ph# 785-393-7982
goddarde@ohsu.edu

Oregon Health & Science University
Cell, Developmental, and Cancer Biology Dept.
3181 SW. Sam Jackson Park Rd
Portland, OR 97239
Lab Ph# 503-494-9729

EDUCATION

Oregon Health & Science University — **Portland, OR**
Ph.D. Cancer Biology — Jan. 2017
Dissertation – Weaning-induced liver involution: a novel mechanism of metastasis in postpartum breast cancer

University of Colorado Anschutz Medical Campus — **Aurora, CO**
Colorado Clinical and Translational Sciences Institute
Clinical-Translational Science Certificate Training — July 2012-Present

University of Colorado Anschutz Medical Campus — **Aurora, CO**
Ph.D. candidate, Cancer Biology Program — Aug. 2011-2014
Transferred with PhD mentor Dr. Pepper Schedin 07/2014

University of Kansas — **Lawrence, KS**
B.S. Microbiology, — May 2011

Johnson County Community College — **Overland Park, KS**
Emergency Medical Technician Certification, — Jan. 2008
First Responder Certification, — Aug. 2006

RESEARCH & PROFESSIONAL EXPERIENCE

Graduate research, — **Portland, OR**
Laboratory of Dr. Pepper Schedin — Aug. 2011-Jan. 2017
Oregon Health & Science University, 2014-2017
University of Colorado Anschutz Medical Campus, 2011-2014
Skills acquired: development of rodent models of liver metastasis, rodent survival surgery, rodent drug intervention studies, flow cytometry, FACS, immunohistochemistry, multiplex immunohistochemistry, endogenous tissue extracellular matrix (ECM) enrichment, 3-D cell culture modeling using enriched tissue-specific ECM, patient data analysis/chart review, IRB and IACUC protocol/modification management.

Clinical Translational Science Certificate — **Aurora, CO**
Colorado Clinical and Translational Sciences Institute — Jan. 2017

Participant, 30th Anniversary Annual Critical Issues in — **Boston, MA**

Tumor Microenvironment: Angiogenesis, Metastasis and Immunology — Oct. 2015

NIH mock study section on the Tumor Microenvironment — **Aurora, CO**
University of Colorado Denver Anschutz Medical Campus — Apr. 2012

PLUS program – Peer Led Undergraduate Supplements, — **Lawrence, KS**
University of Kansas, — 2010 – July 2011
Initiative for Maximizing Student Diversity,
Group Leader for Microbiology Supplements

Undergraduate Research Assistant, — **Lawrence, KS**
University of Kansas, — 2009 – July 2011
Laboratory of Dr. David Davido

MENTORSHIP

Itai Meirom, Cell, Development, and Cancer Biology Department Summer Internship Program, "Characterizing the myeloid populations that increase during weaning-induced liver involution", June – July 2016.

Alexandra Quackenbush, OHSU Cancer Biology Graduate Program Rotation, "Determine the impact of non-steroidal anti-inflammatory drug (NSAID) intervention on weaning-induced liver involution and the pro-metastatic microenvironment", Jan. – Mar. 2016.

Michelle Tran, Cell, Development, and Cancer Biology Department Summer Internship Program, "Investigating a role for lymphangiogenesis in weaning-induced liver involution", June – July 2015.

Lindsey Newby, Ted R. Lilley CURE Internship Program, "The effect of non-steroidal anti-inflammatory drugs (NSAIDs) on weaning-induced liver involution", June – July 2015.

AWARDS

Funding Awards

National Research Service Award (NRSA) F31 Research Fellowship, "Investigating a role for liver involution in postpartum breast cancer metastasis", National Institutes of Health/National Cancer Institute, *$42,676/year for 3 years.* *Awarded 4 years, accepted 3 years, 2014 – 2017.

Kansas-Idea Network for Biomedical Research Excellence (K-INBRE) competitive research grant for undergraduate research, *$12,000 for Spring and Summer semester research,* 2011.

Undergraduate Research Award (UGRA) for undergraduate research, $1000 for Spring semester research, University Honors Program, University of Kansas, declined, 2011.

Kansas-Idea Network for Biomedical Research Excellence (K-INBRE) competitive research grant for undergraduate research, *$12,000 for Spring and Summer semester research,* 2010.

Presentation Awards
OHSU Research Week, Student Oral Presentation Award, *$150,* 2015

University of Colorado, Denver Student Research Day, Best Poster Award, *$250,* 2013.

Other Awards
OHSU Cancer Biology Program Student Travel Award to attend the AACR Tumor Metastasis conference, *$1500,* 2015

Travel and registration award to attend the 30th annual Tumor Microenvironment Course, Boston, MA, 2015.

PUBLICATIONS

Smith MC, **Goddard ET**, Lanfranca MP, Bayless AM, Davido DJ. hTERT extends the life of human fibroblasts without compromising the type I interferon response. PLoS One. 2013; 8(3):e58233

Smith MC, Bayless AM, **Goddard ET**, Davido DJ. CK2 Inhibitors Increase the Sensitivity of HSV-1 to Interferon-β. Antiviral Res. 2011 Sep; 91(3):259-66

Goddard ET, Hill RC, Barrett A, Betts C, Guo Q, et al., Quantitative extracellular matrix proteomics to study mammary and liver tissue. Int J Biochem Cell Biol. 2016 Dec; 81(Pt A):223-232.

Goddard ET, Fischer J, Schedin P. A portal vein injection model to study liver metastasis of breast cancer. J Vis Exp. 2016 Dec; (118).

Goddard ET, Hill RC, Nemkov T, D'Alessandro A, Hansen K, et al., The rodent liver undergoes weaning-induced involution and supports breast cancer metastasis. Cancer Discov. 2016 Dec; Epub ahead of print.

PRESENTATIONS & SELECTED ABSTRACTS

Talks
Cancer Biology/CDCB Research In Progress Seminar Series, Oral Presentation, "Investigating a role for liver involution in supporting postpartum breast cancer

metastasis", Oregon Health and Science University, Portland, OR, October 2015 & Sept. 2014.

OHSU/OSU Cancer Prevention and Control Retreat, Oral Presentation, "Postpartum liver involution and breast cancer metastasis", Salem, OR, Aug. 2015.

OHSU Research Week, Oral Presentation, "Investigating a role for liver involution in postpartum breast cancer metastasis", Oregon Health and Science University, Portland, OR – *Received Student Oral Presentation Award, $150 prize,* May 2015.

Cancer Biology Research In Progress Seminar Series, Oral Presentation, "Investigating a role for liver involution in postpartum breast cancer metastasis", University of Colorado Anschutz Medical Campus, Aurora, CO, May 2014 & Apr. 2013.

Medical Oncology Department Research in Progress Seminar Series, Oral Presentation, "Investigating a role for liver involution in postpartum breast cancer metastasis", University of Colorado Anschutz Medical Campus, Aurora, CO, Nov. 2013.

K-INBRE Research Presentation and Poster Presentation, "Transcriptional Interference of an Antiviral Gene, *PML*, by Herpes Simplex Virus Type-1", Lawrence, KS, June 2010, Jan. 2011, & June 2011.

International/National Conferences Attended & Posters Presented

AACR Tumor Metastasis Conference, Poster Session, "Investigating a role for weaning-induced liver involution in supporting postpartum breast cancer metastasis", Austin, TX, Nov. 2015.

Keystone Symposia Dendritic Cells and Macrophages Reunited, Montreal, Quebec, Canada, Mar. 2015.

Gordon Research Seminar and Conference in Mammary Gland Biology, Poster Session, "Investigating a role for liver involution in postpartum breast cancer metastasis", Lucca, Italy, June 2014.

Institutional Conferences Attended & Posters Presented

Cell, Development, and Cancer Biology/Oregon Center for Spatial Systems Biomedicine Joint Retreat, Poster Session, "Investigating a role for liver involution in supporting postpartum breast cancer metastasis", Oregon Health and Science, Portland, OR, Aug. 2015.

Programs in Molecular and Cellular Biology Annual Retreat, Poster Session, "Investigating a role for liver involution in postpartum breast cancer metastasis", Welches, Oregon, Sept. 2014.

University of Colorado Student Research Forum, Poster Session, "Investigating a role for liver involution in postpartum breast cancer metastasis", University of Colorado

Anschutz Medical Campus, Aurora, CO – *Received best poster award, $250 prize,* Dec. 2013.

Department of Medicine Research Day, Poster Session, "Investigating a role for liver involution in postpartum breast cancer metastasis", University of Colorado Anschutz Medical Campus, Aurora, CO, Nov. 2013.

Women's Health Research Day, Poster Session, "Investigating a role for liver involution in postpartum breast cancer metastasis", University of Colorado Anschutz Medical Campus, Aurora, CO, Oct. 2013.

Cancer Biology Annual Retreat, Poster Session, "Investigating a role for liver involution in postpartum breast cancer metastasis", University of Colorado Anschutz Medical Campus, Aurora, CO, Sept. 2013 & 2012.

Cells, Stem Cells, and Development Annual Retreat, Poster Session, "Elucidating the role of postpartum involution in metastatic niche formation in the liver and consequences for poor prognosis in PABC", University of Colorado Anschutz Medical Campus, Aurora, CO, Oct. 2012.

Women's Health Research Day, Poster Session, "Elucidating the role of postpartum involution in metastatic niche formation in the liver and consequences for poor prognosis in PABC", University of Colorado Anschutz Medical Campus, Aurora, CO, Sept. 2012.

SELF Poster Session, "Transcriptional Interference of an Antiviral Gene, *PML*, by Herpes Simplex Virus Type-1", Lawrence, KS, July 2010 & July 2011.

References:

1 Group, U. S. C. S. W. United States Cancer Statistics: 1999-2013 Incidence and Mortality Web-based Report. *Atlanta (GA): Department of Health and Human Services, Centers for Disease Control and Prevention, and National Cancer Institute. Available at: http://www.cdc.gov/uscs.* (2016).

2 Mehlen, P. & Puisieux, A. Metastasis: a question of life or death. *Nat Rev Cancer* **6**, 449-458, doi:nrc1886 [pii]

10.1038/nrc1886 (2006).

3 Daling, J. R., Malone, K. E., Doody, D. R., Anderson, B. O. & Porter, P. L. The relation of reproductive factors to mortality from breast cancer. *Cancer Epidemiol Biomarkers Prev* **11**, 235-241 (2002).

4 Bladstrom, A., Anderson, H. & Olsson, H. Worse survival in breast cancer among women with recent childbirth: results from a Swedish population-based register study. *Clin Breast Cancer* **4**, 280-285 (2003).

5 Kroman, N. & Mouridsen, H. T. Prognostic influence of pregnancy before, around, and after diagnosis of breast cancer. *Breast* **12**, 516-521 (2003).

6 Whiteman, M. K. *et al.* Reproductive history and mortality after breast cancer diagnosis. *Obstet Gynecol* **104**, 146-154, doi:10.1097/01.AOG.0000128173.01611.ff (2004).

7 Stensheim, H., Moller, B., van Dijk, T. & Fossa, S. D. Cause-specific survival for women diagnosed with cancer during pregnancy or lactation: a registry-based cohort study. *Journal of clinical oncology : official journal of the American Society of Clinical Oncology* **27**, 45-51, doi:10.1200/JCO.2008.17.4110 (2009).

8 Johansson, A. L., Andersson, T. M., Hsieh, C. C., Cnattingius, S. & Lambe, M. Increased mortality in women with breast cancer detected during pregnancy and different periods postpartum. *Cancer Epidemiol Biomarkers Prev* **20**, 1865-1872, doi:1055-9965.EPI-11-0515 [pii]

10.1158/1055-9965.EPI-11-0515 (2011).

9 Callihan, E. B. *et al.* Postpartum diagnosis demonstrates a high risk for metastasis and merits an expanded definition of pregnancy-associated breast cancer. *Breast Cancer Res Treat* **138**, 549-559, doi:10.1007/s10549-013-2437-x (2013).

10 Amant, F. *et al.* Prognosis of women with primary breast cancer diagnosed during pregnancy: results from an international collaborative study. *J Clin Oncol* **31**, 2532-2539, doi:10.1200/JCO.2012.45.6335 (2013).

11 Strasser-Weippl, K. *et al.* Pregnancy-associated breast cancer in women from Shanghai: risk and prognosis. *Breast Cancer Res Treat* **149**, 255-261, doi:10.1007/s10549-014-3219-9 (2015).

12 Lyons, T. R., Schedin, P. J. & Borges, V. F. Pregnancy and breast cancer: when they collide. *J Mammary Gland Biol Neoplasia* **14**, 87-98, doi:10.1007/s10911-009-9119-7 (2009).

13 Howlader N, N. A., Krapcho M, Miller D, Bishop K, Altekruse SF, Kosary CL, Yu M, Ruhl J, Tatalovich Z, Mariotto A, Lewis DR, Chen HS, Feuer EJ, Cronin KA

(eds). SEER Cancer Statistics Review. *National Cancer Institute* **Bethesda, MD** (1975-2013).
14 ACS. Cancer Facts and Figures 2015. *Atlanta* **American Cancer Society** (2015).
15 Schedin, P. Pregnancy-associated breast cancer and metastasis. *Nat Rev Cancer* **6**, 281-291, doi:nrc1839 [pii]

10.1038/nrc1839 (2006).
16 Albrektsen, G., Heuch, I., Hansen, S. & Kvale, G. Breast cancer risk by age at birth, time since birth and time intervals between births: exploring interaction effects. *Br J Cancer* **92**, 167-175, doi:10.1038/sj.bjc.6602302 (2005).
17 Lambe, M. *et al.* Transient increase in the risk of breast cancer after giving birth. *N Engl J Med* **331**, 5-9, doi:10.1056/NEJM199407073310102 (1994).
18 Mathews T.J., H., B.E. Mean Age of Mothers is on the Rise: United States, 2000-2014. (2016).
19 Hamilton, B. E., Martin, J. A. & Ventura, S. J. Births: preliminary data for 2005. *Natl Vital Stat Rep* **55**, 1-18 (2006).
20 ABS, A. B. o. S. One for the country: recent trends in fertility. **4102.0** (2010).
21 Andersson, T. M., Johansson, A. L., Hsieh, C. C., Cnattingius, S. & Lambe, M. Increasing incidence of pregnancy-associated breast cancer in Sweden. *Obstet Gynecol* **114**, 568-572, doi:10.1097/AOG.0b013e3181b19154 (2009).
22 Matsuda, T. *et al.* Cancer incidence and incidence rates in Japan in 2006: based on data from 15 population-based cancer registries in the monitoring of cancer incidence in Japan (MCIJ) project. *Jpn J Clin Oncol* **42**, 139-147, doi:10.1093/jjco/hyr184 (2012).
23 Borges, V. F. Management of the patient with postpartum breast cancer. *Oncology (Williston Park)* **28**, 768-770 (2014).
24 Henderson, B. E., Ross, R. & Bernstein, L. Estrogens as a cause of human cancer: the Richard and Hinda Rosenthal Foundation award lecture. *Cancer Res* **48**, 246-253 (1988).
25 Gottardis, M. M., Wagner, R. J., Borden, E. C. & Jordan, V. C. Differential ability of antiestrogens to stimulate breast cancer cell (MCF-7) growth in vivo and in vitro. *Cancer Res* **49**, 4765-4769 (1989).
26 Rossouw, J. E. *et al.* Risks and benefits of estrogen plus progestin in healthy postmenopausal women: principal results From the Women's Health Initiative randomized controlled trial. *JAMA* **288**, 321-333 (2002).
27 Burtrum, D. *et al.* A fully human monoclonal antibody to the insulin-like growth factor I receptor blocks ligand-dependent signaling and inhibits human tumor growth in vivo. *Cancer Res* **63**, 8912-8921 (2003).
28 Thorne, C. & Lee, A. V. Cross talk between estrogen receptor and IGF signaling in normal mammary gland development and breast cancer. *Breast Dis* **17**, 105-114 (2003).
29 Puckridge, P. J., Saunders, C. M., Ives, A. D. & Semmens, J. B. Breast cancer and pregnancy: a diagnostic and management dilemma. *ANZ J Surg* **73**, 500-503 (2003).

30 Woo, J. C., Yu, T. & Hurd, T. C. Breast cancer in pregnancy: a literature review. *Arch Surg* **138**, 91-98; discussion 99 (2003).
31 Malorni, L. *et al.* Clinical and biologic features of triple-negative breast cancers in a large cohort of patients with long-term follow-up. *Breast Cancer Res Treat* **136**, 795-804, doi:10.1007/s10549-012-2315-y (2012).
32 Lund, M. J. *et al.* Race and triple negative threats to breast cancer survival: a population-based study in Atlanta, GA. *Breast Cancer Res Treat* **113**, 357-370, doi:10.1007/s10549-008-9926-3 (2009).
33 Bauer, K. R., Brown, M., Cress, R. D., Parise, C. A. & Caggiano, V. Descriptive analysis of estrogen receptor (ER)-negative, progesterone receptor (PR)-negative, and HER2-negative invasive breast cancer, the so-called triple-negative phenotype: a population-based study from the California cancer Registry. *Cancer* **109**, 1721-1728, doi:10.1002/cncr.22618 (2007).
34 Parise, C. A., Bauer, K. R. & Caggiano, V. Variation in breast cancer subtypes with age and race/ethnicity. *Crit Rev Oncol Hematol* **76**, 44-52, doi:10.1016/j.critrevonc.2009.09.002 (2010).
35 Arnes, J. B. *et al.* Expression of epidermal growth factor receptor in relation to BRCA1 status, basal-like markers and prognosis in breast cancer. *J Clin Pathol* **62**, 139-146, doi:10.1136/jcp.2008.056291 (2009).
36 Palmer, J. R. *et al.* Parity, lactation, and breast cancer subtypes in African American women: results from the AMBER Consortium. *J Natl Cancer Inst* **106**, doi:10.1093/jnci/dju237 (2014).
37 Lund, L. R. *et al.* Two distinct phases of apoptosis in mammary gland involution: proteinase-independent and -dependent pathways. *Development* **122**, 181-193 (1996).
38 Marti, A., Feng, Z., Altermatt, H. J. & Jaggi, R. Milk accumulation triggers apoptosis of mammary epithelial cells. *Eur J Cell Biol* **73**, 158-165 (1997).
39 Walker, N. I., Bennett, R. E. & Kerr, J. F. Cell death by apoptosis during involution of the lactating breast in mice and rats. *Am J Anat* **185**, 19-32, doi:10.1002/aja.1001850104 (1989).
40 Monks, J., Smith-Steinhart, C., Kruk, E. R., Fadok, V. A. & Henson, P. M. Epithelial cells remove apoptotic epithelial cells during post-lactation involution of the mouse mammary gland. *Biol Reprod* **78**, 586-594, doi:10.1095/biolreprod.107.065045 (2008).
41 Sargeant, T. J. *et al.* Stat3 controls cell death during mammary gland involution by regulating uptake of milk fat globules and lysosomal membrane permeabilization. *Nat Cell Biol* **16**, 1057-1068, doi:10.1038/ncb3043 (2014).
42 Martinson, H. A., Jindal, S., Durand-Rougely, C., Borges, V. F. & Schedin, P. Wound healing-like immune program facilitates postpartum mammary gland involution and tumor progression. *Int J Cancer*, doi:10.1002/ijc.29181 (2014).
43 O'Brien, J. *et al.* Alternatively activated macrophages and collagen remodeling characterize the postpartum involuting mammary gland across species. *Am J Pathol* **176**, 1241-1255, doi:S0002-9440(10)60437-3 [pii]

10.2353/ajpath.2010.090735 (2010).

44 Atabai, K., Sheppard, D. & Werb, Z. Roles of the innate immune system in mammary gland remodeling during involution. *J Mammary Gland Biol Neoplasia* **12**, 37-45, doi:10.1007/s10911-007-9036-6 (2007).
45 Lilla, J. N., Joshi, R. V., Craik, C. S. & Werb, Z. Active plasma kallikrein localizes to mast cells and regulates epithelial cell apoptosis, adipocyte differentiation, and stromal remodeling during mammary gland involution. *J Biol Chem* **284**, 13792-13803, doi:10.1074/jbc.M900508200 (2009).
46 Schedin, P., Mitrenga, T., McDaniel, S. & Kaeck, M. Mammary ECM composition and function are altered by reproductive state. *Mol Carcinog* **41**, 207-220, doi:10.1002/mc.20058 (2004).
47 Lyons, T. R. *et al.* Postpartum mammary gland involution drives progression of ductal carcinoma in situ through collagen and COX-2. *Nat Med* **17**, 1109-1115, doi:10.1038/nm.2416

nm.2416 [pii] (2011).
48 O'Brien, J. H., Vanderlinden, L. A., Schedin, P. J. & Hansen, K. C. Rat mammary extracellular matrix composition and response to ibuprofen treatment during postpartum involution by differential GeLC-MS/MS analysis. *J Proteome Res* **11**, 4894-4905, doi:10.1021/pr3003744 (2012).
49 McDaniel, S. M. *et al.* Remodeling of the mammary microenvironment after lactation promotes breast tumor cell metastasis. *Am J Pathol* **168**, 608-620, doi:S0002-9440(10)62120-7 [pii]

10.2353/ajpath.2006.050677 (2006).
50 Luzzi, K. J. *et al.* Multistep nature of metastatic inefficiency: dormancy of solitary cells after successful extravasation and limited survival of early micrometastases. *Am J Pathol* **153**, 865-873, doi:10.1016/S0002-9440(10)65628-3 (1998).
51 Quail, D. F. & Joyce, J. A. Microenvironmental regulation of tumor progression and metastasis. *Nature medicine* **19**, 1423-1437, doi:10.1038/nm.3394 (2013).
52 Joyce, J. A. & Pollard, J. W. Microenvironmental regulation of metastasis. *Nat Rev Cancer* **9**, 239-252, doi:10.1038/nrc2618

nrc2618 [pii] (2009).
53 Turajlic, S. & Swanton, C. Metastasis as an evolutionary process. *Science* **352**, 169-175, doi:10.1126/science.aaf2784 (2016).
54 Klein, C. A. Parallel progression of primary tumours and metastases. *Nat Rev Cancer* **9**, 302-312, doi:10.1038/nrc2627 (2009).
55 Schmidt-Kittler, O. *et al.* From latent disseminated cells to overt metastasis: genetic analysis of systemic breast cancer progression. *Proc Natl Acad Sci U S A* **100**, 7737-7742, doi:10.1073/pnas.1331931100 (2003).
56 Schardt, J. A. *et al.* Genomic analysis of single cytokeratin-positive cells from bone marrow reveals early mutational events in breast cancer. *Cancer Cell* **8**, 227-239, doi:10.1016/j.ccr.2005.08.003 (2005).

57 Stoecklein, N. H. *et al.* Direct genetic analysis of single disseminated cancer cells for prediction of outcome and therapy selection in esophageal cancer. *Cancer Cell* **13**, 441-453, doi:10.1016/j.ccr.2008.04.005 (2008).
58 Eyles, J. *et al.* Tumor cells disseminate early, but immunosurveillance limits metastatic outgrowth, in a mouse model of melanoma. *The Journal of clinical investigation* **120**, 2030-2039, doi:10.1172/JCI42002 (2010).
59 Husemann, Y. *et al.* Systemic spread is an early step in breast cancer. *Cancer Cell* **13**, 58-68, doi:10.1016/j.ccr.2007.12.003 (2008).
60 Hanahan, D. & Weinberg, R. A. Hallmarks of cancer: the next generation. *Cell* **144**, 646-674, doi:10.1016/j.cell.2011.02.013

S0092-8674(11)00127-9 [pii] (2011).
61 Bergers, G. & Benjamin, L. E. Tumorigenesis and the angiogenic switch. *Nat Rev Cancer* **3**, 401-410, doi:10.1038/nrc1093 (2003).
62 Hanahan, D. & Folkman, J. Patterns and emerging mechanisms of the angiogenic switch during tumorigenesis. *Cell* **86**, 353-364 (1996).
63 Folkman, J. The role of angiogenesis in tumor growth. *Semin Cancer Biol* **3**, 65-71 (1992).
64 Folkman, J. Role of angiogenesis in tumor growth and metastasis. *Semin Oncol* **29**, 15-18, doi:10.1053/sonc.2002.37263 (2002).
65 Lin, E. Y. *et al.* Macrophages regulate the angiogenic switch in a mouse model of breast cancer. *Cancer Res* **66**, 11238-11246, doi:10.1158/0008-5472.CAN-06-1278 (2006).
66 Lin, E. Y. *et al.* Vascular endothelial growth factor restores delayed tumor progression in tumors depleted of macrophages. *Mol Oncol* **1**, 288-302, doi:10.1016/j.molonc.2007.10.003 (2007).
67 Zabuawala, T. *et al.* An ets2-driven transcriptional program in tumor-associated macrophages promotes tumor metastasis. *Cancer Res* **70**, 1323-1333, doi:10.1158/0008-5472.CAN-09-1474 (2010).
68 Mazzieri, R. *et al.* Targeting the ANG2/TIE2 axis inhibits tumor growth and metastasis by impairing angiogenesis and disabling rebounds of proangiogenic myeloid cells. *Cancer Cell* **19**, 512-526, doi:10.1016/j.ccr.2011.02.005 (2011).
69 Yang, L. *et al.* Expansion of myeloid immune suppressor Gr+CD11b+ cells in tumor-bearing host directly promotes tumor angiogenesis. *Cancer Cell* **6**, 409-421, doi:10.1016/j.ccr.2004.08.031 (2004).
70 Ramirez, R. A., Lee, A., Schedin, P., Russell, J. S. & Masso-Welch, P. A. Alterations in mast cell frequency and relationship to angiogenesis in the rat mammary gland during windows of physiologic tissue remodeling. *Dev Dyn* **241**, 890-900, doi:10.1002/dvdy.23778 (2012).
71 Lin, E. Y., Nguyen, A. V., Russell, R. G. & Pollard, J. W. Colony-stimulating factor 1 promotes progression of mammary tumors to malignancy. *J Exp Med* **193**, 727-740 (2001).
72 Zhang, Q. W. *et al.* Prognostic significance of tumor-associated macrophages in solid tumor: a meta-analysis of the literature. *PLoS One* **7**, e50946, doi:10.1371/journal.pone.0050946 (2012).

73 Pollard, J. W. Tumour-educated macrophages promote tumour progression and metastasis. *Nature reviews. Cancer* **4**, 71-78, doi:10.1038/nrc1256 (2004).
74 Wyckoff, J. *et al.* A paracrine loop between tumor cells and macrophages is required for tumor cell migration in mammary tumors. *Cancer Res* **64**, 7022-7029, doi:64/19/7022 [pii]

10.1158/0008-5472.CAN-04-1449 (2004).
75 Pawelek, J. M. & Chakraborty, A. K. Fusion of tumour cells with bone marrow-derived cells: a unifying explanation for metastasis. *Nat Rev Cancer* **8**, 377-386, doi:10.1038/nrc2371 (2008).
76 Powell, A. E. *et al.* Fusion between Intestinal epithelial cells and macrophages in a cancer context results in nuclear reprogramming. *Cancer Res* **71**, 1497-1505, doi:10.1158/0008-5472.CAN-10-3223 (2011).
77 Jindal, S. *et al.* Postpartum breast involution reveals regression of secretory lobules mediated by tissue-remodeling. *Breast Cancer Res* **16**, R31, doi:10.1186/bcr3633 (2014).
78 Provenzano, P. P. *et al.* Collagen density promotes mammary tumor initiation and progression. *BMC Med* **6**, 11, doi:10.1186/1741-7015-6-11 (2008).
79 Conklin, M. W. *et al.* Aligned collagen is a prognostic signature for survival in human breast carcinoma. *Am J Pathol* **178**, 1221-1232, doi:10.1016/j.ajpath.2010.11.076 (2011).
80 Nguyen-Ngoc, K. V. *et al.* ECM microenvironment regulates collective migration and local dissemination in normal and malignant mammary epithelium. *Proc Natl Acad Sci U S A* **109**, E2595-2604, doi:10.1073/pnas.1212834109 (2012).
81 Hamilton, S. R. *et al.* The hyaluronan receptors CD44 and Rhamm (CD168) form complexes with ERK1,2 that sustain high basal motility in breast cancer cells. *J Biol Chem* **282**, 16667-16680, doi:10.1074/jbc.M702078200 (2007).
82 Oskarsson, T. *et al.* Breast cancer cells produce tenascin C as a metastatic niche component to colonize the lungs. *Nat Med* **17**, 867-874, doi:10.1038/nm.2379

nm.2379 [pii] (2011).
83 Jahkola, T. *et al.* Tenascin-C expression in invasion border of early breast cancer: a predictor of local and distant recurrence. *Br J Cancer* **78**, 1507-1513 (1998).
84 Tsunoda, T. *et al.* Involvement of large tenascin-C splice variants in breast cancer progression. *The American journal of pathology* **162**, 1857-1867, doi:10.1016/S0002-9440(10)64320-9 (2003).
85 Ishihara, A., Yoshida, T., Tamaki, H. & Sakakura, T. Tenascin expression in cancer cells and stroma of human breast cancer and its prognostic significance. *Clin Cancer Res* **1**, 1035-1041 (1995).
86 Yoshida, T., Ishihara, A., Hirokawa, Y., Kusakabe, M. & Sakakura, T. Tenascin in breast cancer development--is epithelial tenascin a marker for poor prognosis? *Cancer Lett* **90**, 65-73 (1995).

87 Page-McCaw, A., Ewald, A. J. & Werb, Z. Matrix metalloproteinases and the regulation of tissue remodelling. *Nat Rev Mol Cell Biol* **8**, 221-233, doi:10.1038/nrm2125 (2007).
88 Wolf, K. *et al.* Multi-step pericellular proteolysis controls the transition from individual to collective cancer cell invasion. *Nat Cell Biol* **9**, 893-904, doi:10.1038/ncb1616 (2007).
89 Erler, J. T. *et al.* Lysyl oxidase is essential for hypoxia-induced metastasis. *Nature* **440**, 1222-1226, doi:10.1038/nature04695 (2006).
90 Acerbi, I. *et al.* Human breast cancer invasion and aggression correlates with ECM stiffening and immune cell infiltration. *Integr Biol (Camb)* **7**, 1120-1134, doi:10.1039/c5ib00040h (2015).
91 Levental, K. R. *et al.* Matrix crosslinking forces tumor progression by enhancing integrin signaling. *Cell* **139**, 891-906, doi:10.1016/j.cell.2009.10.027 (2009).
92 Alexander, C. M., Selvarajan, S., Mudgett, J. & Werb, Z. Stromelysin-1 regulates adipogenesis during mammary gland involution. *J Cell Biol* **152**, 693-703 (2001).
93 Barker, H. E. *et al.* LOXL2-mediated matrix remodeling in metastasis and mammary gland involution. *Cancer Res* **71**, 1561-1572, doi:10.1158/0008-5472.CAN-10-2868 (2011).
94 Goddard, E. T. *et al.* Quantitative extracellular matrix proteomics to study mammary and liver tissue microenvironments. *Int J Biochem Cell Biol*, doi:10.1016/j.biocel.2016.10.014 (2016).
95 Bemis, L. T. & Schedin, P. Reproductive state of rat mammary gland stroma modulates human breast cancer cell migration and invasion. *Cancer Res* **60**, 3414-3418 (2000).
96 Ricard-Blum, S. & Vallet, S. D. Proteases decode the extracellular matrix cryptome. *Biochimie* **122**, 300-313, doi:10.1016/j.biochi.2015.09.016 (2016).
97 Dunn, G. P., Old, L. J. & Schreiber, R. D. The three Es of cancer immunoediting. *Annu Rev Immunol* **22**, 329-360, doi:10.1146/annurev.immunol.22.012703.104803 (2004).
98 Kitamura, T., Qian, B. Z. & Pollard, J. W. Immune cell promotion of metastasis. *Nat Rev Immunol* **15**, 73-86, doi:10.1038/nri3789 (2015).
99 Palucka, A. K. & Coussens, L. M. The Basis of Oncoimmunology. *Cell* **164**, 1233-1247, doi:10.1016/j.cell.2016.01.049 (2016).
100 Ruffell, B., DeNardo, D. G., Affara, N. I. & Coussens, L. M. Lymphocytes in cancer development: polarization towards pro-tumor immunity. *Cytokine Growth Factor Rev* **21**, 3-10, doi:10.1016/j.cytogfr.2009.11.002 (2010).
101 Kacha, A. K., Fallarino, F., Markiewicz, M. A. & Gajewski, T. F. Cutting edge: spontaneous rejection of poorly immunogenic P1.HTR tumors by Stat6-deficient mice. *J Immunol* **165**, 6024-6028 (2000).
102 Ostrand-Rosenberg, S., Grusby, M. J. & Clements, V. K. Cutting edge: STAT6-deficient mice have enhanced tumor immunity to primary and metastatic mammary carcinoma. *J Immunol* **165**, 6015-6019 (2000).

103 Schietinger, A. *et al.* Tumor-Specific T Cell Dysfunction Is a Dynamic Antigen-Driven Differentiation Program Initiated Early during Tumorigenesis. *Immunity* **45**, 389-401, doi:10.1016/j.immuni.2016.07.011 (2016).
104 Denardo, D. G. *et al.* Leukocyte Complexity Predicts Breast Cancer Survival and Functionally Regulates Response to Chemotherapy. *Cancer Discov* **1**, 54-67, doi:2159-8274.CD-10-0028 [pii]

10.1158/2159-8274.CD-10-0028 (2011).
105 DeNardo, D. G. *et al.* CD4(+) T cells regulate pulmonary metastasis of mammary carcinomas by enhancing protumor properties of macrophages. *Cancer Cell* **16**, 91-102, doi:10.1016/j.ccr.2009.06.018 (2009).
106 Ruffell, B. *et al.* Macrophage IL-10 blocks CD8+ T cell-dependent responses to chemotherapy by suppressing IL-12 expression in intratumoral dendritic cells. *Cancer Cell* **26**, 623-637, doi:10.1016/j.ccell.2014.09.006 (2014).
107 Pyonteck, S. M. *et al.* CSF-1R inhibition alters macrophage polarization and blocks glioma progression. *Nat Med* **19**, 1264-1272, doi:10.1038/nm.3337 (2013).
108 Cotechini, T., Medler, T. R. & Coussens, L. M. Myeloid Cells as Targets for Therapy in Solid Tumors. *Cancer J* **21**, 343-350, doi:10.1097/PPO.0000000000000132 (2015).
109 Gunderson, A. J. *et al.* Bruton Tyrosine Kinase-Dependent Immune Cell Cross-talk Drives Pancreas Cancer. *Cancer Discov* **6**, 270-285, doi:10.1158/2159-8290.CD-15-0827 (2016).
110 Sharma, P. & Allison, J. P. The future of immune checkpoint therapy. *Science* **348**, 56-61, doi:10.1126/science.aaa8172 (2015).
111 Leach, D. R., Krummel, M. F. & Allison, J. P. Enhancement of antitumor immunity by CTLA-4 blockade. *Science* **271**, 1734-1736 (1996).
112 Iwai, Y. *et al.* Involvement of PD-L1 on tumor cells in the escape from host immune system and tumor immunotherapy by PD-L1 blockade. *Proc Natl Acad Sci U S A* **99**, 12293-12297, doi:10.1073/pnas.192461099 (2002).
113 O'Brien, J. *et al.* Non-steroidal anti-inflammatory drugs target the pro-tumorigenic extracellular matrix of the postpartum mammary gland. *Int J Dev Biol* **55**, 745-755, doi:10.1387/ijdb.113379jo (2011).
114 Lyons, T. R. *et al.* Cyclooxygenase-2-dependent lymphangiogenesis promotes nodal metastasis of postpartum breast cancer. *The Journal of clinical investigation* **124**, 3901-3912, doi:10.1172/JCI73777 (2014).
115 Dvorak, H. F. Tumors: wounds that do not heal. Similarities between tumor stroma generation and wound healing. *N Engl J Med* **315**, 1650-1659, doi:10.1056/NEJM198612253152606 (1986).
116 Dvorak, H. F. Tumors: wounds that do not heal-redux. *Cancer Immunol Res* **3**, 1-11, doi:10.1158/2326-6066.CIR-14-0209 (2015).
117 Bono, P. *et al.* High LYVE-1-positive lymphatic vessel numbers are associated with poor outcome in breast cancer. *Clin Cancer Res* **10**, 7144-7149, doi:10.1158/1078-0432.CCR-03-0826 (2004).

118 Van den Eynden, G. G. *et al.* Distinguishing blood and lymph vessel invasion in breast cancer: a prospective immunohistochemical study. *Br J Cancer* **94**, 1643-1649, doi:10.1038/sj.bjc.6603152 (2006).
119 Arnaout-Alkarain, A., Kahn, H. J., Narod, S. A., Sun, P. A. & Marks, A. N. Significance of lymph vessel invasion identified by the endothelial lymphatic marker D2-40 in node negative breast cancer. *Mod Pathol* **20**, 183-191, doi:10.1038/modpathol.3800728 (2007).
120 Schoppmann, S. F., Horvat, R. & Birner, P. Lymphatic vessels and lymphangiogenesis in female cancer: mechanisms, clinical impact and possible implications for anti-lymphangiogenic therapies (Review). *Oncol Rep* **9**, 455-460 (2002).
121 Skobe, M. *et al.* Induction of tumor lymphangiogenesis by VEGF-C promotes breast cancer metastasis. *Nat Med* **7**, 192-198, doi:10.1038/84643 (2001).
122 Chambers, A. F., Groom, A. C. & MacDonald, I. C. Dissemination and growth of cancer cells in metastatic sites. *Nat Rev Cancer* **2**, 563-572, doi:10.1038/nrc865

nrc865 [pii] (2002).
123 Karaman, S. & Detmar, M. Mechanisms of lymphatic metastasis. *The Journal of clinical investigation* **124**, 922-928, doi:10.1172/JCI71606 (2014).
124 Pasquali, S. *et al.* Lymphatic biomarkers in primary melanomas as predictors of regional lymph node metastasis and patient outcomes. *Pigment Cell Melanoma Res* **26**, 326-337, doi:10.1111/pcmr.12064 (2013).
125 Paduch, R. The role of lymphangiogenesis and angiogenesis in tumor metastasis. *Cell Oncol (Dordr)* **39**, 397-410, doi:10.1007/s13402-016-0281-9 (2016).
126 Maruyama, K. *et al.* Inflammation-induced lymphangiogenesis in the cornea arises from CD11b-positive macrophages. *The Journal of clinical investigation* **115**, 2363-2372, doi:10.1172/JCI23874 (2005).
127 Cho, H. J. *et al.* Bone marrow-derived, alternatively activated macrophages enhance solid tumor growth and lung metastasis of mammary carcinoma cells in a Balb/C mouse orthotopic model. *Breast Cancer Res* **14**, R81, doi:10.1186/bcr3195 (2012).
128 Schoppmann, S. F. *et al.* Tumor-associated macrophages express lymphatic endothelial growth factors and are related to peritumoral lymphangiogenesis. *Am J Pathol* **161**, 947-956, doi:10.1016/S0002-9440(10)64255-1 (2002).
129 Kerjaschki, D. The lymphatic vasculature revisited. *The Journal of clinical investigation* **124**, 874-877, doi:10.1172/JCI74854 (2014).
130 Munn, D. H. & Mellor, A. L. The tumor-draining lymph node as an immune-privileged site. *Immunol Rev* **213**, 146-158, doi:10.1111/j.1600-065X.2006.00444.x (2006).
131 Swartz, M. A. Immunomodulatory roles of lymphatic vessels in cancer progression. *Cancer Immunol Res* **2**, 701-707, doi:10.1158/2326-6066.CIR-14-0115 (2014).

132 Podgrabinska, S. *et al.* Inflamed lymphatic endothelium suppresses dendritic cell maturation and function via Mac-1/ICAM-1-dependent mechanism. *J Immunol* **183**, 1767-1779, doi:10.4049/jimmunol.0802167 (2009).
133 Lund, A. W. *et al.* Lymphatic vessels regulate immune microenvironments in human and murine melanoma. *The Journal of clinical investigation* **126**, 3389-3402, doi:10.1172/JCI79434 (2016).
134 Lund, A. W. *et al.* VEGF-C promotes immune tolerance in B16 melanomas and cross-presentation of tumor antigen by lymph node lymphatics. *Cell Rep* **1**, 191-199, doi:10.1016/j.celrep.2012.01.005 (2012).
135 Cohen, J. N. *et al.* Lymph node-resident lymphatic endothelial cells mediate peripheral tolerance via Aire-independent direct antigen presentation. *J Exp Med* **207**, 681-688, doi:10.1084/jem.20092465 (2010).
136 Robinson, B. D. *et al.* Tumor microenvironment of metastasis in human breast carcinoma: a potential prognostic marker linked to hematogenous dissemination. *Clin Cancer Res* **15**, 2433-2441, doi:10.1158/1078-0432.CCR-08-2179 (2009).
137 Rohan, T. E. *et al.* Tumor microenvironment of metastasis and risk of distant metastasis of breast cancer. *J Natl Cancer Inst* **106**, doi:10.1093/jnci/dju136 (2014).
138 Harney, A. S. *et al.* Real-Time Imaging Reveals Local, Transient Vascular Permeability, and Tumor Cell Intravasation Stimulated by TIE2hi Macrophage-Derived VEGFA. *Cancer Discov* **5**, 932-943, doi:10.1158/2159-8290.CD-15-0012 (2015).
139 Roh-Johnson, M. *et al.* Macrophage contact induces RhoA GTPase signaling to trigger tumor cell intravasation. *Oncogene* **33**, 4203-4212, doi:10.1038/onc.2013.377 (2014).
140 Pignatelli, J. *et al.* Macrophage-dependent tumor cell transendothelial migration is mediated by Notch1/MenaINV-initiated invadopodium formation. *Sci Rep* **6**, 37874, doi:10.1038/srep37874 (2016).
141 Han, W. *et al.* Oriented collagen fibers direct tumor cell intravasation. *Proc Natl Acad Sci U S A* **113**, 11208-11213, doi:10.1073/pnas.1610347113 (2016).
142 Cameron, M. D. *et al.* Temporal progression of metastasis in lung: cell survival, dormancy, and location dependence of metastatic inefficiency. *Cancer Res* **60**, 2541-2546 (2000).
143 Kienast, Y. *et al.* Real-time imaging reveals the single steps of brain metastasis formation. *Nature medicine* **16**, 116-122, doi:10.1038/nm.2072 (2010).
144 Koop, S. *et al.* Fate of melanoma cells entering the microcirculation: over 80% survive and extravasate. *Cancer Res* **55**, 2520-2523 (1995).
145 Larson, C. J. *et al.* Apoptosis of circulating tumor cells in prostate cancer patients. *Cytometry A* **62**, 46-53, doi:10.1002/cyto.a.20073 (2004).
146 Smerage, J. B. *et al.* Monitoring apoptosis and Bcl-2 on circulating tumor cells in patients with metastatic breast cancer. *Mol Oncol* **7**, 680-692, doi:10.1016/j.molonc.2013.02.013 (2013).

147 Kallergi, G. *et al.* Apoptotic circulating tumor cells in early and metastatic breast cancer patients. *Mol Cancer Ther* **12**, 1886-1895, doi:10.1158/1535-7163.MCT-12-1167 (2013).
148 Nieswandt, B., Hafner, M., Echtenacher, B. & Mannel, D. N. Lysis of tumor cells by natural killer cells in mice is impeded by platelets. *Cancer Res* **59**, 1295-1300 (1999).
149 Palumbo, J. S. *et al.* Platelets and fibrin(ogen) increase metastatic potential by impeding natural killer cell-mediated elimination of tumor cells. *Blood* **105**, 178-185, doi:10.1182/blood-2004-06-2272 (2005).
150 Camerer, E. *et al.* Platelets, protease-activated receptors, and fibrinogen in hematogenous metastasis. *Blood* **104**, 397-401, doi:10.1182/blood-2004-02-0434 (2004).
151 Palumbo, J. S. *et al.* Tumor cell-associated tissue factor and circulating hemostatic factors cooperate to increase metastatic potential through natural killer cell-dependent and-independent mechanisms. *Blood* **110**, 133-141, doi:10.1182/blood-2007-01-065995 (2007).
152 Palumbo, J. S. & Degen, J. L. Mechanisms linking tumor cell-associated procoagulant function to tumor metastasis. *Thromb Res* **120 Suppl 2**, S22-28, doi:10.1016/S0049-3848(07)70127-5 (2007).
153 Kopp, H. G., Placke, T. & Salih, H. R. Platelet-derived transforming growth factor-beta down-regulates NKG2D thereby inhibiting natural killer cell antitumor reactivity. *Cancer Res* **69**, 7775-7783, doi:10.1158/0008-5472.CAN-09-2123 (2009).
154 Tan, W. *et al.* Tumour-infiltrating regulatory T cells stimulate mammary cancer metastasis through RANKL-RANK signalling. *Nature* **470**, 548-553, doi:10.1038/nature09707 (2011).
155 Muller, A. *et al.* Involvement of chemokine receptors in breast cancer metastasis. *Nature* **410**, 50-56, doi:10.1038/35065016 (2001).
156 Kaifi, J. T. *et al.* Tumor-cell homing to lymph nodes and bone marrow and CXCR4 expression in esophageal cancer. *J Natl Cancer Inst* **97**, 1840-1847, doi:10.1093/jnci/dji431 (2005).
157 Martin, M. D. *et al.* Rapid extravasation and establishment of breast cancer micrometastases in the liver microenvironment. *Mol Cancer Res* **8**, 1319-1327, doi:10.1158/1541-7786.MCR-09-0551 (2010).
158 Morris, V. L. *et al.* Early interactions of cancer cells with the microvasculature in mouse liver and muscle during hematogenous metastasis: videomicroscopic analysis. *Clin Exp Metastasis* **11**, 377-390 (1993).
159 Mook, O. R. *et al.* Visualization of early events in tumor formation of eGFP-transfected rat colon cancer cells in liver. *Hepatology* **38**, 295-304, doi:10.1053/jhep.2003.50297 (2003).
160 Ding, L. *et al.* In vivo evaluation of the early events associated with liver metastasis of circulating cancer cells. *Br J Cancer* **85**, 431-438, doi:10.1054/bjoc.2001.1911 (2001).
161 Stoletov, K. *et al.* Visualizing extravasation dynamics of metastatic tumor cells. *J Cell Sci* **123**, 2332-2341, doi:10.1242/jcs.069443 (2010).

162 Wang, H. H. *et al.* Regulation of B16F1 melanoma cell metastasis by inducible functions of the hepatic microvasculature. *Eur J Cancer* **38**, 1261-1270 (2002).
163 Al-Mehdi, A. B. *et al.* Intravascular origin of metastasis from the proliferation of endothelium-attached tumor cells: a new model for metastasis. *Nature medicine* **6**, 100-102, doi:10.1038/71429 (2000).
164 Gassmann, P., Hemping-Bovenkerk, A., Mees, S. T. & Haier, J. Metastatic tumor cell arrest in the liver-lumen occlusion and specific adhesion are not exclusive. *Int J Colorectal Dis* **24**, 851-858, doi:10.1007/s00384-009-0694-2 (2009).
165 Wang, H. *et al.* Tumor cell alpha3beta1 integrin and vascular laminin-5 mediate pulmonary arrest and metastasis. *J Cell Biol* **164**, 935-941, doi:10.1083/jcb.200309112 (2004).
166 Biancone, L., Araki, M., Araki, K., Vassalli, P. & Stamenkovic, I. Redirection of tumor metastasis by expression of E-selectin in vivo. *J Exp Med* **183**, 581-587 (1996).
167 Auguste, P. *et al.* The host inflammatory response promotes liver metastasis by increasing tumor cell arrest and extravasation. *The American journal of pathology* **170**, 1781-1792, doi:10.2353/ajpath.2007.060886 (2007).
168 Khatib, A. M. *et al.* Characterization of the host proinflammatory response to tumor cells during the initial stages of liver metastasis. *The American journal of pathology* **167**, 749-759, doi:10.1016/S0002-9440(10)62048-2 (2005).
169 Khatib, A. M. *et al.* Rapid induction of cytokine and E-selectin expression in the liver in response to metastatic tumor cells. *Cancer Res* **59**, 1356-1361 (1999).
170 Qian, B. *et al.* A distinct macrophage population mediates metastatic breast cancer cell extravasation, establishment and growth. *PLoS One* **4**, e6562, doi:10.1371/journal.pone.0006562 (2009).
171 Qian, B. Z. *et al.* CCL2 recruits inflammatory monocytes to facilitate breast-tumour metastasis. *Nature* **475**, 222-225, doi:10.1038/nature10138 (2011).
172 McDonald, B. *et al.* Systemic inflammation increases cancer cell adhesion to hepatic sinusoids by neutrophil mediated mechanisms. *International journal of cancer. Journal international du cancer* **125**, 1298-1305, doi:10.1002/ijc.24409 (2009).
173 Spicer, J. D. *et al.* Neutrophils Promote Liver Metastasis via Mac-1-Mediated Interactions with Circulating Tumor Cells. *Cancer Res* **72**, 3919-3927, doi:0008-5472.CAN-11-2393 [pii]

10.1158/0008-5472.CAN-11-2393 (2012).
174 Spiegel, A. *et al.* Neutrophils Suppress Intraluminal NK Cell-Mediated Tumor Cell Clearance and Enhance Extravasation of Disseminated Carcinoma Cells. *Cancer Discov* **6**, 630-649, doi:10.1158/2159-8290.CD-15-1157 (2016).
175 Coffelt, S. B. *et al.* IL-17-producing gammadelta T cells and neutrophils conspire to promote breast cancer metastasis. *Nature* **522**, 345-348, doi:10.1038/nature14282 (2015).

176 Granot, Z. *et al.* Tumor entrained neutrophils inhibit seeding in the premetastatic lung. *Cancer Cell* **20**, 300-314, doi:10.1016/j.ccr.2011.08.012 (2011).
177 Amirkhosravi, A. *et al.* Inhibition of tumor cell-induced platelet aggregation and lung metastasis by the oral GpIIb/IIIa antagonist XV454. *Thromb Haemost* **90**, 549-554, doi:10.1160/TH03-02-0102 (2003).
178 Felding-Habermann, B., Habermann, R., Saldivar, E. & Ruggeri, Z. M. Role of beta3 integrins in melanoma cell adhesion to activated platelets under flow. *The Journal of biological chemistry* **271**, 5892-5900 (1996).
179 Labelle, M., Begum, S. & Hynes, R. O. Direct signaling between platelets and cancer cells induces an epithelial-mesenchymal-like transition and promotes metastasis. *Cancer Cell* **20**, 576-590, doi:10.1016/j.ccr.2011.09.009 (2011).
180 Paget, S. The distribution of secondary growths in cancer of the breast. *Lancet* **1**, 571-573, doi:10.1016/S0140-6736(00)49915-0 (1889).
181 Ewing, J. Neoplastic Diseases: A Treatise on Tumors. *(W.B. Saunders Co., Philadelphia & London, 1928)*, 77-89 (1928).
182 Lee, Y. T. Breast carcinoma: pattern of metastasis at autopsy. *J Surg Oncol* **23**, 175-180 (1983).
183 Weigelt, B., Peterse, J. L. & van 't Veer, L. J. Breast cancer metastasis: markers and models. *Nat Rev Cancer* **5**, 591-602, doi:10.1038/nrc1670 (2005).
184 Weiss, L. Comments on hematogenous metastatic patterns in humans as revealed by autopsy. *Clin Exp Metastasis* **10**, 191-199 (1992).
185 Weiss, L. *et al.* Haematogenous metastatic patterns in colonic carcinoma: an analysis of 1541 necropsies. *J Pathol* **150**, 195-203, doi:10.1002/path.1711500308 (1986).
186 Weiss, L. & Harlos, J. P. The validity of negative necropsy reports for metastases in solid organs. *J Pathol* **148**, 203-206, doi:10.1002/path.1711480302 (1986).
187 Weiss, L. *et al.* Metastatic patterns of renal carcinoma: an analysis of 687 necropsies. *J Cancer Res Clin Oncol* **114**, 605-612 (1988).
188 Fidler, I. J. Metastasis: quantitative analysis of distribution and fate of tumor emboli labeled with 125 I-5-iodo-2'-deoxyuridine. *J Natl Cancer Inst* **45**, 773-782 (1970).
189 Fidler, I. J. & Nicolson, G. L. Fate of recirculating B16 melanoma metastatic variant cells in parabiotic syngeneic recipients. *J Natl Cancer Inst* **58**, 1867-1872 (1977).
190 Goodison, S. *et al.* Prolonged dormancy and site-specific growth potential of cancer cells spontaneously disseminated from nonmetastatic breast tumors as revealed by labeling with green fluorescent protein. *Clin Cancer Res* **9**, 3808-3814 (2003).
191 Naumov, G. N. *et al.* Persistence of solitary mammary carcinoma cells in a secondary site: a possible contributor to dormancy. *Cancer Res* **62**, 2162-2168 (2002).
192 Suzuki, M., Mose, E. S., Montel, V. & Tarin, D. Dormant cancer cells retrieved from metastasis-free organs regain tumorigenic and metastatic potency. *The*

American journal of pathology **169**, 673-681, doi:10.2353/ajpath.2006.060053 (2006).
193 Psaila, B., Kaplan, R. N., Port, E. R. & Lyden, D. Priming the 'soil' for breast cancer metastasis: the pre-metastatic niche. *Breast Dis* **26**, 65-74 (2006).
194 Peinado, H., Lavotshkin, S. & Lyden, D. The secreted factors responsible for pre-metastatic niche formation: old sayings and new thoughts. *Semin Cancer Biol* **21**, 139-146, doi:10.1016/j.semcancer.2011.01.002

S1044-579X(11)00003-4 [pii] (2011).
195 Sceneay, J., Smyth, M. J. & Moller, A. The pre-metastatic niche: finding common ground. *Cancer Metastasis Rev* **32**, 449-464, doi:10.1007/s10555-013-9420-1 (2013).
196 Hiratsuka, S. *et al.* MMP9 induction by vascular endothelial growth factor receptor-1 is involved in lung-specific metastasis. *Cancer Cell* **2**, 289-300 (2002).
197 Kaplan, R. N. *et al.* VEGFR1-positive haematopoietic bone marrow progenitors initiate the pre-metastatic niche. *Nature* **438**, 820-827, doi:10.1038/nature04186 (2005).
198 Hiratsuka, S., Watanabe, A., Aburatani, H. & Maru, Y. Tumour-mediated upregulation of chemoattractants and recruitment of myeloid cells predetermines lung metastasis. *Nat Cell Biol* **8**, 1369-1375, doi:10.1038/ncb1507 (2006).
199 Catena, R. *et al.* Bone marrow-derived Gr1+ cells can generate a metastasis-resistant microenvironment via induced secretion of thrombospondin-1. *Cancer Discov* **3**, 578-589, doi:10.1158/2159-8290.CD-12-0476 (2013).
200 Raposo, G. & Stoorvogel, W. Extracellular vesicles: exosomes, microvesicles, and friends. *J Cell Biol* **200**, 373-383, doi:10.1083/jcb.201211138 (2013).
201 Costa-Silva, B. *et al.* Pancreatic cancer exosomes initiate pre-metastatic niche formation in the liver. *Nat Cell Biol* **17**, 816-826, doi:10.1038/ncb3169 (2015).
202 Peinado, H. *et al.* Melanoma exosomes educate bone marrow progenitor cells toward a pro-metastatic phenotype through MET. *Nature medicine* **18**, 883-891, doi:10.1038/nm.2753 (2012).
203 Liu, Y. *et al.* Tumor Exosomal RNAs Promote Lung Pre-metastatic Niche Formation by Activating Alveolar Epithelial TLR3 to Recruit Neutrophils. *Cancer Cell* **30**, 243-256, doi:10.1016/j.ccell.2016.06.021 (2016).
204 Hoshino, A. *et al.* Tumour exosome integrins determine organotropic metastasis. *Nature* **527**, 329-335, doi:10.1038/nature15756 (2015).
205 Erler, J. T. *et al.* Hypoxia-induced lysyl oxidase is a critical mediator of bone marrow cell recruitment to form the premetastatic niche. *Cancer Cell* **15**, 35-44, doi:10.1016/j.ccr.2008.11.012 (2009).
206 Wong, C. C. *et al.* Hypoxia-inducible factor 1 is a master regulator of breast cancer metastatic niche formation. *Proceedings of the National Academy of Sciences of the United States of America* **108**, 16369-16374, doi:10.1073/pnas.1113483108 (2011).

207 Gil-Bernabe, A. M. *et al.* Recruitment of monocytes/macrophages by tissue factor-mediated coagulation is essential for metastatic cell survival and premetastatic niche establishment in mice. *Blood* **119**, 3164-3175, doi:10.1182/blood-2011-08-376426

blood-2011-08-376426 [pii] (2012).
208 Kowanetz, M. *et al.* Granulocyte-colony stimulating factor promotes lung metastasis through mobilization of Ly6G+Ly6C+ granulocytes. *Proceedings of the National Academy of Sciences of the United States of America* **107**, 21248-21255, doi:10.1073/pnas.1015855107 (2010).
209 Monteiro, A. C. *et al.* T cells induce pre-metastatic osteolytic disease and help bone metastases establishment in a mouse model of metastatic breast cancer. *PLoS One* **8**, e68171, doi:10.1371/journal.pone.0068171 (2013).
210 Ghajar, C. M. *et al.* The perivascular niche regulates breast tumour dormancy. *Nat Cell Biol* **15**, 807-817, doi:10.1038/ncb2767 (2013).
211 Malanchi, I. *et al.* Interactions between cancer stem cells and their niche govern metastatic colonization. *Nature* **481**, 85-89, doi:10.1038/nature10694

nature10694 [pii] (2012).
212 Barkan, D. *et al.* Inhibition of metastatic outgrowth from single dormant tumor cells by targeting the cytoskeleton. *Cancer Res* **68**, 6241-6250, doi:10.1158/0008-5472.CAN-07-6849 (2008).
213 Barkan, D. *et al.* Metastatic growth from dormant cells induced by a col-I-enriched fibrotic environment. *Cancer Res* **70**, 5706-5716, doi:10.1158/0008-5472.CAN-09-2356 (2010).
214 O'Connell, J. T. *et al.* VEGF-A and Tenascin-C produced by S100A4+ stromal cells are important for metastatic colonization. *Proceedings of the National Academy of Sciences of the United States of America* **108**, 16002-16007, doi:10.1073/pnas.1109493108 (2011).
215 Qian, B. Z. *et al.* FLT1 signaling in metastasis-associated macrophages activates an inflammatory signature that promotes breast cancer metastasis. *J Exp Med* **212**, 1433-1448, doi:10.1084/jem.20141555 (2015).
216 Chen, Q., Zhang, X. H. & Massague, J. Macrophage binding to receptor VCAM-1 transmits survival signals in breast cancer cells that invade the lungs. *Cancer Cell* **20**, 538-549, doi:10.1016/j.ccr.2011.08.025 (2011).
217 Gao, D. *et al.* Myeloid progenitor cells in the premetastatic lung promote metastases by inducing mesenchymal to epithelial transition. *Cancer Res* **72**, 1384-1394, doi:10.1158/0008-5472.CAN-11-2905 (2012).
218 Kitamura, T. *et al.* Inactivation of chemokine (C-C motif) receptor 1 (CCR1) suppresses colon cancer liver metastasis by blocking accumulation of immature myeloid cells in a mouse model. *Proceedings of the National Academy of Sciences of the United States of America* **107**, 13063-13068, doi:10.1073/pnas.1002372107 (2010).

219 Gao, D. *et al.* Endothelial progenitor cells control the angiogenic switch in mouse lung metastasis. *Science* **319**, 195-198, doi:10.1126/science.1150224 (2008).
220 Ewertz, M. *et al.* Effect of obesity on prognosis after early-stage breast cancer. *J Clin Oncol* **29**, 25-31, doi:10.1200/JCO.2010.29.7614 (2011).
221 Sestak, I. *et al.* Effect of body mass index on recurrences in tamoxifen and anastrozole treated women: an exploratory analysis from the ATAC trial. *J Clin Oncol* **28**, 3411-3415, doi:10.1200/JCO.2009.27.2021 (2010).
222 Osman, M. A. & Hennessy, B. T. Obesity Correlation With Metastases Development and Response to First-Line Metastatic Chemotherapy in Breast Cancer. *Clin Med Insights Oncol* **9**, 105-112, doi:10.4137/CMO.S32812 (2015).
223 Wu, Y. *et al.* Insulin-like growth factor-I regulates the liver microenvironment in obese mice and promotes liver metastasis. *Cancer Res* **70**, 57-67, doi:10.1158/0008-5472.CAN-09-2472 (2010).
224 Campisi, J. Senescent cells, tumor suppression, and organismal aging: good citizens, bad neighbors. *Cell* **120**, 513-522, doi:10.1016/j.cell.2005.02.003 (2005).
225 Kaur, A. *et al.* sFRP2 in the aged microenvironment drives melanoma metastasis and therapy resistance. *Nature* **532**, 250-254, doi:10.1038/nature17392 (2016).
226 Olsson, A. K. & Cedervall, J. NETosis in Cancer - Platelet-Neutrophil Crosstalk Promotes Tumor-Associated Pathology. *Front Immunol* **7**, 373, doi:10.3389/fimmu.2016.00373 (2016).
227 Tohme, S. *et al.* Neutrophil Extracellular Traps Promote the Development and Progression of Liver Metastases after Surgical Stress. *Cancer Res* **76**, 1367-1380, doi:10.1158/0008-5472.CAN-15-1591 (2016).
228 Cools-Lartigue, J. *et al.* Neutrophil extracellular traps sequester circulating tumor cells and promote metastasis. *The Journal of clinical investigation*, doi:10.1172/JCI67484 (2013).
229 Cox, T. R. *et al.* LOX-mediated collagen crosslinking is responsible for fibrosis-enhanced metastasis. *Cancer Res* **73**, 1721-1732, doi:10.1158/0008-5472.CAN-12-2233 (2013).
230 Rawson, P. *et al.* Metabolic proteomics of the liver and mammary gland during lactation. *J Proteomics* **75**, 4429-4435, doi:10.1016/j.jprot.2012.04.019

S1874-3919(12)00225-4 [pii] (2012).
231 Patel, O. V., Casey, T., Dover, H. & Plaut, K. Homeorhetic adaptation to lactation: comparative transcriptome analysis of mammary, liver, and adipose tissue during the transition from pregnancy to lactation in rats. *Funct Integr Genomics* **11**, 193-202, doi:10.1007/s10142-010-0193-0 (2011).
232 Loor, J. J. *et al.* Temporal gene expression profiling of liver from periparturient dairy cows reveals complex adaptive mechanisms in hepatic function. *Physiol Genomics* **23**, 217-226, doi:00132.2005 [pii]

10.1152/physiolgenomics.00132.2005 (2005).

233 Goddard, E. T. *et al.* The Rodent Liver Undergoes Weaning-Induced Involution and Supports Breast Cancer Metastasis. *Cancer Discov*, doi:10.1158/2159-8290.CD-16-0822 (2016).
234 Aslakson, C. J. & Miller, F. R. Selective events in the metastatic process defined by analysis of the sequential dissemination of subpopulations of a mouse mammary tumor. *Cancer Res* **52**, 1399-1405 (1992).
235 Fantozzi, A. & Christofori, G. Mouse models of breast cancer metastasis. *Breast cancer research : BCR* **8**, 212, doi:10.1186/bcr1530 (2006).
236 Ellenbroek, S. I. & van Rheenen, J. Imaging hallmarks of cancer in living mice. *Nat Rev Cancer* **14**, 406-418, doi:10.1038/nrc3742 (2014).
237 Entenberg, D. *et al.* In vivo subcellular resolution optical imaging in the lung reveals early metastatic proliferation and motility. *Intravital* **4**, doi:10.1080/21659087.2015.1086613 (2015).
238 Goddard, E., Fischer, J. & Schedin, P. A Portal Vein Injection Model to Study Liver Metastasis of Breast Cancer. *Journal of Visualized Experiments* **Accepted**, doi:10.3791/54903 (2016).
239 Hess, K. R. *et al.* Metastatic patterns in adenocarcinoma. *Cancer* **106**, 1624-1633, doi:10.1002/cncr.21778 (2006).
240 Berman, A. T., Thukral, A. D., Hwang, W. T., Solin, L. J. & Vapiwala, N. Incidence and patterns of distant metastases for patients with early-stage breast cancer after breast conservation treatment. *Clin Breast Cancer* **13**, 88-94, doi:10.1016/j.clbc.2012.11.001 (2013).
241 Savci-Heijink, C. D. *et al.* Retrospective analysis of metastatic behaviour of breast cancer subtypes. *Breast Cancer Res Treat* **150**, 547-557, doi:10.1007/s10549-015-3352-0 (2015).
242 Gerratana, L. *et al.* Pattern of metastasis and outcome in patients with breast cancer. *Clin Exp Metastasis* **32**, 125-133, doi:10.1007/s10585-015-9697-2 (2015).
243 Bonotto, M. *et al.* Measures of outcome in metastatic breast cancer: insights from a real-world scenario. *Oncologist* **19**, 608-615, doi:10.1634/theoncologist.2014-0002 (2014).
244 Wyld, L. *et al.* Prognostic factors for patients with hepatic metastases from breast cancer. *Br J Cancer* **89**, 284-290, doi:10.1038/sj.bjc.6601038 (2003).
245 Tarhan, M. O. *et al.* The clinicopathological evaluation of the breast cancer patients with brain metastases: predictors of survival. *Clin Exp Metastasis* **30**, 201-213, doi:10.1007/s10585-012-9528-7 (2013).
246 Tseng, L. M. *et al.* Distant metastasis in triple-negative breast cancer. *Neoplasma* **60**, 290-294, doi:10.4149/neo_2013_038 (2013).
247 Liu, X. H., Man, Y. N., Cao, R., Liu, C. & Wu, X. Z. Individualized chemotherapy based on organ selectivity: a retrospective study of vinorelbine and capecitabine for patients with metastatic breast cancer. *Curr Med Res Opin* **30**, 1017-1024, doi:10.1185/03007995.2014.895310 (2014).
248 Ahn, S. G. *et al.* Prognostic factors for patients with bone-only metastasis in breast cancer. *Yonsei medical journal* **54**, 1168-1177, doi:10.3349/ymj.2013.54.5.1168 (2013).

249 Purushotham, A. *et al.* Age at diagnosis and distant metastasis in breast cancer--a surprising inverse relationship. *Eur J Cancer* **50**, 1697-1705, doi:10.1016/j.ejca.2014.04.002 (2014).
250 Karimi, A., Delpisheh, A., Sayehmiri, K., Saboori, H. & Rahimi, E. Predictive factors of survival time of breast cancer in kurdistan province of Iran between 2006-2014: a cox regression approach. *Asian Pac J Cancer Prev* **15**, 8483-8488 (2014).
251 Pantel, K. & Brakenhoff, R. H. Dissecting the metastatic cascade. *Nature reviews. Cancer* **4**, 448-456, doi:10.1038/nrc1370 (2004).
252 Psaila, B. & Lyden, D. The metastatic niche: adapting the foreign soil. *Nat Rev Cancer* **9**, 285-293, doi:10.1038/nrc2621

nrc2621 [pii] (2009).
253 Zhao, L. *et al.* Recruitment of a myeloid cell subset (CD11b/Gr1 mid) via CCL2/CCR2 promotes the development of colorectal cancer liver metastasis. *Hepatology* **57**, 829-839, doi:10.1002/hep.26094 (2013).
254 Van den Eynden, G. G. *et al.* The multifaceted role of the microenvironment in liver metastasis: biology and clinical implications. *Cancer Res* **73**, 2031-2043, doi:10.1158/0008-5472.CAN-12-3931 (2013).
255 Kang, Y. *et al.* A multigenic program mediating breast cancer metastasis to bone. *Cancer Cell* **3**, 537-549, doi: doi:10.1016/S1535-6108(03)00132-6 (2003).
256 Minn, A. J. *et al.* Genes that mediate breast cancer metastasis to lung. *Nature* **436**, 518-524, doi:10.1038/nature03799 (2005).
257 Bos, P. D. *et al.* Genes that mediate breast cancer metastasis to the brain. *Nature* **459**, 1005-1009, doi:10.1038/nature08021 (2009).
258 Ogba, N. *et al.* Luminal breast cancer metastases and tumor arousal from dormancy are promoted by direct actions of estradiol and progesterone on the malignant cells. *Breast cancer research : BCR* **16**, 489, doi:10.1186/s13058-014-0489-4 (2014).
259 Zhang, Q. *et al.* CCL5-Mediated Th2 Immune Polarization Promotes Metastasis in Luminal Breast Cancer. *Cancer Res* **75**, 4312-4321, doi:10.1158/0008-5472.CAN-14-3590 (2015).
260 Ruffell, B. & Coussens, L. M. Macrophages and therapeutic resistance in cancer. *Cancer Cell* **27**, 462-472, doi:10.1016/j.ccell.2015.02.015 (2015).
261 Koyama, S. *et al.* Adaptive resistance to therapeutic PD-1 blockade is associated with upregulation of alternative immune checkpoints. *Nat Commun* **7**, 10501, doi:10.1038/ncomms10501 (2016).
262 Quail, D. F. *et al.* The tumor microenvironment underlies acquired resistance to CSF-1R inhibition in gliomas. *Science* **352**, aad3018, doi:10.1126/science.aad3018 (2016).
263 Dexter, D. L. *et al.* Heterogeneity of tumor cells from a single mouse mammary tumor. *Cancer Res* **38**, 3174-3181 (1978).
264 Pulaski, B. A. & Ostrand-Rosenberg, S. Reduction of established spontaneous mammary carcinoma metastases following immunotherapy with major

histocompatibility complex class II and B7.1 cell-based tumor vaccines. *Cancer Res* **58**, 1486-1493 (1998).
265 Doornebal, C. W. *et al.* A preclinical mouse model of invasive lobular breast cancer metastasis. *Cancer Res* **73**, 353-363, doi:10.1158/0008-5472.CAN-11-4208 (2013).
266 Derksen, P. W. *et al.* Somatic inactivation of E-cadherin and p53 in mice leads to metastatic lobular mammary carcinoma through induction of anoikis resistance and angiogenesis. *Cancer Cell* **10**, 437-449, doi:10.1016/j.ccr.2006.09.013 (2006).
267 Pravtcheva, D. D. & Wise, T. L. Metastasizing mammary carcinomas in H19 enhancers-Igf2 transgenic mice. *J Exp Zool* **281**, 43-57, doi:10.1002/(SICI)1097-010X(19980501)281:1<43::AID-JEZ7>3.0.CO;2-C (1998).
268 Lin, S. C. *et al.* Somatic mutation of p53 leads to estrogen receptor alpha-positive and -negative mouse mammary tumors with high frequency of metastasis. *Cancer Res* **64**, 3525-3532, doi:10.1158/0008-5472.CAN-03-3524 (2004).
269 Basse, P., Hokland, P., Heron, I. & Hokland, M. Fate of tumor cells injected into left ventricle of heart in BALB/c mice: role of natural killer cells. *J Natl Cancer Inst* **80**, 657-665, doi:10.1093/jnci/80.9.657 (1988).
270 Campbell, J. P., Merkel, A. R., Masood-Campbell, S. K., Elefteriou, F. & Sterling, J. A. Models of bone metastasis. *J Vis Exp*, e4260, doi:10.3791/4260 (2012).
271 Balathasan, L., Beech, J. S. & Muschel, R. J. Ultrasonography-guided intracardiac injection: an improvement for quantitative brain colonization assays. *The American journal of pathology* **183**, 26-34, doi:10.1016/j.ajpath.2013.03.003 (2013).
272 Werbeck, J. L. *et al.* Tumor microenvironment regulates metastasis and metastasis genes of mouse MMTV-PymT mammary cancer cells in vivo. *Vet Pathol* **51**, 868-881, doi:10.1177/0300985813505116 (2014).
273 Zhou, H. & Zhao, D. Ultrasound imaging-guided intracardiac injection to develop a mouse model of breast cancer brain metastases followed by longitudinal MRI. *J Vis Exp*, doi:10.3791/51146 (2014).
274 Rajendran, S. *et al.* Murine bioluminescent hepatic tumour model. *J Vis Exp*, doi:10.3791/1977 (2010).
275 Soares, K. C. *et al.* A preclinical murine model of hepatic metastases. *J Vis Exp*, 51677, doi:10.3791/51677 (2014).
276 Nahrendorf, M. *et al.* The healing myocardium sequentially mobilizes two monocyte subsets with divergent and complementary functions. *J Exp Med* **204**, 3037-3047, doi:10.1084/jem.20070885 (2007).
277 Swirski, F. K. *et al.* Identification of splenic reservoir monocytes and their deployment to inflammatory sites. *Science* **325**, 612-616, doi:10.1126/science.1175202 (2009).
278 Levy, L. *et al.* Splenectomy inhibits non-small cell lung cancer growth by modulating anti-tumor adaptive and innate immune response. *Oncoimmunology* **4**, e998469, doi:10.1080/2162402X.2014.998469 (2015).

279 Higashijima, J. *et al.* Effect of splenectomy on antitumor immune system in mice. *Anticancer Res* **29**, 385-393 (2009).
280 Wu, T. *et al.* Multimodal imaging of a humanized orthotopic model of hepatocellular carcinoma in immunodeficient mice. *Sci Rep* **6**, 35230, doi:10.1038/srep35230 (2016).
281 Thalheimer, A. *et al.* The intraportal injection model: a practical animal model for hepatic metastases and tumor cell dissemination in human colon cancer. *BMC Cancer* **9**, 29, doi:10.1186/1471-2407-9-29 (2009).
282 Limani, P. *et al.* Selective portal vein injection for the design of syngeneic models of liver malignancy. *Am J Physiol Gastrointest Liver Physiol* **310**, G682-688, doi:10.1152/ajpgi.00209.2015 (2016).
283 Lelekakis, M. *et al.* A novel orthotopic model of breast cancer metastasis to bone. *Clin Exp Metastasis* **17**, 163-170, doi:10.1023/A:1006689719505 (1999).
284 Pulaski, B. A. & Ostrand-Rosenberg, S. Mouse 4T1 breast tumor model. *Current protocols in immunology / edited by John E. Coligan ... [et al.]* **Chapter 20**, Unit 20 22, doi:10.1002/0471142735.im2002s39 (2001).
285 Mahoney, K. H., Miller, B. E. & Heppner, G. H. FACS quantitation of leucine aminopeptidase and acid phosphatase on tumor-associated macrophages from metastatic and nonmetastatic mouse mammary tumors. *J Leukoc Biol* **38**, 573-585 (1985).
286 Rak, J. W., McEachern, D. & Miller, F. R. Sequential alteration of peanut agglutinin binding-glycoprotein expression during progression of murine mammary neoplasia. *Br J Cancer* **65**, 641-648, doi:10.1038/bjc.1992.138 (1992).
287 Allott, E. H. *et al.* Non-steroidal anti-inflammatory drug use, hormone receptor status, and breast cancer-specific mortality in the Carolina Breast Cancer Study. *Breast Cancer Res Treat* **147**, 415-421, doi:10.1007/s10549-014-3099-z (2014).
288 Kim, S. *et al.* Lifetime use of nonsteroidal anti-inflammatory drugs and breast cancer risk: results from a prospective study of women with a sister with breast cancer. *BMC Cancer* **15**, 960, doi:10.1186/s12885-015-1979-1 (2015).
289 Esbona, K. *et al.* COX-2 modulates mammary tumor progression in response to collagen density. *Breast Cancer Res* **18**, 35, doi:10.1186/s13058-016-0695-3 (2016).
290 Andrade, R. J. *et al.* Drug-induced liver injury: an analysis of 461 incidences submitted to the Spanish registry over a 10-year period. *Gastroenterology* **129**, 512-521, doi:10.1016/j.gastro.2005.05.006 (2005).
291 Chalasani, N. *et al.* Causes, clinical features, and outcomes from a prospective study of drug-induced liver injury in the United States. *Gastroenterology* **135**, 1924-1934, 1934 e1921-1924, doi:10.1053/j.gastro.2008.09.011 (2008).
292 Adamson, T. W. *et al.* Assessment of carprofen and buprenorphine on recovery of mice after surgical removal of the mammary fat pad. *J Am Assoc Lab Anim Sci* **49**, 610-616 (2010).
293 Doornebal, C. W. *et al.* Morphine does not facilitate breast cancer progression in two preclinical mouse models for human invasive lobular and HER2(+)

breast cancer. *Pain* **156**, 1424-1432, doi:10.1097/j.pain.0000000000000136 (2015).
294 Fischer, A. H., Jacobson, K. A., Rose, J. & Zeller, R. Paraffin embedding tissue samples for sectioning. *CSH Protoc* **2008**, pdb prot4989, doi:10.1101/pdb.prot4989 (2008).
295 Cardiff, R. D., Miller, C. H. & Munn, R. J. Manual hematoxylin and eosin staining of mouse tissue sections. *Cold Spring Harb Protoc* **2014**, 655-658, doi:10.1101/pdb.prot073411 (2014).
296 Maller, O. *et al.* Collagen architecture in pregnancy-induced protection from breast cancer. *J Cell Sci* **126**, 4108-4110, doi:10.1242/jcs.121590 (2013).
297 Day, C. P. *et al.* "Glowing head" mice: a genetic tool enabling reliable preclinical image-based evaluation of cancers in immunocompetent allografts. *PLoS One* **9**, e109956, doi:10.1371/journal.pone.0109956 (2014).
298 Schafer, M. & Werner, S. Cancer as an overhealing wound: an old hypothesis revisited. *Nat Rev Mol Cell Biol* **9**, 628-638, doi:10.1038/nrm2455 (2008).
299 Kuraishy, A., Karin, M. & Grivennikov, S. I. Tumor promotion via injury- and death-induced inflammation. *Immunity* **35**, 467-477, doi:10.1016/j.immuni.2011.09.006 (2011).
300 Herreros-Villanueva, M., Hijona, E., Cosme, A. & Bujanda, L. Mouse models of pancreatic cancer. *World J Gastroenterol* **18**, 1286-1294, doi:10.3748/wjg.v18.i12.1286 (2012).
301 Johnson, R. L. & Fleet, J. C. Animal models of colorectal cancer. *Cancer Metastasis Rev* **32**, 39-61, doi:10.1007/s10555-012-9404-6 (2013).
302 Clasquin, M. F., Melamud, E. & Rabinowitz, J. D. LC-MS data processing with MAVEN: a metabolomic analysis and visualization engine. *Current protocols in bioinformatics / editoral board, Andreas D. Baxevanis ... [et al.]* **Chapter 14**, Unit14 11, doi:10.1002/0471250953.bi1411s37 (2012).
303 Hill, R. C., Calle, E. A., Dzieciatkowska, M., Niklason, L. E. & Hansen, K. C. Quantification of Extracellular Matrix Proteins from a Rat Lung Scaffold to Provide a Molecular Readout for Tissue Engineering. *Mol Cell Proteomics*, doi:10.1074/mcp.M114.045260 (2015).
304 Wisniewski, J. R., Zougman, A., Nagaraj, N. & Mann, M. Universal sample preparation method for proteome analysis. *Nature methods* **6**, 359-362, doi:10.1038/nmeth.1322 (2009).
305 MacLean, B. *et al.* Skyline: an open source document editor for creating and analyzing targeted proteomics experiments. *Bioinformatics* **26**, 966-968, doi:10.1093/bioinformatics/btq054 (2010).
306 Fornetti, J. *et al.* Mammary epithelial cell phagocytosis downstream of TGF-beta3 is characterized by adherens junction reorganization. *Cell Death Differ* **23**, 185-196, doi:10.1038/cdd.2015.82 (2016).
307 Xia, J., Sinelnikov, I. V., Han, B. & Wishart, D. S. MetaboAnalyst 3.0--making metabolomics more meaningful. *Nucleic Acids Res* **43**, W251-257, doi:10.1093/nar/gkv380 (2015).
308 Bustamante, J. J., Copple, B. L., Soares, M. J. & Dai, G. Gene profiling of maternal hepatic adaptations to pregnancy. *Liver international : official*

journal of the International Association for the Study of the Liver **30**, 406-415, doi:10.1111/j.1478-3231.2009.02183.x (2010).
309 Milona, A. *et al.* The normal mechanisms of pregnancy-induced liver growth are not maintained in mice lacking the bile acid sensor Fxr. *Am J Physiol Gastrointest Liver Physiol* **298**, G151-158, doi:10.1152/ajpgi.00336.2009 (2010).
310 Rudolph, M. C. *et al.* Metabolic regulation in the lactating mammary gland: a lipid synthesizing machine. *Physiol Genomics* **28**, 323-336, doi:10.1152/physiolgenomics.00020.2006 (2007).
311 Harkness, M. L. & Harkness, R. D. The collagen content of the liver in pregnancy and lactation. *J Physiol* **134**, 135-138 (1956).
312 Burnier, J. V. *et al.* Type IV collagen-initiated signals provide survival and growth cues required for liver metastasis. *Oncogene* **30**, 3766-3783, doi:10.1038/onc.2011.89 (2011).
313 Freire-de-Lima, C. G. *et al.* Apoptotic cells, through transforming growth factor-beta, coordinately induce anti-inflammatory and suppress pro-inflammatory eicosanoid and NO synthesis in murine macrophages. *J Biol Chem* **281**, 38376-38384 (2006).
314 Ramachandran, P. *et al.* Differential Ly-6C expression identifies the recruited macrophage phenotype, which orchestrates the regression of murine liver fibrosis. *Proc Natl Acad Sci U S A* **109**, E3186-3195, doi:10.1073/pnas.1119964109 (2012).
315 Cook, R. S. *et al.* MerTK inhibition in tumor leukocytes decreases tumor growth and metastasis. *The Journal of clinical investigation* **123**, 3231-3242, doi:10.1172/JCI67655 (2013).
316 Fornetti, J., Martinson, H., Borges, V. & Schedin, P. Emerging targets for the prevention of pregnancy-associated breast cancer. *Cell Cycle* **11**, 639-640, doi:19358 [pii]

10.4161/cc.11.4.19358 (2012).
317 Fornetti, J. *et al.* Mammary gland involution as an immunotherapeutic target for postpartum breast cancer. *J Mammary Gland Biol Neoplasia* **19**, 213-228, doi:10.1007/s10911-014-9322-z (2014).
318 Fornetti, J., Jindal, S., Middleton, K. A., Borges, V. F. & Schedin, P. Physiological COX-2 expression in breast epithelium associates with COX-2 levels in ductal carcinoma in situ and invasive breast cancer in young women. *Am J Pathol* **184**, 1219-1229, doi:10.1016/j.ajpath.2013.12.026 (2014).
319 Wang, D. & Dubois, R. N. Eicosanoids and cancer. *Nat Rev Cancer* **10**, 181-193, doi:10.1038/nrc2809 (2010).
320 Ricciotti, E. & FitzGerald, G. A. Prostaglandins and inflammation. *Arterioscler Thromb Vasc Biol* **31**, 986-1000, doi:10.1161/ATVBAHA.110.207449 (2011).
321 Dubois, R. N. *et al.* Cyclooxygenase in biology and disease. *FASEB J* **12**, 1063-1073 (1998).
322 Vane, J. R., Bakhle, Y. S. & Botting, R. M. Cyclooxygenases 1 and 2. *Annu Rev Pharmacol Toxicol* **38**, 97-120, doi:10.1146/annurev.pharmtox.38.1.97 (1998).

323 Dennis, E. A. & Norris, P. C. Eicosanoid storm in infection and inflammation. *Nat Rev Immunol* **15**, 511-523, doi:10.1038/nri3859 (2015).
324 Zelenay, S. *et al.* Cyclooxygenase-Dependent Tumor Growth through Evasion of Immunity. *Cell* **162**, 1257-1270, doi:10.1016/j.cell.2015.08.015 (2015).
325 Markosyan, N. *et al.* Deletion of cyclooxygenase 2 in mouse mammary epithelial cells delays breast cancer onset through augmentation of type 1 immune responses in tumors. *Carcinogenesis* **32**, 1441-1449, doi:10.1093/carcin/bgr134 (2011).
326 Sinha, P., Clements, V. K., Fulton, A. M. & Ostrand-Rosenberg, S. Prostaglandin E2 promotes tumor progression by inducing myeloid-derived suppressor cells. *Cancer Res* **67**, 4507-4513, doi:10.1158/0008-5472.CAN-06-4174 (2007).
327 Snijdewint, F. G., Kalinski, P., Wierenga, E. A., Bos, J. D. & Kapsenberg, M. L. Prostaglandin E2 differentially modulates cytokine secretion profiles of human T helper lymphocytes. *J Immunol* **150**, 5321-5329 (1993).
328 Huang, M. *et al.* Non-small cell lung cancer cyclooxygenase-2-dependent regulation of cytokine balance in lymphocytes and macrophages: up-regulation of interleukin 10 and down-regulation of interleukin 12 production. *Cancer Res* **58**, 1208-1216 (1998).
329 Baratelli, F. *et al.* Prostaglandin E2 induces FOXP3 gene expression and T regulatory cell function in human CD4+ T cells. *J Immunol* **175**, 1483-1490 (2005).
330 Obermajer, N., Muthuswamy, R., Lesnock, J., Edwards, R. P. & Kalinski, P. Positive feedback between PGE2 and COX2 redirects the differentiation of human dendritic cells toward stable myeloid-derived suppressor cells. *Blood* **118**, 5498-5505, doi:10.1182/blood-2011-07-365825 (2011).
331 von Bergwelt-Baildon, M. S. *et al.* CD25 and indoleamine 2,3-dioxygenase are up-regulated by prostaglandin E2 and expressed by tumor-associated dendritic cells in vivo: additional mechanisms of T-cell inhibition. *Blood* **108**, 228-237, doi:10.1182/blood-2005-08-3507 (2006).
332 Ahmadi, M., Emery, D. C. & Morgan, D. J. Prevention of both direct and cross-priming of antitumor CD8+ T-cell responses following overproduction of prostaglandin E2 by tumor cells in vivo. *Cancer Res* **68**, 7520-7529, doi:10.1158/0008-5472.CAN-08-1060 (2008).
333 Zeddou, M. *et al.* Prostaglandin E2 induces the expression of functional inhibitory CD94/NKG2A receptors in human CD8+ T lymphocytes by a cAMP-dependent protein kinase A type I pathway. *Biochem Pharmacol* **70**, 714-724, doi:10.1016/j.bcp.2005.05.015 (2005).
334 Chang, S. H. *et al.* Role of prostaglandin E2-dependent angiogenic switch in cyclooxygenase 2-induced breast cancer progression. *Proceedings of the National Academy of Sciences of the United States of America* **101**, 591-596, doi:10.1073/pnas.2535911100 (2004).
335 Wang, D. *et al.* CXCL1 induced by prostaglandin E2 promotes angiogenesis in colorectal cancer. *J Exp Med* **203**, 941-951, doi:10.1084/jem.20052124 (2006).

336 Na, Y. R., Yoon, Y. N., Son, D. I. & Seok, S. H. Cyclooxygenase-2 inhibition blocks M2 macrophage differentiation and suppresses metastasis in murine breast cancer model. *PLoS One* **8**, e63451, doi:10.1371/journal.pone.0063451 (2013).
337 Zhou, J. *et al.* Interactions between prostaglandin E(2), liver receptor homologue-1, and aromatase in breast cancer. *Cancer Res* **65**, 657-663 (2005).
338 Buchanan, F. G., Wang, D., Bargiacchi, F. & DuBois, R. N. Prostaglandin E2 regulates cell migration via the intracellular activation of the epidermal growth factor receptor. *The Journal of biological chemistry* **278**, 35451-35457, doi:10.1074/jbc.M302474200 (2003).
339 Larkins, T. L., Nowell, M., Singh, S. & Sanford, G. L. Inhibition of cyclooxygenase-2 decreases breast cancer cell motility, invasion and matrix metalloproteinase expression. *BMC Cancer* **6**, 181, doi:10.1186/1471-2407-6-181 (2006).
340 Stolina, M. *et al.* Specific inhibition of cyclooxygenase 2 restores antitumor reactivity by altering the balance of IL-10 and IL-12 synthesis. *J Immunol* **164**, 361-370 (2000).
341 Dannenberg, A. J. & Subbaramaiah, K. Targeting cyclooxygenase-2 in human neoplasia: rationale and promise. *Cancer Cell* **4**, 431-436 (2003).
342 Eberhart, C. E. *et al.* Up-regulation of cyclooxygenase 2 gene expression in human colorectal adenomas and adenocarcinomas. *Gastroenterology* **107**, 1183-1188 (1994).
343 Haffty, B. G., Yang, Q., Moran, M. S., Tan, A. R. & Reiss, M. Estrogen-dependent prognostic significance of cyclooxygenase-2 expression in early-stage invasive breast cancers treated with breast-conserving surgery and radiation. *Int J Radiat Oncol Biol Phys* **71**, 1006-1013, doi:10.1016/j.ijrobp.2007.11.063 (2008).
344 Kulkarni, S. *et al.* COX-2 and PPARgamma expression are potential markers of recurrence risk in mammary duct carcinoma in-situ. *BMC Cancer* **8**, 36, doi:10.1186/1471-2407-8-36 (2008).
345 Generali, D. *et al.* COX-2 expression is predictive for early relapse and aromatase inhibitor resistance in patients with ductal carcinoma in situ of the breast, and is a target for treatment. *Br J Cancer* **111**, 46-54, doi:10.1038/bjc.2014.236 (2014).
346 Denkert, C. *et al.* Elevated expression of cyclooxygenase-2 is a negative prognostic factor for disease free survival and overall survival in patients with breast carcinoma. *Cancer* **97**, 2978-2987, doi:10.1002/cncr.11437 (2003).
347 Ristimaki, A. *et al.* Prognostic significance of elevated cyclooxygenase-2 expression in breast cancer. *Cancer Res* **62**, 632-635 (2002).
348 Spizzo, G. *et al.* Correlation of COX-2 and Ep-CAM overexpression in human invasive breast cancer and its impact on survival. *Br J Cancer* **88**, 574-578, doi:10.1038/sj.bjc.6600741 (2003).

349 Urban, J. *et al.* Stromal, rather than epithelial cyclooxygenase-2 (COX-2) expression is associated with overall survival of breast cancer patients. *BMC Cancer* **14**, 732, doi:10.1186/1471-2407-14-732 (2014).
350 Henry, W. S. *et al.* Aspirin suppresses growth in PI3K-mutant breast cancer by activating AMPK and inhibiting mTORC1 signaling. *Cancer Res*, doi:10.1158/0008-5472.CAN-16-2400 (2016).
351 Liao, X. *et al.* Aspirin use, tumor PIK3CA mutation, and colorectal-cancer survival. *N Engl J Med* **367**, 1596-1606, doi:10.1056/NEJMoa1207756 (2012).
352 Holmes, M. D. *et al.* COX-2 expression predicts worse breast cancer prognosis and does not modify the association with aspirin. *Breast Cancer Res Treat* **130**, 657-662, doi:10.1007/s10549-011-1651-7 (2011).
353 Holmes, M. D. *et al.* Aspirin intake and survival after breast cancer. *J Clin Oncol* **28**, 1467-1472, doi:10.1200/JCO.2009.22.7918

JCO.2009.22.7918 [pii] (2010).
354 Kwan, M. L., Habel, L. A., Slattery, M. L. & Caan, B. NSAIDs and breast cancer recurrence in a prospective cohort study. *Cancer Causes Control* **18**, 613-620, doi:10.1007/s10552-007-9003-y (2007).
355 Norris, P. C., Reichart, D., Dumlao, D. S., Glass, C. K. & Dennis, E. A. Specificity of eicosanoid production depends on the TLR-4-stimulated macrophage phenotype. *J Leukoc Biol* **90**, 563-574, doi:10.1189/jlb.0311153 (2011).
356 Vancheri, C., Mastruzzo, C., Sortino, M. A. & Crimi, N. The lung as a privileged site for the beneficial actions of PGE2. *Trends Immunol* **25**, 40-46 (2004).
357 Liu, F. *et al.* Feedback amplification of fibrosis through matrix stiffening and COX-2 suppression. *J Cell Biol* **190**, 693-706, doi:10.1083/jcb.201004082 (2010).
358 Huang, S., Wettlaufer, S. H., Hogaboam, C., Aronoff, D. M. & Peters-Golden, M. Prostaglandin E(2) inhibits collagen expression and proliferation in patient-derived normal lung fibroblasts via E prostanoid 2 receptor and cAMP signaling. *Am J Physiol Lung Cell Mol Physiol* **292**, L405-413, doi:10.1152/ajplung.00232.2006 (2007).
359 Sugimoto, Y. & Narumiya, S. Prostaglandin E receptors. *The Journal of biological chemistry* **282**, 11613-11617, doi:10.1074/jbc.R600038200 (2007).
360 Casado, M. *et al.* Contribution of cyclooxygenase 2 to liver regeneration after partial hepatectomy. *FASEB J* **15**, 2016-2018, doi:10.1096/fj.01-0158fje (2001).
361 O'Brien, A. J. *et al.* Immunosuppression in acutely decompensated cirrhosis is mediated by prostaglandin E2. *Nature medicine* **20**, 518-523, doi:10.1038/nm.3516 (2014).
362 Chavez, E. *et al.* Antifibrotic and fibrolytic properties of celecoxib in liver damage induced by carbon tetrachloride in the rat. *Liver international : official journal of the International Association for the Study of the Liver* **30**, 969-978, doi:10.1111/j.1478-3231.2010.02256.x (2010).

363 Yamamoto, H. *et al.* JTE-522, a cyclooxygenase-2 inhibitor, is an effective chemopreventive agent against rat experimental liver fibrosis1. *Gastroenterology* **125**, 556-571 (2003).
364 Paik, Y. H. *et al.* Celecoxib induces hepatic stellate cell apoptosis through inhibition of Akt activation and suppresses hepatic fibrosis in rats. *Gut* **58**, 1517-1527, doi:10.1136/gut.2008.157420 (2009).
365 Li, T. *et al.* Hepatocellular carcinoma-associated fibroblasts trigger NK cell dysfunction via PGE2 and IDO. *Cancer Lett* **318**, 154-161, doi:10.1016/j.canlet.2011.12.020 (2012).
366 FDA. Guidance for Industry: Estimating the maximum safe starting dose in initial clinical trials for therapeutics in adult healthy volunteers. *http://www.fda.gov/downloads/drugs/guidances/ucm078932.pdf* (2005).
367 O'Brien, J., Hansen, K., Barkan, D., Green, J. & Schedin, P. Non-steroidal anti-inflammatory drugs target the pro-tumorigenic extracellular matrix of the postpartum mammary gland. *Int J Dev Biol* **55**, 745-755, doi:113379jo [pii]

10.1387/ijdb.113379jo (2011).
368 Mohammed, N. A., Abd El-Aleem, S. A., El-Hafiz, H. A. & McMahon, R. F. Distribution of constitutive (COX-1) and inducible (COX-2) cyclooxygenase in postviral human liver cirrhosis: a possible role for COX-2 in the pathogenesis of liver cirrhosis. *J Clin Pathol* **57**, 350-354 (2004).
369 Wojcik, M. *et al.* Immunodetection of cyclooxygenase-2 (COX-2) is restricted to tissue macrophages in normal rat liver and to recruited mononuclear phagocytes in liver injury and cholangiocarcinoma. *Histochem Cell Biol* **137**, 217-233, doi:10.1007/s00418-011-0889-9 (2012).
370 Peltekian, K. M., Makowka, L., Williams, R., Blendis, L. M. & Levy, G. A. Prostaglandins in liver failure and transplantation: regeneration, immunomodulation, and cytoprotection. Prostaglandins in Liver Transplantation Research Group. *Liver Transpl Surg* **2**, 171-184 (1996).
371 Zidar, N. *et al.* Cyclooxygenase in normal human tissues--is COX-1 really a constitutive isoform, and COX-2 an inducible isoform? *J Cell Mol Med* **13**, 3753-3763, doi:10.1111/j.1582-4934.2008.00430.x (2009).
372 Hill, R. C., Calle, E. A., Dzieciatkowska, M., Niklason, L. E. & Hansen, K. C. Quantification of extracellular matrix proteins from a rat lung scaffold to provide a molecular readout for tissue engineering. *Mol Cell Proteomics* **14**, 961-973, doi:10.1074/mcp.M114.045260 (2015).
373 Tsujikawa, T. *et al.* Multiplex immunohistochemistry for immune profiling of HPV-associated head and neck cancer. *Journal for ImmunoTherapy of Cancer* **3(Suppl 2)**, 419, doi:10.1186/2051-1426-3-S2-P419 (2015).
374 Tran-Thi, T. A., Gyufko, K., Henninger, H., Busse, R. & Decker, K. Studies on synthesis and degradation of eicosanoids by rat hepatocytes in primary culture. *J Hepatol* **5**, 322-331 (1987).
375 Okumura, T., Nakayama, R., Sago, T. & Saito, K. Identification of prostaglandin E metabolites from primary cultures of rat hepatocytes. *Biochim Biophys Acta* **837**, 197-207 (1985).

376 Anadol, E. *et al.* Prostaglandin F receptor expression in intrauterine tissues of pregnant rats. *J Vet Sci* **15**, 125-131 (2014).
377 Saito, O. *et al.* Expression of the prostaglandin F receptor (FP) gene along the mouse genitourinary tract. *Am J Physiol Renal Physiol* **284**, F1164-1170, doi:10.1152/ajprenal.00441.2002 (2003).
378 Sugimoto, Y. *et al.* Failure of parturition in mice lacking the prostaglandin F receptor. *Science* **277**, 681-683 (1997).
379 Liston, T. E. & Roberts, L. J., 2nd. Transformation of prostaglandin D2 to 9 alpha, 11 beta-(15S)-trihydroxyprosta-(5Z,13E)-dien-1-oic acid (9 alpha, 11 beta-prostaglandin F2): a unique biologically active prostaglandin produced enzymatically in vivo in humans. *Proceedings of the National Academy of Sciences of the United States of America* **82**, 6030-6034 (1985).
380 Samuelsson, B., Granstrom, E., Green, K., Hamberg, M. & Hammarstrom, S. Prostaglandins. *Annu Rev Biochem* **44**, 669-695, doi:10.1146/annurev.bi.44.070175.003321 (1975).
381 Huang, Y. *et al.* Pulmonary vascular destabilization in the premetastatic phase facilitates lung metastasis. *Cancer Res* **69**, 7529-7537, doi:10.1158/0008-5472.CAN-08-4382 (2009).
382 Qualtrough, D. *et al.* Prostaglandin F(2alpha) stimulates motility and invasion in colorectal tumor cells. *International journal of cancer. Journal international du cancer* **121**, 734-740, doi:10.1002/ijc.22755 (2007).
383 Sales, K. J., Boddy, S. C. & Jabbour, H. N. F-prostanoid receptor alters adhesion, morphology and migration of endometrial adenocarcinoma cells. *Oncogene* **27**, 2466-2477, doi:10.1038/sj.onc.1210883 (2008).
384 Basu, S. Novel cyclooxygenase-catalyzed bioactive prostaglandin F2alpha from physiology to new principles in inflammation. *Med Res Rev* **27**, 435-468, doi:10.1002/med.20098 (2007).
385 Basu, S. Oxidative injury induced cyclooxygenase activation in experimental hepatotoxicity. *Biochem Biophys Res Commun* **254**, 764-767, doi:10.1006/bbrc.1998.9956 (1999).
386 Basu, S. & Eriksson, M. Oxidative injury and survival during endotoxemia. *FEBS Lett* **438**, 159-160 (1998).
387 Reid, J., Hughes, C. M., Murray, L. J., Parsons, C. & Cantwell, M. M. Non-steroidal anti-inflammatory drugs for the treatment of cancer cachexia: a systematic review. *Palliat Med* **27**, 295-303, doi:10.1177/0269216312441382 (2013).
388 Kihara, Y. *et al.* Modeling of eicosanoid fluxes reveals functional coupling between cyclooxygenases and terminal synthases. *Biophys J* **106**, 966-975, doi:10.1016/j.bpj.2014.01.015 (2014).
389 Demetz, E. *et al.* The arachidonic acid metabolome serves as a conserved regulator of cholesterol metabolism. *Cell Metab* **20**, 787-798, doi:10.1016/j.cmet.2014.09.004 (2014).
390 Hardwick, J. P. *et al.* Eicosanoids in metabolic syndrome. *Adv Pharmacol* **66**, 157-266, doi:10.1016/B978-0-12-404717-4.00005-6 (2013).

391 Hui, A. Y. *et al.* Effect of celecoxib on experimental liver fibrosis in rat. *Liver international : official journal of the International Association for the Study of the Liver* **26**, 125-136, doi:10.1111/j.1478-3231.2005.01202.x (2006).
392 Hui, A. Y. *et al.* Prostaglandin E2 inhibits transforming growth factor beta 1-mediated induction of collagen alpha 1(I) in hepatic stellate cells. *J Hepatol* **41**, 251-258, doi:10.1016/j.jhep.2004.04.033 (2004).
393 Roche-Nagle, G., Connolly, E. M., Eng, M., Bouchier-Hayes, D. J. & Harmey, J. H. Antimetastatic activity of a cyclooxygenase-2 inhibitor. *Br J Cancer* **91**, 359-365, doi:10.1038/sj.bjc.6601967 (2004).
394 Tomozawa, S. *et al.* Inhibition of haematogenous metastasis of colon cancer in mice by a selective COX-2 inhibitor, JTE-522. *Br J Cancer* **81**, 1274-1279, doi:10.1038/sj.bjc.6694262 (1999).
395 Rainsford, K. D. Ibuprofen: from invention to an OTC therapeutic mainstay. *Int J Clin Pract Suppl*, 9-20, doi:10.1111/ijcp.12055 (2013).
396 Hudson, N., Balsitis, M., Everitt, S. & Hawkey, C. J. Enhanced gastric mucosal leukotriene B4 synthesis in patients taking non-steroidal anti-inflammatory drugs. *Gut* **34**, 742-747 (1993).
397 Wculek, S. K. & Malanchi, I. Neutrophils support lung colonization of metastasis-initiating breast cancer cells. *Nature* **528**, 413-417, doi:10.1038/nature16140 (2015).
398 Anwar, A., Anwar, I. J. & Delafontaine, P. Elevation of cardiovascular risk by non-steroidal anti-inflammatory drugs. *Trends Cardiovasc Med* **25**, 726-735, doi:10.1016/j.tcm.2015.03.006 (2015).
399 Mardini, I. A. & FitzGerald, G. A. Selective inhibitors of cyclooxygenase-2: a growing class of anti-inflammatory drugs. *Mol Interv* **1**, 30-38 (2001).
400 Xu, L. *et al.* COX-2 inhibition potentiates antiangiogenic cancer therapy and prevents metastasis in preclinical models. *Sci Transl Med* **6**, 242ra284, doi:10.1126/scitranslmed.3008455 (2014).
401 Dawood, S. *et al.* Defining breast cancer prognosis based on molecular phenotypes: results from a large cohort study. *Breast Cancer Res Treat* **126**, 185-192, doi:10.1007/s10549-010-1113-7 (2011).
402 Cianfrocca, M. & Goldstein, L. J. Prognostic and predictive factors in early-stage breast cancer. *Oncologist* **9**, 606-616, doi:10.1634/theoncologist.9-6-606 (2004).
403 Payne, S. J., Bowen, R. L., Jones, J. L. & Wells, C. A. Predictive markers in breast cancer--the present. *Histopathology* **52**, 82-90, doi:10.1111/j.1365-2559.2007.02897.x (2008).
404 Kennecke, H. *et al.* Metastatic behavior of breast cancer subtypes. *J Clin Oncol* **28**, 3271-3277, doi:10.1200/JCO.2009.25.9820 (2010).
405 Cheang, M. C. *et al.* Ki67 index, HER2 status, and prognosis of patients with luminal B breast cancer. *J Natl Cancer Inst* **101**, 736-750, doi:10.1093/jnci/djp082 (2009).
406 Rosenberg, S. M. & Partridge, A. H. Management of breast cancer in very young women. *Breast* **24 Suppl 2**, S154-158, doi:10.1016/j.breast.2015.07.036 (2015).

407 Schedin, P., O'Brien, J., Rudolph, M., Stein, T. & Borges, V. Microenvironment of the involuting mammary gland mediates mammary cancer progression. *J Mammary Gland Biol Neoplasia* **12**, 71-82, doi:10.1007/s10911-007-9039-3 (2007).
408 Parker, J. S. *et al.* Supervised risk predictor of breast cancer based on intrinsic subtypes. *Journal of clinical oncology : official journal of the American Society of Clinical Oncology* **27**, 1160-1167, doi:10.1200/JCO.2008.18.1370 (2009).
409 Perou, C. M. *et al.* Molecular portraits of human breast tumours. *Nature* **406**, 747-752, doi:10.1038/35021093 (2000).
410 Sorlie, T. *et al.* Repeated observation of breast tumor subtypes in independent gene expression data sets. *Proceedings of the National Academy of Sciences of the United States of America* **100**, 8418-8423, doi:10.1073/pnas.0932692100 (2003).
411 Hu, Z. *et al.* The molecular portraits of breast tumors are conserved across microarray platforms. *BMC Genomics* **7**, 96, doi:10.1186/1471-2164-7-96 (2006).
412 Russnes, H. G., Navin, N., Hicks, J. & Borresen-Dale, A. L. Insight into the heterogeneity of breast cancer through next-generation sequencing. *The Journal of clinical investigation* **121**, 3810-3818, doi:10.1172/JCI57088 (2011).
413 Guo, Y. *et al.* RNA Sequencing of Formalin-Fixed, Paraffin-Embedded Specimens for Gene Expression Quantification and Data Mining. *Int J Genomics* **2016**, 9837310, doi:10.1155/2016/9837310 (2016).
414 Eikrem, O. *et al.* Transcriptome Sequencing (RNAseq) Enables Utilization of Formalin-Fixed, Paraffin-Embedded Biopsies with Clear Cell Renal Cell Carcinoma for Exploration of Disease Biology and Biomarker Development. *PLoS One* **11**, e0149743, doi:10.1371/journal.pone.0149743 (2016).
415 Naba, A., Clauser, K. R., Lamar, J. M., Carr, S. A. & Hynes, R. O. Extracellular matrix signatures of human mammary carcinoma identify novel metastasis promoters. *Elife* **3**, e01308, doi:10.7554/eLife.01308 (2014).
416 Aggeler, J., Park, C. S. & Bissell, M. J. Regulation of milk protein and basement membrane gene expression: the influence of the extracellular matrix. *Journal of dairy science* **71**, 2830-2842 (1988).
417 Streuli, C. H., Bailey, N. & Bissell, M. J. Control of mammary epithelial differentiation: basement membrane induces tissue-specific gene expression in the absence of cell-cell interaction and morphological polarity. *The Journal of cell biology* **115**, 1383-1395 (1991).
418 Werb, Z. *et al.* Extracellular matrix remodeling and the regulation of epithelial-stromal interactions during differentiation and involution. *Kidney international* **54**, S68-74 (1996).
419 Fata, J. E., Werb, Z. & Bissell, M. J. Regulation of mammary gland branching morphogenesis by the extracellular matrix and its remodeling enzymes. *Breast cancer research : BCR* **6**, 1-11, doi:10.1186/bcr634 (2004).
420 Nelson, C. M., Vanduijn, M. M., Inman, J. L., Fletcher, D. A. & Bissell, M. J. Tissue geometry determines sites of mammary branching morphogenesis in organotypic cultures. *Science (New York, N.Y* **314**, 298-300 (2006).

421 Bissell, M. J. & Barcellos-Hoff, M. H. The influence of extracellular matrix on gene expression: is structure the message? *J Cell Sci Suppl* **8**, 327-343 (1987).
422 Barcellos-Hoff, M. H., Aggeler, J., Ram, T. G. & Bissell, M. J. Functional differentiation and alveolar morphogenesis of primary mammary cultures on reconstituted basement membrane. *Development (Cambridge, England)* **105**, 223-235 (1989).
423 Howlett, A. R. & Bissell, M. J. The influence of tissue microenvironment (stroma and extracellular matrix) on the development and function of mammary epithelium. *Epithelial Cell Biol* **2**, 79-89 (1993).
424 Weigelt, B., Ghajar, C. M. & Bissell, M. J. The need for complex 3D culture models to unravel novel pathways and identify accurate biomarkers in breast cancer. *Adv Drug Deliv Rev* **69-70**, 42-51, doi:10.1016/j.addr.2014.01.001 (2014).
425 Shaw, K. R., Wrobel, C. N. & Brugge, J. S. Use of three-dimensional basement membrane cultures to model oncogene-induced changes in mammary epithelial morphogenesis. *J Mammary Gland Biol Neoplasia* **9**, 297-310, doi:10.1007/s10911-004-1402-z (2004).
426 Lee, G. Y., Kenny, P. A., Lee, E. H. & Bissell, M. J. Three-dimensional culture models of normal and malignant breast epithelial cells. *Nature methods* **4**, 359-365, doi:10.1038/nmeth1015 (2007).
427 Fischbach, C. *et al.* Engineering tumors with 3D scaffolds. *Nature methods* **4**, 855-860, doi:10.1038/nmeth1085 (2007).
428 Krause, S., Maffini, M. V., Soto, A. M. & Sonnenschein, C. A novel 3D in vitro culture model to study stromal-epithelial interactions in the mammary gland. *Tissue Eng Part C Methods* **14**, 261-271, doi:10.1089/ten.tec.2008.0030 (2008).
429 Schmeichel, K. L., Weaver, V. M. & Bissell, M. J. Structural cues from the tissue microenvironment are essential determinants of the human mammary epithelial cell phenotype. *Journal of mammary gland biology and neoplasia* **3**, 201-213 (1998).
430 DuFort, C. C., Paszek, M. J. & Weaver, V. M. Balancing forces: architectural control of mechanotransduction. *Nature reviews. Molecular cell biology* **12**, 308-319, doi:10.1038/nrm3112 (2011).
431 Schedin, P. & Keely, P. J. Mammary gland ECM remodeling, stiffness, and mechanosignaling in normal development and tumor progression. *Cold Spring Harb Perspect Biol* **3**, a003228, doi:10.1101/cshperspect.a003228

a003228 [pii]

cshperspect.a003228 [pii] (2011).
432 Hancox, R. A. *et al.* Tumour-associated tenascin-C isoforms promote breast cancer cell invasion and growth by matrix metalloproteinase-dependent and independent mechanisms. *Breast Cancer Res* **11**, R24, doi:10.1186/bcr2251 (2009).
433 Maity, G. *et al.* Culture of human breast cancer cell line (MDA-MB-231) on fibronectin-coated surface induces pro-matrix metalloproteinase-9

expression and activity. *Tumour Biol* **32**, 129-138, doi:10.1007/s13277-010-0106-9 (2011).
434 Boyd, N. F. *et al.* Mammographic densities and breast cancer risk. *Breast Dis* **10**, 113-126 (1998).
435 Li, T. *et al.* The association of measured breast tissue characteristics with mammographic density and other risk factors for breast cancer. *Cancer Epidemiol Biomarkers Prev* **14**, 343-349, doi:10.1158/1055-9965.EPI-04-0490 (2005).
436 Goto, R., Nakamura, Y., Takami, T., Sanke, T. & Tozuka, Z. Quantitative LC-MS/MS Analysis of Proteins Involved in Metastasis of Breast Cancer. *PLoS One* **10**, e0130760, doi:10.1371/journal.pone.0130760 (2015).
437 Naba, A. *et al.* Extracellular matrix signatures of human primary metastatic colon cancers and their metastases to liver. *BMC Cancer* **14**, 518, doi:10.1186/1471-2407-14-518 (2014).
438 Hansen, K. C. *et al.* An in-solution ultrasonication-assisted digestion method for improved extracellular matrix proteome coverage. *Mol Cell Proteomics* **8**, 1648-1657, doi:10.1074/mcp.M900039-MCP200 (2009).
439 Didangelos, A. *et al.* Proteomics characterization of extracellular space components in the human aorta. *Mol Cell Proteomics* **9**, 2048-2062, doi:10.1074/mcp.M110.001693 (2010).
440 Baiocchini, A. *et al.* Extracellular Matrix Molecular Remodeling in Human Liver Fibrosis Evolution. *PLoS One* **11**, e0151736, doi:10.1371/journal.pone.0151736 (2016).
441 Geiger, T. *et al.* Initial quantitative proteomic map of 28 mouse tissues using the SILAC mouse. *Mol Cell Proteomics* **12**, 1709-1722, doi:10.1074/mcp.M112.024919 (2013).
442 Johnson, T. D. *et al.* Quantification of decellularized human myocardial matrix: A comparison of six patients. *Proteomics Clin Appl* **10**, 75-83, doi:10.1002/prca.201500048 (2016).
443 Hattar, R. *et al.* Tamoxifen induces pleiotrophic changes in mammary stroma resulting in extracellular matrix that suppresses transformed phenotypes. *Breast Cancer Res* **11**, R5, doi:10.1186/bcr2220 (2009).
444 Pratt, J. M. *et al.* Multiplexed absolute quantification for proteomics using concatenated signature peptides encoded by QconCAT genes. *Nat Protoc* **1**, 1029-1043, doi:10.1038/nprot.2006.129 (2006).
445 Dennis, G., Jr. *et al.* DAVID: Database for Annotation, Visualization, and Integrated Discovery. *Genome Biol* **4**, P3 (2003).
446 Harrell, J. C. *et al.* Genomic analysis identifies unique signatures predictive of brain, lung, and liver relapse. *Breast Cancer Res Treat* **132**, 523-535, doi:10.1007/s10549-011-1619-7 (2012).
447 Mouw, J. K., Ou, G. & Weaver, V. M. Extracellular matrix assembly: a multiscale deconstruction. *Nat Rev Mol Cell Biol* **15**, 771-785, doi:10.1038/nrm3902 (2014).
448 Iyengar, P. *et al.* Adipocyte-derived collagen VI affects early mammary tumor progression in vivo, demonstrating a critical interaction in the tumor/stroma

microenvironment. *The Journal of clinical investigation* **115**, 1163-1176, doi:10.1172/JCI23424 (2005).
449 Ioachim, E. *et al.* Immunohistochemical expression of extracellular matrix components tenascin, fibronectin, collagen type IV and laminin in breast cancer: their prognostic value and role in tumour invasion and progression. *Eur J Cancer* **38**, 2362-2370 (2002).
450 Yee, K. O. *et al.* The effect of thrombospondin-1 on breast cancer metastasis. *Breast Cancer Res Treat* **114**, 85-96, doi:10.1007/s10549-008-9992-6 (2009).
451 Zhang, H. *et al.* Galectin-3 as a marker and potential therapeutic target in breast cancer. *PLoS One* **9**, e103482, doi:10.1371/journal.pone.0103482 (2014).
452 Karagiannis, G. S. *et al.* Proteomic signatures of the desmoplastic invasion front reveal collagen type XII as a marker of myofibroblastic differentiation during colorectal cancer metastasis. *Oncotarget* **3**, 267-285, doi:10.18632/oncotarget.451 (2012).
453 Yen, T. Y. *et al.* Using a cell line breast cancer progression system to identify biomarker candidates. *J Proteomics* **96**, 173-183, doi:10.1016/j.jprot.2013.11.006 (2014).
454 Cummings, M. C. *et al.* Metastatic progression of breast cancer: insights from 50 years of autopsies. *J Pathol* **232**, 23-31, doi:10.1002/path.4288 (2014).
455 Lai, K. K., Kolippakkam, D. & Beretta, L. Comprehensive and quantitative proteome profiling of the mouse liver and plasma. *Hepatology* **47**, 1043-1051, doi:10.1002/hep.22123 (2008).
456 Lai, K. K. *et al.* Extracellular matrix dynamics in hepatocarcinogenesis: a comparative proteomics study of PDGFC transgenic and Pten null mouse models. *PLoS Genet* **7**, e1002147, doi:10.1371/journal.pgen.1002147 (2011).
457 Da Costa, G. G. *et al.* Comparative Proteomics of Tumor and Paired Normal Breast Tissue Highlights Potential Biomarkers in Breast Cancer. *Cancer Genomics Proteomics* **12**, 251-261 (2015).
458 Moreira, J. M. *et al.* Tissue proteomics of the human mammary gland: towards an abridged definition of the molecular phenotypes underlying epithelial normalcy. *Mol Oncol* **4**, 539-561, doi:10.1016/j.molonc.2010.09.005 (2010).
459 Chu, M. L. *et al.* The structure of type VI collagen. *Ann N Y Acad Sci* **580**, 55-63 (1990).
460 Hughes, K., Wickenden, J. A., Allen, J. E. & Watson, C. J. Conditional deletion of Stat3 in mammary epithelium impairs the acute phase response and modulates immune cell numbers during post-lactational regression. *J Pathol* **227**, 106-117, doi:10.1002/path.3961 (2012).
461 Chapman, R. S. *et al.* Suppression of epithelial apoptosis and delayed mammary gland involution in mice with a conditional knockout of Stat3. *Genes Dev* **13**, 2604-2616 (1999).
462 Li, M. *et al.* Mammary-derived signals activate programmed cell death during the first stage of mammary gland involution. *Proc Natl Acad Sci U S A* **94**, 3425-3430 (1997).

463 O'Brien, J., Martinson, H., Durand-Rougely, C. & Schedin, P. Macrophages are crucial for epithelial cell death and adipocyte repopulation during mammary gland involution. *Development* **139**, 269-275, doi:dev.071696 [pii]

10.1242/dev.071696 (2012).
464 Burnett, S. H. *et al.* Conditional macrophage ablation in transgenic mice expressing a Fas-based suicide gene. *J Leukoc Biol* **75**, 612-623, doi:10.1189/jlb.0903442

jlb.0903442 [pii] (2004).
465 Bilzer, M., Roggel, F. & Gerbes, A. L. Role of Kupffer cells in host defense and liver disease. *Liver international : official journal of the International Association for the Study of the Liver* **26**, 1175-1186, doi:10.1111/j.1478-3231.2006.01342.x (2006).
466 Shimabukuro, M., Zhou, Y. T., Levi, M. & Unger, R. H. Fatty acid-induced beta cell apoptosis: a link between obesity and diabetes. *Proceedings of the National Academy of Sciences of the United States of America* **95**, 2498-2502 (1998).
467 Akazawa, Y. & Nakao, K. Lipotoxicity pathways intersect in hepatocytes: Endoplasmic reticulum stress, c-Jun N-terminal kinase-1, and death receptors. *Hepatol Res* **46**, 977-984, doi:10.1111/hepr.12658 (2016).
468 Chokkathukalam, A., Kim, D. H., Barrett, M. P., Breitling, R. & Creek, D. J. Stable isotope-labeling studies in metabolomics: new insights into structure and dynamics of metabolic networks. *Bioanalysis* **6**, 511-524, doi:10.4155/bio.13.348 (2014).
469 Fan, T. W. *et al.* Stable isotope-resolved metabolomics and applications for drug development. *Pharmacol Ther* **133**, 366-391, doi:10.1016/j.pharmthera.2011.12.007 (2012).
470 Russell, T. D. *et al.* Myoepithelial cell differentiation markers in ductal carcinoma in situ progression. *Am J Pathol* **185**, 3076-3089, doi:10.1016/j.ajpath.2015.07.004 (2015).
471 Kang, J. X., Wang, J., Wu, L. & Kang, Z. B. Transgenic mice: fat-1 mice convert n-6 to n-3 fatty acids. *Nature* **427**, 504, doi:10.1038/427504a (2004).
472 Weylandt, K. H. *et al.* Suppressed liver tumorigenesis in fat-1 mice with elevated omega-3 fatty acids is associated with increased omega-3 derived lipid mediators and reduced TNF-alpha. *Carcinogenesis* **32**, 897-903, doi:10.1093/carcin/bgr049

bgr049 [pii] (2011).
473 Rose, D. P., Connolly, J. M. & Coleman, M. Effect of omega-3 fatty acids on the progression of metastases after the surgical excision of human breast cancer cell solid tumors growing in nude mice. *Clin Cancer Res* **2**, 1751-1756 (1996).
474 Di Minno, M. N. *et al.* Omega-3 fatty acids for the treatment of non-alcoholic fatty liver disease. *World J Gastroenterol* **18**, 5839-5847, doi:10.3748/wjg.v18.i41.5839 (2012).

475 Kim, E. H., Bae, J. S., Hahm, K. B. & Cha, J. Y. Endogenously synthesized n-3 polyunsaturated fatty acids in fat-1 mice ameliorate high-fat diet-induced non-alcoholic fatty liver disease. *Biochem Pharmacol* **84**, 1359-1365, doi:10.1016/j.bcp.2012.08.029 (2012).
476 Grant, D. S. *et al.* The basement-membrane-like matrix of the mouse EHS tumor: II. Immunohistochemical quantitation of six of its components. *The American journal of anatomy* **174**, 387-398 (1985).
477 Colognato, H. & Yurchenco, P. D. Form and function: the laminin family of heterotrimers. *Dev Dyn* **218**, 213-234, doi:10.1002/(SICI)1097-0177(200006)218:2<213::AID-DVDY1>3.0.CO;2-R (2000).
478 Peela, N. *et al.* A three dimensional micropatterned tumor model for breast cancer cell migration studies. *Biomaterials* **81**, 72-83, doi:10.1016/j.biomaterials.2015.11.039 (2016).
479 Lin, C. H., Lee, J. K. & LaBarge, M. A. Fabrication and use of microenvironment microarrays (MEArrays). *J Vis Exp*, doi:10.3791/4152 (2012).
480 Flaim, C. J., Chien, S. & Bhatia, S. N. An extracellular matrix microarray for probing cellular differentiation. *Nature methods* **2**, 119-125, doi:10.1038/nmeth736 (2005).
481 Gobaa, S. *et al.* Artificial niche microarrays for probing single stem cell fate in high throughput. *Nature methods* **8**, 949-955, doi:10.1038/nmeth.1732 (2011).
482 Uygun, B. E. *et al.* Organ reengineering through development of a transplantable recellularized liver graft using decellularized liver matrix. *Nat Med* **16**, 814-820, doi:10.1038/nm.2170 (2010).
483 Navarro-Tableros, V. *et al.* Recellularization of rat liver scaffolds by human liver stem cells. *Tissue Eng Part A* **21**, 1929-1939, doi:10.1089/ten.TEA.2014.0573 (2015).
484 O'Brien, J., Fornetti, J. & Schedin, P. Isolation of mammary-specific extracellular matrix to assess acute cell-ECM interactions in 3D culture. *J Mammary Gland Biol Neoplasia* **15**, 353-364, doi:10.1007/s10911-010-9185-x (2010).
485 Hu, C. & Li, L. In vitro culture of isolated primary hepatocytes and stem cell-derived hepatocyte-like cells for liver regeneration. *Protein Cell* **6**, 562-574, doi:10.1007/s13238-015-0180-2 (2015).
486 Skardal, A. *et al.* Tissue specific synthetic ECM hydrogels for 3-D in vitro maintenance of hepatocyte function. *Biomaterials* **33**, 4565-4575, doi:10.1016/j.biomaterials.2012.03.034 (2012).
487 Nishida, Y. & Taniguchi, A. A three-dimensional collagen-sponge-based culture system coated with simplified recombinant fibronectin improves the function of a hepatocyte cell line. *In Vitro Cell Dev Biol Anim* **52**, 271-277, doi:10.1007/s11626-015-9973-0 (2016).
488 Rockwell, S. C., Kallman, R. F. & Fajardo, L. F. Characteristics of a serially transplanted mouse mammary tumor and its tissue-culture-adapted derivative. *J Natl Cancer Inst* **49**, 735-749 (1972).
489 Naugler, W. E. Bile acid flux is necessary for normal liver regeneration. *PLoS One* **9**, e97426, doi:10.1371/journal.pone.0097426 (2014).

490 Naugler, W. E. *et al.* Fibroblast Growth Factor Signaling Controls Liver Size in Mice With Humanized Livers. *Gastroenterology* **149**, 728-740 e715, doi:10.1053/j.gastro.2015.05.043 (2015).
491 Auffray, C., Sieweke, M. H. & Geissmann, F. Blood monocytes: development, heterogeneity, and relationship with dendritic cells. *Annu Rev Immunol* **27**, 669-692, doi:10.1146/annurev.immunol.021908.132557 (2009).
492 Wang, J. & Kubes, P. A Reservoir of Mature Cavity Macrophages that Can Rapidly Invade Visceral Organs to Affect Tissue Repair. *Cell* **165**, 668-678, doi:10.1016/j.cell.2016.03.009 (2016).
493 Mouta Carreira, C. *et al.* LYVE-1 is not restricted to the lymph vessels: expression in normal liver blood sinusoids and down-regulation in human liver cancer and cirrhosis. *Cancer Res* **61**, 8079-8084 (2001).
494 Truman, L. A. *et al.* ProxTom lymphatic vessel reporter mice reveal Prox1 expression in the adrenal medulla, megakaryocytes, and platelets. *Am J Pathol* **180**, 1715-1725, doi:10.1016/j.ajpath.2011.12.026 (2012).
495 Schneider, C. A., Rasband, W. S. & Eliceiri, K. W. NIH Image to ImageJ: 25 years of image analysis. *Nature methods* **9**, 671-675 (2012).
496 Grompe, M., Jones, S. N., Loulseged, H. & Caskey, C. T. Retroviral-mediated gene transfer of human ornithine transcarbamylase into primary hepatocytes of spf and spf-ash mice. *Hum Gene Ther* **3**, 35-44, doi:10.1089/hum.1992.3.1-35 (1992).